



Emily McDonnell, B.A.I, M.A.I

From “Bench to Bedside”: *In-Silico* Modelling to Inform the
Assessment of Intervertebral Disc Cell-Based Therapies

Trinity College Dublin, April 2023

A thesis submitted to the University of Dublin in partial
fulfilment of the requirements for the degree of
Doctor in Philosophy

Supervisor: Prof. Conor T. Buckley

Internal Examiner: Prof. Cairíona Lally

External Examiner: Prof. Morgan Giers

Declaration

I declare that this thesis has not been submitted as an exercise for a degree at this or any other university and it is entirely my own work.

I agree to deposit this thesis in the University's open access institutional repository or allow the Library to do so on my behalf, subject to Irish Copyright Legislation and Trinity College Library conditions of use and acknowledgement.

I consent to the examiner retaining a copy of the thesis beyond the examining period, should they so wish (EU GDPR May 2018).

Emily McDonnell

Summary

With an aging and increasingly sedentary population, significant research is being undertaken to halt or reverse intervertebral disc (IVD) degeneration, which is believed to be a primary contributor to lower back pain. Despite its debilitating consequences current clinical treatments mainly aim to alleviate pain rather than treat the underlying degeneration. Encouragingly, the spine field is filled with a growing body of basic research and many promising therapies have demonstrated pre-clinical efficacy and potential. Nonetheless, the IVD is a large avascular structure, hampered by significant diffusion distances, thus giving rise to metabolite gradients which are confounded further by several pathological features. Subsequently, this thesis focuses on the importance of the nutrient microenvironment throughout the full development and assessment process, in order to accelerate the translation endeavours of cell therapies, all the way from “bench to bedside”.

To achieve this, *in-silico* modelling was utilised together with experimental investigations, which either propelled the models as key input parameters or worked towards their experimental validation. Firstly, this work sought to consolidate early metabolite measurements and employ *in-silico* models, underpinned by more recent experimental parameters, with the objective of re-evaluating the current knowledge in terms of grade-specific stages of degeneration. Taken together, pre-existing measurements and the results predicted in this work suggest that concentrations may not be as critically low as commonly believed. Furthermore, this work predicted that calcification does not appear to have a detrimental effect at earlier stages of degeneration when cell-based regeneration is a viable treatment. Ultimately, this work advances *in-silico* modelling through a strong foundation of experimentally determined data on degeneration grade-specific metabolically active cell densities, tissue hydration, diffusion parameters and calcification. However, there are assumptions and limitations and further intradiscal measurements are needed to ascertain confidence in nutrient-transport models and may need to be assessed in a patient-specific manner. Nonetheless, *in-silico* modelling can provide a wealth of information on the degenerating IVD, which is a relatively complex and challenging structure to access and assess *in vivo*.

The research field has been challenged by heterogeneous results in terms of the regenerative potential of cell therapies, even at a basic *in vitro* culture stage. Consequently, there is an agenda of standardisation across the field to advance reproducibility. To this extent, this work sought to consolidate commonly used culturing parameters over the last ~ 15 years. Nutrient-transport *in-silico* models were used to characterise the local nutrient microenvironment in 2D cell monolayers and commonly used 3D *in vitro* culture systems, in order to (i) highlight the effect of culturing parameters and (ii) to place “standard practice” culturing conditions into

context in terms of physiological relevance. The results showed that a disconnect often occurs between the external incubator or media concentrations and the actual local cellular concentrations. Furthermore, large variations and gradients in concentrations are easily established without the careful consideration of key parameters and this diversity currently exists across the research field. Following *in vitro* characterisation, *ex vivo* organ culture systems offer unparalleled advantages for the testing of new therapies. However, prior to this thesis, the metabolite concentrations within these systems had never been directly measured. Therefore, this work established an *ex vivo* bovine caudal culture system under standard high glucose (25 mM) and normoxic (20 %O₂) conditions. The metabolically active cell density of the tissue was determined and used to create *in-silico* models of the cultured discs. Experimental validation of these models was performed by measuring oxygen, glucose and pH in discs cultured for seven days. This work found that supraphysiological levels of glucose exist in the centre of bovine caudal discs under these conditions. Although this work initially sought to provide specific guidelines for *in vitro* culture conditions, every system is unique and while one external concentration may be suitable for one configuration, it may not be appropriate for another. For example, depending on the choice of culture vessel, geometry, external concentrations, and cell seeding density, different and distinct local nutrient microenvironments will be established. As a result, this work calls for greater attention to the combined effects of these parameters on the local microenvironment and the confounding downstream influences on gene expression and matrix synthesis, particularly when attempting to understand heterogeneity of results between studies.

Next, these developing therapies typically undergo pre-clinical assessment in an *in vivo* animal model and even after demonstrating promise, results are stunted clinically. For the first time this work presents GAG regeneration *in-silico* models which correlate favourably to pre-clinical literature in terms of the regeneration capabilities of a small and large animal model and predict that compromised nutrition is not a significant challenge in small animal discs. These *in-silico* models were built on a strong foundation of experimentally determined parameters including species-specific geometries, cell densities, metabolic rates and matrix synthesis rates for rat, goat and human nucleus pulposus and annulus fibrosus cells. However, this work highlights a very fine clinical balance between an adequate cell dose for sufficient repair, through de novo matrix deposition, without exacerbating the human microenvironmental niche. While these findings help to explain the failed translation of promising pre-clinical data and the limited results emerging from clinical trials at present, they also enable the research field and clinicians to manage expectations on cell-based regeneration. Furthermore, these results may inform the design of clinical trials in terms of more long term follow up assessment (over a number of years) for positive functional change. Additionally, as computing power and software capabilities increase, it is conceivable that the future holds the generation of patient-specific models which could be used for patient assessment, as well as pre- and intraoperative planning.

Acknowledgements

First and foremost, I would like to sincerely thank my supervisor Prof. Conor Buckley for his unwavering support and continued belief in me. His passion for research, dedication to his students and enthusiasm to teach is inspiring. I really could not have asked for a better mentor during both my undergraduate and postgraduate studies. I would like to extend my appreciation to Prof. Caitríona Lally and Prof. Danny Kelly for serving on my committee and providing their valuable advice and expertise throughout the doctoral process. I would also like to thank my external examiner Prof. Morgan Giers for taking the time to read this thesis and travel all the way to examine it in person.

There have been a number of people who have made this work feasible. For the animal work, I would like to thank Dr. Audrey Carroll from the School of Biochemistry and Immunology for the supply of rats and Prof. Pieter Brama from School of Veterinary Medicine UCD for all his help getting goat samples. For the human work, I would like to thank the spinal orthopaedic team from the Mater Misericordiae University Hospital who provided me with very timely and valuable surgical samples.

There have been many great members in the Buckley group and throughout TCBE, past and present, to all of whom I am very grateful for offering help and support whenever possible. In particular, I would like to send thanks and appreciation to Brooke, who has shared so much of this journey with me, both in and outside of work. There is nobody I would rather have done it all with. To Ross, there were many days I would not have got through without your friendship, advice, and invaluable knowledge. To Meena, maybe all of this would have been wrapped up sooner without our coffee breaks, but I wouldn't change a thing.

I would like to thank my family for all their loving support and patience during my time as a student in Trinity, an entire decade. To my dad, the whole thesis would have felt an impossible endeavour without your help proof-reading. Last but not least, I would like to thank 'my Conor' without whom I would have spent many more weekends in the lab. You have been a constant source of happiness throughout the PhD, surrounding me with endless love, understanding, colour and positivity.

List of Publications and Conference Proceedings

First-author publications

McDonnell, E. E. and Buckley, C. T. (2021) ‘Investigating the physiological relevance of ex vivo disc organ culture nutrient microenvironments using in-silico modeling and experimental validation’, *JOR Spine*, 4(2), doi: <https://doi.org/10.1002/jsp2.1141>

Contribution: Substantial contribution to study design, data acquisition and computational modelling, data analysis and presentation, interpretation of data, drafting of the article, revising it critically and final approval.

McDonnell, E. E. and Buckley, C. T. (2022) ‘Consolidating and re-evaluating the human disc nutrient microenvironment’, *JOR Spine*, 5(1), doi: <https://doi.org/10.1002/jsp2.1192>

Contribution: Contributed substantially to the conception and design of the work, performed the acquisition, analysis, and interpretation of literature data, computational modelling, analysis presentation and interpretation of results, drafting of the article, revising it critically, and final approval.

McDonnell, E. E. and Buckley, C. T. (2022) ‘Two-and three-dimensional in vitro nucleus pulposus cultures: An in-silico analysis of local nutrient microenvironments’, *JOR Spine*, 5(3), doi: <https://doi.org/10.1002/jsp2.1222>

Contribution: Performed the acquisition and interpretation of literature data, computational modelling, analysis presentation and interpretation of results, drafting of the article, revising it critically, and final approval.

McDonnell, E. E., Wilson, N., Barcellona, M. N., Ní Néill, T., Brama, P. A., Cunniffe, G., Darwish, S., Butler, J. S., and Buckley C. T. (2023) ‘Preclinical to Clinical Translation: Effects of Species-Specific Scale, Metabolism and Matrix Synthesis Rates on Intervertebral Disc Cell-Based Regeneration’ *Preparation in progress.*

Contribution: Substantial contribution to the conception and study design, performed the data acquisition, analysis, and interpretation. Performed the computational modelling, presentation and interpretation of results, drafting of the article, revising it critically, and final approval.

Co-first author publications

Barcellona, M. N., **McDonnell, E. E.**, Samuel, S., and Buckley, C. T. (2022) ‘Rat tail models for the assessment of injectable nucleus pulposus regeneration strategies’, *JOR Spine*, 5(3), doi: <https://doi.org/10.1002/jsp2.1216>

Contribution: Contributed to the conception and design of the work. Formed the acquisition, analysis, and interpretation of literature data. Performed the pilot rat study, acquisition, analysis, presentation, and interpretation of results, drafting of the article, revising it critically and final approval. In particular the rat geometrical analysis is presented in Chapter 7 of this thesis.

Co-author publications

Basatvat, S., **McDonnell, E. E.** *et al.* (2023) ‘Harmonization and standardization of nucleus pulposus cell extraction and culture methods’, *JOR Spine*, available for early view, doi: <https://doi.org/10.1002/jsp2.1238>

Contribution: Contributed to the acquisition of laboratory data for rat, performed data analysis, data interpretation and drafted the manuscript.

Samuel, S., **McDonnell, E. E.** and Buckley, C. T. (2022) ‘Effects of Growth Factor Combinations TGF β 3, GDF5 and GDF6 on the Matrix Synthesis of Nucleus Pulposus and Nasoseptal Chondrocyte Self-Assembled Microtissues’, *Applied Sciences*. 12(3), doi: <https://doi.org/10.3390/app12031453>

Contribution: Designed and fabricated the positive mould stamp for the micro-spheroid system. and *in-silico* modelling Developed and performed the *in-silico* modelling, analysis, interpretation, and presentation. This work is not published in this thesis, but it did inform the methods established in Chapter 7.

Gansau, J., **McDonnell, E. E.**, and Buckley, C. T. (2023) ‘Antacid Microcapsules to Buffer the Acidic Intervertebral Disc Microenvironment’, *Preparation in progress*.

Contribution: Bovine caudal disc isolation and explant cage fabrication which is not published in this thesis.

Borrelli, C., **McDonnell, E. E.**, Barcellona, M. N., and Buckley, C. T. (2023) ‘Differential Response of Nasal Chondrocytes at Different Seeding Densities and Assessment in a Disc Explant Culture Model System’, *Preparation in progress*.

Contribution: Predictive *in-silico* modelling and probe measurement of the microenvironment of the disc explant cultures. This work was not published in this thesis, but it was based on the protocols established in Chapter 6. Performed the pilot rat study, acquisition, analysis, presentation, and interpretation of results.

International Conference proceedings

McDonnell, E. E., Barcellona, M. N., Wilson, N., Ní Néill, T., Brama, P. A. J., Cunniffe, G., Darwish, S., Butler, J. S., and Buckley C. T. (2022) ‘From Preclinical to Clinical Translation of Intervertebral Disc Cell-based Regeneration: Effects of Species-Specific Scale, Metabolism and Matrix Synthesis Rates’ *ORS PSRS 6th International Spine Research Symposium*. Skytop, Pennsylvania, USA.

McDonnell, E. E. and Buckley, C. T. (2021) ‘In-Silico Modelling as a Tool to Recapitulate the Nutrient Microenvironment of the Intervertebral Disc for the Development of Cell Therapies’, *6th Tissue Engineering and Regenerative Medicine International Society (TERMIS) World Congress*. Maastricht, The Netherlands.

McDonnell, E. E., Tornifoglio, B., Gansau, J., and Buckley, C. T. (2019) ‘Elucidating and Optimising the Distribution of Metabolites within Ex Vivo Disc Organ Culture’ *ORS PSRS 5th International Spine Research Symposium*. Skytop, Pennsylvania, USA.

Gansau, J., **McDonnell, E. E.,** and Buckley, C. T. (2019) ‘Altering the Local Acidic Microenvironment of the Degenerated Intervertebral Disc using Injectable Antacid Microcapsules’ *ORS PSRS 5th International Spine Research Symposium*. Skytop, Pennsylvania, USA.

Samuel, S., **McDonnell, E. E.,** and Buckley, C. T. (2019) ‘Effect of Growth Factor Priming to Promote a Discogenic Phenotype of Tissue Spheroids for Intervertebral Disc Regeneration’ *ORS PSRS 5th International Spine Research Symposium*. Skytop, Pennsylvania, USA.

National Conference proceedings

McDonnell, E. E., Barcellona, M. N., Wilson, N., Ní Néill, T., Brama, P. A. J., Cunniffe, G., Darwish, S., Butler, J. S., and Buckley, C. T. (2023) ‘From Preclinical to Clinical Translation of Intervertebral Disc Cell-based Regeneration: In-Silico Modelling to Elucidate the Effects of Species-Specific Scale, Metabolism and Matrix Synthesis Rates’ *Proceedings of the 28th Annual Conference of the Section of Bioengineering of the Royal Academy of Medicine in Ireland*. Meath, Ireland.

Wilson, N., **McDonnell, E. E.**, Moore, S., Brama, P. A. J and Buckley, C. T. (2023) ‘Microenvironmental Impact on the Matrix Synthesis Rates of Nucleus Pulposus Cells’ *Proceedings of the 28th Annual Conference of the Section of Bioengineering of the Royal Academy of Medicine in Ireland*. Meath, Ireland.

McDonnell, E. E. and Buckley, C. T. (2020) ‘Elucidating and Optimising the Distribution of Metabolites within Ex Vivo Disc Organ Culture’, *Proceedings of the 26th Annual Conference of the Section of Bioengineering of the Royal Academy of Medicine in Ireland*. Carlow, Ireland.

Gansau, J., **McDonnell, E. E.** and Buckley, C. T. (2020) ‘Enhancing the Local Acidic Microenvironment found in Degenerated Intervertebral Discs using pH Neutralisation Microcapsules’, *Proceedings of the 26th Annual Conference of the Section of Bioengineering of the Royal Academy of Medicine in Ireland*. Carlow, Ireland.

Samuel, S., **McDonnell, E. E.** and Buckley, C. T. (2020) ‘Effect of Growth Factor Priming to Promote a Discogenic Phenotype of Tissue Spheroids for Intervertebral Disc Regeneration’, *Proceedings of the 26th Annual Conference of the Section of Bioengineering of the Royal Academy of Medicine in Ireland*. Carlow, Ireland.

McDonnell, E. E. and Buckley, C. T. (2019) ‘Simulating Nutrient Distribution within Degenerated Discs and Optimising Physiological Culturing Conditions for Bovine Organ Models’, *Proceedings of the 25th Annual Conference of the Section of Bioengineering of the Royal Academy of Medicine in Ireland*. Limerick, Ireland.

Table of Content

Declaration	i
Summary	ii
Acknowledgements	iv
List of Publications and Conference Proceedings	v
Table of Content.....	ix
List of Figures	xiv
List of Tables	xviii
Nomenclature	xix
Chapter 1. Introduction.....	1
1.1 Research Motivation - The Challenge of Clinical Translation	1
1.2 Thesis Objectives	3
Chapter 2. Literature Review.....	5
2.1 The Human Intervertebral Disc.....	5
2.1.1 Structure and tissue composition.....	5
2.1.2 Cells of the intervertebral disc	7
2.2 Aetiology of Intervertebral Disc Degeneration.....	8
2.2.1 Stages of disc degeneration.....	10
2.3 Nutrient Microenvironment within the Intervertebral Disc	10
2.3.1 Nutrient transport within the avascular disc.....	10
2.3.2 Experimental metabolite measurement in disc tissue.....	12
2.3.3 Energy metabolism of disc cells.....	14
2.4 <i>In-Silico</i> Models of Solute Transport in the Intervertebral Disc	21
2.5 Cell Strategies for the Treatment of Disc Degeneration	28
2.5.1 Basic science development: <i>in vitro</i> and <i>ex vivo</i>	28
2.5.2 Pre-clinical animal models.....	29
2.5.3 Clinical assessment	31
2.6 Summary and Clinical Significance.....	33

Chapter 3.	General Methods	34
3.1	Establishing the <i>In-Silico</i> Nutrient-Transport Models.....	34
3.1.1	Additional parameters of the FEM.....	36
3.3	Determining the Total Cell Density and the Proportion of Metabolically Active Cells within Disc Tissue	37
3.4	Qualitative Histological Analysis.....	38
3.4.1	Cell culture sample fixation.....	38
3.4.2	Native disc tissue fixation	38
3.4.3	Sample dehydration and histological staining.....	38
3.5	Cell Isolation and Monolayer Expansion	39
3.5.1	Animal cell isolation	39
3.5.2	Human cell isolation.....	40
3.7	Quantitative Biochemical Analysis	41
3.7.1	Glucose assay	41
3.7.2	Determination of DNA and sulphated glycosaminoglycan content	42
3.8	Other Conversion Factors and Curves.....	43
3.8.1	Oxygen units.....	43
3.8.2	pH to lactate concentration.....	44
3.9	Statistical analysis	44
Chapter 4.	Consolidating and Re-evaluating the Human Disc Nutrient Microenvironment	45
4.1	Introduction	45
4.2	Materials & Methods.....	47
4.2.1	Re-evaluating the nutrient microenvironment of the human IVD.....	47
4.2.2	Compiling metabolite diffusion coefficients for intervertebral disc sub-tissues.	48
4.2.3	Identifying experimental degeneration grade-dependent input parameters for <i>in-silico</i> models.....	51
4.2.4	Establishing <i>in-silico</i> models as a function of degeneration grade.....	55
4.2.5	Investigating the optimal cell number for intradiscal injection	55
4.3	Results	57
4.4	Discussion	63

4.5	Conclusion	68
Chapter 5. Two- and Three-Dimensional <i>In Vitro</i> Nucleus Pulposus Cultures: An <i>In-Silico</i> Analysis of Local Nutrient Microenvironments.....		
5.1	Introduction.....	69
5.2	Materials & Methods.....	70
5.2.1	Two-dimensional cell culture models	70
5.2.2	Metabolic rates and proliferation kinetics	72
5.2.3	Three-dimensional cell culture models	74
5.2.4	External boundary concentrations: Glucose and oxygen	75
5.3	Results.....	77
5.4	Discussion	86
5.5	Conclusion	92
Chapter 6. Investigating the Physiological Relevance of <i>Ex Vivo</i> Disc Organ Culture Nutrient Microenvironments using <i>In-Silico</i> Modelling and Experimental Validation		
6.1	Introduction.....	93
6.2	Materials & Methods.....	95
6.2.1	Geometrical characterisation of disc caudal level.....	95
6.2.2	Disc isolation and organ culture setup	95
6.2.3	Determining metabolically active cell density	96
6.2.4	Experimental measurements of oxygen, pH and glucose.....	97
6.2.5	<i>In-silico</i> model of nutrient concentration profiles.....	98
6.3	Results.....	99
6.3.1	Geometrical variation of bovine discs as a function of caudal level.....	99
6.3.2	Metabolically active cell density of <i>ex vivo</i> disc organ cultures is an important input parameter for <i>in-silico</i> modelling.....	99
6.3.3	Predicted and experimentally determined metabolite concentrations in <i>ex vivo</i> bovine caudal discs	102
6.3.4	Additional validation of the <i>in-silico</i> model through media analysis.....	105
6.4	Discussion	107
6.5	Conclusion	111

Chapter 7. Preclinical to Clinical Translation: Effects of Species-Specific Scale, Metabolism and Matrix Synthesis Rates on Cell-Based Regeneration	112
7.1 Introduction	112
7.2 Materials & Methods.....	115
7.2.1 Pre-clinical literature and registered clinical trials of cell-based disc regeneration 115	
7.2.2 Establishing species-specific <i>in-silico</i> models using experimentally determined geometries and cell densities	117
7.2.3 Establishing a spheroid culture system for rat, goat, and human disc cells.....	119
7.2.4 Metabolic flux analysis for experimentally determined nutrient consumption and lactate production rates.....	121
7.2.5 Towards experimental validation of <i>in-silico</i> nutrient transport models.....	122
7.2.6 Experimentally determining species-specific GAG synthesis rates to compare animal and human cell-based regeneration <i>in-silico</i>	126
7.3 Results	129
7.3.1 Experimentally determined species-specific parameters.....	129
7.3.2 Predicted differences in regeneration capacity and nutrient microenvironments between species.	135
7.4 Discussion	142
7.5 Conclusion.....	148
Chapter 8. Final Discussion	149
8.1 Limitations and Future Perspectives	154
Chapter 9. Concluding Remarks	158
References	159
Appendices	i
Appendix A – Standard operating protocols (SOPs) established within this thesis work.....	i
A.1 Bovine Disc Organ Culture	i
A.2 Determining the Metabolically Active Cell Density of Disc Tissue	vi
A.3 Calibration of Resources for Assessing Metabolic Concentrations.....	viii
A.4 Enzymatic Isolation of Rat, Goat and Human NP and AF Cells.....	xii

A.5 Disc Micro-Spheroid Formation using Rat, Goat and Human cells (NP and AF)	xvii
A.6 Basel Metabolic Rates of Disc Spheroids using Seahorse Analysis	xix
Appendix B – Chapter 4 (Human microenvironment).....	xxv
B.1 Mesh convergence study	xxv
B.2 List of reviewed clinical trials involving cell injection of the treatment of intervertebral disc degeneration.....	xxvi
Appendix C – Chapter 5 (FE culture)	xxix
C.1 List of reviewed manuscripts for nucleus pulposus (NP) culture and relevant experimental details extracted from the literature to inform the development of <i>in-silico</i> models	xxix
C.2 Additional two-dimensional cell culture <i>in-silico</i> models	xxxvii
Appendix D – Chapter 6 (Organ culture).....	xxxix
Appendix E – Chapter 7 (Species comparison)	xl
E.1 List of reviewed manuscripts and relevant experimental details extracted for rat tail models	xl
E.2 List of reviewed manuscripts and relevant experimental details extracted for goat/caprine models	l
E.3 Full geometrical analysis of goat lumbar disc L1-2 to L5-6 (N = 3).....	lii
E.4 List of studies using Seahorse Flux analysis on disc cells.....	liv
E.5 Miscellaneous species histology – including lapin/rabbit lumbar	lv
E.6 Histological evaluation of metabolic spheroids.....	lx
Appendix F – Abstract	lxi

List of Figures

Figure 1.1 Graphical summary of the development process and requisite steps to demonstrate efficacy of cell-based therapies for disc regeneration.	2
Figure 2.1 Anatomy of the spinal column and physiology of the intervertebral disc (IVD).....	6
Figure 2.2 Literature measurements for the cell density across healthy and degenerated human intervertebral disc (IVD).	8
Figure 2.3 Progression of disc degeneration in a human intervertebral disc (IVD).	9
Figure 2.4 Nutrient and metabolite transport routes into the centre of the avascular intervertebral disc (IVD).....	11
Figure 2.5 Schematic representation of ATP production by disc cells.	15
Figure 2.6 Geographical demographic, clinical phase, and status of registered clinical trials for cell-based disc regeneration.	32
Figure 3.1. An example of an extremely fine physics-controlled mesh of tetrahedral elements within a 3D quadrant of a rat caudal, goat lumbar and human lumbar disc.	36
Figure 3.2 Assessing the accuracy of the biochemical glucose assay.	42
Figure 3.3 Conversion curve from DNA content to cell number.	42
Figure 3.4 Conversion curve from pH reading to lactate concentration using the Seahorse Flux Analyser.	44
Figure 4.1. Consolidating current knowledge on the human nutrient microenvironment.	46
Figure 4.2 A corrected predicted profile to account for elevated oxygen inhalation during surgery was determined using an <i>in-silico</i> model.	49
Figure 4.3. Metabolite diffusion coefficients for intervertebral disc sub-tissue.....	50
Figure 4.4. In-silico input parameters gathered from experimental literature.....	52
Figure 4.5 Human intervertebral disc (IVD) dimension as a function of degeneration.	53
Figure 4.6. Predicted glucose concentrations within a healthy adult (Grade II), mildly (Grade III) and moderately (Grade IV) degenerated in-silico intervertebral disc model.	58
Figure 4.7. Predicted pH levels concentrations within a healthy adult (Grade II), mildly (Grade III) and moderately (Grade IV) degenerated in-silico intervertebral disc model.	59
Figure 4.8. Predicted oxygen concentrations within a healthy adult (Grade II), mildly (Grade III) and moderately (Grade IV) degenerated in-silico intervertebral disc model.	60
Figure 4.9 Predicted metabolite concentrations within a calcified degenerated (Grade III and IV) intervertebral disc injected with discogenic cells.	62
Figure 5.1 Consolidating commonly used cell culture parameters and metabolic rates reported across the intervertebral disc research field.....	71

Figure 5.2 Comparing the effect of different proliferation kinetics in terms of growth rate or population doubling (PD).....	73
Figure 5.3 Sensitivity analysis on the effect of the lowest and highest rates of metabolism reported in the literature on the minimum oxygen, glucose and pH values in an alginate bead or hydrogel construct containing 4 million cells/mL.....	75
Figure 5.4 External incubator gas concentrations and local metabolite concentrations in 2D cell culture vessels.	76
Figure 5.5 Investigating the effect of three different seeding densities on the oxygen concentration in a single 30µl alginate bead in 2 mL of low glucose (LG) or high glucose (HG) media (24-well) at normoxia (NX), physioxia (PX) and hypoxia (HX).....	78
Figure 5.6 Investigating the effect of three different seeding densities on the glucose and pH concentration in a single 30µl alginate bead in 2 mL of low glucose (LG) or high glucose (HG) media (24-well) at normoxia (NX), physioxia (PX) and hypoxia (HX).	79
Figure 5.7 . Investigating the effect of multiple alginate beads (4 or 10 beads of 4 million cells/mL) in a single culture vessel (12-well).....	80
Figure 5.8 Comparing the effect of a standard twice weekly media exchange to a daily media refresh on concentrations within a 4 and 10 bead culture.	81
Figure 5.9 Investigating the oxygen microenvironment within a cylindrical construct (radius: 2.5 mm, height: 3 mm, or 1.5 mm) containing a seeding density of either 4 or 20 million cells/ml. 82	82
Figure 5.10 Transient analysis of glucose concentration and pH values within a cylindrical construct (radius: 2.5 mm, height: 3 mm, or 1.5 mm) containing a seeding density of either 4 or 20 million cells/ml with a media exchange performed at the midpoint.	83
Figure 5.11 Comparing the effect of a standard twice weekly media exchange to a daily media refresh on concentrations within a 4 million cells/mL hydrogel construct.	84
Figure 5.12 Comparing the nutrient microenvironment of a 250,000-cell pellet in 1 mL (Eppendorf) or 200 µL (96-well) of media and a 35,000-cell microaggregate in 50 µL (96-well) of media.....	85
Figure 6.1 Capturing the popularity of bovine <i>ex vivo</i> disc organ culture systems and their typical external nutrient conditions.	94
Figure 6.2 Establishing an <i>in-silico</i> and <i>ex vivo</i> disc organ culture model.	96
Figure 6.3 Schematic of the PreSens oxygen and pH probe measurement setup.	98
Figure 6.4 Experimental characterisation of key parameters needed to establish the <i>in-silico</i> disc organ culture model.	101
Figure 6.5 A sensitivity analysis was performed to assess the active cell density of annulus fibrosus (AF) as an influential parameter on the central metabolite concentrations.	102
Figure 6.6 Predicted and experimentally determined oxygen concentrations in <i>ex vivo</i> bovine caudal discs.	103

Figure 6.7 Predicted and experimentally determined glucose concentrations in <i>ex vivo</i> bovine caudal discs.	104
Figure 6.8 Predicted and experimentally determined pH in <i>ex vivo</i> bovine caudal discs.	105
Figure 6.9 Predicted and experimentally determined glucose and pH levels in the culture media.	106
Figure 7.1 Preferred Reporting Items for Systematic Reviews and Meta-Analysis (PRISMA) diagram indicating screening process and exclusion criteria.	115
Figure 7.2 Experimental parameters gathered from key pre-clinical animal models in the literature and registered clinical trials for cell-based disc regeneration.....	116
Figure 7.3 Geometrical analysis of goat lumbar and rat caudal disc using macroscopic and microscopic image analysis, respectively.....	117
Figure 7.4 Rat caudal (Cd7-8), goat lumbar (L3-4) and human lumbar (L4-5 at Grade III) discs presented in scale to one another.....	118
Figure 7.5 Agarose microwell array fabrication and the formation of disc spheroids.	120
Figure 7.6 An example of raw measurements from the Seahorse XFe96 analyser showing simultaneous measurement in real time of the reduction in oxygen and pH level for rat, goat, and human nucleus pulposus cells.	122
Figure 7.7 Towards experimental validation of in-silico modelling of the nutrient microenvironment in pre-clinical animal models.....	124
Figure 7.8 Geometrical analysis of rat caudal level Cd3-4 to Cd9-10 and goat lumbar level L1-2 to L5-6.....	130
Figure 7.9 Experimentally determined metabolically active cell density for the nucleus pulposus (NP) and annulus fibrosus (AF) of rat caudal and goat lumbar discs.....	131
Figure 7.10 Temporal assessment of disc spheroids (nucleus pulposus: NP and annulus fibrosus: AF) from rat, goat, and human over a 7-day culture period.....	132
Figure 7.11 Viability assessment and measured metabolic rates of nucleus pulposus (NP) and annulus fibrosus (AF) spheroids from rat, goat, and human.	133
Figure 7.12 Species-specific matrix synthesis rates and histological evaluation of nucleus pulposus (NP) micro-spheroids.	134
Figure 7.13 <i>In-silico</i> modelling of the microwell culture system to inform the external boundary concentrations necessary to create a physiologically relevant microenvironment within the spheroids.....	136
Figure 7.14 Predicted glycosaminoglycan (GAG) matrix regeneration in the nucleus pulposus (NP) of a pre-clinical rat model, goat model and human clinical trials for cell-based therapies.	138
Figure 7.15 Predicted nutrient microenvironments within pre-clinical rat and goat animal models assessing cell-based therapies.	140

Figure 7.16 Predicted nutrient microenvironments within a Grade III human intervertebral disc (IVD) undergoing clinical assessment for a range of injected cell numbers..... 141

List of Tables

Table 2.1 Summary of experimentally determined metabolites and the species in which they were measured.....	13
Table 2.2 Oxygen consumption rates (OCR) (nmol/million cells/hr) measured at different glucose concentration for nucleus pulposus cells from a range of species and age/degeneration stages. 18	
Table 2.3 Glucose consumption rates (GCR) (nmol/million cells/hour) measured at different glucose concentrations and varying oxygen levels for nucleus pulposus cells from a range of species and age/degeneration stages. Abbreviations: NX (normoxia), PX (physioxia) and HX (hypoxia).	19
Table 2.4 Lactate production rates (LPR) (nmol/million cells/hour) measured at different glucose concentrations and varying oxygen levels for nucleus pulposus cells from a range of species and age/degeneration stages. Abbreviations: NX (normoxia), PX (physioxia) and HX (hypoxia). ..	20
Table 2.5 Summary of <i>in-silico</i> models from the literature which have been used to investigate nutrient distribution within the human disc <i>in vivo</i>	22
Table 3.1 An approximate oxygen unit conversion table with the multiplication factors required to convert the current unit (row) into the desired unit (column).	43
Table 4.1 Cell density parameters used in the nucleus pulposus (NP), annulus fibrosus (AF) and cartilage endplate (CEP) for each grade-specific <i>in-silico</i> model.	51
Table 4.2 Finalised input parameters used in the grade-specific <i>in-silico</i> model to capture the effective diffusion of the relevant metabolites (oxygen, glucose, and lactate) through the nucleus pulposus (NP), annulus fibrosus (AF) and cartilage endplate (CEP).	56
Table 5.1. Metabolic parameters used in each <i>in-silico</i> model based on external boundary conditions and the species or degeneration stage being investigated. Abbreviations: LG (low glucose) NX (normoxia), PX (physioxia), HX (hypoxia), OCR (oxygen consumption rate), GCR (glucose consumption rate) LPR (lactate production rate) and HG (high glucose).	74
Table 6.1 Input parameters and boundary conditions used in the <i>in-silico</i> models for nucleus pulposus (NP), annulus fibrosus (AF), endplates (EP) and media.	100
Table 7.1 Effective diffusion coefficients (mm ² /hr) used <i>in-silico</i> for the nucleus pulposus (NP) and annulus fibrosus (AF) domains of rat, goat, and human discs.....	123
Table 7.2 Boundary concentrations used <i>in-silico</i> at the nucleus pulposus (NP)/cartilage endplate (CEP) interface and the periannular surface of the annulus fibrosus (AF) for rat, goat, and human.	125
Table 7.3 Glycosaminoglycan (GAG) parameters used <i>in-silico</i> for the nucleus pulposus (NP) and annulus fibrosus (AF) domains of rat, goat, and human discs.	128

Nomenclature

2D	Two-dimensional	HIF	Hypoxia-inducible factor
3D	Three-dimensional	HX	Hypoxia
AB	Alcian blue	IL-1β	Interleukin-1 β
AF	Annulus fibrosus	IVD	Intervertebral disc
A-P	Anterior to posterior	LBP	Lower back pain
ASICs	Acid sensing ion channel	LG	Low glucose
ATP	Adenosine triphosphate	LPR	Lactate production rate
BEP	Bony endplate	MMP	Matrix metalloproteinases
CAD	Computer aided design	MRI	Magnetic resonance imaging
CEP	Cartilage endplate	MSCs	Mesenchymal stem cells
DAPI	4',6-diamidino-2-phenylindole	MTT	Methyl-thiazolyl diphenyl-tetrazolium
DDD	Degenerative disc disease	NX	Normoxia
DHI	Disc height index	OCT	Optimal cutting temperature
DMEM	Dulbecco's modified eagle medium	ODI	Oswestry disability index score
DMMB	Dimethyl methylene blue	PBS	Phosphate buffered saline
DNA	Deoxyribonucleic acid	PFA	Paraformaldehyde
dw	Dry weight	PG	Proteoglycan
ECM	Extracellular matrix	PSR	Picrosirius red
EP	Endplate	PX	Physioxia
GCR	Glucose consumption rate	sGAG	Sulphated glycosaminoglycan
HCL	Hydrochloric acid	TNF	Tumour necrosis factor
HDS	Histological degeneration score	VAS	Visual analogue scale
H&E	Haematoxylin and eosin	VEP	Vertebral endplate
HG	High glucose	ww	Wet weight

Chapter 1. Introduction

1.1 Research Motivation - The Challenge of Clinical Translation

Lower back pain (LBP) is a major global socio-economic burden. It is the leading cause of disability worldwide affecting 80% of the adult population and costing the EU €240 billion annually.¹ The primary cause of LBP is believed to be degenerative disc disease (DDD), a common clinical diagnosis characterised by permanent structure changes which go on to impair the biomechanical function of the intervertebral disc (IVD). When patients first present with LBP, current conservative treatments (e.g. physical therapy and pain management) only focus on relieving symptoms in an attempt to alleviate pain rather than treat the underlying causes of degeneration. Even in more severe cases, the only current effective method of pain relief is invasive surgical intervention, such as microdiscectomy or spinal fusion. In the United States, surgical interventions for lumbar DDD increased from 21,223 in 2000 to 55,467 in 2009, while more than 1 million spinal fusions were performed between 2010 and 2019.^{2,3} This significant upward trend is expected to continue with an aging population and an increasing shift towards sedentary lifestyles. However, these surgical treatments do not restore normal biomechanics and only provide temporary pain relief. Surgery may even exacerbate degeneration of adjacent healthy discs, with reported failure rates as high as 40%.⁴ Therefore, there is an urgent need for a regenerative therapy to intervene and slow down the degenerative process or repair the already degenerated IVD.

Over the past twenty years, significant research has been undertaken to discover new breakthrough cell-based therapies for the treatment of DDD. Encouragingly, it has been a stage of rapid development, with a growing body of basic research and many promising therapies demonstrating therapeutic potential in pre-clinical animal models. Nonetheless, cell-based disc regeneration at a clinical level remains in its infancy and clinical studies are only beginning to take their first steps with twenty-six registered worldwide. Prior to clinical trials, these new therapies undergo extensive *in vitro* testing and *in vivo* animal model assessment. However, even after demonstrating safety and efficacy in animals, many of these therapies enter into a critical period between preclinical validation and clinical evaluation, where they do not appear to work to the same extent in humans. It is commonly believed that the harsh nutrient microenvironment and “hostile” nature of the degenerating IVD is linked to the weak outcomes of prospective studies.⁵⁻⁷

The IVD is the largest avascular structure in the human body. As a result, the intradiscal cells rely on the diffusion of nutrients through the disc extracellular matrix (ECM), from blood vessels surrounding the annulus fibrosus (AF) and capillary buds in the vertebral bodies. This gives rise

to gradients throughout the tissue and is can be confounded further by degenerative features such as endplate (EP) calcification.⁸ Thus the biochemical microenvironment of the degenerating IVD is often characterised by low concentrations of nutrients and increased matrix acidity.^{9,10} NP cells have been shown to adapt to their harsh microenvironment.^{11,12} Nonetheless, it has been demonstrated that these conditions may adversely affect the survival and regenerative potential of injected cell therapies. Understanding how potential cell-based therapies will respond to limited nutrient availability is a key factor for clinical translation and has been linked to the high failure of prospective studies.⁵ As a result, it is imperative to test the efficacy of potential cell therapeutics in a biochemical microenvironment which is comparable to the degenerative niche, throughout the full development process.

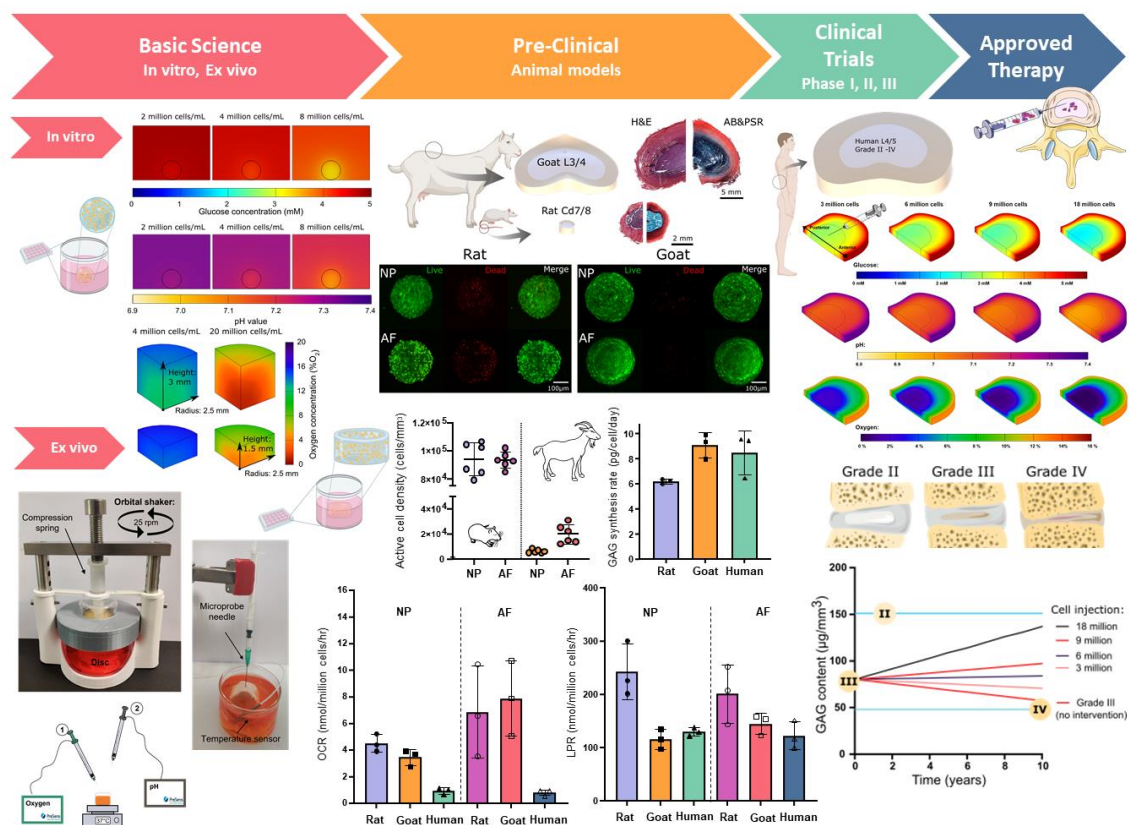


Figure 1.1 Graphical summary of the development process and requisite steps to demonstrate efficacy of cell-based therapies for disc regeneration. The nutrient microenvironment at each stage of assessment will be investigated throughout this work, putting them into the context of physiological relevance and their contribution towards more successful clinical translation.

1.2 Thesis Objectives

As presented in Figure 1.1, this thesis work investigates the stages of testing that a new developing therapy goes through from the perspective of the nutrient microenvironment, all the way from “bench to bedside”. First this work attempts to bridge the translational gap of cell-based therapies within the IVD field by elucidating the nutrient microenvironment of degenerated humans IVDs and identifying discrepancies in the microenvironments being established in commonly used *in vitro* testing using *in-silico* modelling. Next this work theoretically assesses commonly used pre-clinical animal models and registered human clinical trials from both the perspective of the nutrient microenvironment and regenerative matrix synthesis capacity. Therefore, this thesis provides *in-silico* models which can be used to establish more physiologically relevant *in vitro* systems, ascertain the relevance of animal studies, and inform the design of cell therapy assessment at both a pre-clinical and clinical stage. Together this work aims to drive towards greater standardisation and harmonisation, reduce the *in vitro* to *in vivo* gap and maximise the potential of successful clinical translation based on nutritional demands.

1. To consolidate and re-evaluate the human disc nutrient microenvironment

Given the intrinsic difficulty and ethical constraints in obtaining accurate *in vivo* human measurements of the nutrient microenvironment, the field relies heavily on early seminal work and *in-silico* modelling as a complementary approach in providing valuable insight into the physiological or pathophysiological microenvironment. **Chapter 4** of this thesis will reflect on these early measurements and employ *in-silico* models underpinned by more recent experimentally determined parameters of degeneration and nutrient transport, with the objective of re-evaluating the current knowledge in terms of grade-specific stages of degeneration. To maximise future advances the research field requires a more thorough understanding of the nutrient microenvironment, how it changes with degeneration and how potential cell-based therapies will respond to the specific microenvironment into which they are administered. Together this work aims to provoke greater deliberation and consideration of the nutrient microenvironment when designing *in vitro* cell culture experiments and cell therapy development. This not only has important scientific merit but also significant value for clinical translation.

2. To predict the local nutrient microenvironments of two- and three-dimensional *in vitro* nucleus pulposus cultures using *in-silico* modelling

IVD research has been challenged with heterogeneous results in terms of the regenerative potential and matrix synthesis of promising new therapies *in vitro*. Consequently, harmony and standardisation are currently a topic of discussion across the research field to advance reproducibility and accelerate clinical translation. Unless studies are specifically investigating the

effect of microenvironmental conditions, there is an under appreciation for the effect of culturing conditions and a disconnect often occurs between the external incubator or media concentrations and the actual local concentrations experienced by the cells. The objective of **Chapter 5** in this thesis is to characterise the local nutrient microenvironment of two-dimensional (2D) cell monolayers and commonly used three-dimensional (3D) *in vitro* culture systems, and to highlight the effect of culturing parameters such as diffusion rate, media volume and cell density. Furthermore, this work aims to place “standard practice” culturing conditions into context in terms of physiological relevance.

3. To investigate the physiological relevance of *ex vivo* disc organ culture nutrient microenvironments using *in-silico* modelling and experimental validation

Ex vivo disc organ culture systems have become an important tool for the assessment of cellular therapies at an early stage of development, as they provide a link between cell culture and *in vivo* studies. While it is important to verify research findings in a system where the cells are in their native 3D environment and highly specialised ECM, it is still unknown whether the metabolite microenvironment of these systems truly represent an appropriate niche to test potential regenerative therapies. **Chapter 6** aims to characterise the nutrient microenvironment of common *ex vivo* bovine caudal disc culture systems using *in-silico* models incorporating geometrical differences between caudal level and a metabolically active cell density. Furthermore, the validity of these nutrient-transport models will be assessed through experimentally measuring the concentration of glucose and oxygen, as well as the pH level in the centre of bovine caudal disc cultured for seven days.

4. To investigate the effects of species-specific scale, metabolism, and matrix synthesis rates on intervertebral disc cell-based regeneration

Lastly, **Chapter 7** will explore differences in metabolism between species. Taking a commonly used small and large animal model, this work will investigate species-specific metabolic activity and regenerative capacity in an attempt to ascertain their clinical relevance. Firstly, this work will geometrically characterise rat caudal, goat lumbar discs and quantify their native cell density compared with the human IVD. Differences in metabolism across the species will be assessed in terms of nutrient demands and regenerative proteoglycan (sulphated glycosaminoglycan, sGAG) synthesis rates. Finally, these experimentally determined parameters will be modelled *in-silico* to elucidate species-specific nutrient microenvironments and predict differences in temporal regeneration between animal models. Ultimately this work will provide a path towards understanding “time to regeneration” within commonly used pre-clinical animal models and the stunted success or expectations of cell-based clinical trials.

Chapter 2. Literature Review

2.1 The Human Intervertebral Disc

The human spine or vertebral column is a complex anatomic structure which provides the scaffolding for the entire body. It functions in many capacities by transmitting loads, allowing for a wide range of motion, and protecting the vital neural components of the spinal cord. The spinal column consists of 24 individual bones called vertebrae and 2 sections of naturally fused vertebrae called the sacrum and the coccyx at the base of the spine. As shown in Figure 2.1(A), the individual vertebrae are grouped into the cervical spine (C1-C7), the thoracic spine (T1-T12) and the lumbar spine (L1-L5). Starting at C3, each vertebrae is separated by a unique soft tissue structure known as the intervertebral disc (IVD). The IVDs, Figure 2.1(B), act as interbody spacers and shock absorbers, playing an integral mechanical role in allowing the spine to fulfil its functions. The lower lumbar spine is where most back pain occurs and is the region of the spine most often affected by DDD.

2.1.1 Structure and tissue composition

The IVD is a fibrocartilage pad of tissue, with a complex and non-uniform structure. It consists of a hydrated gelatinous core, the nucleus pulposus (NP), surrounded peripherally by a fibrous ring, the annulus fibrosus (AF), and it is superiorly and inferiorly anchored in place by a thin layer of cartilaginous endplate (CEP). The composition and structure of each of these components are distinct, indicating a unique mechanical role for each region. In the lumbar IVD, the NP is located towards the posterior of the disc and fills approximately 50% of the total cross-sectional area (Figure 2.1(C)). It is composed of randomly orientated collagen fibres and radially arranged elastin fibres embedded in a proteoglycan gel consisting mainly of aggrecan, a major proteoglycan (PG) of the IVD (10-60% dw). Due to the hydrophilic nature of the PGs, healthy IVDs have a high water content (65-90% ww), causing the NP to swell, sustain axial compression and distribute loads throughout the disc. The swelling pressure is constrained axially by the endplates (EPs) as well as circumferentially by the AF, which is composed of a series of 15-25 concentric lamellae consisting of collagen fibres. The fibres lie parallel within each lamella, but run an alternating pattern between the layers at an angle approximately 30° to the horizontal axis, providing high tensile strength and anisotropic mechanical properties to resist tensile and shearing forces applied in the radial direction by the compressed NP.¹³

The CEP is generally thinner centrally, above the NP than peripherally at the AF and plays an integral role in nutrient transport, allowing for passage of nutrients and metabolites between

the NP and the vertebral capillaries.^{14,15} The thickness ranges from 0.1 to 2 mm with a mean value of 0.62 ± 0.29 mm and a chemical composition similar to that of hyaline cartilage with considerable variation in composition through the depth.^{16,17} Similar to the disc, PG and water content is highest and collagen content lowest in the centre, adjacent to the NP. Collagen content increases sharply as PG and water content decrease from the disc to the bone and from the centre towards the periphery of the disc.¹⁶ The EPs also contribute to the even distribution of the pressure within the NP and the tension in the AF on the vertebral bodies.

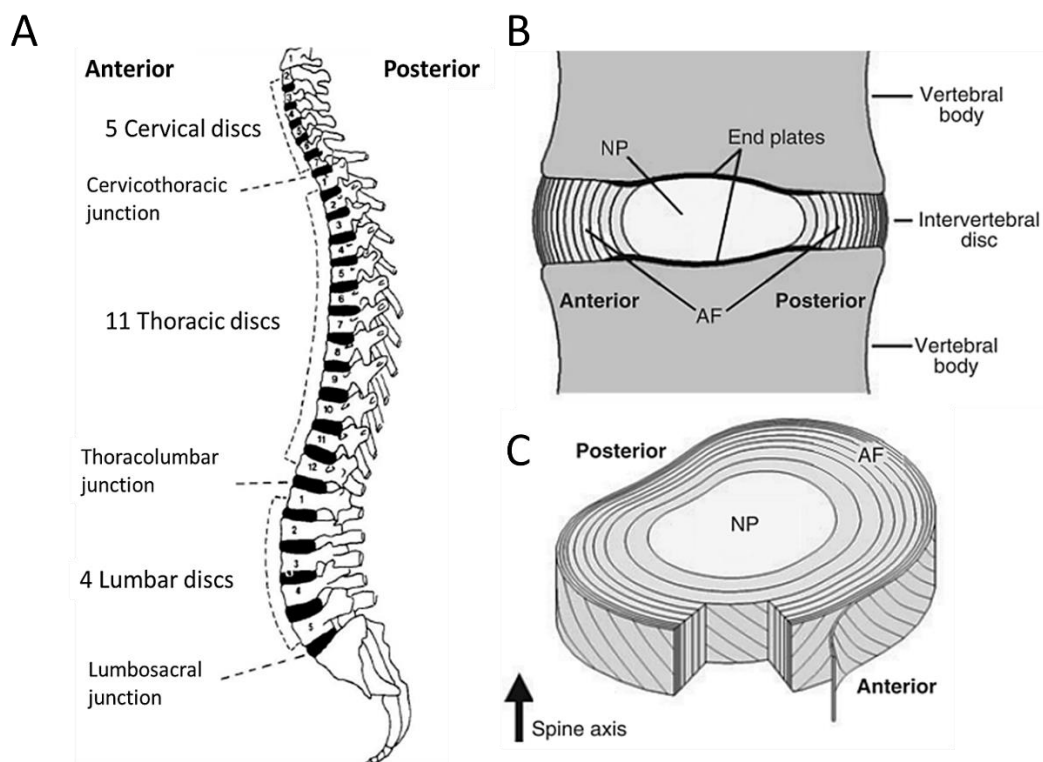


Figure 2.1 Anatomy of the spinal column and physiology of the intervertebral disc (IVD). (A) Lateral view of the human spinal column divided into its regional sections. (B) Midsagittal cross section of the motion section highlighting the different anatomical tissues of the IVD. (C) Schematic of a 3D IVD with its central nucleus pulposus (NP) and the surrounding lamellar structure of the annulus fibrosus (AF). Adapted from (Smith *et al.*, 2011).¹⁸

2.1.2 Cells of the intervertebral disc

The IVD consists of a sparse population of cells which account for less than 1% of the disc volume. The cells are surrounded by an abundant extracellular matrix (ECM) which they play an integral role in synthesising and maintaining.¹⁹ The cell density and phenotype varies by region within the IVD.

In the early human embryo, the NP is densely populated with notochordal cells, which become undetectable between 4 – 10 years, when the NP becomes more sparsely populated by round chondrocyte-like cells.¹⁹ These cells may be closely packed, and contain smaller and more densely arranged nuclei.²⁰ In adulthood, the cell population varies according to species, for example: in rabbit, rat, pig, and dogs notochordal cells persist well into adult life, whereas in cattle, notochordal cells have virtually disappeared by birth.²⁰ The cells in the AF originate from the mesenchyme and exhibit many characteristics of fibroblasts and chondrocytes.²¹ The cells in the inner annulus are spheroidal, chondrocyte-like and sparsely distributed, similar to the NP region,^{20,22} while the cells in the outer annulus are thin, elongated fibroblast-like cells, which align with the oriented collagen fibres within the lamellae.²³ The CEP contains a larger cell density of rounded chondrocytes.²⁴ The collagen fibres within the CEP run horizontally and parallel to the vertebral bodies, with the fibres continuing into the disc, the cells are interspersed among the matrix and tend to be aligned along these fibres.^{16,20}

The regional variations in disc cell density are presented in in Figure 2.2. With an overall average of 3,000 cells/mm³ across both the NP and AF, the IVD has a significantly lower cell density than that in most mammalian tissues, even articular cartilage.²⁵ It has been suggested that the regional variation in cell density and cell phenotypes is a result of the distinct microenvironment within each region, including differences in nutritional supply and mechanical factors.²⁴ Cells play a vital role in maintaining disc health and function, and local concentrations of nutrients and metabolites have been shown to have a significant effect on cellular activity and survival.²⁶⁻²⁹ They synthesise the ECM of the disc, thereby controlling the composition and turnover of IVD tissue.²⁶ Furthermore, these nutrient concentrations are also regulated by cellular demand.³⁰

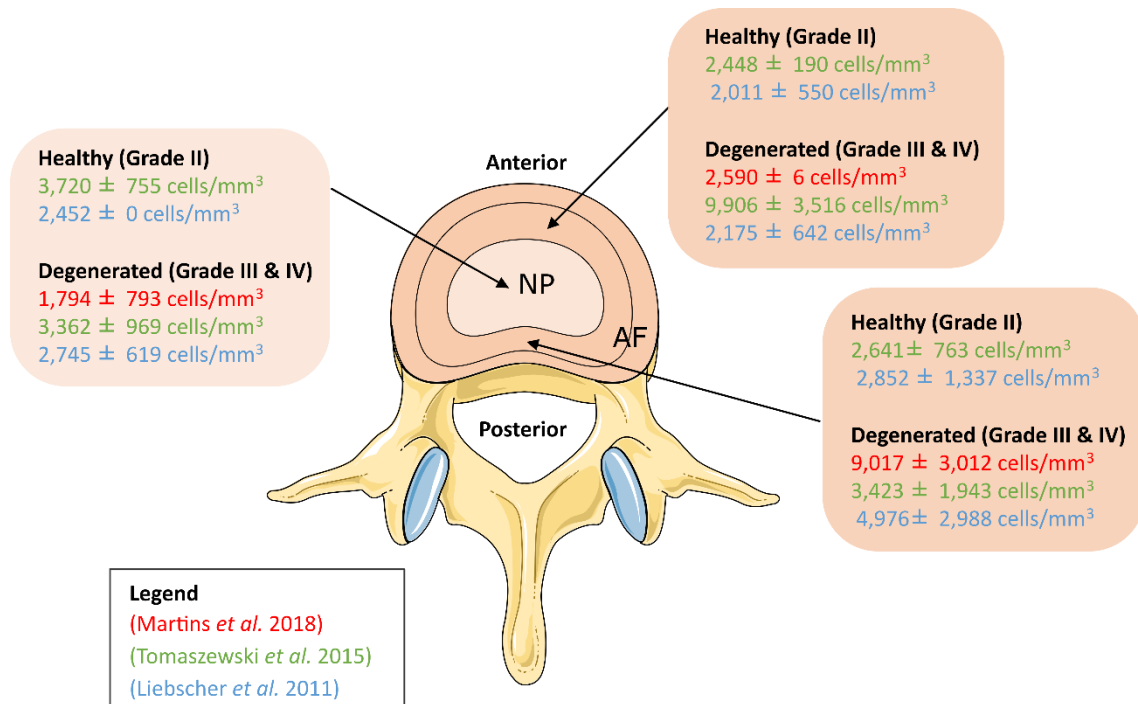


Figure 2.2 Literature measurements for the cell density across healthy and degenerated human intervertebral disc (IVD). Three recent studies which have investigated the human cell density regionally across the nucleus pulposus (NP) and anterior/posterior of the annulus fibrosus (AF).^{25,31,32}

2.2 Aetiology of Intervertebral Disc Degeneration

Although there is still no unanimously accepted definition of DDD across the research field, it is generally characterised by cellular and matrix changes and the deterioration of the tissue structure, resulting in a loss of biomechanical function. As shown in Figure 2.3, degeneration typically manifests within the central NP and even early degenerative changes are deemed irreversible, before progressing outwards through the AF and entire intervertebral joint.^{33,34} The NP loses its gel-like properties and becomes stiffer and more fibrous resulting in poor demarcation of the interface between the NP and AF. In some degenerated discs, cleft formation and degenerative fissures occur in the AF, leading to the ingrowth of nerves and blood vessels into the tissue extending into the inner AF.^{35,36} The most significant biochemical change in the degenerated disc is the loss of PG content in the NP and inner AF regions. This is responsible for the fall in osmotic pressure and tissue hydration, leading to the collapse of the intervertebral space, a common observation in pathological disc degeneration, and a trigger for stress redistributions within the AF.^{37–40}

For over 50 years, poor nutrition of disc cells is believed to be one of the main causes of degeneration.^{26,27,41,42} The blood vessels in the EP have been observed to diminish after the first decade of life, when the first signs of disc degeneration are evident.⁴³ Furthermore, it is

hypothesised that CEP calcification may trigger degeneration through impeding the passage of nutrients to NP cells.⁴¹ Although less is known about changes in cell morphology specific to degeneration, early studies have shown increased calcium deposition concomitant with aging and degeneration grade,^{44,45} as well as a correlation between the ease of nutrient transport and calcification.⁴⁶ More recently glucose transport impaired by the presence of calcium has been observed in *ex vivo* organ cultures.⁴⁷ Furthermore, increasing levels of calcium appear to diminish collagen and PG synthesis, and thus may impede solute diffusion through adversely impacting tissue hydration.^{47,48} The hypothesis of calcification as a degenerative trigger is supported by early *in vitro* studies where limited nutrient supply has reduced cell viability and functionality.^{27–29,49,50} However, despite a decrease in cell viability and a high incidence of necrotic cells in aged NP tissue, an increased presence of other cell types including nerve fibres, Schwann cells, endothelial cells and fibroblasts have also been reported.^{51,52}

More recent work has explored the effects of additional matrix constituents impeding solute uptake.^{53,54} For example, one study directly investigating solute diffusivity through cadaveric human CEP tissue (38 – 66 years) found significant variation in diffusion, with the least permeable CEPs having lower aggrecan, collagen-2, and matrix metalloproteinases-2 (MMP MMP-2) gene expression.⁵³ Therefore, knowledge of the response of tissue transport and metabolic properties to calcification as well as other aspects of degeneration are important in understanding the aetiology of IVD degeneration.⁵⁵

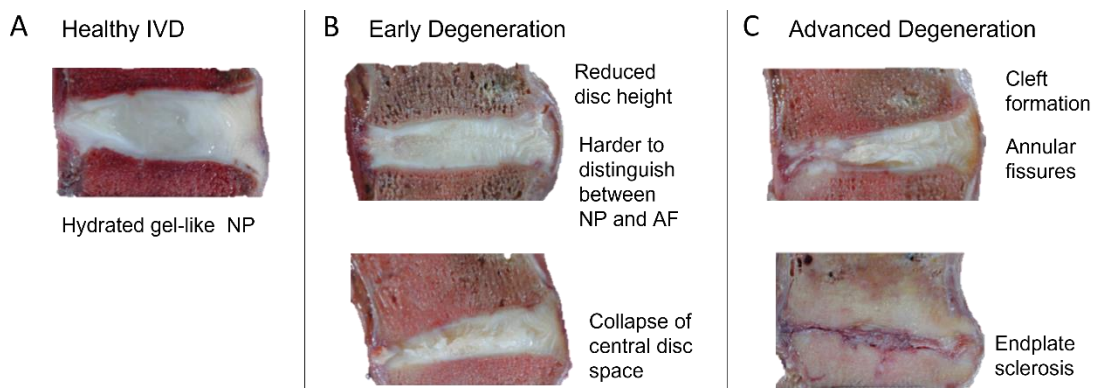


Figure 2.3 Progression of disc degeneration in a human intervertebral disc (IVD). (A) Healthy IVD with a highly hydrated gelatinous nucleus pulposus (NP). (B) Early signs of degeneration including a decrease in disc height, reduced hydration, and collapse of the central disc space. (C) Advanced degeneration indicating cleft formation, annular tears, and endplate sclerosis. Adapted from (Galbusera *et al.* 2014).⁵⁶

2.2.1 Stages of disc degeneration

When a patient presents with LBP, magnetic resonance imaging (MRI) is the most important method for the clinical assessment of IVD pathology. It provides a non-invasive imaging tool to provide soft tissue delineation of specific regions of interest. Morphologic grading systems such as the Thompson or Pfirrmann grading scales are then used relating to observed structural characteristics of degeneration such as the integrity of the CEP, and fibre orientation,³⁹ or disc height and hydration of the NP.³⁸ However, the current clinical tools do not provide insight into the biochemical microenvironment of the IVD. It has been debated that without better patient cohort stratification even the best cell therapy will not succeed if applied to the wrong disc.⁶ Severe tissue granulation, scarring and adhesions may be considered beyond the intervention stage for cell-based regeneration and instead such therapies are most appropriate at an earlier stage in the degenerative cascade (Pfirrmann grade III or IV) where measurable functional improvement is more assessable. Furthermore, with biochemical characterisation of degenerating IVDs, personalised grade- or patient-specific cell therapeutics could be designed to ensure compatibility with the unique microenvironment to maximise clinical success.

2.3 Nutrient Microenvironment within the Intervertebral Disc

2.3.1 Nutrient transport within the avascular disc

Due to the large avascular nature of the IVD, nutrients and metabolites must be transported to and from the cells through the ECM, giving rise to gradients throughout the tissue.⁸ As shown in Figure 2.4, there are two possible pathways of transport through the IVD, axially via the CEP route, or radially through the periannular route via the blood vessels which surround the outer AF. In the CEP route, nutrients are supplied by capillary buds which emerge through the marrow contact channels.⁵⁷ These capillaries connect the trabecular spaces to the CEP, however, they do not penetrate the cartilaginous layer.⁴¹ Several studies suggest that the central region of the EP is the predominant pathway for exchange between the surrounding vasculature and the NP and inner AF, while more minor solutes (e.g. negatively charged sulphates) are predominately supplied via the AF route.^{41,58-60} Nutrients must first diffuse through the CEP and then through the dense ECM of the NP. Due to the slenderness of the CEP and its similarity in composition to the disc, particularly above the NP, it is not believed to act as a significant transport barrier, providing little resistance to the diffusion of nutrients such as glucose and oxygen.¹⁶ However, as mentioned previously, pathological features of the EP which may hamper transport include calcification and sclerosis of the vertebral bone, as well as several factors which could significantly affect the blood supply to the vertebral body, such as atherosclerosis and sickle cell anaemia.⁶¹

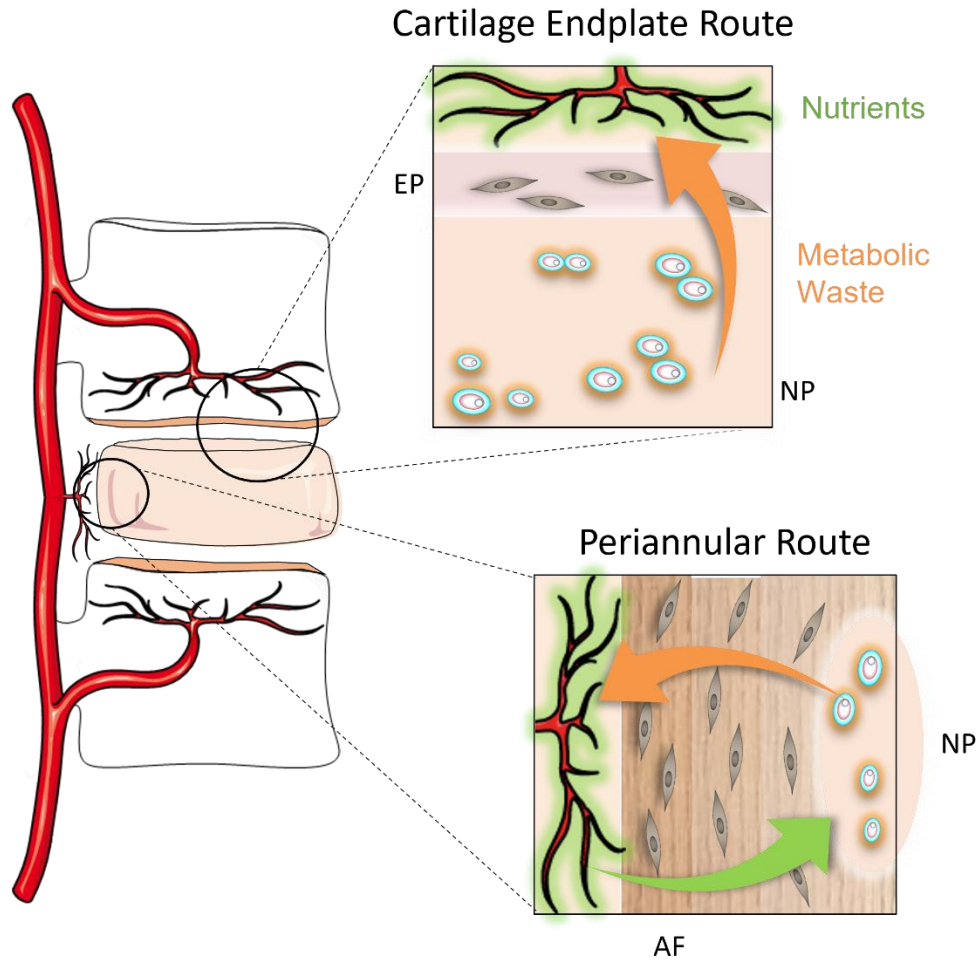


Figure 2.4 Nutrient and metabolite transport routes into the centre of the avascular intervertebral disc (IVD). Small solutes such as nutrients and metabolite waste diffuse to and from the centre of the nucleus pulposus (NP) through the cartilage endplate (CEP) route, or radially through the denser matrix of the annulus fibrosus (AF) via the periannular route.

Glucose and oxygen have been identified as the critical nutrients necessary for IVD cell survival.²⁶ It is generally believed that diffusion is the main mechanism of transport for these small solutes through the ECM of the disc,^{24,59,62} while convection plays a role transporting the larger solutes.^{24,62,63} Diffusion is defined as the movement of matter driven by a concentration gradient.⁶⁴ Adolf Fick first proposed a mathematical model for one-dimensional diffusion in fluids known as Fick's law:

$$J = -D \frac{\partial C}{\partial x} \quad (2-1)$$

where J is the diffusive flux (moles per unit area per unit time), D is the diffusion coefficient (m^2/s), C is the concentration of solute in the solution, and x (m) is the distance along the path of solute transport.⁶⁴ Furthermore, transport properties or diffusion coefficients will be influenced

by both the solute size and the tissue matrix composition and organisation. Diffusion coefficients can be measured by a variety of methods. Recently, more advanced imaging techniques such as MRI, nuclear magnetic resonance (NMR) and fluorescence recovery after photo bleaching (FRAP) have been employed to determine solute diffusivities.⁶⁵ However, direct measurement based on Fick's law (2-1), as mentioned previously, remains the most common method.⁶⁶⁻⁷¹ Several studies have experimentally investigated the diffusivity of solutes in both human and animal tissues.^{67,72-74}

2.3.2 Experimental metabolite measurement in disc tissue

The microenvironmental niche of disc cells is unique, with concentrations coupled to both the supply of solutes and the cellular demand. Even in a healthy human IVD, the microenvironment is delineated by lower oxygen and glucose concentrations than those in the surrounding blood plasma and higher lactic acid concentrations, particularly at the centre of the disc.^{9,10} Furthermore, degeneration has often been characterised by reduced glucose and oxygen concentrations as well as matrix acidity.⁴⁹ And although poor nutrition of disc cells is believed to be one of the main causes of degeneration, an *in vivo* study by Bartels *et al.* (1998) found that the correlation between nutrition and degree of degeneration, pathology or age could not be determined from metabolite concentration alone.¹⁰

A number of studies have measured metabolite concentrations in canine discs through desorption post mortem (glucose and lactate) and *in vivo* probe measurement (oxygen).^{42,58,75,76} These are the key studies often referred to for characterising metabolite concentrations within the IVD. However, due to the inherent complexity of the IVD, nutrient-metabolite measurements in human tissue are scarce. Table 2.1 summarises the literature containing metabolite measurements and specifies the species investigated. The first studies to investigate metabolite concentrations measured the intradiscal pH using a custom-made needle electrode in patients with lumbar rhizopathies.^{77,78} The full range of intradiscal pH measurements were between 5.7 and 7.5, with no significant difference between discs with prolapses (6.6 - 7.5) and those without visible pathologies (6.8-7.4). The only study of oxygen measurement in humans was carried out amperometrically *in vivo* using an electrode consisting of a 50 µm gold-wire epoxy embedded in a 21-gauge needle. Measurements were taken at a single disc level per patient, with discs exposed via an anterior approach. In all discs the oxygen tension fell steeply in the first 5 mm from the disc surface. However, oxygen concentrations varied considerably within the centre of the NP (5 - 150 mmHg), among the LBP cohort, and as mentioned above, no correlation was determined between oxygen level and age or degeneration.¹⁰ These human measurements are considerably higher than those recorded *in vivo* for canine discs, where Holm *et al.* (1981) reported a steep oxygen gradient, with the measured concentration falling more than 90% from the disc-bone

interface to the centre of the NP.^{58,79} To the best of this author's knowledge, Bibby *et al.* (2002) is the only study to investigate glucose concentrations across the human IVD. Tissue samples were excised, papain digested, and glucose concentration determined from quantitative enzymatic determination of the supernatant.²⁶ Unfortunately, from a quantitative perspective, concentrations were presented normalised relative to the curve apex and do not give further insight into the glucose level *in vivo*.

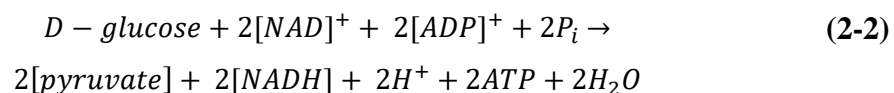
Table 2.1 Summary of experimentally determined metabolites and the species in which they were measured.

Species	Metabolite	Reference
Human	Lactate & pH	78
Human	pH	77
Canine	Lactate & oxygen	58
Canine	Glucose & lactate	42
Canine	Lactate & oxygen	75
Canine	Oxygen	76
Caprine	Oxygen & pH	80
Human	Lactate & oxygen	10
Human	Glucose, lactate & oxygen	26

2.3.3 Energy metabolism of disc cells

Steep gradients of important nutrients are a result of cells metabolising at much higher rates compared with the low rates of solute diffusion across the avascular tissue and to maintain cell viability, the levels of nutrients and pH within the disc must remain above critical values. Cellular metabolism is a catabolic process during which glucose is gradually broken down, releasing energy to be used by the cell or stored in an adenosine triphosphate (ATP) molecule.^{28,58} ATP is the primary energy carrier in living organisms and it provides the energy necessary for metabolic processes at a cellular level. The process of energy production starts when the substrate glucose is transported into the cytoplasm of the cell, Figure 2.5(A). ATP is then produced through a series of complex enzyme catalysed reactions. The first step in all types of cellular respiration is glycolysis; it is anaerobic and does not require oxygen. Under aerobic conditions, the intermediate of glycolysis, pyruvate, enters into the mitochondria and is converted to Acetyl-coenzyme A, the initiating substrate of the Krebs cycle as shown in Figure 2.5(A). The Krebs cycle yields intermediates such as NADH, which continue the aerobic pathway into oxidative phosphorylation in the inner membrane of the mitochondria. Oxidative phosphorylation is made up of the electron transport chain and chemiosmosis. In the electron transport chain, electrons are transferred from one molecule to another creating an electrochemical gradient and during chemiosmosis the energy stored in the gradient is used to make ATP. Oxygen is the final electron acceptor in the electron transport chain. Therefore, in the absence of oxygen the electron transport chain will stop running, and ATP will no longer be produced by chemiosmosis. Aerobic respiration produces thirty-six ATP molecules per molecule of substrate, while anaerobic glycolysis only produces two ATP and the energy molecule NAD⁺ undergoes regeneration by lactate dehydrogenase to produce two lactate molecules per molecule of glucose.

Due to the low oxygen conditions of the IVD, disc cells are believed to primarily obtain their energy through glycolysis where the glucose is converted into lactic acid yielding two ATP per molecule of glucose.^{28,58} Regulation of glycolysis is mediated by hypoxia-inducible factor (HIF)-1 α .⁸¹ HIF-1 is a transcription factor regulating expression of molecules connected with glycolysis, mitochondrial respiratory chain and oxidative phosphorylation. It has a heterodimer structure composed of a constitutively expressed oxygen-sensitive α - subunit. A more detailed overview of glycolysis is shown in Figure 2.5(B), where ten intermediates are each catalysed by a different enzyme to produce two molecules of pyruvate. The overall glycolysis reaction equation with D-glucose as the initial substrate is:



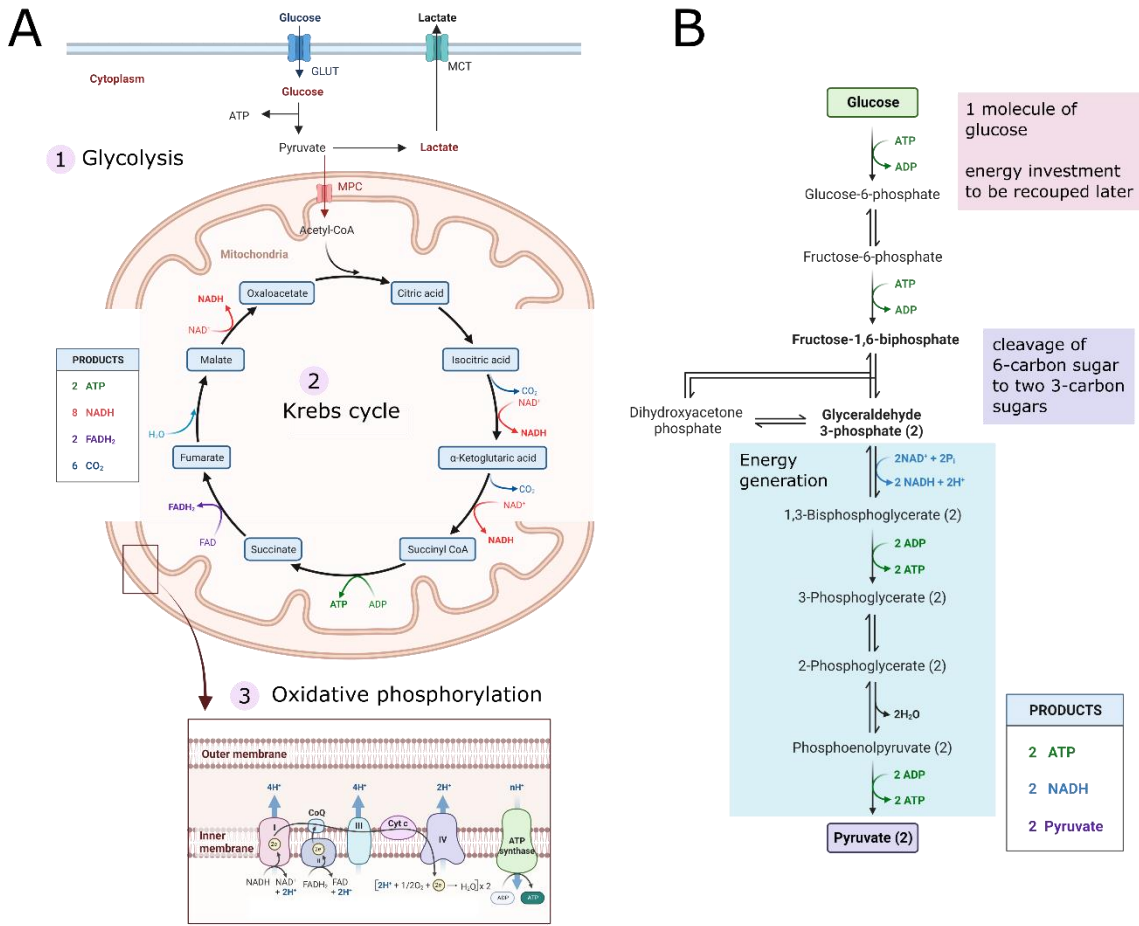


Figure 2.5 Schematic representation of ATP production by disc cells. (A) Glycolysis is the first step in all types of cellular respiration, and it takes place in the cytoplasm. Pyruvate, an intermediate of glycolysis, can then enter the mitochondria to continue through the Krebs cycle and followed by oxidative phosphorylation where the final electron acceptor is oxygen. (B) In glycolysis one molecule of glucose is broken down into ten intermediates which are each catalysed by a different enzyme to finally produce two molecules of pyruvate which are converted to lactate by lactate dehydrogenase. Adapted from BioRender templates for Glycolysis, Krebs cycle and the Electron Transfer Chain (2022).

As mentioned, disc cells primarily obtain their energy through anaerobic glycolysis, as a result glucose is considered the critical nutrient and several studies have report threshold glucose concentrations necessary to maintain cell viability. Bovine NP cells have reported reduced viability when glucose concentration falls below 0.5 mM for more than 3 days, while a bovine articular chondrocyte study concluded that if glucose concentration falls below 0.2 mM the efficiency of glucose transport into cells is likely to reduce within 24 hours.^{27,82} Meanwhile low pH, due to the accumulation of lactic acid, has also been long connected with induced cell death and viability has been reported to reduce at pH 6.0 even in the presence of adequate glucose.⁴⁹ Contrastingly, disc cells have remained viable up to 13 days in the absence of oxygen.^{27,49} Although oxygen does not appear necessary for maintaining disc cell viability, oxygen level plays a dominant role in maintaining the NP cell phenotype and controlling the synthesis of key water-

binding PG molecules of the ECM.^{28,83} The highest synthesis rates have been recorded at approximately 5 % O₂. However, once oxygen tension falls below this level, synthesis appears to be inhibited significantly in an oxygen tension-dependent manner.²⁸ Furthermore, acidic conditions have also been shown to hamper PG synthesis,^{9,49,50,84} but more recently both hypoxia and acidity have also been associated with progression of a pro-inflammatory microenvironment and upregulation of pain-related neurogenic factors.^{85,86} A study investigating the mechanisms by which the disc cells accommodate their low pH and hypertonicity environment found that the expression and regulation of the acid sensing ion channel 3 (ASIC3) in rat NP cells suggested an adaptation of the disc cells to their stressed and acidic microenvironment.⁸⁷ Carbonic anhydrases (CA) play a vital role in acid/base kinetics and mediate between different forms of metabolic acid production. CA XI and CA XII, which catalyse the reversible hydration of carbon dioxide and are responsible for the regulation of intracellular pH, have been highly expressed in human NP cells in order to maintain homeostasis in a hostile niche.⁸⁸ However, it has been suggested that expression of these molecules decreases with degeneration and that disc cells may not be able to sustain the acidic microenvironment over a prolonged period of time.⁸⁹

The viability and biosynthesis of a sparse population of disc cells are critical to the maintenance of a highly specific ECM composition which is required for the inherent biomechanical function of the IVD. Hence the effect of nutrient concentrations and pH on native NP cells,^{9,27,49,50,90-95} and potential cell therapies have been extensively investigated.⁹⁶⁻¹⁰⁰ Furthermore, the rates at which disc cells metabolise glucose and consume oxygen depend on the nutrient concentrations and local acidity, as well as among other factors such as matrix stresses and growth factors.^{9,101} In order to determine oxygen consumption rate (OCR) or glucose consumption rate (GCR) by disc cells, a diffusional uptake problem has been used throughout the literature. The equation defining the functional relationship between the OCR or GCR and oxygen or glucose concentration, respectively, is given by:

$$\frac{dC}{dt} = -Q = -\frac{V_{max}C}{K_m + C} \rho_{cell} \quad (2-3)$$

Where Q is the nutrient consumption rate ($\mu\text{M}/\text{h}$), t is the time (h), C is the local nutrient concentration (μM), and ρ_{cell} is the cell density (million cell/mL).⁹⁰ V_{max} is the maximum consumption rate (nmol/million cells/h) at high nutrient concentrations and K_m is the rate limiting Michaelis-Menten constant i.e., the solute concentration (μM) at which the consumption rate is at half of its maximum. The Michaelis-Menten constants, V_{max} and K_m , are determined by measuring the change in concentration over time and curve-fitting to the analytical solution.

Table 2.2 presents studies from the literature which have experimentally measured OCR of animal and human NP cells at different glucose concentrations. The Crabtree effect describes

the phenomenon where respiration or OCR is suppressed by high concentrations of glucose e.g. a negative Crabtree effect indicates no inhibition of OCR was observed under higher glucose concentrations. A positive Crabtree effect has been observed in porcine AF cells, but not for bovine and porcine NP cells, with glucose not appearing to affect OCR over the range of 1 – 5 mM.^{9,90} Healthy human cells have reported a trend towards a positive effect but nothing significant, while degenerated cells demonstrated a positive Crabtree with a significant shift towards an oxidative phenotype.⁹³

Due to the low oxygen presence in the disc *in vivo*, in addition to the rate limiting effect of oxygen levels on OCR, the effect of oxygen concentration on glycolysis is also imperative to a better understanding of the relationship between cellular metabolism and the low nutrient availability. However, it is important to note that these studies are not in full agreement on the effect of oxygen tension and glucose concentration on cellular metabolic activity. Moreover, in contrast to the Crabtree effect, the Pasteur effect describes the phenomenon where glycolysis or GCR is suppressed by high oxygen concentrations and subsequently results in an increase in respiration. Several disc cell studies have observed a positive Pasteur effect in NP and AF cells (canine, porcine and bovine).^{28,58,91,94} However, a recent study with porcine cells detected a positive Pasteur in AF cells but not NP cells.⁹⁵ Additionally, Bibby *et al.* (2005) demonstrated that below 8 %O₂, oxygen decreased the rate of lactate production (LPR) and above 10 %O₂, the effect of oxygen concentration was insignificant (i.e. a negative Pasteur effect). A summary of these studies from the literature can be found below, where Table 2.3 and Table 2.4 present experimentally measured GCR and LPR, respectively, for animal and human NP cells at varying levels of glucose and oxygen.

Table 2.2 Oxygen consumption rates (OCR) (nmol/million cells/hr) measured at different glucose concentration for nucleus pulposus cells from a range of species and age/degeneration stages.

Glucose (mM)	OCR			Species	Age	Configuration	Reference
	<i>mean</i>	<i>std</i>	<i>n</i>				
1	13.43	7.35	5	Porcine	3–5-month-old	Agarose gel	90
	23.10	12.87	5	Human (healthy adult)	21 - 65 years (grade 1 or 2)	P1-P2 cell suspension	93
	95.28	11.02	5	Human (degenerated)	43 - 62 years (grade 3 or 4)	P1-P2 cell suspension	
2.5	11.59	3.91	5	Porcine	3–5-month-old	Agarose gel	90
5	12.00	25.00	68	Bovine	-	Alginate bead	9
	14.70	3.00	3	Bovine	18 – 20 months	Alginate bead	91
	60.90	17.00	3	Porcine	10 – 15 months	Alginate bead	
	15.26	4.75	5	Porcine	3 – 5-month-old	Alginate bead	90
	18.06	12.17	5	Human (healthy adult)	21 – 65 years (grade 1 or 2)	P1-P2 cell suspension	93
	62.24	6.57	5	Human (degenerated)	43 – 62 years (grade 3 or 4)	P1-P2 cell suspension	
25	11.50	6.31	5	Porcine	3 – 5-month-old	Agarose gel	90
	13.24	9.41	5	Human (healthy adult)	21 – 65 years (grade 1 or 2)	P1-P2 cell suspension	93
	52.09	19.57	5	Human (degenerated)	43 – 62 years (grade 3 or 4)	P1-P2 cell suspension	

Table 2.3 Glucose consumption rates (GCR) (nmol/million cells/hour) measured at different glucose concentrations and varying oxygen levels for nucleus pulposus cells from a range of species and age/degeneration stages. Abbreviations: NX (normoxia), PX (physioxia) and HX (hypoxia).

Glucose (mM)	NX (21%)			PX (5%)			HX (1-2%)			Species	Age	Configuration	Reference
	mean	std	n	mean	std	n	mean	std	n				
0.5	51	8	9	33	3	9				Porcine	4 - 5 months	Agarose gel	95
1	65	41	9	60	35	9	34	21	9	Human (healthy adult)	21 - 65 years (grade 1 or 2)	P1 cell suspension	102
	121	79	9	48	47	9	15	9	9	Human (degenerated)	43 - 62 years (grade 3 or 4)		
	39	3	-	54	17	-	-	-	-	Porcine	3 - 4 months	Alginate bead	98
1.25	75	7	9	66	6	9				Porcine	4 - 5 months	Agarose gel	95
2.5	130	10	9	90	6	9							
3.75	160	9	9	121	10	9							
5	251	23	9	176	15	9				Porcine	3 - 4 months	Agarose gel	94
	208	14	-	250	13	-	280	14	-	Human (healthy adult)	21 - 65 years (grade 1 or 2)	P1 cell suspension	102
	124	102	9	160	109	9	68	29	9	Human (degenerated)	43 - 62 years (grade 3 or 4)		
	86	47	9	103	46	9	148	106	9	Porcine	3 - 4 months	Alginate bead	98
	46	11	-	111	11	-				Human (degenerated)	43 - 62 years (grade 3 or 4)	P2 cell suspension	20
	107	13	6	253	74	6	74	10	6	Bovine	18 - 20 months	Alginate bead	91
	95	14	3							Porcine	10 - 15 months		
25	64	39	9	686	316	9	165	94	9	Human (healthy adult)	21 - 65 years (grade 1 or 2)	P1 cell suspension	102
	196	118	9	83	45	9	207	131	9	Human (degenerated)	43 - 62 years (grade 3 or 4)		
	83	23	-	56	27	-				Porcine	3 - 4 months	Alginate bead	98
	321	39	-							Porcine	4 - 6 months	Agarose gel	103

Table 2.4 Lactate production rates (LPR) (nmol/million cells/hour) measured at different glucose concentrations and varying oxygen levels for nucleus pulposus cells from a range of species and age/degeneration stages. Abbreviations: NX (normoxia), PX (physioxia) and HX (hypoxia).

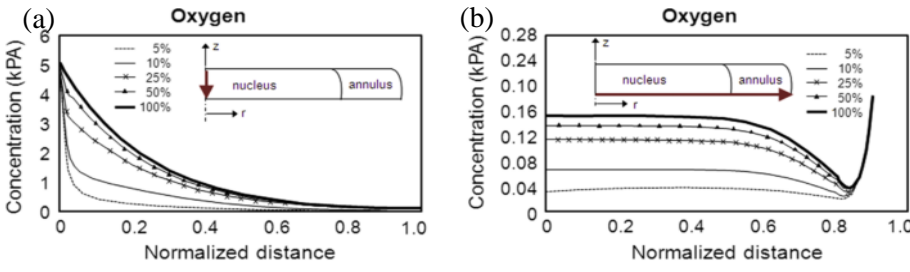
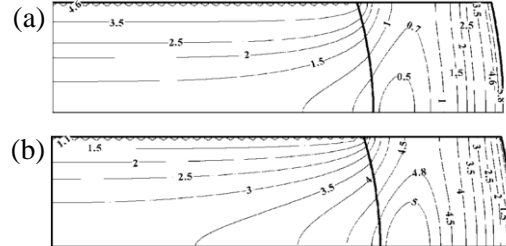
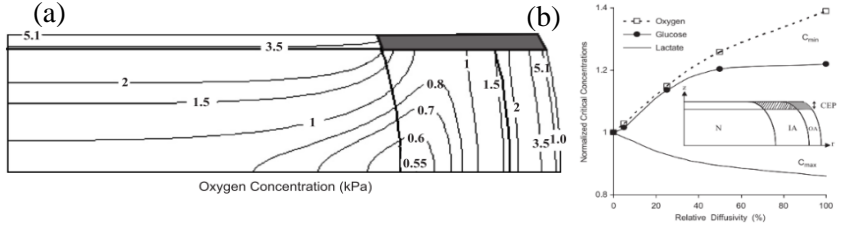
Glucose (mM)	NX (21%)			PX (5%)			HX (1-2%)			Species	Age	Configuration	Reference
	mean	std	n	mean	std	n	mean	std	n				
1	197	70	68	113	47	68	67	57	68	Bovine	-	Alginate bead	9
	92	62	9	127	53	9	30	16	9	Human (healthy adult)	21 - 65 years (grade 1 or 2)	P1 cell suspension	102
	244	149	9	118	78	9	68	53	9	Human (degenerated)	43 - 62 years (grade 3 or 4)		
5	89	59	9	168	80	9	98	15	9	Human (healthy adult)	21 - 65 years (grade 1 or 2)	P1 cell suspension	102
	203	94	9	189	83	9	298	204	9	Human (degenerated)	43 - 62 years (grade 3 or 4)		
	69	5	6	229	18	6	125	17	6	Human (degenerated)	43 - 62 years (grade 3 or 4)	P2 cell suspension	20
	197	70	68	113	47	68	67	57	68	Bovine	-	Alginate bead	9
	204	16	3	-	-	-	-	-	-	Bovine	18 - 20 months	Alginate bead	91
	355	36	3	-	-	-	-	-	-	Porcine	10 - 15 months		
	363	32	3	-	-	-	358	39	3	Bovine	18 - 20 months		
	537	49	3	-	-	-	652	49	3	Porcine	10 - 15 months		
25	67	31	9	72	32	9	239	111	9	Human (healthy adult)	21 - 65 years (grade 1 or 2)	P1 cell suspension	102
	210	76	9	169	79	9	296	218	9	Human (degenerated)	43 - 62 years (grade 3 or 4)		
	395	11	-	-	-	-	-	-	-	Porcine	4 - 6 months	Agarose gel	103

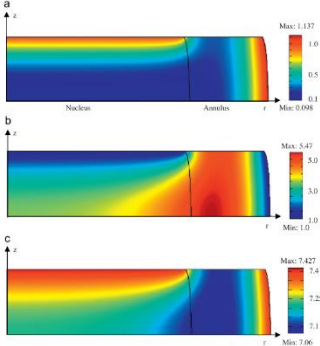
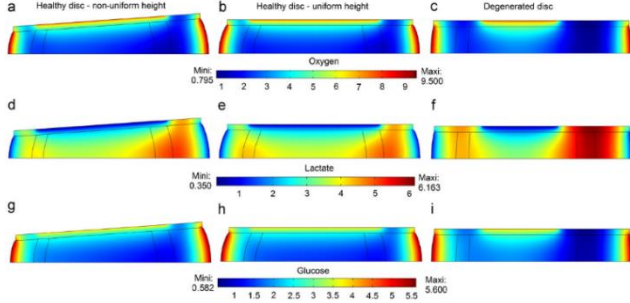
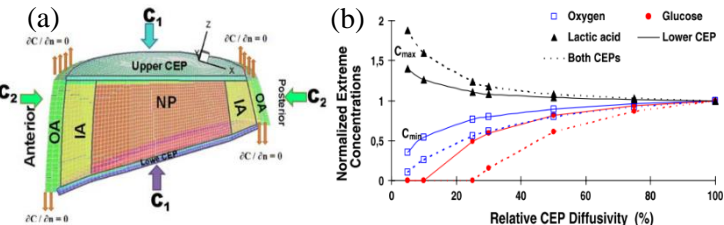
2.4 *In-Silico* Models of Solute Transport in the Intervertebral Disc

Predictive *in-silico* modelling is a powerful tool routinely used to study complex biological systems. For the last four decades, the human IVD has been the focus of many such investigations due to the difficulty of obtaining appropriate specimens, *in vivo* human measurements, and the complexity inherent in the IVD with biochemical, biomechanical, nutritional, and metabolic factors acting simultaneously. Schmidt *et al.* (2013) have compiled a comprehensive overview of *in-silico* models for IVD investigation, highlighting a number of nutrient transport models elucidating the metabolite concentrations in both healthy and degenerated IVDs.^{64,104–112} Theoretical transport modelling coupled with cellular activity can be an invaluable tool to investigate the nutrient distribution *in vivo* and supplement the limitations of *in vivo* and *in vitro* studies when it comes to accurately quantifying the spatial and temporal variations in the concentration and transport of solutes. Furthermore, *in-silico* models have proven themselves as reliable and robust tools, particularly when combined with experimental *in vitro* and *in vivo* measurements with a number of models having been compared to experimental results for verification of the implemented theory.^{105,113}

The last twenty years have seen continued advancements in mathematical modelling techniques to study transport phenomena in the human IVD from idealised axisymmetric discs to quadriphasic models incorporating nutrient transport and non-linear coupled cellular metabolism, to patient-specific diffusion parameters.^{65,104,105} A summary of some of the key nutrient-transport models of the human IVD can be found in Table 2.5. These models specifically study nutrient concentrations dependent on boundary concentration supplied, ease of transport into and throughout the disc ECM as well as the effect of cell population and metabolic activity. Typically, the IVD is compartmentalised into three distinct regions, the NP, AF and CEP, with each assigned their own experimentally determined transport properties i.e., diffusion coefficients for glucose, oxygen and lactate, cell densities and metabolic rates. Early models have demonstrated nutrient concentrations decrease with increasing distance from the boundary supply.^{104,105,114,115} These models have been extended to investigate the effects of various factors on nutrient microenvironment, e.g. cell metabolism, cell density/viability, EP calcification and porosity. For example, as diffusivity decreases (due to changes in calcification, porosity or composition) or cell density/metabolism increases, nutrient concentrations diminish and lactate acid accumulation increases within the IVD.^{64,105,107,115,116}

Table 2.5 Summary of *in-silico* models from the literature which have been used to investigate nutrient distribution within the human disc *in vivo*.

Results	Significance	References
 <p>Figure Variation of the oxygen concentration along (a) the z-axis and (b) the radius at mid-height for exchange areas on the endplate adjacent to the nucleus region.</p>	<p>First model to study nutrient transport in an axisymmetric disc with metabolic rates depending nonlinearly on the corresponding solute concentration. Results showed that nutrient concentrations fell towards the disc centre. Concentration levels decreased with a decrease in fractional exchange area and diffusivity, or with an increase in disc height and consumption rate.</p>	<p>104</p>
 <p>Figure Computed results for the coupled model (a) oxygen concentration [kPa] and (b) lactate concentration [nmol/mm³].</p>	<p>More complex metabolic reaction rates modelled by taking the coupling between GCR and LPR. This influenced the oxygen and lactic concentration, in particular the gradient of concentrations along the disc mid-height to the NP and AF interface where the most critical values are found i.e. minimum oxygen and maximum lactate</p>	<p>114</p>
 <p>Figure (a) Oxygen [kPa] within the disc with the CEP above the inner AF taken as impermeable (b) Effect of changes in CEP relative diffusivity above the inner annulus. CEP above the NP remains completely permeable.</p>	<p>This study considered the dependence of metabolic rates on the oxygen and lactate content. Oxygen and glucose levels changed dramatically once permeability fell below ~ 20%. Results indicate that disruptions in nutrient supply, due to the EP, shifts the location of the critical zones towards the centre of the disc NP.</p>	<p>115</p>

 <p>Figure Distribution of (a) oxygen, (b) lactate and (c) pH under static compression with 50% permeable EP boundary above the NP. Concentrations of oxygen and lactate were normalised by boundary concentrations at EP region above NP. A constant displacement (10% of disc height) was applied.</p>	<p>First study to characterise the IVD behaviour using new formulation of triphasic theory – examining the effect of mechanical compression (static & dynamic) on metabolism and distribution of oxygen and lactate. Dynamic compression increased oxygen, reduced lactate accumulation, and promoted OCR and LPR (i.e., energy conversion). Such effects of dynamic loading were dependent on strain level and loading frequency, and more pronounced in the IVD with less permeable EP. In contrast, static compression exhibited inverse effects on transport and metabolism. This coupling is considered necessary to determine how osmomechanical properties and load affect the spatial distribution of nutrients and thus the cellular metabolism.¹⁰⁵</p>	<p>116</p>
 <p>Figure Oxygen pressure (kPa) (a–c) and lactate (d–f) and glucose (g–i) concentrations (nmol/mm³) in a healthy disc with non-uniform height (a, d, g), uniform height (b, e, h) and in the degenerated disc (c, f, i).</p>	<p>2D model with quadriphasic theory coupled to solute transport. Chronic disc cell nutrition insufficiency prevents the cells from renewing the ECM and thus leads to the loss of PGs. Hence, the osmotic power of the disc is decreased, causing osmomechanical impairments. To study solute diffusion in a mechanically or osmotically loaded disc, the osmomechanical and diffusive effects were coupled in this model.</p> <p>The numerical results shows that solute distribution depends very little on the elastic modulus or the PG concentration but greatly on the porosity, diffusion coefficient and EP diffusion area.</p>	<p>105</p>
 <p>Figure (a) L5-S1 cut at the mid-sagittal plane to depict the distinct regions. (b) Effect of changes in relative diffusivity in the lower or both EP on extreme concentration values.</p>	<p>This study demonstrated the importance of realistic 3D disc geometry when results were compared with those from previous simplified axisymmetric models. Solute concentrations, particularly those of glucose, substantially diminish because of disturbances in supply at the EP and increases in cell metabolic rate.</p>	<p>106</p>

	<p>Figure Computed profile of the oxygen concentration [kPa] in the disc for the CEP relative permeability of 5% considering the cell viability criteria of glucose with or without pH.</p>	<p>First study to incorporate the consequences of cell death into the diffusion-reaction model. Measurement based cell viability–nutrient supply relationships employed to regulate cell population. Results indicated that as the exchange area across the CEP fell below ~ 40%, cell death was initiated and increased thereafter in an exponential manner. However, this model assumes that cell density varies instantaneously with glucose concentration.</p>	<p>107</p>
	<p>Figure Glucose concentration in the IVD for (a) normal and (b) 'calcified' CEP.</p>	<p>First study to compute effects of degenerative calcification and static strain. EP calcification was simulated by reducing EP permeability (~ 79%) and three static strain conditions through deformation. Min. glucose concentrations decreased 45% with calcification, whereas deformation led to a 4.8–63% reduction. Calcification more strongly affected glucose concentrations in the NP compared with the AF region.</p>	<p>64</p>
		<p>In this model, the cellular metabolic activities and viability were related to nutrient concentrations, and transport properties were dependent on tissue deformation. Tissue properties were altered to reflect degeneration, including reduced water content, fixed charge density, height, and EP permeability (mechano-electrochemical mixture theory). Deformation (10% static compressive strain) caused a 6.2% and 80% decrease in the minimum glucose in the normal and degenerated IVD, respectively. Although cell density was not affected in the undeformed normal disc, there was a decrease in cell viability in the degenerated case, in which average cell density fell 11% compared with the normal case. A disadvantage of this model is that resurrection of cells would occur when the glucose level recovers after falling below the critical level. Therefore, it is not capable of adequately describing the effect of nutrition levels on cell viability in a time-dependent manner.¹⁰⁹</p>	<p>108</p>

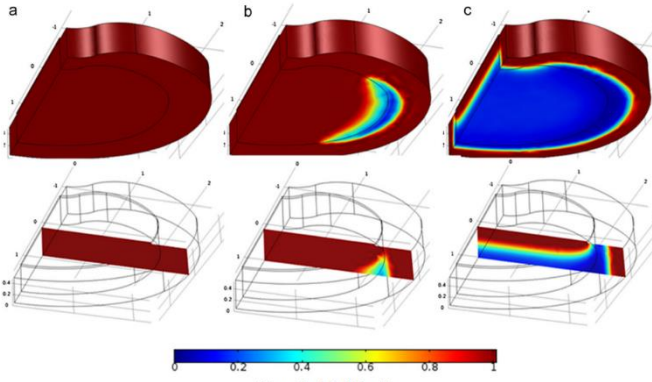
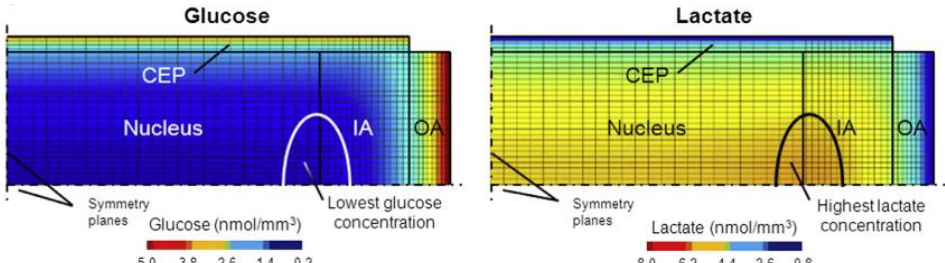
	<p>Figure Effects of reducing nutrition at the boundaries on cell density in non-degenerated IVDs at the end of a 10-day period—cell density distribution with (a) normal (i.e., 100%) nutrition level (b) 50% of normal level (minimum:0.11) and (c) 30% of normal level (minimum:0.02). The cell density was normalised by its initial value in each region.</p>	<p>Development of a novel constitutive cell density model, incorporated into the formulation of the mechano-electrochemical mixture theory to investigate the effects of nutrition limitation, degeneration, and dynamic loading on the cell viability. Cell density decreased substantially with reduction of nutrition supply.</p> <p>Cell death was initiated primarily near the NP–AF interface on the mid-plane. Dynamic loading did not result in a change in the degenerated cell density since glucose levels did not fall below the minimum value for cell survival. In the degenerated disc, increased frequency, and amplitude both resulted in higher cell density, as dynamic compression facilitates diffusion.</p>	<p>109</p>
	<p>This study investigated the effect of some degenerative changes on cell viability. OCR, GCR and LPR were expressed as a function of oxygen, pH and cell density. For ‘grade 0’, NP cell death was initiated for EP diffusivities below 20% of physiological values. However, for a ‘grade 3’ disc, cell death was initiated at the NP and AF interface in contrast to observations which show initial degeneration in the centre of the NP.¹¹⁷</p> <p>Reduced disc height and cyclic loading enhanced the cell nutrition. Vascularisation observed in the EP and disc of severely degenerated specimens which might significantly sustain the nutrition process, was not considered.¹¹⁸</p>	<p>110</p>	

Figure Glucose and lactate concentrations at steady-state for a ‘grade 0’ disc. Viability criteria was based on local glucose concentration and pH. In general, diffusion in the CEP and disc tissue fibrotisation played a major role in limiting the sustainable cell population.

	<p>Figure Changes in (A) cell density (normalised) (B) glucose concentration and (C) GAG content over time.</p>	<p>Simulation of degenerative changes in cell density, nutrition and PG content using bio-mechano-electro-chemical theory. Cell-mediated degeneration due to limited nutrition was simulated and validated with experimental results. Cell density reached equilibrium 30 days after reduced nutrition, while PG took 55 years. A decrease in PG content began ~ 100 days after glucose level decreased, starting near the NP-AF interface. Distribution of PG was consistent with results measured in the literature, except for the distribution of PG in the sagittal direction. The min. pH was 7.08 for reduced glucose and > 6.8 in the case where both glucose and the oxygen levels were reduced. Thus, no direct relationship between cell viability and pH was incorporated.</p>	<p>113</p>
	<p>Figure 3D distributions of glucose in (A) non-calcified EP (B) calcified EP. 3D distributions of oxygen in (C) non-calcified EP (D) calcified EP. Units: mM.</p>	<p>This model examined effects of EP calcification and the cell injection on nutrition. Calcification was simulated by reduction of tissue porosity and cell injection through increased cell density in the NP. Under EP calcification, glucose and oxygen concentrations were drastically reduced, with a 69.3% and 33.9% decrease in min. glucose and oxygen concentrations, respectively. Moreover, concentration levels in the NP, compared with the AF, were more significantly affected. The increase in cell density within the NP region significantly decreased the extreme oxygen and glucose concentrations.</p>	<p>111</p>
	<p>Figure Schematic illustration of included factors in the agent-based model simulations. Boundary glucose and lactate concentrations were manually set to 0 – 5 mM and 0 -10 mM, respectively.</p>	<p>Hybrid agent based model which combines experimental data to simulate cell behaviour exposed to a multifactorial environment, the present methodology was capable of reproducing cell death within 3 days under glucose deprivation and a 50% decrease in cell viability after 7 days in an acidic environment.</p>	<p>119</p>

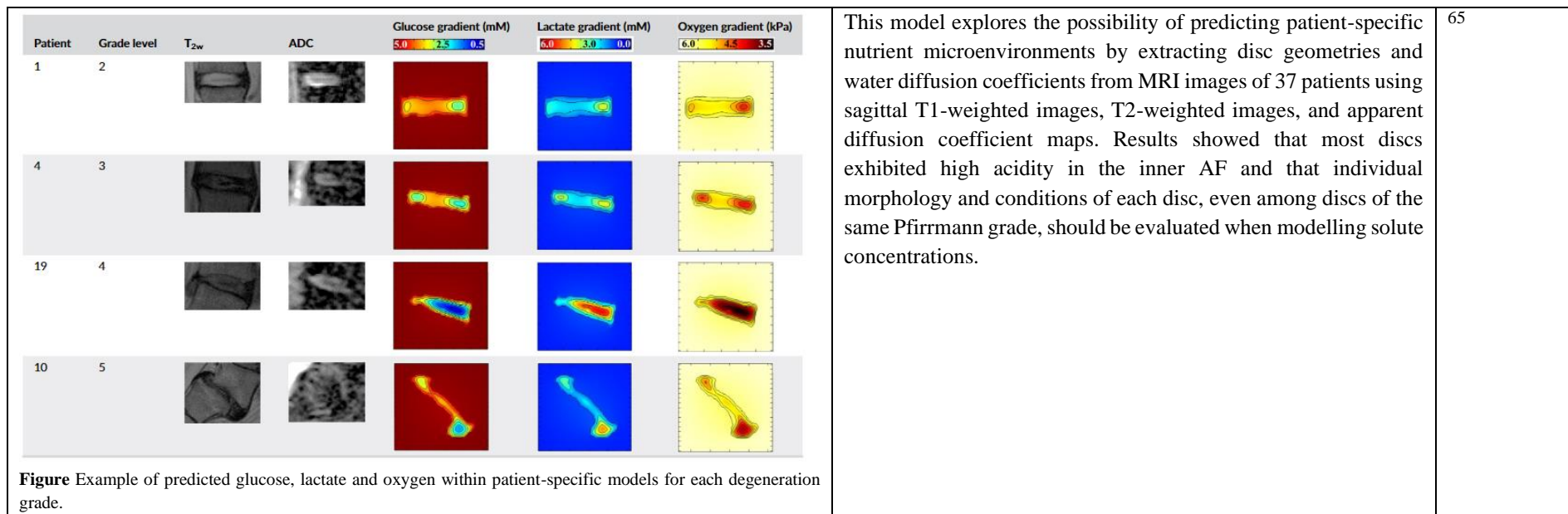


Figure Example of predicted glucose, lactate and oxygen within patient-specific models for each degeneration grade.

2.5 Cell Strategies for the Treatment of Disc Degeneration

Cell-based therapies are being readily explored as a regenerative strategy for several tissue types including cartilage, bone, and cardiac tissue. Therapeutically, they aim to replenish the number of viable cells and augment ECM anabolism by implanting healthy autologous or allogenic cells inside the diseased tissue and subsequently restoring tissue function. Degeneration typically manifests within the centre of the IVD. As a result, injectable cell-based therapies are being explored as early strategies, focusing on stimulating intrinsic repair and/or recreating the biochemical composition and structural integrity of NP tissue through the use of an appropriate cell-type and biomaterial carrier.^{18,120} The past twenty years have been a period of rapid development for cell-based regeneration, with a growing body of basic research and many promising therapies demonstrating therapeutic potential in pre-clinical animal models. Nonetheless, cell-based disc regeneration is still very much in its infancy, particularly at a clinical level. The IVD is a challenging biochemical microenvironment and its effects on viability and normal cell function will undoubtedly impact the degree of subsequent regeneration. To help improve future advances the research field requires a more thorough understanding of the NP nutrient microenvironment, how it changes with degeneration and how potential cell-based therapies will respond to the specific microenvironment into which they are administered.

2.5.1 Basic science development: *in vitro* and *ex vivo*

Prior to progressing to *in vivo* animal models, potential therapies must undergo extensive *in vitro* and *ex vivo* testing in culture systems which mimic those of the degenerated niche in order to determine their capability to survive and deposit appropriate ECM. For 2D *in vitro* cell culture, the *in vivo* disc nutrient microenvironment can be implemented simply by culturing cells in low oxygen, reduced glucose, and increased acidity. However, the physical 3D microenvironment is also important for its influence on cell behaviour and phenotype. A number of studies have used soft scaffolds such as hydrogels to mimic ECM, as well as bioreactor systems which apply dynamic compressive loads and/or hydrostatic pressure to simulate *in vivo* mechanical stresses.⁶ However, it is important to verify research findings in a system where the cells are in their native and highly specialised ECM, whose effect on cell behaviour is not fully understood.¹²¹ As a result, whole disc organ culture systems have become an important link between cell culture and *in vivo* studies for addressing fundamental research questions associated with disc degeneration,^{122–130} or for the assessment of regenerative cell therapies at an early stage of development.^{131,132,141,133–140} An additional benefit of these *ex vivo* culture systems is that they provide a high-throughput platform, where investigations can be performed in a more controlled environment while refining and reducing animal studies and their associated financial and ethical burdens.¹⁴²

Several research groups have realised a variety of *ex vivo* disc organ culture systems, which have been optimised through user experience over time. *Ex vivo* disc organ models involve the long term culturing of isolated discs from small and large animals, as well as cadaveric human IVD models. The *ex vivo* discs are typically cultured in bioreactor systems which are force-controlled and mimic the natural forces *in vivo*. So far, these are mainly uniaxial compression bioreactors.¹⁴² Gantenbein *et al.* (2015) have presented a thorough review of organ culture bioreactor-platforms which have been used to study human IVD degeneration and regenerative strategies.¹⁴² While systems which employ *ex vivo* degenerate discs from human donors may be the ultimate platform, human material is difficult to obtain due to ethical and government regulatory restrictions, making it unfeasible for all research labs. Discs from a variety of different species including mouse^{143,144}, rat^{145,146}, lapine^{122,147}, bovine^{148–151}, ovine^{152,153}, caprine^{154,155}, porcine^{156,157} and human^{124,139} have been used. However, the bovine caudal disc has been widely accepted as the most suitable model, as reflected by their popularity in published works, due to similar biological and biochemical properties. The attractiveness of this model is reinforced in their affordability and ease of accessibility in large numbers. The musculature of the bovine tail maintains an *in vivo* pressure which approximates the human disc in the prone position (0.1 - 0.3 MPa).¹²¹ While the bovine disc is 30% smaller than the human IVD, it possesses similar barriers to nutrient diffusion as the human lumbar disc, with a normalised aspect ratio (disc height normalised to lateral diameter) of 0.2.^{158–160} Furthermore, bovine discs have been shown to be comparable to human discs in terms of biochemical composition and loss of notochordal cells following birth.^{161,162}

Despite the promising development and increased complexity of disc organ culture in recent years, standardisation of *in vitro* and *in vivo* protocols is a popular topic across the research field. It has been well established that the microenvironment provides a significant barrier for the regenerative potential of implanted cell treatments. However, despite extensive testing of these cell-therapies in *ex vivo* disc organ culture systems at an early stage of development, it remains to be elucidated whether the microenvironment within *ex vivo* cultures are physiologically relevant to human degeneration. Furthermore, the most appropriate model will depend on the research question being addressed and both advantages and limitations of each model need to be carefully considered in the design of the experiment.

2.5.2 Pre-clinical animal models

After showing promise *in vitro*, new therapies must demonstrate efficacy and that the benefits of the treatment outweigh its risks under pre-clinical assessment prior to progressing to clinical evaluation. Although animal testing is not required by all regulatory agencies, pre-clinical animal studies are used to support the application process and the U.S. Food and Drug

Administration (FDA) issued draft guidelines to ensure such studies are conducted rigorously.¹⁶³ Animal models are crucial for understanding the progression of degeneration, how risk factors initiate, promote, or otherwise regulate degenerative changes and how potential therapeutics alleviate, resolve, or prevent degeneration. Large animal models have been accepted as good models for studying disc structure, geometry, biochemistry and biomechanics.^{164,165} Larger animals have a disc structure analogous to humans and they tend to undergo degeneration slowly. Examples include dogs, pigs, goats, sheep, cows, and nonhuman primates.¹⁶⁶ Alternatively, small animal models such as mice, rats, and rabbits undergo degenerative changes rapidly and have, in general, been used to answer metabolic questions.¹⁶⁷ Animal studies are expensive, labour intensive, involve uncontrollable physiological factors and ethical considerations limit their widespread use. In addition, as no perfect animal model exists their relevance to the human condition engenders much debate. Furthermore, degenerative animal models are typically induced by spontaneous injury or enzymatic induction and do not capture the natural pathological progression of degeneration and the importance of genetics.^{168,169}

A profound difference between animal discs is cell population (type and density) and the scale of the disc geometry and structure. It is hypothesised that the diffusion distance for solutes entering and metabolites leaving the disc will play a significant role in establishing a unique microenvironment along with cellular density and metabolic activity. For example, nutrients must first diffuse through the CEP and then through the dense ECM of the NP, a distance which could be up to almost 6 mm (half the disc height) in some human IVDs.¹⁷⁰ A young, healthy human NP contains notochordal cells and mature NP cells, and as discussed in Section 0, the former are large vacuolated cells which originate from the embryonic notochord and generally disappear in an age-dependent manner. Like humans, notochord cells of sheep, goats, horses, and cattle virtually disappear after birth and the NP remains more sparsely populated by rounded chondrocyte-like cells. However, in most other mammals, the notochord cells persist throughout adult life, including mice, rats, rabbits, pigs and non-chondrodystrophoid dogs.^{121,171} The presence of notochordal cells in animal models has significance, as they are a completely different cell type in terms of morphology and function and the disappearance of notochord cells in humans is considered predominant in the initiation and development of degeneration.^{172,173} Therefore, results obtained from animals which retain notochordal cells well into adulthood may require careful interpretation compared to the human condition.¹²¹

2.5.3 Clinical assessment

As mentioned previously, cell-based disc regeneration at a clinical level remains in its infancy, lagging behind equivalent therapeutics under clinical evaluation in the cartilage and bone field. There are currently twenty-six clinical trials registered worldwide (<https://clinicaltrials.gov/> search performed November 2022) and most of these trials are carried out across the United States (42.8%), as shown in Figure 2.6(A). The largest registered trial took place across 48 locations in the United States and Australia (NCT02412735) and involved 404 participants, while the next largest consisted of 13 – 14 locations within the United States and involved 60 – 200 participants. The largest multicentre European trial took place in ten locations across Germany and Austria (NCT01640457) and involved 120 participants, while trials across Asia appear to be on a smaller scale involving < 50 participants each. A full table summarising the results of the clinical search can be found in Appendix B.2. Participant selection includes patients anywhere from 18 – 100 years with chronic back pain i.e. > 4 visual analogue scale (VAS) and > 40 Oswestry disability index score (ODI) and who are resistant to conservative care for more than six months. Exclusion criteria include evidence of clinically-relevant vertebral or spinal abnormalities, including spondylolisthesis, spondylolysis, scoliosis, fracture, fracture, severe kyphosis, or disc herniation.⁶

After demonstrating safety and efficacy in animals, therapies enter three main clinical phases. Phase 1 is the earliest trial phase, with Phase 3 being the latest, while 43.8% of cell-based disc regeneration trials appear to be in Phase 2, Figure 2.6(B). However, it is reported that during this critical evaluation period, these promising new treatments do not appear to work to the same extent in humans as did under *in vitro* or pre-clinical assessment and it is commonly believed that the “hostile” nature of the degenerating IVD is linked to the weak outcomes of prospective studies.⁵⁻⁷ This is reflected in the status of clinical trials in Figure 2.6(C), where almost every year one or more clinical trials are withdrawn, terminated or suspended for undisclosed reasons. Furthermore, despite eight completed clinical trials over the last ten years, publication of these results are limited, and the true status and progress of these clinical evaluations are challenging to discover. Cell-based trials include both allogenic and autologous cells from a range of cell sources (e.g. bone marrow (BM-) and adipose (AD-) derived mesenchymal stem cells (MSCs) and discogenic or juvenile chondrocyte cells) with large heterogeneity on the number of injected cells (1-40 million).¹⁷⁴ More deliberation and careful consideration may be necessary to identify a precise cell number for intradiscal delivery, as the exact number of cells required for functional regeneration is unclear as well as the maximum number of implanted cells which will sustain the IVD microenvironment without exacerbating the limited nutrient supply. The urgency for consensus on this may be reflected in the limited pre-clinical data and clinical trial report available. This is shown, for example, where Mesoblast Ltd. used 6 and 18 million cell doses in their Phase 2 trial (NCT01290367) before progressing into Phase 3 with just the lower dose of six

million cells (NCT02412735). Additionally, DiscGenics Inc. used ten million cells in their pre-clinical animal rabbit model,¹⁷⁵ before progressing with a low dose of three million and a high dose of six million cells in their ongoing clinical trials (NCT03347708).

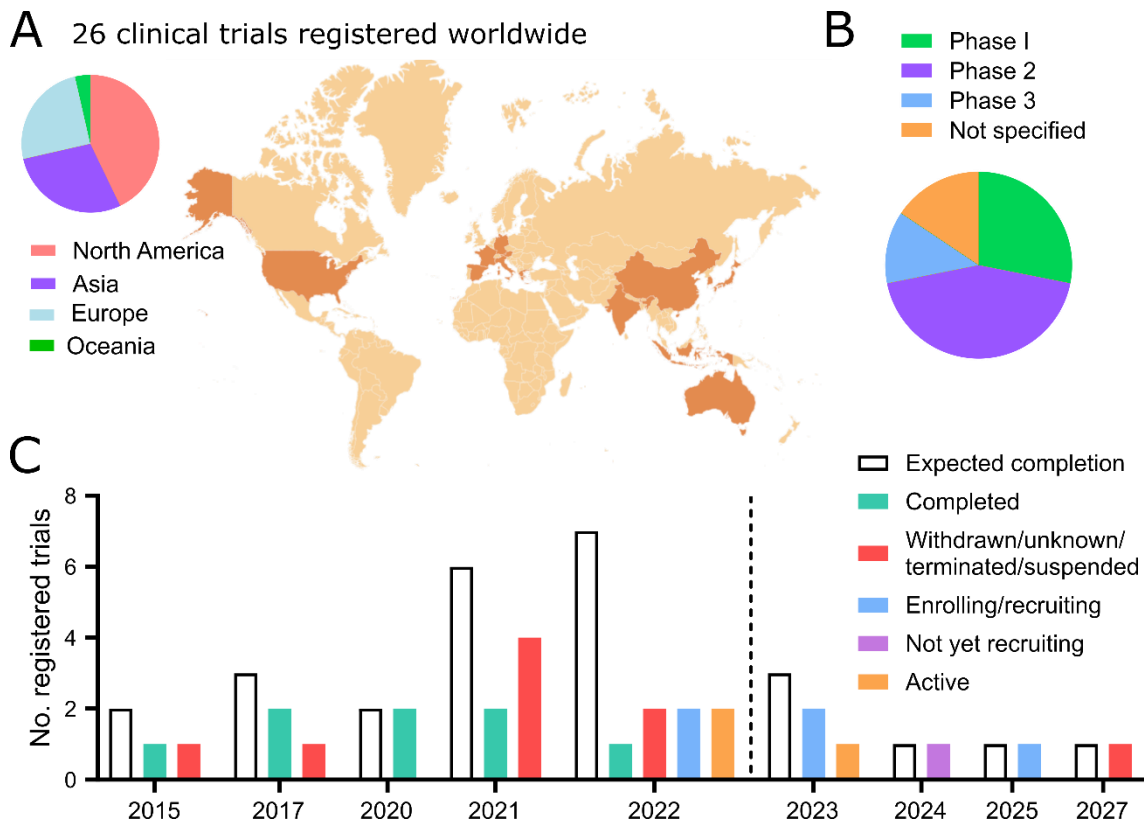


Figure 2.6 Geographical demographic, clinical phase, and status of registered clinical trials for cell-based disc regeneration. (A) Geographical demographic of registered clinical trials, with 42.8% in North America, 28.6% in Asia, 25% in Europe and 3.6% in Oceania. (B) 28.1% registered as Phase 1, 43.8% as Phase 2, 12.5% as Phase 3 and 15.6% did not specify on clinicaltrials.gov. (C) Status of past and current trials. The expected completion date (total) is specified along with the number which were successfully completed or withdrawn/unknown/terminated/suspended.

2.6 Summary and Clinical Significance

This thesis investigates the stages of assessment which a new developing cell therapy undergoes from the perspective of the nutrient microenvironment, all the way from “bench to bedside”. To begin with, *in-silico* models will be employed to re-evaluate the current knowledge on the nutrient microenvironment in terms of grade-specific stages of degeneration. To maximise future advances, the research field requires a more thorough understanding of the nutrient microenvironment and how it changes with degeneration. This understanding of the NP niche will improve the development of potential cell-based therapies by allowing the field to study how inherent microenvironmental conditions may adversely affect the survival and regenerative capacity of administered cells, which is often believed to be a key factor linked to high failure of prospective studies.⁵⁻⁷ Even at the basic science stage IVD research has been challenged with heterogeneous results in terms of the regenerative potential and matrix synthesis of new therapies *in vitro*. Consequently, this thesis will characterise the local nutrient microenvironment of *in vitro* and *ex vivo* culture systems to elucidate the metabolite concentrations which are being established and to place “standard practice” culturing conditions into context in terms of physiological relevance. Lastly this work explores differences in metabolism between animal models and clinical trials in terms of nutrient demands and regenerative capacity. Not only will this ascertain the clinical relevance of animal models, but it will provide a path towards understanding “time to regeneration” between pre-clinical assessment and clinical evaluation and the stunted success or expectations of cell-based clinical trials.¹⁷⁶ Together this work aims to reduce the *in vitro* to *in vivo* gap and maximise the chances of more successful clinical translation based on nutritional demands. This not only has important scientific merit but also significant value for clinical translation, particularly with the burden of an aging and increasingly sedentary population and thus exciting developments are anticipated in the next few decades.¹⁷⁷

Chapter 3. General Methods

All standard operating protocols established within this thesis work are attached in Appendix A.

3.1 Establishing the *In-Silico* Nutrient-Transport Models

As presented in the literature review, *in-silico* models of varying complexities have been developed to incorporate nutrient concentrations coupled to metabolic rates in the human IVD.^{104–108,114–116} However, no studies have used these methods to predict the metabolite concentration in *ex vivo* disc organ culture systems or *in vivo* discs from other species. To accurately predict nutrient distributions within a disc or culture sample, models must incorporate accurate 3D geometry, nutrient concentrations coupled to cellular metabolic rates and transport properties such as diffusion rates under strain due to physiological loading of the disc or the appropriate hydrogel concentration.

Briefly, the finite element method (FEM) is a computational technique used to obtain approximate solutions of boundary value or field problems where the field variables are the dependent variables of interest governed by the differential equation. The boundary conditions are the specified values of the field variables (in this case solute concentrations) on the boundaries of the field or domain. The model body is discretised by dividing it into an equivalent system of many smaller bodies called finite elements which are interconnected at points common to two or more elements (nodes) and/or boundary lines. The nodes are the specific points in the finite element at which the value of the solute concentrations is to be explicitly calculated.

In the case of modelling an intact IVD, whether *in vivo* or *ex vivo*, a 3D anatomical disc was created using SOLIDWORKS® CAD software and consisting of distinct tissue domains (e.g. NP, AF, and CEP). Due to symmetry and to simplify the model, typically only a quadrant of the assembled discs was imported into COMSOL Multiphysics 6 (COMSOL Inc., Burlington, USA) using the LiveLink™ for SOLIDWORKS®. The physics of the FEM was established using “Transport of Dilute Species” within the Chemical reaction Engineering Module, which was based on Fick’s Law (2-1) applied across all domains for oxygen, glucose, and lactate (pH). The *in-silico* models were governed by coupled reaction-diffusion equations which account for the metabolically active cell population and metabolite diffusion parameters through the different domains (e.g. tissue, media, or hydrogel). The governing equation was formed by substituting Fick’s first law (2-1) into the conservation of mass equation:

$$\frac{\partial C}{\partial t} = D \frac{\partial^2 C}{\partial x^2} \pm Q \quad (3-1)$$

Where Q is the reaction term for the metabolic rates (solute consumption or production). The metabolic rates were modelled as being dependent on local oxygen and pH levels by employing equations derived and published previously.⁹ Oxygen consumption rate (OCR or Q^{O_2}) was modelled using Michaelis-Menten kinetics. Huang *et al.* have used the Michaelis-Menten equation to describe the functional relationship between OCR and both oxygen concentration and pH level:

$$Q^{O_2} = -\frac{V_{max}(pH - 4.95)C^{O_2}}{K_m(pH - 4.59) + C^{O_2}}\rho_{cell} \quad (3-2)$$

where Q^{O_2} is the consumption rate ($\mu\text{M}/\text{h}$), t is the time (h), C^{O_2} is the local oxygen concentration (μM), pH is the local pH level and ρ_{cell} is the cell density (million cells/mL).^{90,116} V_{max} is the maximum consumption rate (nmol/million cells/h) and K_m is the rate limiting Michaelis-Menten constant i.e., the oxygen concentration (μM) at which the consumption rate is at half of its maximum. The rate of lactate production (LPR or Q^{lac}), which is exponentially dependent on local pH and oxygen levels, was also based on that of bovine NP cells from the literature:⁹

$$Q^{lac} = \exp(-2.47 + 0.93 \times pH + 0.16 \times C^{O_2} - 0.0058 \times C^{O_2^2})\rho_{cell} \quad (3-3)$$

The rate of glucose consumption (GCR or Q^{gluc}) was incorporated based on the assumption that disc cell metabolism is primarily glycolytic, a process where one molecule of glucose is broken down to produce two molecules of lactate. Therefore, glucose consumption was simply modelled as:

$$Q^{gluc} = -0.5 \times Q^{lac} \quad (3-4)$$

The pH level in the disc model was calculated from the lactate concentration based on an approximately linear relationship established from experimental data:^{9,114}

$$pH = A \times C^{lac} + B \quad (0 < C^{lac} < 30 \text{ mM}) \quad (3-5)$$

where $A = -0.1 \text{ mM}^{-1}$ and $B = 7.5$.¹¹⁶ This was implemented into the computational model as a piecewise function, bound at 0 mM and 30 mM of lactate.

3.1.1 Additional parameters of the FEM

A physics-controlled mesh was used, where COMSOL Multiphysics creates a mesh that is adapted to the current physics interface settings in the model. Extremely fine element size parameters were assigned to the 3D *in vivo* disc models (maximum element size 1.31 mm, minimum element size 0.00131 mm, maximum element growth rate 1.3 and a curvature factor of 0.2), as shown in Figure 3.1. Extra fine element size parameters were assigned to the 3D *in vitro* cell culture models (maximum element size 1.16 mm, minimum element size 0.00161 mm, maximum element growth rate 1.3 and a curvature factor of 0.2). A sample of a mesh convergence study can be found for the human disc model in Appendix B.2, justifying the choice of an extra fine and extremely fine mesh size.

Time-dependent problems were solved using the default COMSOL Multiphysics setting of a physics controlled adaptive timestepping scheme. This means that COMSOL automatically adjusted the timestep size to maintain the desired relative tolerance (0.001). During the solution, the solver automatically made the timestep smaller to resolve any fast variations in the solution, as needed. Similarly, it made the timestep larger during periods when the solution was only varying gradually.

COMSOL Multiphysics supports a number of consistent unit systems, including the SI unit system, which is the default unit and the system used within this work. The physics interface displays the applicable unit or SI prefix used to define the input quantities.

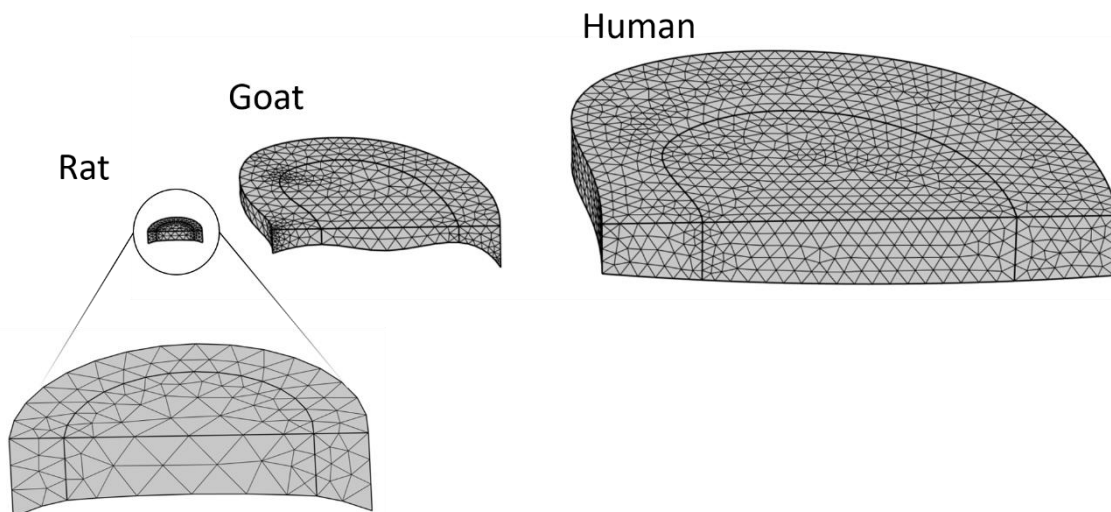


Figure 3.1. An example of an extremely fine physics-controlled mesh of tetrahedral elements within a 3D quadrant of a rat caudal, goat lumbar and human lumbar disc.

3.2 Determining the Total Cell Density and the Proportion of Metabolically Active Cells within Disc Tissue

The metabolically active cell density of tissue was determined using methylthiazolyldiphenyl-tetrazolium bromide (3-(4,5-Dimethyl-2-thiazolyl)-2,5-diphenyl-2H-tetrazolium bromide) (MTT) and a 4',6-diamidino-2-phenylindole (DAPI) (both Sigma–Aldrich) counterstain as previously described.^{127,178,179} MTT metabolic staining is a commonly used assay to assess cell viability and metabolic activity. The MTT assay is based on the conversion of MTT into a blue-coloured formazan product by mitochondrial dehydrogenases in viable cells. MTT passes through the cell membrane and is taken up by the mitochondria. The mitochondrial enzymes convert MTT into formazan, which accumulates in the cells. The formazan is insoluble and is most commonly visualised by solubilising it with a detergent and measuring the absorbance of the resulting solution using a spectrophotometry where the absorbance is directly proportional to the number of viable cells and their metabolic activity. Briefly, a 0.5 mg/mL MTT solution was made up in phenol-free Dulbecco's Modified Eagle Medium (LG-DMEM, Thermo Fisher Scientific). For bovine and goat tissue, approximately 2 – 3 mm thick sections were taken transversely across the disc incorporating both the NP and AF. The sections were placed in 6-well plates and incubated in ~ 5 mL of solution for 3 hours in the dark under gentle agitation and 37°C. For rat tissue, the skin of the tail was removed and cleaned by removing the tendons and excess tissue making the caudal discs visible. The intact vertebral column was incubated in a 15 mL tube rotating at 10 r.p.m. in the dark and 37°C for 16 hours.

Following incubation, the tissues were washed thoroughly with phosphate buffered saline (PBS, Sigma-Aldrich). Bovine and goat tissue was dabbed dry against a Kimwipe before embedding in optimal cutting temperature (OCT) compound (VWR) and kept overnight at 4°C before snap freezing in isopentane (2-Methylbutane, Sigma–Aldrich). For the rat tissue, the discs were carefully removed from the tail retaining the CEP to prevent swelling. The intact discs were then placed into 30% (w/v) sucrose and kept at 4°C until the samples sink to the bottom, approximately 3 – 4 hours. The samples were then dabbed dry, the disc tissue was exposed by inserting a blade as close as possible to the bounding CEP along the transverse plane, avoiding the central plane of the disc to maintain NP integrity. The same was done along the other bounding CEP to remove the disc in a thin slice. The tissue was then embedded in OCT compound at 4°C for another 4 – 5 hours before snap freezing. All samples were stored at –80°C until sectioning on a cryotome.

For cell density analysis, 10 µm slices were cut, randomly selected for mounting on a microscope slide using fluoroshield with DAPI (Sigma–Aldrich). Slides were examined under both brightfield, to capture active MTT+ cells, and fluorescence in order to capture all cell nuclei stained with DAPI (Olympus BX51 upright microscope). The metabolically active proportion

was assessed qualitatively by merging the brightfield and DAPI image using ImageJ (National Institutes of Health, Maryland). The total number of cells (DAPI) was determined automatically using the particle analyser while the number of dual stained cells (overlapping formazan crystals and blue nuclei) was performed manually using the cell counter plug-in.

3.3 Qualitative Histological Analysis

3.3.1 Cell culture sample fixation

Micro-spheroids were removed from culture, washed with PBS and fixed with 4% paraformaldehyde (PFA) at 4°C for 1 – 2 hours. PFA was removed and micro-spheroids were washed again with PBS before gathering them in the bottom of a flat-bottomed 96-well. Cooled molten agarose (2% w/v) was used to embed the micro-spheroids. Once set, the agarose discs were removed from the well and were ready to undergo the dehydration process.

3.3.2 Native disc tissue fixation

For goat disc samples, the lumbar discs were isolated from the spinal column using a Mitre saw (Evolution Power Tools, Sheffield, UK). Discs, with a section of the vertebral body still attached, were fixed for 72 hours in 10% Formalin (Sigma–Aldrich), gently shaking at room temperature. The vertebral segments were rinsed thoroughly and placed into Decalcifying Solution-Lite (Sigma–Aldrich) for 2 – 3 weeks, gently shaking at room temperature. Samples were checked regularly to assess the softness of the vertebral bone, and when possible, the soft bone was paired back with a scalpel until the lumbar disc remained with only a thin layer of VEP.

For rat disc samples, the skin was removed, and the intact tail was fixed for 48 hours in 10% Formalin, gently rotating at room temperature. After 24 hours the tails were cleaned by removing the tendons and excess tissue making the caudal discs visible. The tails were rinsed thoroughly and placed into Decalcifying Solution-Lite until the vertebral bodies were soft (3 - 5 days). Caudal discs were isolated by cutting through the vertebral body with a scalpel and retaining only a thin layer of VEP.

3.3.3 Sample dehydration and histological staining

Fixed samples were washed with PBS, dehydrated in a graded series of ethanol solutions (50 – 100%), cleared in xylene and embedded in paraffin wax (all Sigma-Aldrich). Sections (8 µm) were obtained with a microtome (Leica RM2125rt, Ashbourne, Ireland) and secured to microscope slides (Polylysine™, VWR). Tissue sections were rehydrated prior to staining with

either hematoxylin and eosin (H&E) to determine cellular distribution, 1% (w/v) alcian blue (AB) 8GX in 0.1 M hydrochloric acid (HCL) to visualise sGAG deposition or picosirius red (PSR) to visualise collagen content (all Sigma-Aldrich). Native disc samples underwent a dual staining of 5 mins in AB followed by 45 mins in PSR to visualise sGAG and collagen distribution together. Stained samples were imaged using an Aperio ScanScope slide scanner.

3.4 Cell Isolation and Monolayer Expansion

3.4.1 Animal cell isolation

Disc tissue was harvested from the caudal spine of ~ 6-month-old Wistar rats (male and female) and the lumbar spine of skeletally mature (4 – 5 years) Saanen goats (female) within 1 and 5 – 6 hours of sacrifice, respectively. Rat/goat tissue was obtained from discarded tissue of animals undergoing procedures approved by the Health Products and Regulatory Authority (HPRA) in the Comparative Medicine Unit (CMU), Trinity College Dublin or the School of Veterinary Medicine, University College Dublin.

Under sterile conditions, IVDs were carefully exposed by inserting a blade as close as possible to the bounding EP along the transverse plane. The NP tissue removed first from the central section of the disc. The AF was then removed by cutting along the other bounding endplate to remove the AF tissue in slices which were then diced into smaller pieces on a sterile petri dish. The tissue from 3 – 6 rat tails was pooled into each biological repeat or “prep” to ensure sufficient cell numbers from the isolation.

Tissue was enzymatically digested using a combined pronase (Millipore, Sigma) and collagenase type II (Gibco, Thermo Fisher Scientific) serum-free digestion media consisting of LG-DMEM (low glucose) supplemented with 2% penicillin-streptomycin (Pen-Strep) and 0.2% Primocin (InvivoGen). Rat tissue (NP and/or AF) was digested in 5 mL of digestion media per tail (10 – 12 discs/tail) and goat tissue (NP and/or AF) was digested in 10 mL per disc. Pronase was used at an activity of 70 U/mL and 100 U/mL of digestion media for rat and goat, respectively. Collagenase type II was used at an activity of 400 U/mL and 300 U/mL of digestion media for rat and goat, respectively. The enzymes were dissolved in the digestion media in a 37°C water bath before sterile filtering (0.2 µm filter).

Rat tissue was incubated for a period of 5 – 6 hours at 37°C under constant rotation (10 r.p.m.). Rat NP digest was triturated with a 18G needle as the tissue started to break up (after ~ 1 – 2 hours). Rat AF and both goat tissues underwent additional physical agitation every 2 hours using a gentleMACS Tissue Dissociator (Miltenyi Biotech GentleMACS Tissue Dissociator). Digests were stopped when there was a good proportion of single cells, rather than cell clusters, visible under a haemocytometer. Digested tissue/cell suspension was passed through a 70 µm cell

strainer to separate cells from tissue debris and filtrate was rinsed with PBS (2% Pen-Strep) by repeated centrifugation (650 x g for 5 mins) and aspiration. Cell yield and viability were determined using a haemocytometer and trypan blue exclusion before seeding at an initial cell density of 5×10^3 cells/cm² and expanded in LG-DMEM supplemented with 10% foetal bovine serum (FBS) and 2% Pen-Strep (all Gibco, Thermo Fisher Scientific). Cells were expanded to passage 2 (P2) with medium exchanges performed every three days (37 °C in a humidified atmosphere with 5 %CO₂ and 10 %O₂).

3.4.2 Human cell isolation

Human disc tissue was collected through informed consent of patients undergoing discectomy procedures and approved by the Mater Misericordiae University Hospital IRB (Ref 1/378/2229) and Trinity College Dublin (TCDFSTEMSREC/15032021/Buckley). Under sterile conditions, tissue was weighted and washed with PBS (2% Pen-Strep) by repeated centrifugation (650 x g for 5 mins) and aspiration. To confirm the absence of bacterial growth, tissue was placed in a 70 mL tub with serum-free LG-DMEM supplemented with 2% Pen-Strep and 100 µg/mL kanamycin sulfate (Gibco, Thermo Fisher Scientific) and cultured overnight (37 °C in a humidified atmosphere with 5 %CO₂ and 10 %O₂).

Under sterile conditions, the tissue was separated into NP and AF using the overnight swelling of the NP and the clear laminar structure of the AF as a guide. NP and AF were then diced into smaller pieces on separate sterile petri dishes. Like the animal cell isolations, the human NP and AF was enzymatically digested using a combined pronase and collagenase type II digestion media (serum-free, LG-DMEM, 2% Pen-Strep and 0.2% Primocin). 10 mL of digestion media was used per g of tissue and an enzyme activity of 100 U/mL and 300 U/mL was used for pronase and collagenase, respectively. Consistent enzyme concentrations were used for NP and AF tissue. However, NP and AF tissue were digested in separate 50 mL tubes at 37°C under constant rotation (10 r.p.m.) for 3 – 4 hours. Similar, to the animal cell isolation, digests were stopped when there was a good proportion of single cells, the remaining suspension was passed through a cell strainer (70 µm), the filtrate was centrifuged and rinsed with PBS before counting the cell yield. To promote cells attachment the culture flasks were first coated with 0.2% (w/v) gelatin (porcine skin Type A, Sigma). Briefly, the gelatin was left to coat the flask for one hour at room temperature before pouring off the gelatin and leaving the flasks to dry for 15 – 20 mins in the cell culture hood before seeding at 5×10^3 cells/cm².

3.6 Quantitative Biochemical Analysis

Prior to biochemical analysis, all samples (i.e. tissue or micro-spheroids) were digested in a papain enzyme solution of 100 mM sodium phosphate/5 mM Na₂EDTA buffer, 3.88 U/ml of papain enzyme and 5 mM L-cysteine, pH 6.5 (all from Sigma-Aldrich) at 60°C under constant rotation (10 r.p.m) for 18 hours.

3.6.1 Glucose assay

The total glucose content of the digested sample was quantified using an enzymatic-colorimetric assay (Sentinel Diagnostics, Italy), which was then normalised to the water content of the original tissue samples to obtain a concentration (mol/L). The glucose assay was validated for both media samples and digested tissue samples of a known glucose concentration. The tissue samples were created by soaking biopsies in a known concentration of glucose, under constant agitation, until they were fully equilibrated. A soaking duration was calculated as sufficient time for the glucose molecules to adequately perfuse the tissue, using Fick's dimensionless number as a criterion of closeness to the steady state:

$$\frac{Dt}{L^2} \quad (3-6)$$

where D is the diffusivity of glucose in the disc tissue, t is the soaking time and L is the total diffusion distance. When the resulting dimensionless number is calculated as much larger than unity (i.e. $\gg L^2$) an equilibrium or steady state may be assumed. Additionally, the medium was refreshed after a quarter of the soaking time to account for displacement of the original tissue fluid.

A diabetic glucose meter was used as another method of glucose measurement (FreeStyle Optimum, Abbot Diabetes Care, Ireland). When the sample is applied to the test strip the glucose present reacts with the chemicals on the test strip and produces a small electrical current. The size of the current, which depends on the amount of glucose in the sample, is measured and a result is displayed in mmol/L by the monitor. The accuracy of the meter on media samples has been tested previously and the method published.⁹⁸ Media readings using the glucose meter strips and glucose assay are compared in Figure 3.2(A). It was found that the biochemical assay underestimates the glucose content across five tissue concentrations ranging from 5.5 mM to 25 mM (Figure 3.2 (B)). However, due to the linearity of the data, a standard curve was created as a correction factor to apply to the biochemical reading (Figure 3.2(C)).

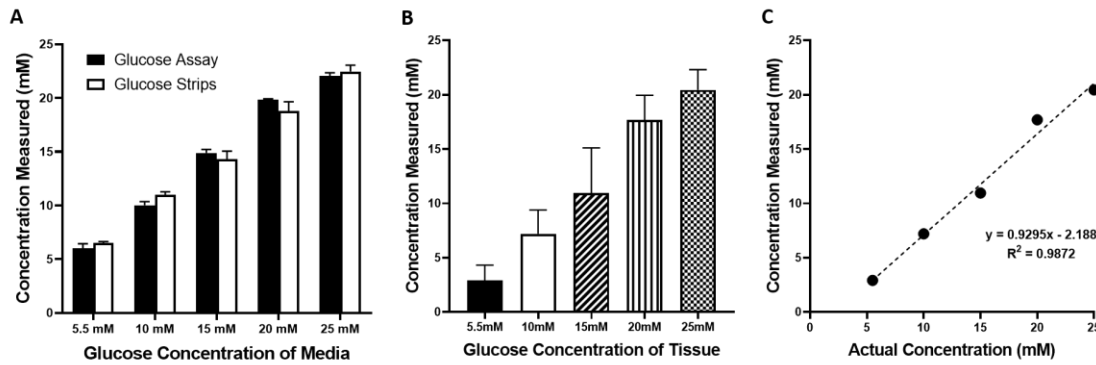


Figure 3.2 Assessing the accuracy of the biochemical glucose assay.(A) Media samples of known glucose concentration tested using the glucose assay and the glucose meter strips. (B) Results of the measured glucose concentration in tissue samples of a known glucose concentration. (C) Standard curve with an equation of the line to be used as a correction factor for the biochemically determined glucose concentration.

3.6.2 Determination of DNA and sulphated glycosaminoglycan content

DNA content of each sample was quantified using the Quant-iT PicoGreen dsDNA kit (Thermo Fisher Scientific) with a lambda DNA standard. Proteoglycan content was estimated by quantifying the amount of sulphated glycosaminoglycan (sGAG) in constructs using the dimethylmethylene blue dye-binding assay (DMMB Blyscan, Biocolor Ltd.), with a chondroitin sulphate standard.

In order to calculate metabolic or synthesis rates per cell a standard curve for DNA content versus cell number was created. As shown in Figure 3.3, following a cell count using a haemocytometer, cell aggregates of known cell numbers were created in triplicate ($n = 3$). The suspension media was aspirated, and the cell aggregates were papain digested before performing a DNA assay on the digested samples.

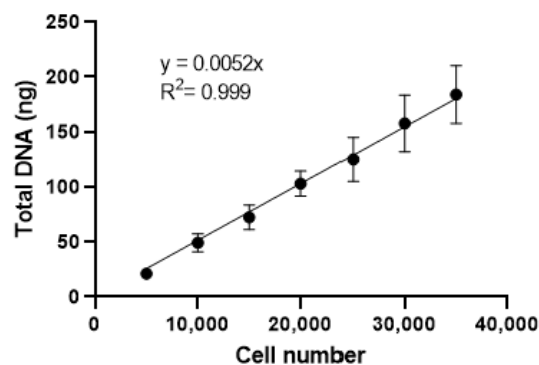


Figure 3.3 Conversion curve from DNA content to cell number. Cell aggregates of a known cell number were created ($n = 3$), papain digested and sampled using a biochemical DNA assay.

3.7 Other Conversion Factors and Curves

3.7.1 Oxygen units

In the absence of haemoglobin *in vitro*, oxygen delivery to cells, either in a monolayer or 3D configuration, is defined largely by the partial pressure (mmHg or kPa) of the culture medium. However, most biologists prefer to express gas concentrations *in vitro* as a percentage of atmospheric composition (e.g. cultured in a standard humidified 37°C, 5 %CO₂ incubator). Furthermore, convention within COMSOL Multiphysics is to express components of a chemical reaction as a concentration (i.e. moles per litre). As stated by Henry's law, the final dissolved gaseous concentration in a liquid is proportional to its partial pressure within the corresponding gas phase:

$$C = kP \quad (3-7)$$

where C is the concentration of dissolved gas (μM), k is the Henry's constant and P is the partial pressure of the gas (mmHg or kPa). Henry's constant takes into account changes in temperature and solubility with an oxygen solubility coefficient of 1.3 $\mu\text{M}/\text{mmHg}$ reported for culture media at 37°C.^{180,181} A conversion table from Keeley, T. P. and Mann, G. E. (2019) 'Defining physiological normoxia for improved translation of cell physiology to animal models and humans' has been recreated below (Table 3.1) and used throughout this work to change between units.¹⁸⁰

Table 3.1 An approximate oxygen unit conversion table with the multiplication factors required to convert the current unit (row) into the desired unit (column).

	%	kPa	mmHg	μM
%	-	1.02	7.65	13.5
kPa	0.98	-	7.5	13.2
mmHg	0.13	0.132	-	1.76
μM	0.074	0.076	0.57	-

3.7.2 pH to lactate concentration

A standard curve (Figure 3.4) for converting from the pH reading using the Seahorse Flux Analyser to lactate concentration within the micro-chamber (2.4 μL) of the seahorse 96-well spheroid microplate was created using the same assay media containing different known concentrations of lactate.

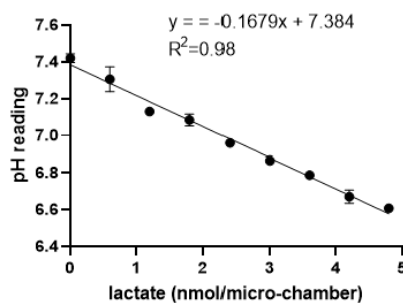


Figure 3.4 Conversion curve from pH reading to lactate concentration using the Seahorse Flux Analyser. The different lactate concentrations were made up in the same assay media and the micro-chamber has a volume of 2.4 μL .

3.8 Statistical analysis

One-way or two-way analysis of variance (ANOVA) were performed using GraphPad Prism (version 9). Tukey's multiple comparisons test was used to compare between groups. Results were typically displayed as mean \pm standard deviation, where N represents the number of biological replicates. Specifically, in the case of the cell density analysis, each biological replicate for the bovine caudal discs had six technical replicates, while three separate disc levels were analysed across the species comparison (rat and goat) with $N = 6$ for each. Significance was accepted at a level of $p < 0.05$.

The ROUT method within GraphPad Prism was used to identify outliers from the metabolic rate measurements using robust nonlinear regression. It is based on the False Discovery Rate (FDR), Q, which is the maximum desired FDR, was set to 1%.

Chapter 4. Consolidating and Re-evaluating the Human Disc Nutrient Microenvironment

A significant amount of this Chapter has been published previously in **McDonnell, E. E.** and Buckley, C. T. (2022) ‘Consolidating and re-evaluating the human disc nutrient microenvironment’, *JOR Spine*, 5(1), doi: <https://doi.org/10.1002/jsp2.1192>

Contribution: Contributed substantially to the conception and design of the work, performed the acquisition, analysis, and interpretation of literature data, *in-silico* modelling, analysis presentation and interpretation of results, drafting of the article, revising it critically, and final approval.

4.1 Introduction

A number of early studies have measured metabolite (glucose, lactate and oxygen) concentrations in animal discs.^{42,58,75,76} However, their physiological relevance to the human IVD continues to be an area of debate, for example: geometrical scale, nutrient supply, species-specific differences in cells and metabolic rates, not to mention differences in aging and pathophysiological effects.¹⁸² Given the inherent complexity of the IVD and difficulty in obtaining *in vivo* measurements, the research field is fortunate to avail of two seminal studies investigating intradiscal pH and oxygen in patients suffering from pathological backpain.^{10,77} Only one study has experimentally investigated the human glucose microenvironment through enzymatic analysis of digested human tissue.²⁶ Unfortunately, from a quantitative perspective, normalised results were presented (e.g. relative to the IVD concentration at the apex of the scoliotic curvature) and do not provide further insight into the glucose concentrations *in vivo*. As a result, *in-silico* modelling acts as a complementary approach and a valuable tool to providing insights into the *in vivo* glucose concentrations.

By gathering the results from the aforementioned literature, the current knowledge of the human nutrient microenvironment is consolidated in Figure 4.1. The exact location of NP glucose concentrations extracted from the *in-silico* studies is highlighted in Figure 4.1(A) and the range of predicted concentrations are presented in Figure 4.1(B) all of which will be discussed in more detail later. Figure 4.1(A) also highlights the direction of experimental measurements: Nachemson (1969) measured the intradiscal pH in 31 patients using a custom-made needle electrode introduced through a posterolateral approach,^{77,78} while Bartels *et al.* (1998) measured the oxygen profile in 13 patients suffering from scoliosis and 11 suffering from back pain using an anterior approach.¹⁰ The full range of intradiscal pH measurements was between 5.7 and 7.5, with no significant difference between discs with prolapses (6.6 - 7.5) and those without visible

pathologies (6.8-7.4). To re-evaluate these measurements with respect to potential cell-therapy intervention stage, the results from this early study are re-graphed in Figure 4.1(C) according to perceived pain level (Section 4.2.1 for details). Lumbar oxygen profiles for patients suffering from back pain are presented in Figure 4.1(D), as they are a relevant cohort with respect to this work. However, the authors did observe considerable variability in oxygen among the LBP cohort and no correlation was determined between oxygen level and age or stage of degeneration. The metabolite profiles and concentrations presented in Figure 4.1 will be discussed in greater depth and re-evaluated with respect to cell-based regeneration throughout this Chapter.

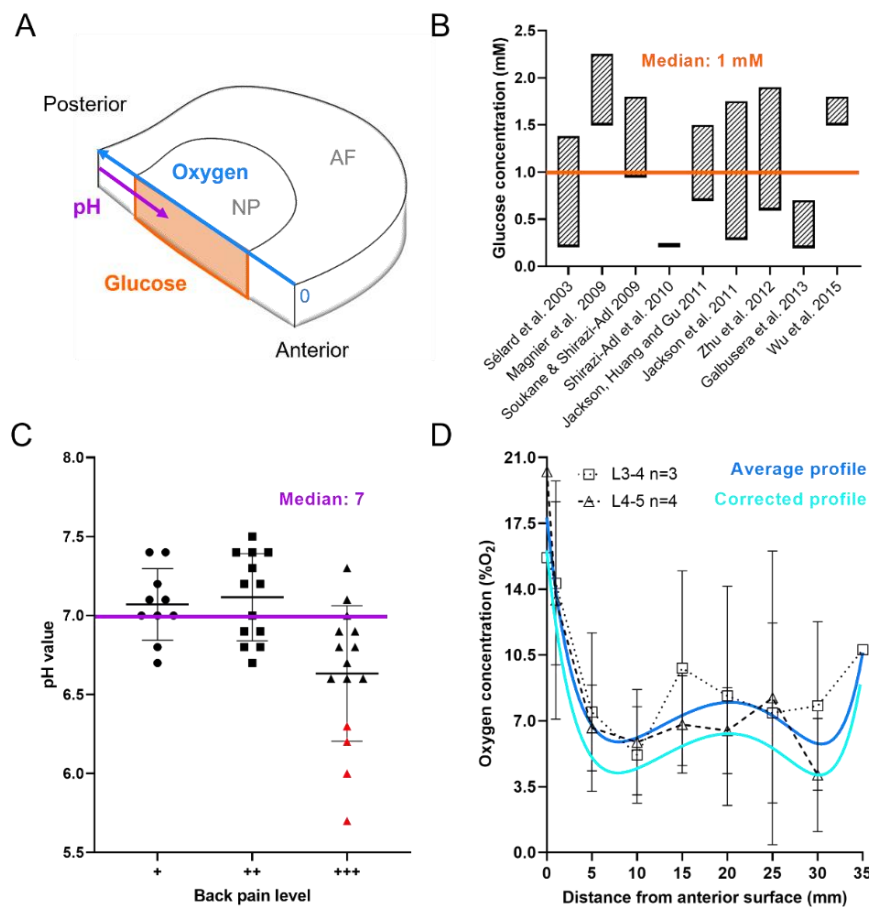


Figure 4.1. Consolidating current knowledge on the human nutrient microenvironment. (A) A quadrant of a human intervertebral disc (IVD) indicating the location of predicted glucose, experimental pH and oxygen values. (B) A range of glucose concentrations predicted in a degenerated human IVD from *in-silico* models over the last 20 years. A median concentration of 1mM is highlighted across all studies. (C) The pH level in lumbar IVDs of patients experiencing different levels of back pain, extracted from Nachemson (1969). Data points highlighted in red included details of severe visible degeneration and were excluded from the calculated median as they are considered too late stage for regeneration through cell therapy. (D) Oxygen measurements by Bartels *et al.* (1998) from patients suffering from back pain were pooled based on their lumbar level and an average profile was fit using non-linear regression. A corrected predicted profile to account for elevated oxygen inhalation during surgery was determined using an *in-silico* model as explained in Section 4.2.1.

In summary, this Chapter reflects on early measurements of the *in vivo* nutrient microenvironment. Using *in-silico* modelling, underpinned by more recent experimentally determined parameters of degeneration and nutrient transport, I seek to re-evaluate the current knowledge in terms of grade-specific stages of degeneration. This work focusing on the effect of considering a metabolically active cell population and grade-specific CEP calcification on the nutrient microenvironment and their implications for cell-based regeneration. Together this work aims to provoke greater deliberation and consideration of the nutrient microenvironment when designing *in vitro* cell culture experiments and cell therapy development.

4.2 Materials & Methods

4.2.1 Re-evaluating the nutrient microenvironment of the human IVD

NP glucose concentrations were extracted from nutrient transport models developed over the last two decades and a median value of 1 mM was calculated (Figure 4.1(B)) across these studies.^{64,104-111} Intradiscal pH measurements from Nachemson (1969) were graphed based on the level of perceived pain (Figure 4.1(C)) and a median of pH 7 was calculated across the three categories of pain. It is important to note that four measurements in group +++ (red), with severe tissue granulation, scarring and adhesions were excluded as they are considered beyond the intervention stage for regeneration through cell therapy.¹⁸

Lumbar oxygen profiles extracted from Bartels *et al.* (1998) were pooled by lumbar level (7 donors; three L3/L4 and four L4/L5) and the profile was plotted as the mean \pm standard deviation. One profile (CS-48yF-L4/L5) was excluded as the intradiscal concentrations were higher than the boundary concentration. Values were converted from partial pressure (mmHg) to %O₂, using an approximate conversion table.¹⁸⁰ An average lumbar profile was created using a non-linear least squares curve fit (Figure 4.1(D)). It is important to acknowledge that the patients inhaled 30 %O₂ for at least one hour during surgery as part of general anaesthesia, as a result oxygenation was increased by 50% compared to normal respired air. Although the authors postulate that this should not significantly alter concentrations beyond 5 mm from the AF disc surface, the main supply route to the NP through the CEP was not considered. Furthermore, a canine study found that alterations in inspired oxygen caused an immediate change in arterial oxygen concentration (within 10 seconds) and an intradiscal response time of minutes (depending on the distance from the endplate).⁷⁶ Taking these observations into account, an *in-silico* model was established with an elevated oxygen boundary (Figure 4.2).

4.2.2 Compiling metabolite diffusion coefficients for intervertebral disc sub-tissues

Several studies have characterised glucose diffusivity in the NP, AF and CEP of both human IVDs and bovine discs.^{24,67,74,183,184} However, many of the values reported are apparent diffusion coefficients, while it is the intrinsic diffusivity or effective diffusion coefficient which is necessary for *in-silico* modelling. Based on statistical insignificance observed by the work of Jackson *et al.* (2012), a strain independent CEP partition coefficient was used to convert reported apparent coefficients to approximated effective glucose and lactate diffusion coefficients.^{24,184} Where diffusion coefficients were determined at room temperature, the values were temperature corrected by using relative diffusivity in an aqueous solution.⁷⁴ Effective glucose diffusion coefficients in IVD tissue at 37°C are presented in Figure 4.3(A) highlighting diffusional direction (AF), anatomical location (CEP) and the applied strain condition. The percentage change in effective glucose diffusion due to increasing applied strain was calculated and plotted in Figure 4.3(B) for NP, AF, and CEP. As measurements for lactate diffusion through NP and AF tissue are rare in the literature, the values presented in Figure 4.3(C) are estimated from experimental glucose diffusion using the relative diffusivity between glucose and lactate in aqueous solution. The percentage change in effective lactate diffusion due to increasing applied strain was calculated and plotted in Figure 4.3(D) for NP, AF, and CEP. In Figure 4.3(E) effective oxygen diffusion coefficients in both bovine and human AF were corrected for temperature as mentioned previously.^{73,74} To the best of this author's knowledge, oxygen diffusion has not been experimentally measured in NP and CEP tissue. Therefore, theoretically calculated oxygen diffusion coefficients are presented⁵⁸, accompanied by typical values for cartilaginous tissue.¹⁸⁵⁻¹⁸⁷ Due to the limited oxygen data, the percentage change in oxygen diffusion due to increasing applied strain could only be calculated for the AF, Figure 4.3(F).

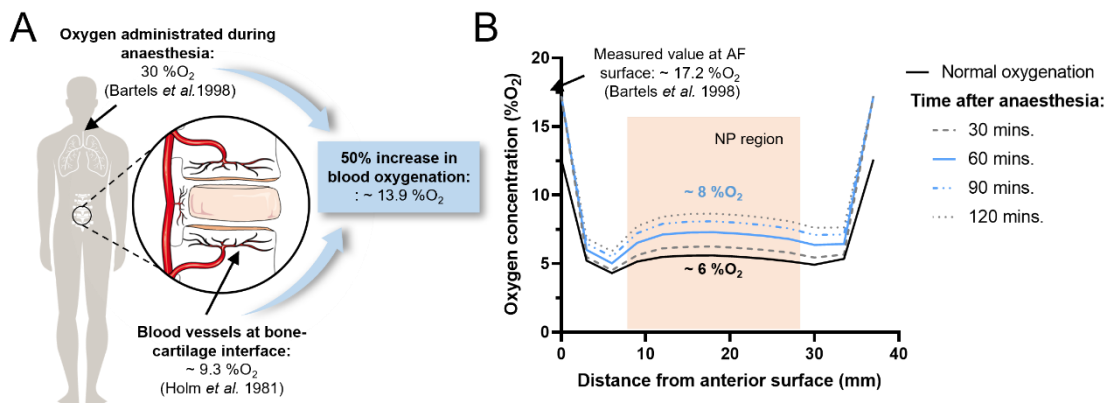


Figure 4.2 A corrected predicted profile to account for elevated oxygen inhalation during surgery was determined using an *in-silico* model. (A) Patients were reported to have inhaled 30 %O₂ for at least one hour as part of general anaesthesia. As a result oxygenation is increased by 50% compared to normal respired air. An *in-silico* model was established with an elevated oxygen boundary condition at the bone-cartilage interface of the endplate. The oxygen concentration on the surface of the annulus fibrosus (AF) was measured by Bartels *et al.* (B) Firstly, a steady-state oxygen gradient through the disc was established for normal (basal) oxygenation levels (solid black line). Secondly, a time-dependent analysis was performed with elevated boundary concentrations to determine the effect of the duration of anaesthesia on the central oxygen concentration. The profile at mid-height through the disc from the anterior to the posterior surface is presented graphically. Due to the elevated oxygen inhalation lasting at least 1 hour, it is predicted that the oxygen concentration is inflated by ~ 2 %O₂ in the disc centre due to the cartilage endplate transport route.

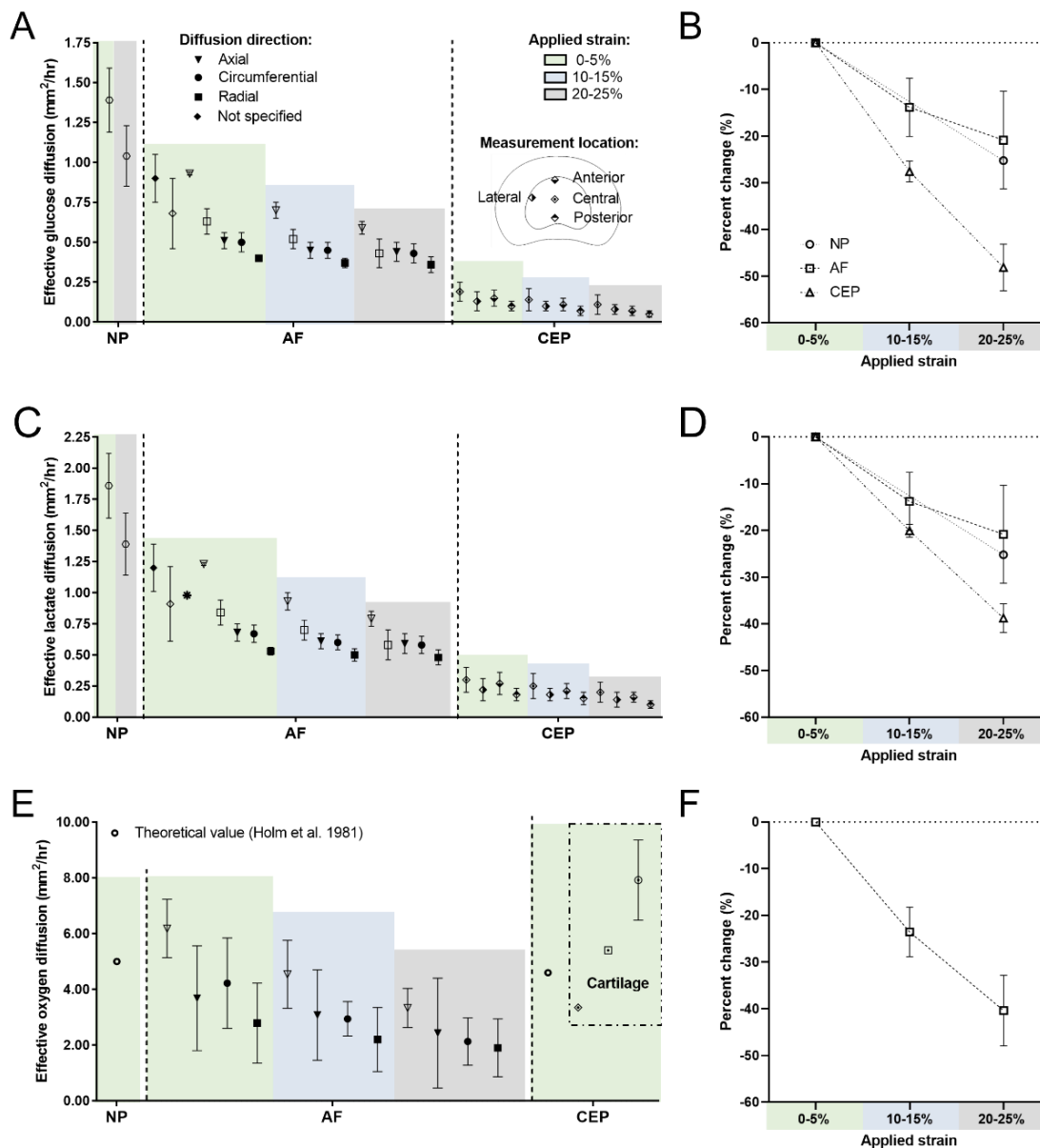


Figure 4.3. Metabolite diffusion coefficients for intervertebral disc sub-tissue. (A) Effective glucose diffusion through nucleus pulposus (NP),¹⁸³ annulus fibrosus (AF)^{24,67,74,183} and cartilage endplate (CEP) tissue.¹⁸⁸ Experimental measurement conditions such as directionality through the anisotropic AF, applied strain for each tissue domain and measurement location within the CEP are highlighted. NP & AF: solid = human, outline = bovine. CEP: all human. (B) Change in glucose diffusivity due to applied strain for the two recorded strain levels in NP and three levels in both AF and CEP. (C) Effective lactate diffusion for NP and AF were estimated from the above glucose diffusion using relative diffusivity, while CEP values were experimentally measured.¹⁸⁸ (D) Change in lactate diffusivity due to applied strain for the two recorded strain levels in NP and three levels in both AF and CEP. (E) Theoretical calculations of effective oxygen diffusion in the NP and CEP have been reported,⁵⁸ while AF values have been experimentally measured.^{67,74} Values for oxygen diffusion in cartilage are also included for comparison.^{185,187,189} (F) Change in oxygen diffusivity due to applied strain within AF only, data subjected to different applied strains are not available for NP and CEP tissue.

4.2.3 Identifying experimental degeneration grade-dependent input parameters for *in-silico* models

This work defines Grade II as healthy adult, Grade III as mild degeneration and Grade IV as moderate degeneration, while Grade V is considered too severe a stage of degeneration for regeneration using cell therapies.^{6,190}

Total cell density values were taken from a study which investigated degeneration-related variation in cell density using H&E staining and Histological Degeneration Score (HDS) to grade 49 lumbar IVDs (22 donors) from Grade I-IV.²⁵ A more recent study determined the active or viable percentage of the NP and AF cell population by counting the proportion of cells stained positively for the formazan product of MTT.³¹ The Pfirrmann scale was used to classify the degenerative status of two groups: Middle-aged (35-50 years) and Old-aged (>80 years). All 15 IVDs in the middle-aged group were Grade I-III and all 13 IVDs in the old-aged group were Grade IV or V. As a result, an active Criteria 1 (middle-aged) was created to apply to total cell densities from Grade II & III and Criteria 2 (old-aged) to apply to total cell densities from Grade IV. The percentage of active AF cells was averaged over the anterior and posterior regions. As there was no significant difference between the active criteria of NP and AF, an average active percentage was applied to the CEP cells. Figure 4.4(A-C) presents the total cell density from Liebscher *et al.* (2011) and an estimated active cell density after applying the relevant criteria from Martins *et al.* (2018)) across the IVD tissue and grades of degeneration. The exact numbers used as input parameters for the cell density of the grade-specific *in-silico* models can be found in Table 4.1.

Table 4.1 Cell density parameters used in the nucleus pulposus (NP), annulus fibrosus (AF) and cartilage endplate (CEP) for each grade-specific *in-silico* model.

		Cell density (cells/mm ³)		
		NP	AF	CEP
Grade II	<i>Total</i>	2,452	2,432	27,215
	<i>Active</i>	1,155	1,048	12,246
Grade III	<i>Total</i>	3,183	1,855	10,149
	<i>Active</i>	1,499	800	4,567
Grade IV	<i>Total</i>	2,307	5,297	10,574
	<i>Active</i>	1,373	2,998	6,133

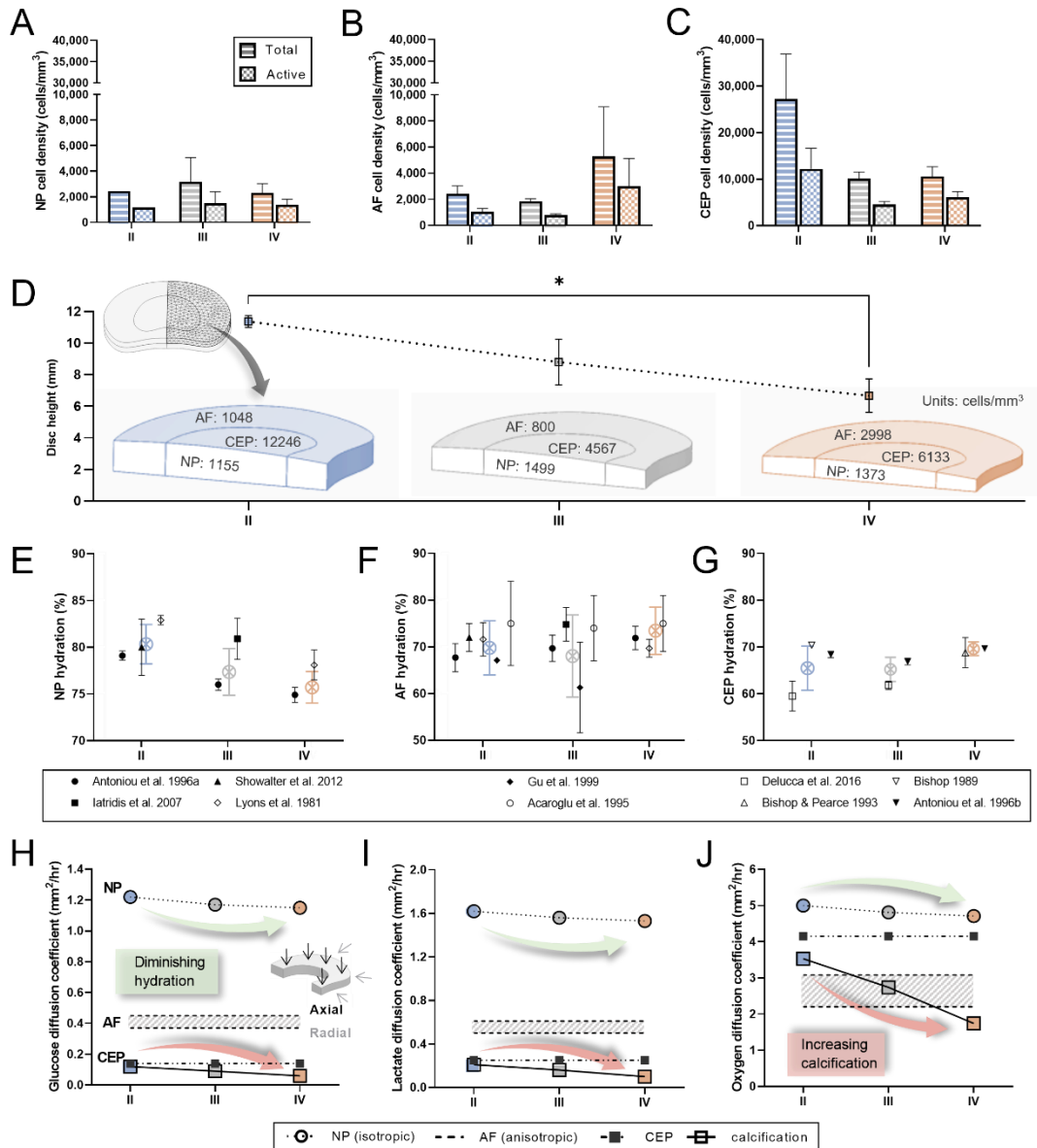


Figure 4.4. In-silico input parameters gathered from experimental literature. (A-C) Total and active cell density for the nucleus pulposus (NP), annulus fibrosus (AF) and cartilage endplate (CEP). The total values were extracted directly from a study by Liebscher et al. (2011), while the active density was extrapolated by applying an active criterion.³¹ (D) Disc height as a function of degeneration determined through image analysis of sagittal lumbar IVD sections.⁵⁶ Inlay of model geometry which represented a quadrant of a human L4/L5 IVD with an active cell density for each tissue domain highlighted (cells/mm³). (E-G) Tissue hydration as a function of degeneration grade obtained from the literature for NP, AF and CEP. An overall mean tissue hydration was calculated and highlighted (colour) by combining the summary statistics across studies. (H-J) Finalised glucose, lactate, and oxygen diffusion coefficients used in the *in-silico* model. NP diffusivity reduces with diminishing hydration; anisotropic AF diffusion is captured within the shaded range, with higher diffusivity in the axial direction and lower in the radial direction; CEP diffusivity reduces in the presence of calcification.

A 3D model geometry was created using published dimensions for a human L4/L5 IVD.¹⁵⁹ While the anterior to posterior (A-P) and lateral width was assumed to remain constant, disc height was reduced with degeneration, Figure 4.4(D). Disc height was determined using ImageJ analysis on macroscopic images of sagittal sections of lumbar IVD: average values for Grade II = 11.5 mm, Grade III = 8.8 mm and Grade IV = 6.7 mm.⁵⁶ For simplification the model is presented as a symmetrical quadrant of the full IVD, as highlighted in Figure 4.4(D) with each distinct tissue domain allocated its own cell density (only active is shown). Although an anatomically accurate CEP is explicitly modelled,¹⁹¹ it is not shown for easier interpretation of the results within the NP, and further details on the geometrical dimensions can be found below in Figure 4.5.

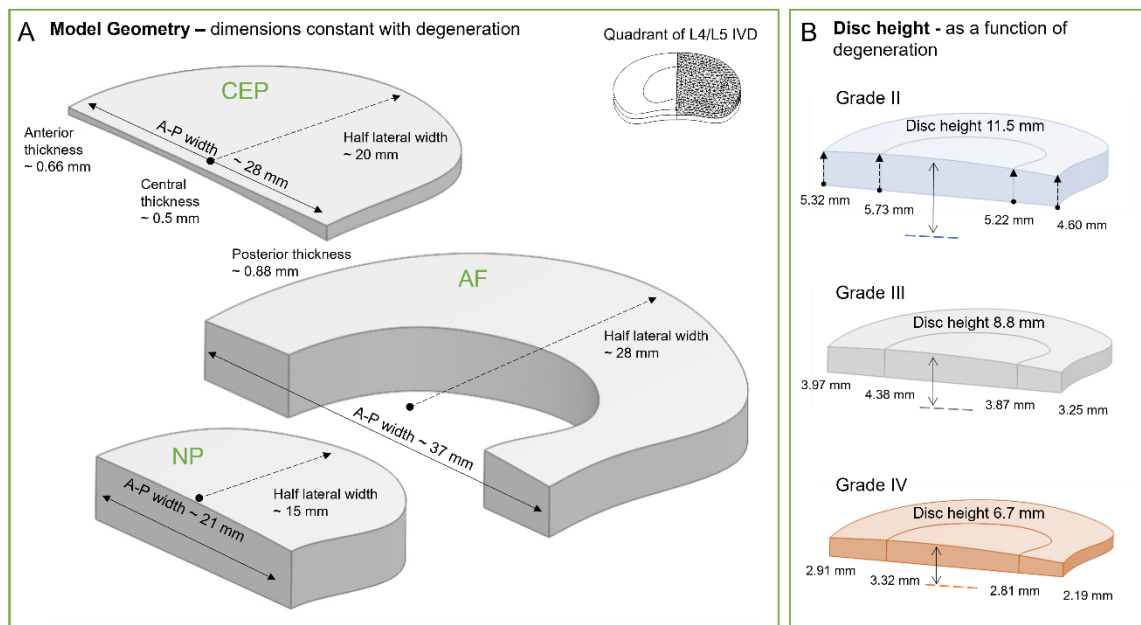


Figure 4.5 Human intervertebral disc (IVD) dimension as a function of degeneration. (A) Model geometry for a quadrant of a L4/L5 intervertebral disc with distinct cartilage endplate (CEP), annulus fibrosus (AF) and nucleus pulposus (NP) regions. The lateral and anterior to posterior (A-P) widths remain constant with degeneration for each region and so does the thickness of the CEP. **(B)** The disc height reduces as a function of degeneration. Half the thickness of the disc is shown for the external edges and at the AF-NP interface for each grade. Additionally, the maximum central disc height has been added for the full thickness of the IVD.

Mean hydration values were extracted from experimental studies which provided detail on degenerative appearance or grade and age as well as standard deviation and sample size. All extracted values are presented in Figure 4.4(E-G), together with an overall mean hydration for each grade, calculated by combining the summary statistics across studies.¹⁹² NP hydration incorporated four studies,¹⁹³⁻¹⁹⁶ with two providing values for two or more grades of degeneration.^{193,196} AF hydration incorporated six studies, two of which were additional to those reported for NP.^{197,198} Lyons *et al.* (1981) presented a hydration profile through “healthy” and “degenerated” discs. The profile was split into NP and AF and the average was taken within those regions. Based on the adult age of the “healthy” group it was assigned to Grade II and since the “degenerated” group underwent spinal fusion it was assumed to be at least Grade IV. Iatridis *et al.* (2007) presented their values for Grade II (n = 2) and Grade III (n = 7) combined. However, the authors stated that both grades displayed degeneration while Grade I was classified as “healthy” with no indication of age. Taking this into account as well as the higher proportion of Grade III samples, it was considered most applicable to the Grade III definition within this work. CEP hydration incorporated four studies,^{191,199-201} two of which provided values for two or more grades of degeneration.^{191,199} Where values were presented separately for different anatomical regions within tissue type e.g. anterior/posterior AF or superior/inferior CEP, an overall average was calculated for each study.^{193,194,198}

As studies have shown ~ 10% strain under axial compression simulates physiological weightbearing,^{170,202,203} effective diffusion coefficients at 10 – 15% strain were used in the *in-silico* model. Where NP diffusion was only available for 0 – 5% and 20 – 25% strains (Figure 4.3), a midpoint was taken. Reduced NP hydration with degeneration (Figure 4.4(E)) was incorporated by decreasing the diffusion coefficients accordingly between Grades II, III and IV. Anisotropic diffusion in the AF was captured with lowest diffusivity in the radial direction and highest axially. Diffusion parameters through the central zone of the CEP were chosen as the zonal differences were relatively small and it is believed that the central region of the CEP is the predominant transport route to the NP.^{41,58,59} With no clear trend between hydration and degeneration in the AF and CEP (Figure 4.4(F),(G)), the solute diffusion coefficients were maintained constant. However, in the case of modelling the effect of CEP calcification on metabolite concentrations, diffusion through the CEP was reduced in accordance with the increase in calcium deposition. Calcification values of 15% for Grade II, 34% for Grade III and 58% for Grade IV were extracted from a study investigating the percentage of calcified tissue and Thompson degeneration classification in 60 cervical IVDs.³² Diffusion through the CEP reduces in accordance with an increase in calcium deposition. As a result, the effective diffusion coefficients were reduced according to the increase in percentage of calcification between grades of degeneration. The finalised effective diffusion coefficients of glucose, lactate and oxygen through the different tissue domains are presented in Figure 4.4(H-J) and in

Table 4.2.

4.2.4 Establishing *in-silico* models as a function of degeneration grade

The *in-silico* nutrient transport model was created using COMSOL Multiphysics as outlined in Section 3.1. Briefly, the steady-state nutrient microenvironment was governed by coupled reaction-diffusion equations accounting for the total or metabolically active cell density and metabolite diffusion parameters through the different tissue domains, specific to degeneration grade. Michaelis-Menten constants for NP cells ($V_{max} = 12$ nmol/million cells/h and $K_m = 12$ μ M) and AF cells ($V_{max} = 8.6$ nmol/million cells/h and $K_m = 40$ μ M) were taken from experimental literature considered to be the most representative of the *in vivo* microenvironment in terms of maintaining a 3D freshly isolated cell phenotype and physiologically relevant glucose concentrations.^{9,90,91} With limited data available for CEP cells, values were obtained from culture expanded cells in suspension ($V_{max} = 14.1$ nmol/million cells/hr and $K_m = 15$ μ M).⁹³ Similar to previous numerical models,¹⁰⁴⁻¹⁰⁶ it was assumed that glucose and oxygen concentrations at the disc boundary are that of blood plasma in the surrounding blood vessels, 5.33 mM and 12.6 %O₂, respectively.^{76,204} Holm *et al.* (1981) measured an oxygen concentration ~ 9.3 %O₂ in the vertebral bodies close to the CEP. A typical blood plasma pH of 7.35 – 7.45 was converted to lactate using a linear conversion and assumed constant at the AF and CEP boundaries.⁹

4.2.5 Investigating the optimal cell number for intradiscal injection

To identify an optimal cell number for intradiscal transplantation the active and calcified *in-silico* models for Grade II and III were used. 3, 6, 9 and 18 million cells were investigated based on parameters of ongoing clinical trials from Mesoblast Ltd. (NCT01290367 & NCT02412735) and DiscGenics Inc. (NCT03347708). Cells were assumed to be homogeneously distributed throughout the NP, remain viable after delivery, and possess a discogenic phenotype, thus having similar metabolic rates and nutrient couplings as native NP cells.

Table 4.2 Finalised input parameters used in the grade-specific *in-silico* model to capture the effective diffusion of the relevant metabolites (oxygen, glucose, and lactate) through the nucleus pulposus (NP), annulus fibrosus (AF) and cartilage endplate (CEP).

		Diffusion coefficients (mm ² /hr)				
		NP	AF		CEP	
			<i>Axial</i>	<i>Radial</i>	<i>No calcification</i>	<i>Calcification</i>
Grade II	<i>Oxygen</i>	5	3.08	2.20	4.15	3.53
	<i>Glucose</i>	1.22	0.45	0.37	0.14	0.12
	<i>Lactate</i>	1.62	0.61	0.50	0.25	0.21
Grade III	<i>Oxygen</i>	4.81	3.08	2.20	4.15	2.74
	<i>Glucose</i>	1.17	0.45	0.37	0.14	0.09
	<i>Lactate</i>	1.56	0.61	0.50	0.25	0.16
Grade IV	<i>Oxygen</i>	4.71	3.08	2.20	4.15	1.74
	<i>Glucose</i>	1.15	0.45	0.37	0.14	0.06
	<i>Lactate</i>	1.53	0.61	0.50	0.25	0.10

4.3 Results

The developed *in-silico* models predict the relationship between metabolite concentration and the previously determined tissue properties of healthy adult (Grade II), mildly (Grade III) and moderately degenerated (Grade IV) human IVDs. The results are presented in the form of contour plots of just the lower quadrant of the disc, the concentration profile from anterior to posterior at mid-height through the disc, the centre most value in the NP and the percentage change in concentration due to the different conditions investigated e.g., active cell criteria and CEP calcification. These results are grouped by metabolite with glucose shown in Figure 4.6, pH in Figure 4.7 and oxygen in Figure 4.8.

As expected for a large avascular structure, the results showed that nutrient concentration decreases with distance from the blood supply at the disc periphery. This is most apparent in Grade II where the disc height is greatest (~ 11.4 mm) and the lowest glucose and oxygen concentrations are observed at the NP and inner AF (Figure 4.6(A) and Figure 4.8(A)). However, as the CEP transport route shortened with reduced disc height of Grade III (~ 8.8 mm) and Grade IV (~ 6.7 mm), the nutrient concentrations and pH within the NP increased. Focusing first on the total cell density model, this is evident in the contour plots (Figure 4.6(A) - Figure 4.8(A)) but is also summarised in Figure 4.6(C) - Figure 4.8(C) where the centre-most value is compared for all degeneration grades. However, diffusion distance from the supply source is only one factor influencing the distribution of metabolites within the IVD. By considering the density of specifically metabolically active cells, rather than assuming that the total cell density present are contributing to consumption and production rates, the nutrient demands within the tissue are altered. Applying the active cell criteria resulted in an increase in glucose concentration (Figure 4.6(A)) and a reduction in lactic acid build-up due to glycolysis (Figure 4.7(A)). The greatest impact can be observed in the oxygen contour plots (Figure 4.8(A)) where there is a notable smoothing of the gradient through the AF due to the lowest activity within this domain and a significant increase in oxygen within the NP. To quantitatively compare total and active cell density, the predicted concentration profiles at mid-height through the IVD are presented in Figure 4.6(B) - Figure 4.8(B). The predicted profiles are overlaid with values reported in the literature for the NP region of the disc. As previously highlighted in Figure 4.1, the overlaid glucose range is from published *in-silico* models^{64,104-111}, pH values are those experimentally measured together with a clinically relevant median value⁷⁷ and the oxygen range are experimental measurements which have been corrected for an elevated boundary concentration during the surgical procedure.¹⁰

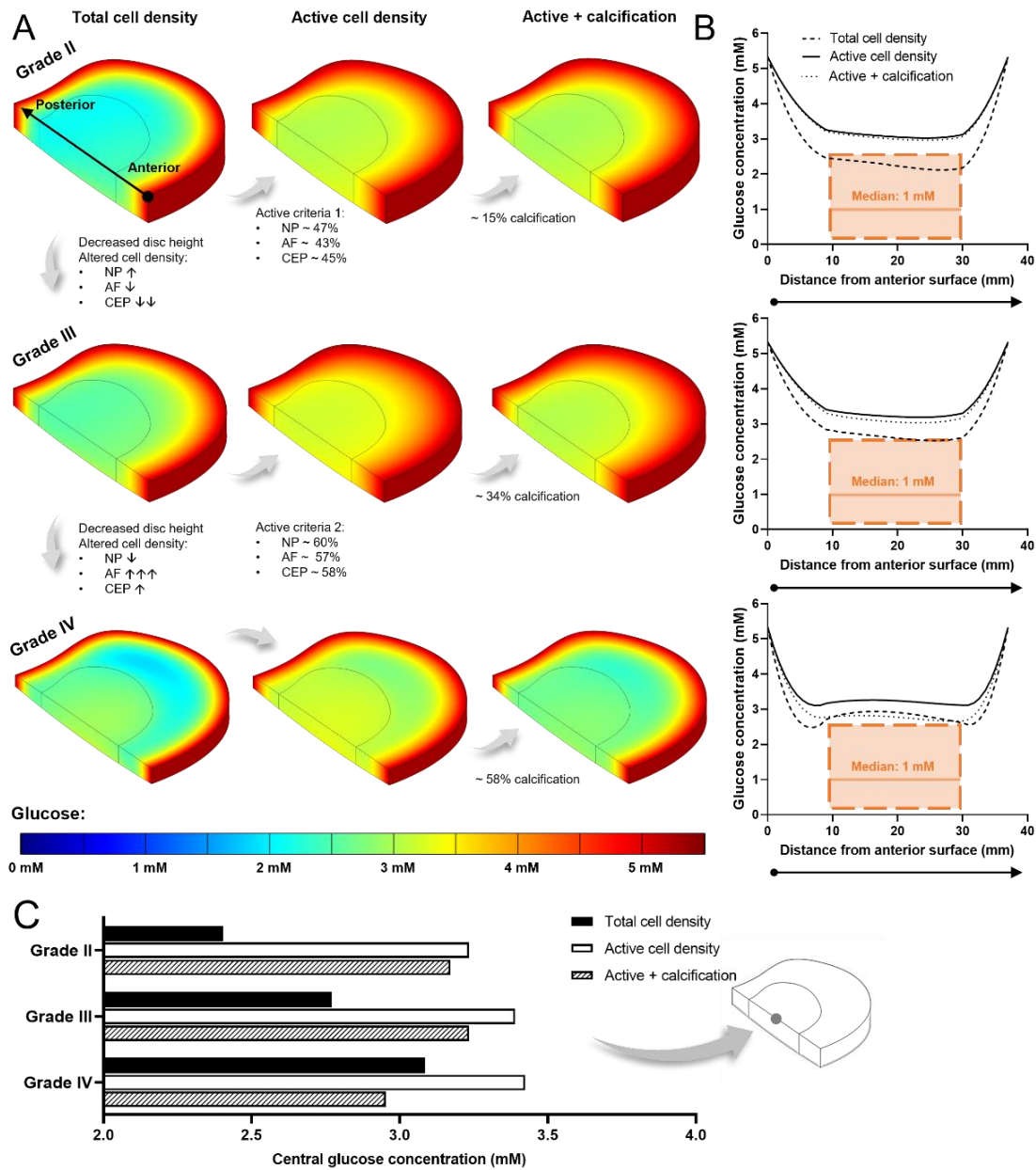


Figure 4.6. Predicted glucose concentrations within a healthy adult (Grade II), mildly (Grade III) and moderately (Grade IV) degenerated in-silico intervertebral disc model. (A) Contour plots for each degeneration grade investigating a total cell density, a metabolically active cell density and the effect of cartilage endplate (CEP) calcification in the active model. Cell density was altered for degeneration grades, as highlighted for each tissue domain: ↑ and ↓ indicates < 30% increase and decrease, respectively; ↓↓ = ~ 60% decrease and ↑↑↑ = ~ 180% increase. **(B)** Predicted glucose profile at mid-height through the corresponding *in-silico* model, from the anterior to the posterior surface. The range of concentrations predicted within the nucleus pulposus (NP) by previously published models is overlaid in orange, together with a median value calculated across those studies. **(C)** Central glucose concentration for all three degeneration grades under each of the investigated conditions.

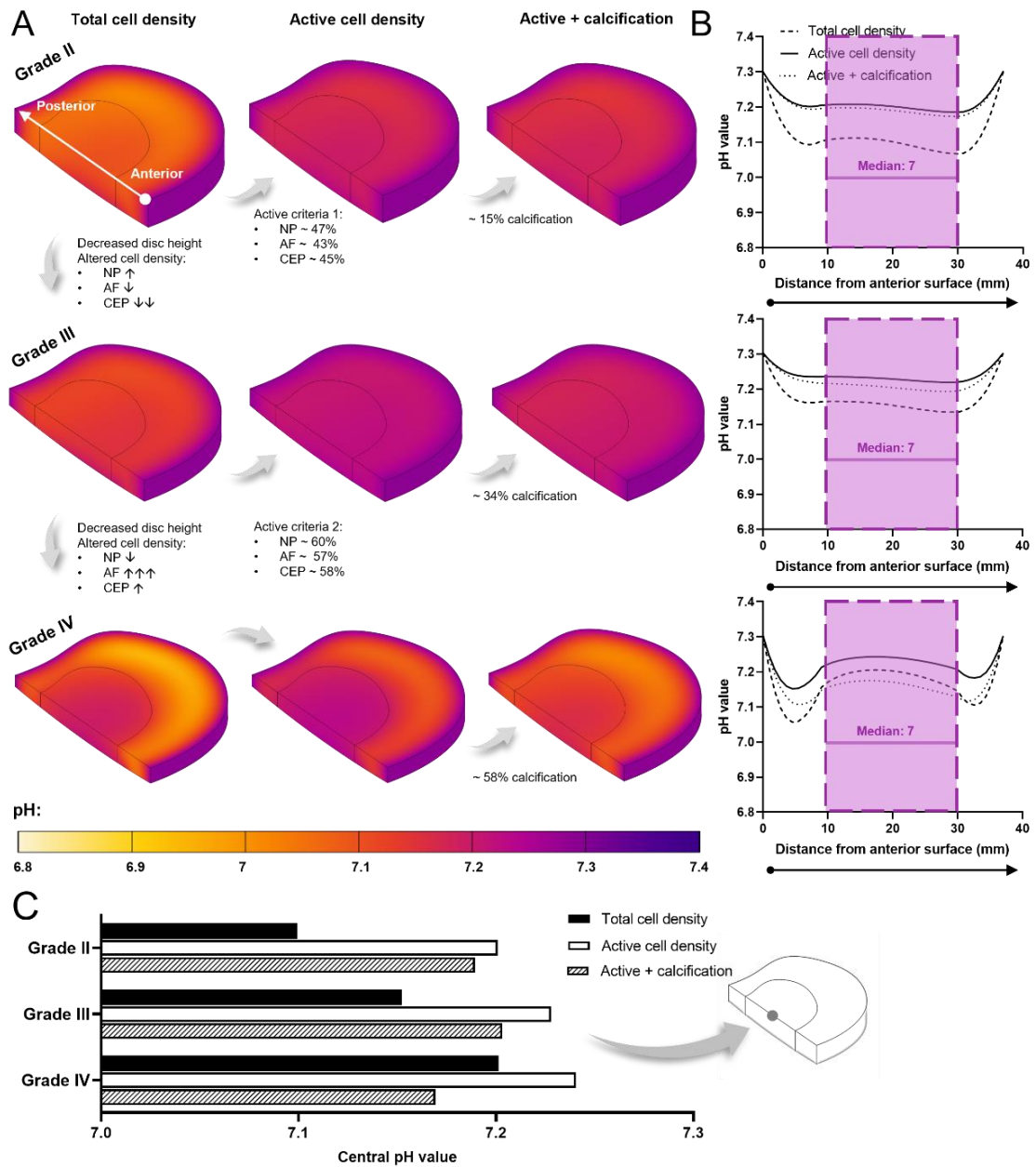


Figure 4.7. Predicted pH levels concentrations within a healthy adult (Grade II), mildly (Grade III) and moderately (Grade IV) degenerated in-silico intervertebral disc model. (A) Contour plots for each degeneration grade investigating a total cell density, a metabolically active cell density and the effect of cartilage endplate (CEP) calcification in the active model. Cell density was altered for degeneration grades, as highlighted for each tissue domain: ↑ and ↓ indicates < 30% increase and decrease, respectively; ↓↓ = ~ 60% decrease and ↑↑↑ = ~ 180% increase. **(B)** Predicted pH profile at mid-height through the corresponding *in-silico* model, from the anterior to the posterior surface. The range of pH values measured with the nucleus pulposus (NP) is overlaid in purple, together with a clinically relevant median value.⁷⁷ **(C)** Central pH for all three degeneration grades under each of the investigated conditions.

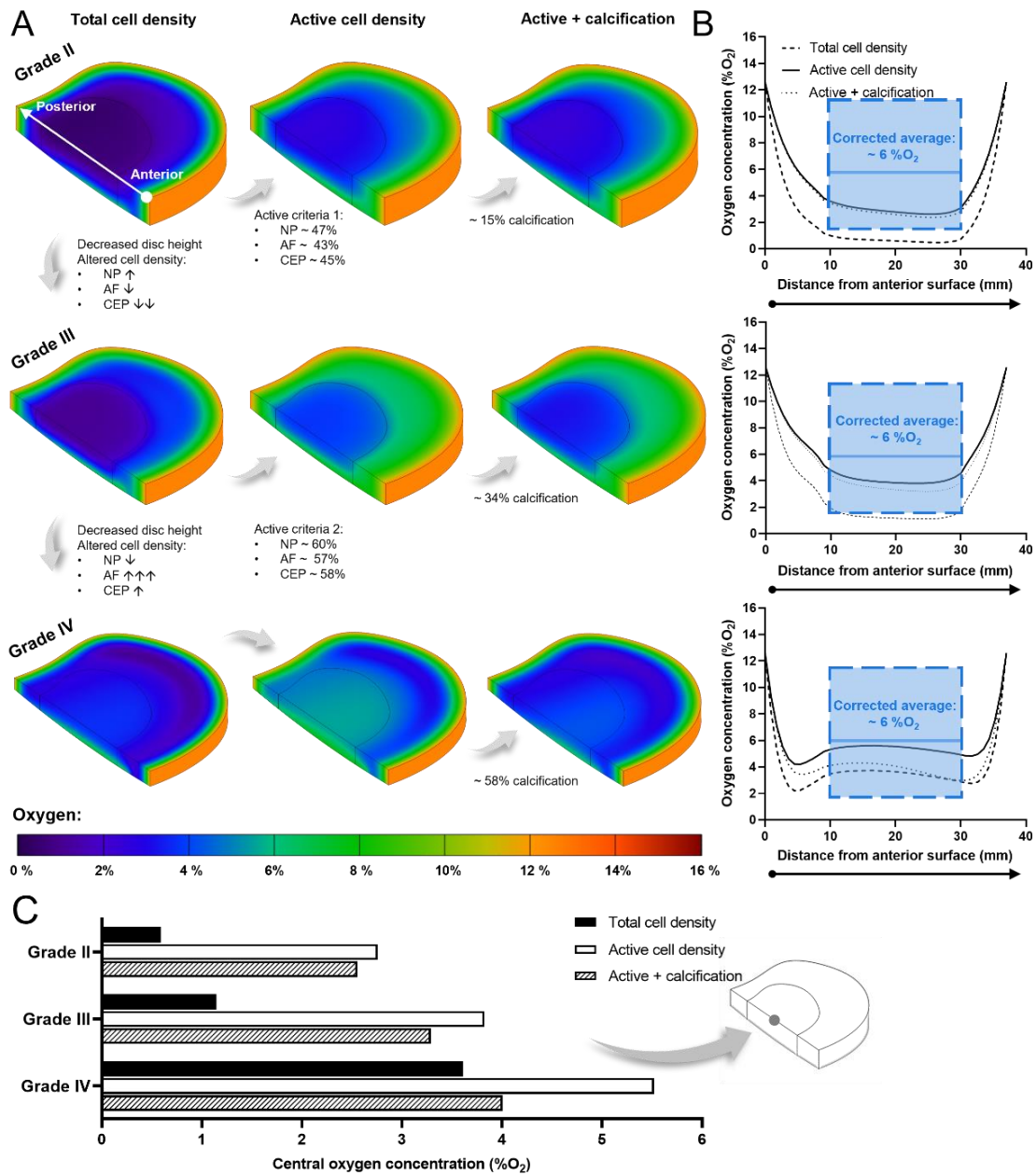


Figure 4.8. Predicted oxygen concentrations within a healthy adult (Grade II), mildly (Grade III) and moderately (Grade IV) degenerated in-silico intervertebral disc model. (A) Contour plots for each degeneration grade investigating a total cell density, a metabolically active cell density and the effect of cartilage endplate (CEP) calcification in the active model. Cell density was altered for degeneration grades, as highlighted for each tissue domain: ↑ and ↓ indicates < 30% increase and decrease, respectively; ↓↓ = ~ 60% decrease and ↑↑↑ = ~ 180% increase. **(B)** Predicted oxygen profile at mid-height through each of the corresponding *in-silico* models, from the anterior surface to the posterior surface. The range of boundary corrected oxygen measurements within the nucleus pulposus (NP) and average central concentration are overlaid in blue.¹⁰ **(C)** Predicted central oxygen concentration for all three degeneration grades under each of the investigated conditions.

While the number of metabolising cells influences the minimum concentrations within the IVD, changes in cell distribution between the NP, AF and CEP affect the metabolite gradients between degeneration grades. Focusing on the total and/or active cell density contour plots in Figure 4.6(A) - Figure 4.8(A). When advancing from Grade II to mildly degenerated Grade III, not only does the axial transport route shorten but the CEP cell density decreases $\sim 60\%$, facilitating greater diffusion of nutrients into the NP and metabolic waste out, despite modelling a slight increase in NP cell density (less than 30%). It is important to note this is assuming a constant boundary supply and not considering other impeding artefacts such as calcification at this point. Advancing from Grade III to moderately degenerated Grade IV, despite a slight increase in CEP cell density (less than 30%), further reduction in disc height and a slight decrease in NP cell density (less than 30%) predicts an increase in nutrient concentration in the NP. However, modelling a very significant increase in AF cell density ($\sim 180\%$) predicts greater impedance of nutrients through the peripheral AF transport route due to high consumption and a shift in the location of lowest nutrients laterally. Similarly, more concentrated lactate production within the densely populated degenerated AF results in greater acidity in the disc periphery rather than centrally. The effect of AF cell density in Grade IV is most apparent in the anterior and posterior regions of the metabolite profiles in Figure 4.6(B) - Figure 4.8(B).

Calcification of the CEP, at each degeneration grade, decreased the glucose, pH and oxygen concentrations within the NP and inner AF, with close to no effect on the outer AF region. Calcification was simulated in the active cell density models only and the regional effects can be seen in both the contour plots (Figure 4.6(A) - Figure 4.8(A)) and the anterior to posterior profiles (Figure 4.6(B) - Figure 4.8(B)). At Grade II with $\sim 15\%$ calcification, a minor reduction on transport in and out of the NP through the CEP transport route was observed, with an insignificant effect on the central metabolite levels within the IVD (Figure 4.6(C) - Figure 4.8(C)). At Grade III ($\sim 34\%$ calcification), nutrient concentrations did not appear to change significantly. Meanwhile Grade IV, with $\sim 58\%$ calcification, resulted in nutrient and pH values dropping below those predicted within the NP for a total cell density (i.e., assuming every cell present is contributing to consumption). This can be seen in the anterior to posterior metabolite profiles for Grade IV (Figure 4.6(B) - Figure 4.8(B)) and in Figure 4.6(C) - Figure 4.8(C) where the centre-most glucose, pH and oxygen values are summarised for all degeneration grades under all investigated conditions.

Figure 4.9(A-F) elucidates the effect of injecting 3, 6, 9 or 18 million into the NP of the calcified Grade III model. As expected, the concentration of nutrients and the pH reduces with an increase in the number of cells injected. As the cells are assumed to be homogeneously injected into the NP, the change in metabolite concentrations within the disc are concentrated within the NP, as highlighted in the contour plots (A-C) and the A-P profile (D-F). Although the contour

plots are not shown for Grade IV, the minimum nutrient concentrations and pH predicted within the NP for Grades III and IV are compared in Figure 4.9(G-I).

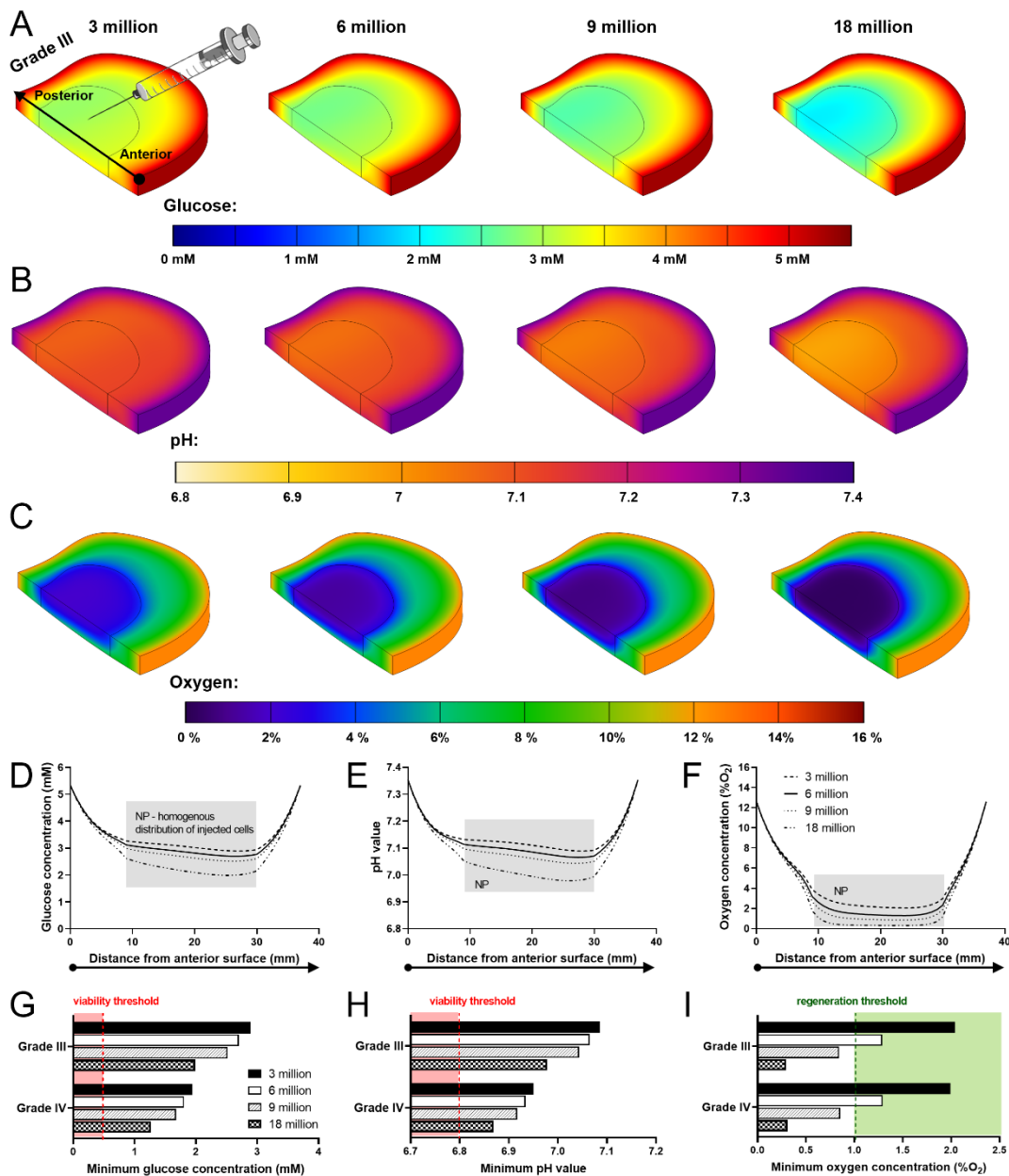


Figure 4.9 Predicted metabolite concentrations within a calcified degenerated (Grade III and IV) intervertebral disc injected with discogenic cells. (A) Predicted glucose, (B) pH and (C) oxygen contour plots resulting from an injection of 3, 6, 9 or 18 million discogenic cells in the calcified Grade III model. (D-F) Predicted metabolite profile at mid-height through each of the corresponding *in-silico* models, from the anterior surface to the posterior surface. The shaded region highlights the nucleus pulposus (NP) where the injected cells are assumed to be homogeneously distributed. The predicted minimum concentration of (G) glucose, (H) pH and (I) oxygen within the NP of a calcified Grade III and Grade IV disc following transplantation of 3, 6, 9 or 18 million cells. The threshold below which cell viability is affected is highlighted in red for glucose and pH,^{27,49,84,91} while the oxygen concentration for optimal regeneration is highlighted in green.^{28,83,98,205,206}

4.4 Discussion

Due to the avascularity of the IVD, tissue nutrient transport rates and inherent cell metabolic rates naturally give rise to concentration gradients. This study aimed to reflect on what is already known about these concentrations *in vivo* and re-evaluate them in terms of clinically relevant degeneration grades. Using *in-silico* modelling, this work incorporated newer experimental data on degeneration grade-specific metabolically active cell densities,³¹ tissue hydration,^{191,193–201} diffusion parameters^{24,67,73,74,183–187} and calcification²⁵ and assessed the implications for developing cell-based regeneration strategies.

Disc cells primarily obtain their energy through anaerobic glycolysis making glucose the critical nutrient for disc cell survival.^{28,58} However, there is a lack of directly measured values of glucose concentration in disc tissue and *in-silico* modelling is typically used to surmise or predict *in vivo* concentrations. Models presented in the literature have estimated a glucose range from 0.25 mM to above 2 mM with the median NP concentration across all the studies being 1 mM. Together these have established the conjecture that NP glucose concentrations are critically low, making it particularly inhospitable to potential cell therapies.^{207–209} It is however important to note that each of these studies investigated effects such as reducing nutrient supply or exchange area^{104,109} and altering tissue diffusivity,^{104,106,107} particularly through reducing CEP permeability or porosity through parametric analysis.^{64,108,111} Other osmo-mechanical properties include altering water content, fixed charge, deformation^{105,108} and dynamic loading.^{109,110} Despite significant advances interrelating metabolic rates^{9,116} and incorporating cell death with nutrient deprivation,^{107,210} *in-silico* models remain limited by availability of experimental data, both as input parameters and for subsequent validation of predictions. Therefore, it is believed that the multivariate models presented in this work advance the research field through pooled grade specific experimental data for more accurate modelling parameters of a dehydrated NP, anisotropic AF, and calcified CEP. Additionally, this work consolidates what has previously been measured *in vivo* and used this information to help validate the predictive models with these key experimental studies.

Slightly higher glucose concentrations within the disc were predicted compared with the overlaid range from previous reported *in-silico models* in the literature. As expected, the total cell density model was most comparable with the overlay, as the previous models had not accounted for a proportion of the cell population not being metabolically active. Overall, the current models predict a trend of increasing glucose concentration with degeneration (ignoring calcification in this instance), as there is a compensation of decreased diffusional distance due to reduced disc height. This has also been predicted in another *in-silico* model where halving the disc height reduced the cell death ratio through increasing critical glucose and reducing pH levels.¹¹⁰ It is important to reiterate that the literature models investigate a wide range of parameters and several

studies circumvent the lack of experimental input through parametric analysis.^{104,106} Consequently, it is possible that the modelling scenarios presented for glucose are far more severe than the clinically relevant grades of degeneration being elucidated here, thus over-estimating the harshness of the microenvironment. Experimental glucose measurements in other species include dogs and pigs with one study reporting levels below 1 mM through micro-dialysis measurement, and the other measured a central NP concentration of ~ 3 mM through biochemical analysis.^{42,211,212} The predictive models in this work are in good agreement with the latter and are more plausible in terms of sustaining the NP cell population which has been shown to experience significant cell death when glucose drops below 0.5 mM for more than three days.^{9,27,49} Even with an array of predicted and measured glucose concentrations (0.25 – 3.5 mM) it is a relatively narrow range confined by the upper supply limit of blood glucose levels (2.6 – 6.1 mM).²⁰⁴ Despite this more than 50% of publications utilising NP cells report high glucose culture medium (25 mM or 4.5 g/L). Together this highlights an urgency for robust experimental glucose measurements in healthy and degenerating human IVDs, not only to permit validation of *in-silico* models but to significantly advance the field in fully elucidating the glucose microenvironment and refinement of *in vitro* culture conditions for physiological relevance.

A significant advancement in the current model is the availability of recent data on human cell densities and particularly metabolically active cell densities, which explains important differences with the *in-silico* literature. Previously, studies have relied on cell densities from early work, limited in sample size and donor age, while techniques have also developed and advanced significantly since.²⁴ The current work has greater precision at capturing degeneration grades by employing values from a study, with a far larger sample size, specifically investigating degeneration-related variation in cell density.²⁵ Furthermore, the inclusion of only cells positive for metabolic activity is particularly important as NP cells have been shown to experience a loss of both proliferative capacity and anabolic activity with normal aging and degeneration.^{11,12} While the MTT assay is a reliable and widely used method to assess cell viability and metabolic activity in many different types of cells and tissues, it is important to note that the assay measures mitochondrial dehydrogenase activity and may not necessarily reflect overall cell viability or proliferation. Therefore, this technique may need to be combined with another viability assay such as Live/Dead to confirm the state of the cells which stained negatively for the presence of formazan deposition. Furthermore, as senescent cells have shown to be more metabolically active it would be interesting to investigate senescence-associated beta-galactosidase (SA- β -gal) activity, a widely used biomarker of cellular senescence both in cultured cells and in tissue sections, which would combine with the MTT technique with using histochemical staining. As captured by the results, when there is a reduction in the number of cells metabolising, there is an increase in the nutrient concentrations and a reduction in the build-up of lactic acid within the

disc. Therefore, this reinforces the importance of also capturing a potential senescence population with a higher metabolic rates.²¹³

Additionally, the models capture a potential shift in the overall distribution of metabolites due to the changes in local cell density and activity between the different tissue domains. For example, pH was predicted to reduce within the AF of Grade IV, rather than the NP, due to an almost 2-fold increase in the total AF cell density and an increase in the percentage of active cells. However, the current model assumes no change in nutrient supply or waste removal, while the relationship between the surrounding microvasculature and transport is not straightforward. A recent review reported the prevalence of vascular ingrowths extending into the inner AF through degenerative fissures, which may explain the large increase in AF cell density and their ability to remain viable.^{35,36} Alternatively, subchondral bone sclerosis and occlusion of marrow contact channels may affect the vertebral supply route, with a correlation reported between functional capillary bud density and diffusion.^{214,215} This may contribute to lower nutrient availability through the EP route,^{57,216–218} which could create a shift in the predominance of the transport routes. Thus, more quantitative measurements of nutrient supply and metabolite concentrations at the boundary of the IVD are needed to ascertain confidence in nutrient-transport models and may need to be assessed in a patient-specific manner.

Acidity has been shown to be important for maintaining NP cell activity.²⁰⁹ However, too low a pH is detrimental for PG synthesis rates which have been seen to reduce significantly below pH 6.8.^{9,50,84} Hence, it is vital to consider the *in vivo* pH microenvironment at different stages of degeneration in developing a cell therapy to survive and reach full regenerative capacity within the patient's specific microenvironment. Additionally, it is of utmost importance to re-evaluate the typical "disc-like" conditions used during *in vitro* cell assessment. As mentioned previously, a healthy state is typically represented by pH 7.1, mild degeneration by pH 6.8 and severe degeneration by pH 6.5.^{96,97,99,100,219,220} However, when the data from Nachemson (1969) is visualised, it appears that the pH may not be as critically low as commonly believed (Figure 4.1(C)). Only 4 out of 38 measurements were below 6.5 and each of these were noted as having an abundance of degenerative artifacts (granulation tissue, scars and adhesions) in conjunction with severe pain, thus making their degenerative state too advanced for regeneration through cell therapy.^{6,190} A median value of pH 7 was observed across the three levels of back pain (excluding the aforementioned statistically different values). Furthermore, 50% of measurements were actually at or above pH 7 and only 18% of the + or ++ groups were below pH 7. Therefore, if cell-based therapies are to be used to suppress deterioration and restore IVD homeostasis, at an earlier stage of the degenerative cascade, then pH may not play as significant a role as commonly believed.

The pH profiles predicted in the current work all fall within the range of intradiscal measurements, although above the calculated median of pH 7. The total cell density model at

Grade II and III, the most comparable to published literature as mentioned earlier, also show good agreement with *in-silico* models which predicted a range of 7 – 7.2 within the NP.^{105,106,111} However, it is important to note that the intradiscal measurement range of 7 – 7.5 is large in terms of the pH scale and most prolapsed discs showed values above pH 7, although the author states that no statistical difference due to prolapse was demonstrable.⁷⁷ The conjecture that pH may not be as critical as commonly believed is supported by human lactate concentrations of 2 – 6 mM (pH 7.3 – 6.9) from Bartels *et al.* (1998), which saw only one outlier below pH 6.5 in a disc adjacent to a fused motion segment.¹⁰

Oxygen plays a pivotal role in regulating the biosynthesis of native NP cells and many of the potential regenerative cell sources being explored.⁹⁸ Highest PG synthesis rates have been recorded at approximately 5 %O₂ and synthesis appears to be inhibited significantly in an oxygen-dependent manner below this.²⁸ Although disc cells reside in an avascular niche which is commonly characterised as hypoxic, potential cell therapies are still often assessed under normoxic conditions (20 – 21 %O₂).^{99,189,219,221} “Physioxia” (~ 5 %O₂) remains the most commonly accepted culturing condition *in vitro* for the musculoskeletal field. However, studies have used lower hypoxic concentrations of 0.1 – 1 %O₂ and a higher concentration of 10 %O₂.^{189,222} Although lower oxygen appears to provide optimal functioning for native NP cells and some potential cell sources,^{209,223} hypoxia and matrix acidity are also linked to the progression of a pro-inflammatory microenvironment,^{85,86} in particular, interleukin (IL)-1 β and tumour necrosis factor (TNF)- α which are believed to be critical in inducing degeneration of the ECM through cell senescence and upregulation of MMPs.^{224,225} Therefore, there is a need to consolidate what “physioxia” means in terms of the IVD microenvironment and re-evaluate the culturing conditions used *in vitro*.

The average lumbar profile curve fitted to the data of Bartels *et al.* (1998) suggests that the central NP concentration is slightly higher than traditional hypoxia (2 – 5 %O₂), with a value of ~ 8 %O₂ from the raw measurements or closer to 6 %O₂ when corrected for the elevated oxygen administered during general anaesthesia (Figure 4.2). In the current work, the oxygen profiles predicted for an active cell density fall within the range of intradiscal measurements, while the total cell density profiles fall just below the measured range. This supports the author’s conviction that identifying the metabolically active cell density is a particularly important parameter for *in-silico* modelling. It is unlikely in a healthy adult (Grade II) that NP cells could sustain ECM homeostasis at less than 1 %O₂ as was predicted in the total cell density model. Like glucose, oxygen concentration appears to increase with degeneration and in particular, Grade IV shows good agreement with the overlaid measurements. This may be credible as the majority of patients undergoing spinal surgery were at least Grade IV.¹⁰ Furthermore, a recent review also suggests that oxygen concentration increases with degeneration due to blood vessel invasion and speculates that this may in fact aggravate the “physioxic” conditions favoured by potential cell sources.²⁰⁹ Therefore, the research field should re-evaluate the *in vivo* oxygen microenvironment in order to

ascertain the clinical relevance of *in vitro* testing conditions and potentially consider patient or degeneration grade-specific treatments based on microenvironmental concentrations.

Like previous models, calcification effects were simulated in this work through reduced CEP diffusion,⁶⁴ although degeneration grade specific levels of calcification were applied based on experimental quantification.³² In this work, the levels of calcification at Grade II and Grade III were not predicted to significantly impact the central metabolite concentrations. Only at Grade IV did calcification appear to impede diffusion to a greater extent, with central glucose and pH levels dropping below those predicted of the total cell density models. Therefore, the current work suggests that at mild and moderate stages of degeneration, the effect of calcification would not appear to be as critical a factor on nutrient supply as commonly speculated for cell-based regeneration, with the glucose concentration only reducing by less than 1 mM and oxygen concentration reducing by ~ 1.5 %O₂ (Grade IV). However, if the central concentrations are lower than those predicted, then such a reduction in nutrients may be critical. Additionally, lactic acid build-up due to calcification did result in a 0.1 reduction on the pH scale. From this work it can be speculated that the effect of calcification becomes more pertinent at Grade V, which has already been deemed too degenerated for cell-based regeneration. It is also important to note that human disc histopathology studies have revealed that not all degenerated discs exhibit calcification of the CEPs.²²⁶ Therefore, this work sought to capture models of each grade with and without calcification, despite the limitation of generic models of each grade with mean parameters rather than a range of plausible bounds to the mean.

When investigating the effect of injecting 3 – 18 million discogenic cells into the NP of a calcified Grade III and IV disc, the current work found that glucose and pH did not appear to be the limiting factor, with minimum concentrations remaining above the threshold at which viability has been reported to be impaired (0.5 mM glucose or pH 6.8).^{27,49,84,91} However, simulating an injection of 9 or 18 million cells predicted that the oxygen level drops below 1 %O₂. This is important in terms of the regenerative potential as studies have shown 5 %O₂ oxygen to be optimal for GAG synthesis,^{28,98} while others have shown that hypoxia as low as 1 %O₂ did not significantly reduce regenerative capacity.^{83,205,206} Although the concentrations were not critical, comparing glucose and pH results for Grade III and IV show that it is likely that different cell numbers will be needed based on degeneration stage and patient-specific factors which affect the local microenvironment, as discussed previously. Interestingly, this work did not see a difference in the minimum oxygen concentration between Grade III and IV due to the injected cells. This suggests that any reduction in disc height between grades compensates for the effect of calcification, which is more prominent for the larger solutes (glucose and lactate). The current work, while considering all caveats of the *in-silico* models, suggests that 3 or 6 million cells is the optimal number for intradiscal injection. These results provide further insight into the progression of clinical trials and the potential to refine the design of trials. For example, some of

the earlier clinical trials used 20 – 60 million cells per disc,^{227–230} while more recent trials from Mesoblast Ltd. used 6 and 18 million cell doses in their Phase 2 trial (NCT01290367) before progressing into Phase 3 with just the lower dose of 6 million cells (NCT02412735). Additionally, DiscGenics Inc. used 10 million cells in their pre-clinical animal rabbit model,¹⁷⁵ before progressing with a low dose of 3 million and a high dose of 6 million cells in their ongoing clinical trials (NCT03347708).

The causal link between degeneration and transport inadequacy remains complicated and a limitation of the current work is the assumption of pure diffusion, while mechanical loading could enhance nutrition through forced solute convection. This may be particularly important in aging and degeneration with the CEP becoming less porous, less hydrated and the presence of calcification impeding diffusion.²³¹ However, studies have also reported increased porosity, due to osteoporosis and osteochondral remodelling, and speculate it to be linked to degenerative features such as the loss of NP osmotic pressure, antigen exposure and immune inflammation.²³² Therefore, the significance of convection due to dynamic loading may vary significantly from patient to patient depending on individual matrix composition and porosity.

4.5 Conclusion

As tissue engineering and regenerative approaches advance rapidly there is a pressing need for a more thorough understanding of the metabolite concentrations present in the human IVD microenvironment and how they govern the behaviour of potential cell therapies. This Chapter consolidates glucose, pH and oxygen levels previously measured or predicted within the NP, with the aim of re-evaluating the microenvironment at stages of degeneration which are clinically relevant for cell-based regeneration. Additionally, this work has advanced *in-silico* modelling through a strong foundation of experimentally determined grade-specific input parameters (diffusion coefficients, cell density, tissue hydration, disc height and CEP calcification). Taken together, pre-existing measurements and the predicted results suggest that metabolite concentrations may not be as critically low as commonly believed. In fact, nutrient concentrations may increase due to reduced disc height and vasculature ingrowth. Additionally, calcification does not appear to have a detrimental effect at earlier stages of degeneration when cell therapies are deemed an appropriate treatment. Ultimately the goal is to recapitulate the different microenvironmental niches *in vitro*, leading to more effective therapies with greater potential for reversing or slowing down degeneration in patient-specific microenvironments.

Chapter 5. Two- and Three-Dimensional *In Vitro* Nucleus Pulposus Cultures: An *In-Silico* Analysis of Local Nutrient Microenvironments

A significant amount of this Chapter has been published previously in **McDonnell, E. E.** and Buckley, C. T. (2022) ‘Two-and three-dimensional in vitro nucleus pulposus cultures: An in-silico analysis of local nutrient microenvironments’, *JOR Spine*, 5(3), doi: <https://doi.org/10.1002/jsp2.1222>

Contribution: Performed the acquisition and interpretation of literature data, *in-silico* modelling, analysis presentation and interpretation of results, drafting of the article, revising it critically, and final approval.

5.1 Introduction

The previous chapter sought to consolidate the current knowledge of the IVD nutrient microenvironment. Furthermore, this work suggests that at a stage of degeneration when cell-based regeneration remains a viable treatment option, the central NP microenvironment consists of glucose concentrations of approximately 1 – 3.5 mM, an average oxygen level of 6 – 8 %O₂ and a median pH of 7. Therefore, when investigating the response of potential cell therapies *in vitro*, there is a need to tailor the biochemical microenvironments to these values to ensure that results are more physiologically relevant and clinically translatable. These conditions can be simply implemented *in vitro* through culturing cells in low oxygen, reduced glucose and/or serum and increased acidity. However, aside from studies which specifically study the effect of microenvironmental conditions, the majority of disc cell culture across the research field do not adjust the pH of the culture media. Glucose concentration of the culture media and the incubator oxygen levels are more commonly regarded as controllable *in vitro* boundary conditions. Despite this, only 32 (58.2%) of 55 reviewed papers reported on the glucose concentration and only 23 (41.78%) reported on incubator oxygen level 2D cell expansion. Figure 5.1(A) shows that among the studies that reported on the boundary nutrient concentrations 62.5% used high glucose (HG: 25 mM or 4.5 g/L) and 37.5% used low glucose (LG: 5.5mM or 1 g/L), while 44.8% used “normoxia” (NX: 20 – 21 %O₂), 34.5% used “physioxia” (PX: ~ 5 %O₂) and 20.7% used “hypoxia” (HX: ~ 2 %O₂). Taking note that of the 23 studies reporting oxygen values, six studies investigated more than one oxygen level. This not only highlights large variation across the field but also that parameters which are critical for reproducibility are not routinely being reported. There is an urgency for this to be addressed, particularly with a recent push towards harmonisation within disc research and the increased attention to the reproducibility of research findings across all scientific fields.^{233,234}

Furthermore, a disconnect often occurs between the external incubator or media concentrations and the actual local cellular concentrations.^{181,235–237} There is an underappreciation of the effects of parameters such as diffusion rate, media volume and cell density on the true nutrient microenvironment of cell culture systems. A number of studies use soft scaffolds such as hydrogels to mimic the native disc tissue and maintain cells in their 3D phenotype. However, potential nutrient gradients through these systems will not only affect cell viability and differentiation but also regulate gene expression and metabolism, creating distinct regions of ECM deposition. Therefore, it is critical to carefully consider the combined effects key culture parameters may have on the microenvironment of *in vitro* systems and the downstream confounding influence on heterogenous matrix synthesis. This chapter aims to characterise the local nutrient microenvironment of 2D cell monolayers and commonly used 3D *in vitro* culture systems, to highlight the effect of culturing parameters and to place “standard practice” culturing conditions into context in terms of physiological relevance.

5.2 Materials & Methods

Long-term leaders in disc cell culture were identified through the ORS Spine subgroup involved in standardisation and harmonisation of cell isolation and culture methods.²³⁴ This incorporated studies over the last ~ 15 years from 20 prominent disc groups from across 14 different universities/medical centres. A list of the reviewed literature with a summary of key parameters can be found in Appendix C (Table C.1 and C.2).

5.2.1 Two-dimensional cell culture models

Figure 5.1(B) highlights the frequency of different cell culture vessels used for 2D monolayer cell culture and expansion. The *in-silico* nutrient transport models were created using COMSOL Multiphysics 6 (COMSOL Inc., Burlington, MA) for the most used culture vessels. Geometries were created based on Corning™ Costar™ culture plates and SARSTEDT flasks with a standard working volume of media (6-well = 2 mL, T-25 = 5 mL, T-75 = 10 mL and T-175 = 20 mL) and an effective diffusion coefficient of $2.8 \times 10^{-9} \text{ m}^2/\text{s}$ for oxygen, $5.67 \times 10^{-10} \text{ m}^2/\text{s}$ for glucose and $5.68 \times 10^{-10} \text{ m}^2/\text{s}$ for lactate at 37°C.^{238–240} Nutrient concentrations at the cell surface were established using a transient analysis of coupled reaction-diffusion equations together with cell proliferation kinetics.

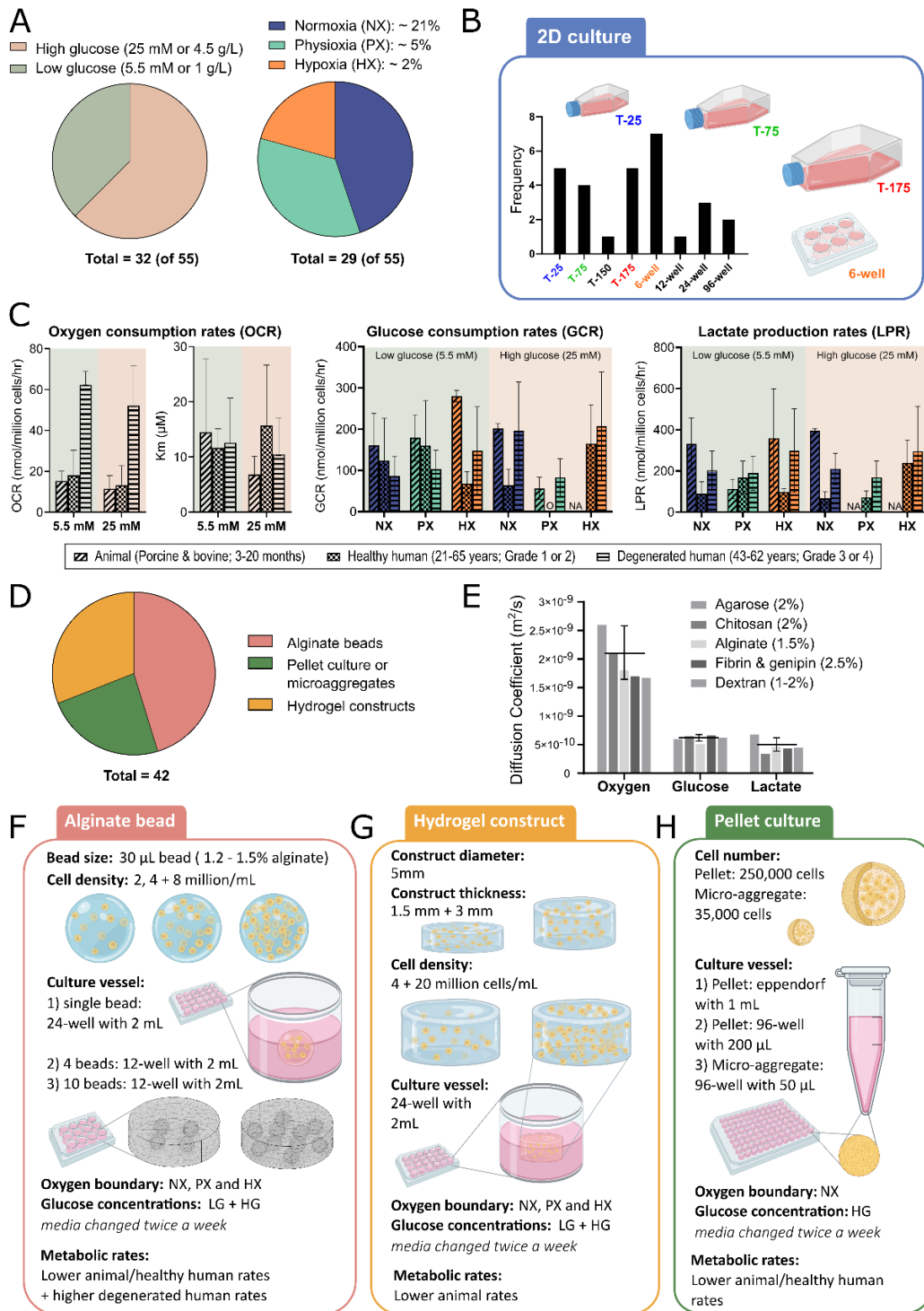


Figure 5.1 Consolidating commonly used cell culture parameters and metabolic rates reported across the intervertebral disc research field. (A) The most used glucose concentrations and incubator oxygen levels across 55 reviewed studies. (B) The frequency of culture vessel used across these studies for 2D NP cell expansion and culture. (C) Compiled metabolic rates gathered from the literature and graphed according to glucose concentration and external oxygen concentration. (D) Most commonly used 3D culture system for NP cells across 42 studies. (E) Effective diffusion coefficients for oxygen, glucose, and lactate through several relevant hydrogels at 37°C. (F–H) Most common configurations (geometrical dimensions, cell density, boundary concentrations, and culture vessels) for alginate beads, cylindrical hydrogel constructs, and pellet culture. Nomenclature: high glucose (HG), low glucose (LG), normoxia (NX), physioxia (PX) and hypoxia (HX).

5.2.2 Metabolic rates and proliferation kinetics

Several studies have reported oxygen consumption rates (OCR),^{9,90,91,93} glucose consumption rates (GCR) and lactate production rates (LPR) for NP cells from animals and humans under varying nutrient conditions.^{9,91,94,95,98,102,103} Tabulated rates from these studies can be found in Section 2.3.3. For this work the literature has been compiled based on the external boundary conditions of glucose (LG or HG) and oxygen (NX, PX or HX), as shown in Figure 5.1(C). Significantly higher oxygen consumption has been reported for degenerated human cells (aged 43 – 62 years, Thompson Grade III or IV),⁹³ and as a result OCRs can be separated into a “lower” rate group comprising values reported for animal and healthy human cells (aged 21 – 65 years, Thompson Grade I or II) and a “higher” rate group for a degenerated phenotype. However, similar categorising of glycolytic rates does not appear to be possible with the literature available and average GCR and LPR values will be used regardless of species/degeneration stage. As previously demonstrated together with successful *ex vivo* validation,²⁴¹ OCR ($\mu\text{M}/\text{h}$) is modelled as being dependent on local pH and oxygen by employing Michaelis-Menten equations (3-2).^{9,90,114,116}

In this study GCR or Q^{gluc} was more explicitly modelled using a maximum GCR based on the external glucose boundary conditions (as no clear and obvious difference exists between 5.5 mM and 25 mM in Figure 5.1(C) but becomes rate limited at ~ 2 mM, by curve fitting Michaelis-Menten kinetics to experimental measurements at lower glucose concentrations (< 5 mM).^{95,98}

$$Q^{gluc} = -\frac{V_{max}(C^{gluc})}{K_m + C^{gluc}} \rho_{cell} \quad (5-1)$$

where C^{gluc} is the local glucose concentration (mM), ρ_{cell} is the cell density (million cells/mL). V_{max} is the maximum consumption rate (nmol/million cells/h) and K_m is the rate limiting Michaelis-Menten constant (mM). In order to capture rate limited glycolysis, LPR was implicitly modelled based on the ratio of lac:gluc molecules which is typically 2:1.^{9,90,114,116} However, considering the compiled experimental literature this ratio appears to vary as a function of oxygen. Furthermore, when the pH drops below 6.7 in certain culture configurations, LPR was modelled explicitly to capture experimental observations of rates dropping from ~ 200 nmol/million cells/h at pH 7.4 to ~ 150 nmol/million cells/h at pH 6.7 and to ~ 50 nmol/million cells/h at pH 6.2.⁹ The finalised metabolic parameters used in the models, based on the media glucose and external oxygen levels, are presented in Table 5.1.

Cell proliferation was modelled using first order kinetics based on observed population doubling time (the time for the doubling of a single cell under mitosis). Based on experience of culturing NP derived porcine cells and assuming an initial seeding density of 5×10^3 cells/cm² and an upper limit of 5×10^6 from a T-175 after 5 – 6 days (i.e. $\sim 28,571$ cells/cm² at 80% confluency),

an exponential growth rate (k) of 0.348 [1/d] can be calculated using the population doubling time.

$$N_t = N_0 e^{kt} \quad (5-2)$$

$$k = \frac{\ln\left(\frac{N_t}{N_0}\right)}{t} \quad (5-3)$$

Where k is the frequency of cell cycles per unit time, N_t is cell number at time t , N_0 is the initial cell number and t is the culture time in days.

Given that it is common practice to perform a media exchange twice a week and given the assumption of 5 – 6 days to ~ 80% confluency, the transient 2D analysis was modelled for seven days, incorporating a media exchange at the midway point. Although other studies may report different growth rates, the culture time is arbitrary; whether cells reach 80% confluency at 5 – 6 days or 12 – 15 days,²⁴² the results at 80% confluency will be the same regardless of the timeframe. An example of this is highlighted in Figure 5.2.

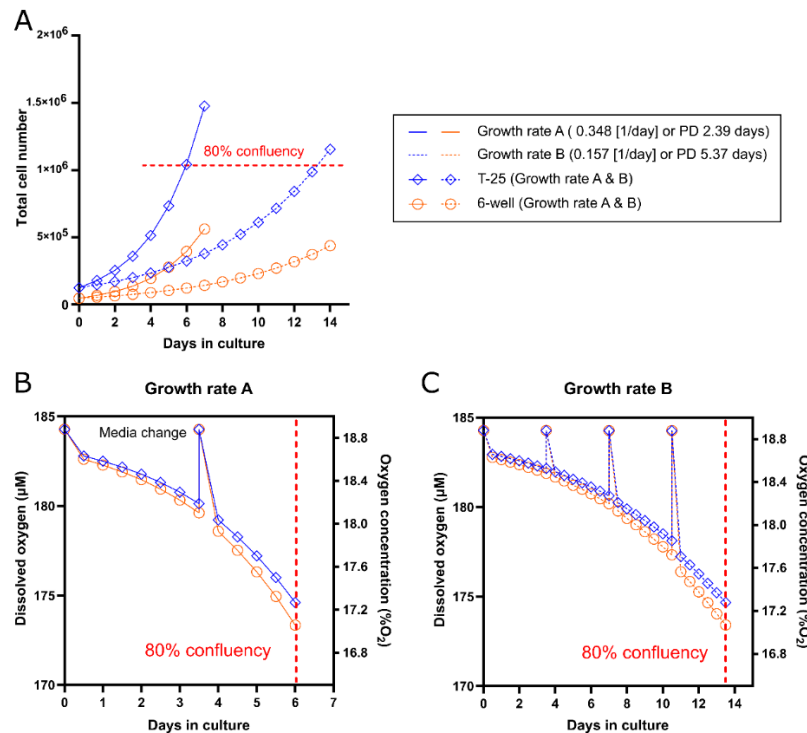


Figure 5.2 Comparing the effect of different proliferation kinetics in terms of growth rate or population doubling (PD). (A) The exponential increase in total cell number within a T-25 flask or a 6-well plate based on our own lab groups observed PD time (Growth rate A) or a slower PD time reported by Sakai *et al.* where rabbit cells in a T-25 flask reached 80% confluency in 12–15 days (Growth rate B). (B) The oxygen concentration at the cell surface over time for cells cultured at normoxia (NX) with Growth rate A and incorporating one media exchange. (C) The oxygen concentration at the cell surface over time for cells cultured at NX with Growth rate B and incorporating three media exchanges.

Table 5.1. Metabolic parameters used in each in-silico model based on external boundary conditions and the species or degeneration stage being investigated. Abbreviations: LG (low glucose) NX (normoxia), PX (physioxia), HX (hypoxia), OCR (oxygen consumption rate), GCR (glucose consumption rate) LPR (lactate production rate) and HG (high glucose).

LG + varying oxygen	LG + NX	LG + PX	LG + HX
OCR (Vmax) Units: nmol/million cells/h	Animal + healthy human: 17 Degenerated human: 62		
Rate limiting oxygen (Km) Units: μM	12		
GCR Units: nmol/million cells/h	143	103	165
Rate limiting glucose (Km) Units: mM	2		
LPR Units: nmol/million cells/h	207	168	296
Ratio (lac:gluc)	1.4:1	1.6:1	1.8:1
HG + varying oxygen	HG + NX	HG + PX	HG + HX
OCR (Vmax) Units: nmol/million cells/h	Animal + healthy human: 12 Degenerated human: 52		
Rate limiting oxygen (Km) Units: μM	12		
GCR Units: nmol/million cells/h	143	103	165
Rate limiting glucose (Km) Units: mM	2		
LPR Units: nmol/million cells/h	207	168	296
Ratio (lac:gluc)	1.4:1	1.6:1	1.8:1

5.2.3 Three-dimensional cell culture models

Across 42 studies from prominent research groups in disc cell culture, alginate beads were the most popular 3D culture system (45.2%), followed by cylindrical hydrogel constructs (31.0%) and then pellet or microaggregate cultures (23.8%), Figure 5.1(D). The effective diffusion coefficient of oxygen,^{243–246} glucose,^{247–250} and lactate,^{250–253} through a number of different hydrogels were gathered to experimentally inform the *in-silico* models, Figure 5.1(E). Within the bead model alginate-specific diffusion coefficients for oxygen ($1.8 \times 10^{-9} \text{ m}^2/\text{s}$), glucose ($5.1 \times 10^{-10} \text{ m}^2/\text{s}$) and lactate ($4.67 \times 10^{-10} \text{ m}^2/\text{s}$) were used.^{243,247,251} The cylindrical constructs in the literature use a range of different hydrogel material types, thus an average diffusion coefficient across a number of typical hydrogel concentrations was implemented ($2.1 \pm 0.5 \times 10^{-9} \text{ m}^2/\text{s}$, $6.3 \pm 0.6 \times 10^{-10} \text{ m}^2/\text{s}$ and $5.1 \pm 1.1 \times 10^{-10} \text{ m}^2/\text{s}$, for oxygen, glucose and lactate, respectively). Diffusion through culture media was the same as for the 2D models. As an idealised model, diffusion was not modelled through the base of the construct which was in contact with the tissue culture plastic.

Hydrogel geometry, cell seeding densities, culture vessel type and media volume, external boundary concentrations and metabolic rates all play a role in establishing the local cell nutrient microenvironment. The most utilised configurations for alginate beads, cylindrical constructs, and pellet cultures are presented in Figure 5.1(F-H), providing a schematic for the different model iterations presented in this work. Because all possible combinations cannot be investigated within the scope of this work, a sensitivity analysis for the lowest/highest rates of metabolism reported from the literature can be found in Figure 5.3.

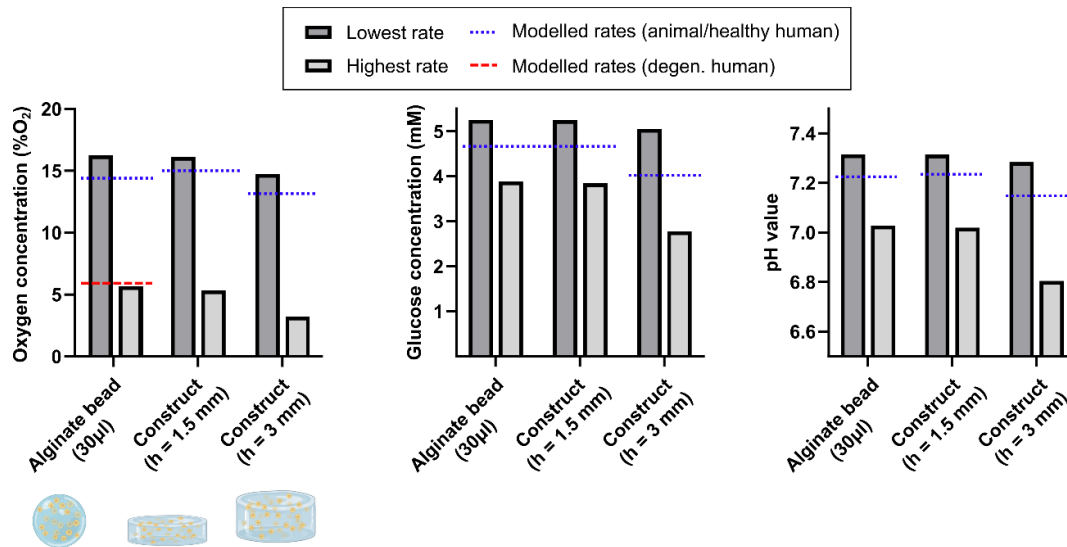


Figure 5.3 Sensitivity analysis on the effect of the lowest and highest rates of metabolism reported in the literature on the minimum oxygen, glucose and pH values in an alginate bead or hydrogel construct containing 4 million cells/mL. The dashed coloured lines represent the concentrations predicted in the corresponding culture configuration using the averaged rates for the appropriate external boundary conditions (NX and LG in this case).

5.2.4 External boundary concentrations: Glucose and oxygen

As mentioned previously, culture media is typically either LG (5.5 mM) or HG (25 mM) and both concentrations will be investigated for all culture configurations except pellet culture, as all pellet literature report the use of HG only. However, in terms of oxygen the v/v ratio of oxygen to other gases in an incubator is decreased compared with dry room air (21.2 kPa or 159 mmHg at sea level), Figure 5.4(A). As a result, the relative gas concentration in a NX, PX or HX incubator, with the addition of 5 %CO₂ (38 mmHg) and 75% humidity (47 mmHg), is lower than the conventional concentrations typically cited.¹⁸⁰ Furthermore, for modelling through COMSOL, the partial pressure of incubator oxygen must be converted into the concentration of dissolved oxygen by using Henry's law (oxygen solubility coefficient of 1.3 µM/mmHg in culture media at 37°C).^{180,181} The resulting oxygen concentration of the culture media equilibrated within each oxygen incubator is shown in Figure 5.4(B).

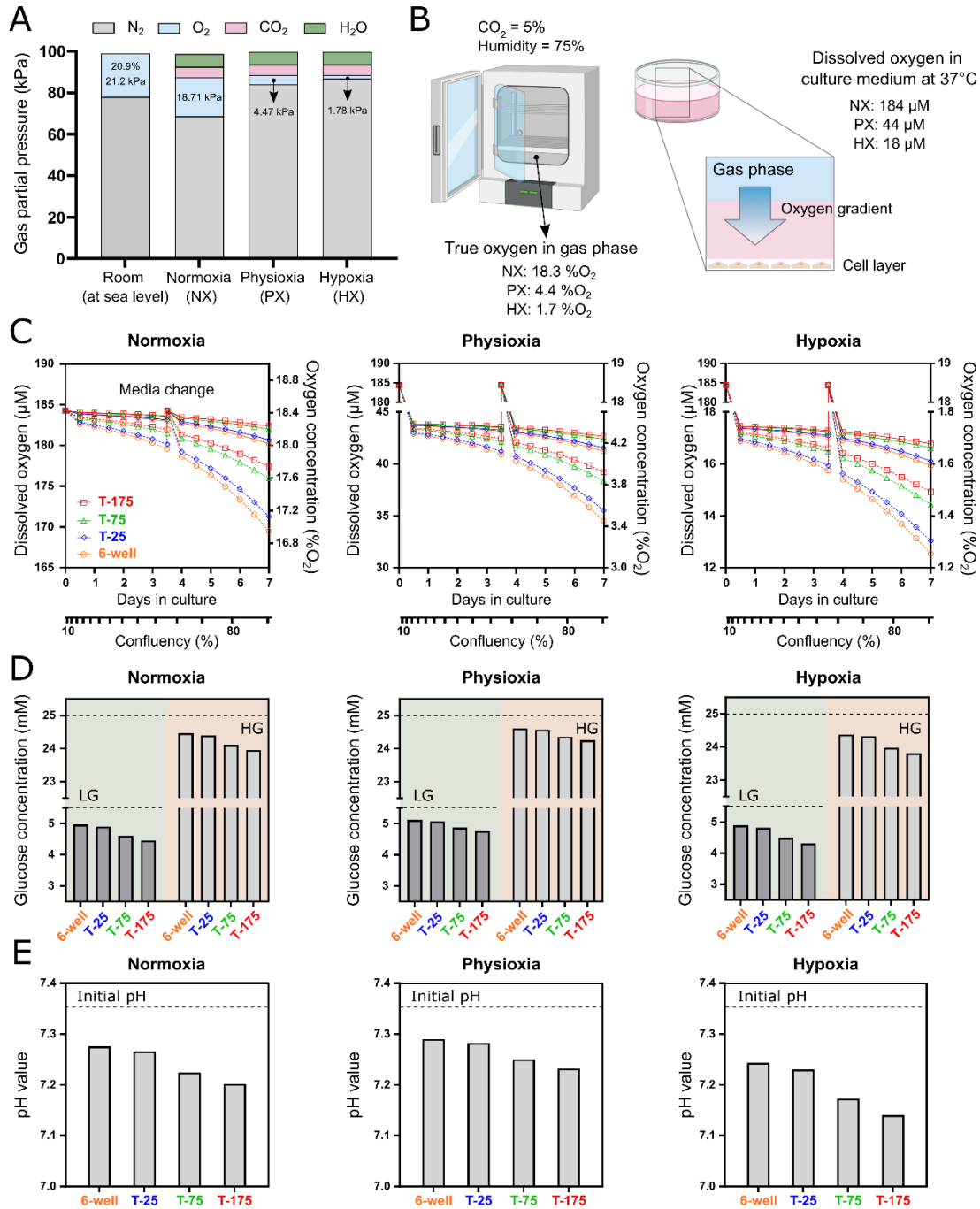


Figure 5.4 External incubator gas concentrations and local metabolite concentrations in 2D cell culture vessels. (A) The volume/volume ratio of oxygen to other gases in an incubator is decreased compared with that of dry air in a room. Values are shown for sea level. (B) As a result, the relative gas concentration in a normoxia (NX), physioxia (PX), or hypoxia (HX) incubator, with the addition of 5% CO_2 and 75% humidity, are lower than the conventional concentrations often cited. These incubator oxygen levels can then be converted to the concentration of dissolved oxygen by using an oxygen solubility coefficient in culture media at 37°C. (C) A temporal analysis of the oxygen concentration at the cell surface for cells proliferating over a 7-day period in either an NX, PX or HX incubator. Solid line indicates a lower animal/healthy human metabolism, dashed lines indicate a higher degenerated phenotype. (D) Glucose concentration of the media at 80% confluency for both low (5.5 mM) and high (25 mM) glucose media in a NX, PX, and HX incubator. (E) pH concentration of the media at 80% confluency in a NX, PX, and HX incubator

5.3 Results

2D results are presented as a transient analysis to capture the effect of cell proliferation and media exchange over a 7-day period. Figure 5.4(C) shows the oxygen concentration at the cell surface of a 6-well plate, T-25, T-75 or T-175 flask as a function of confluency in either a NX, PX or HX incubator. As expected, oxygen decreases at the cell surface as the cells multiply creating greater demand for oxygen. However, there is no major difference in surface concentration between the culture vessels, particularly for cells categorised as having lower metabolic rates. Even at higher degenerated rates of oxygen metabolism, concentrations at the cell surface are predicted to only drop a maximum of 1.3 %O₂ at NX, 0.78 %O₂ at PX and 0.43 %O₂ at HX over the expansion period. Figure 5.4(D) shows the average glucose concentration of both LG and HG culture media at ~ 80% confluency (day 5 – 6), following a standard media exchange of twice weekly, while Figure 5.4(E) shows the corresponding pH level of the media. As expected, glucose and pH are predicted highest in the culture vessel with the lowest cell yield (6-well) and lowest in the culture vessel with the greatest cell yield (T-175). Additionally, no significant difference was seen in glucose between the different oxygen incubators in 2D due to a surplus of glucose, while pH reduces slightly more under HX due to increased glycolytic rates.

Figure 5.5 presents the oxygen gradients through a single alginate bead (30 µL) cultured in 2 mL of media in a 24-well plate, while Figure 5.6 presents the corresponding glucose and pH results for all glucose and oxygen conditions. Like the 2D models, a transient analysis was performed incorporating a regular feeding schedule of twice weekly. Subsequently the results are presented at day three, just prior to a media exchange, to capture the minimum concentrations established within the alginate bead. Naturally the oxygen gradients will stabilise more quickly, but nonetheless they are presented at this timepoint for consistency. For cells with lower rates of oxygen metabolism (Figure 5.5(A)), oxygen does not appear to reduce significantly within a bead of 2 or 4 million cells/mL (16.4 or 14.4 %O₂ at NX and LG), while at 8 million cells/mL oxygen drops to 11.1 %O₂. As expected, the reduction in oxygen within beads cultured in HG is less due to the slightly lower OCR under these conditions. However, even at NX conditions, cells with very high rates of oxygen metabolism (Figure 5.5(B)), predict minimum oxygen levels of 11.3 %O₂, 5.9 %O₂ and 1.4 %O₂ within beads with 2, 4 and 8 million cells/mL, respectively. In Figure 5.5(C) the minimum oxygen concentrations predicted within the beads can be compared across both OCR, for all seeding densities and external boundary concentrations. Similarly, Figure 5.6(A), (B) present the glucose gradients within the culture well and minimum bead concentrations for the different seeding densities and external boundary conditions. Glucose appears in excess at HG and even at LG conditions with 8 million cells/mL, glucose does not fall critically low between media exchanges. Nonetheless, under HG conditions glycolysis is not rate limited by low glucose (< 5 mM) and as a result pH is predicted to drop lower within the beads

cultured at HG compared to LG (Figure 5.6(C)). This is most apparent in Figure 5.6(D) under HX conditions, where glycolytic rates are modelled to be highest. A bead with 8 million cells/mL is predicted to have a minimum pH of ~ 7.0 under LG conditions compared to ~ 6.9 under HG conditions, just prior to media exchange.

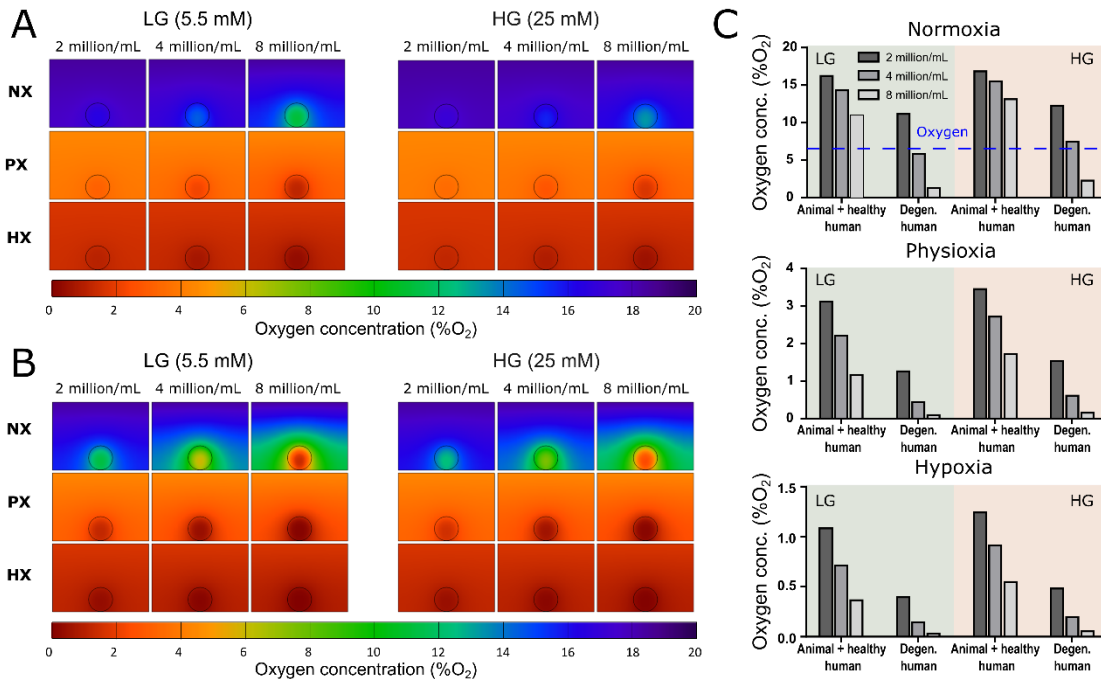


Figure 5.5 Investigating the effect of three different seeding densities on the oxygen concentration in a single 30 μ l alginate bead in 2 mL of low glucose (LG) or high glucose (HG) media (24-well) at normoxia (NX), physioxia (PX) and hypoxia (HX). Oxygen contour plots for lower animal/healthy human metabolism. (B) Oxygen contour plots for a higher degenerated phenotype. (C) Minimum oxygen concentrations in the alginate bead at steady-state for the different seeding densities, metabolic rates, and nutrient conditions. The dashed line indicates the *in vivo* concentration from the previous chapter.

Figure 5.7 compares the effect of culturing 4 or 10 beads with 4 million cells/mL in a 12-well plate. This is a transient analysis looking at the depletion of a finite supply of glucose and the build-up of acidity between media exchanges. As a result, oxygen is not shown as it is readily available to the media surface. Figure 5.7(A) presents the glucose gradient through the centre of beads just prior to a media exchange. Concentrations were observed to drop substantially lower in the well containing 10 beads at both LG and HG. Figure 5.7(B) shows the beginning of a plateauing effect of glucose limited glycolysis in LG but not HG. Figure 5.7(C) presents the corresponding pH gradient through the alginate beads. As expected, there are significantly lower pH levels within one of the 10 beads under HX conditions and HG media. Again, Figure 5.7(D) shows the strong effect of glycolysis not being rate limited by glucose under HG culture. Figure 5.8 investigates the effect of a daily media refresh on the glucose and pH levels within the beads

compared to the standard twice weekly media exchange. The results predict that glucose drops, and pH builds up substantially over three days when culturing ten beads and suggest that more frequent media refresh may be necessary to maintain a homogeneous nutrient microenvironment throughout the culture period.

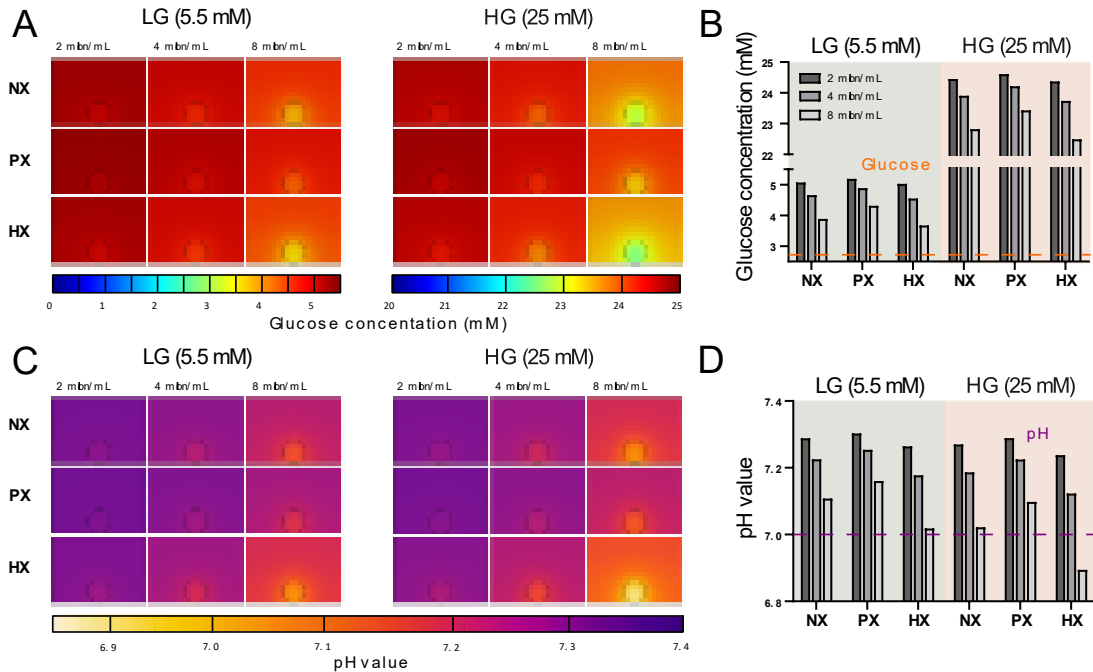


Figure 5.6 Investigating the effect of three different seeding densities on the glucose and pH concentration in a single 30µl alginate bead in 2 mL of low glucose (LG) or high glucose (HG) media (24-well) at normoxia (NX), physioxia (PX) and hypoxia (HX). Contour plots showing the glucose concentration in a single alginate bead of different seeding densities in low glucose (LG) and high glucose (HG) media, just prior to a media exchange, at normoxia (NX), physioxia (PX) and hypoxia (HX). **(B)** Corresponding minimum glucose concentrations within the alginate bead prior to media exchange. **(C)** Contour plots showing the pH level in a single alginate bead of different seeding densities in LG and HG media, just prior to a media exchange, at NX, PX and HX. **(D)** Corresponding minimum pH levels within the alginate bead prior to media exchange. The dashed lines indicate the *in vivo* concentrations from the previous chapter.

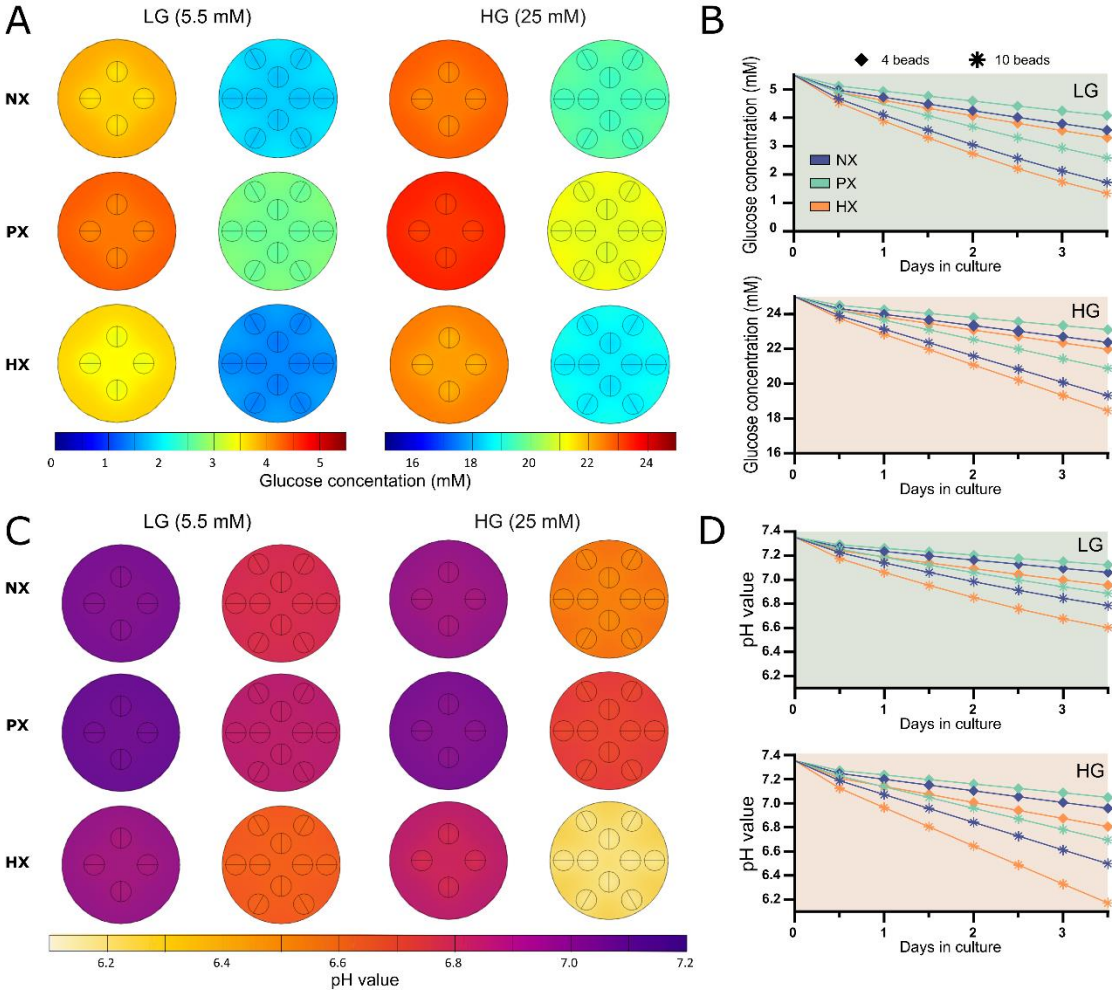


Figure 5.7 . Investigating the effect of multiple alginate beads (4 or 10 beads of 4 million cells/mL) in a single culture vessel (12-well). (A) Contour plots showing the glucose concentration in a transverse plane through the centre of the beads in low glucose (LG) and high glucose (HG) media, just prior to a media exchange, at normoxia (NX), physioxia (PX), and hypoxia (HX). (B) Transient analysis of the minimum glucose concentration within an arbitrary bead within the 4 or 10 bead configurations up until the media exchange, for both LG and HG media. (C) Contour plots showing the pH in a transverse plane through the centre of the beads in LG and HG media, just prior to a media exchange, at NX, PX, and HX. (D) Transient analysis of the minimum pH level within an arbitrary bead within the 4 or 10 bead configurations up until the media exchange, for both LG and HG media.

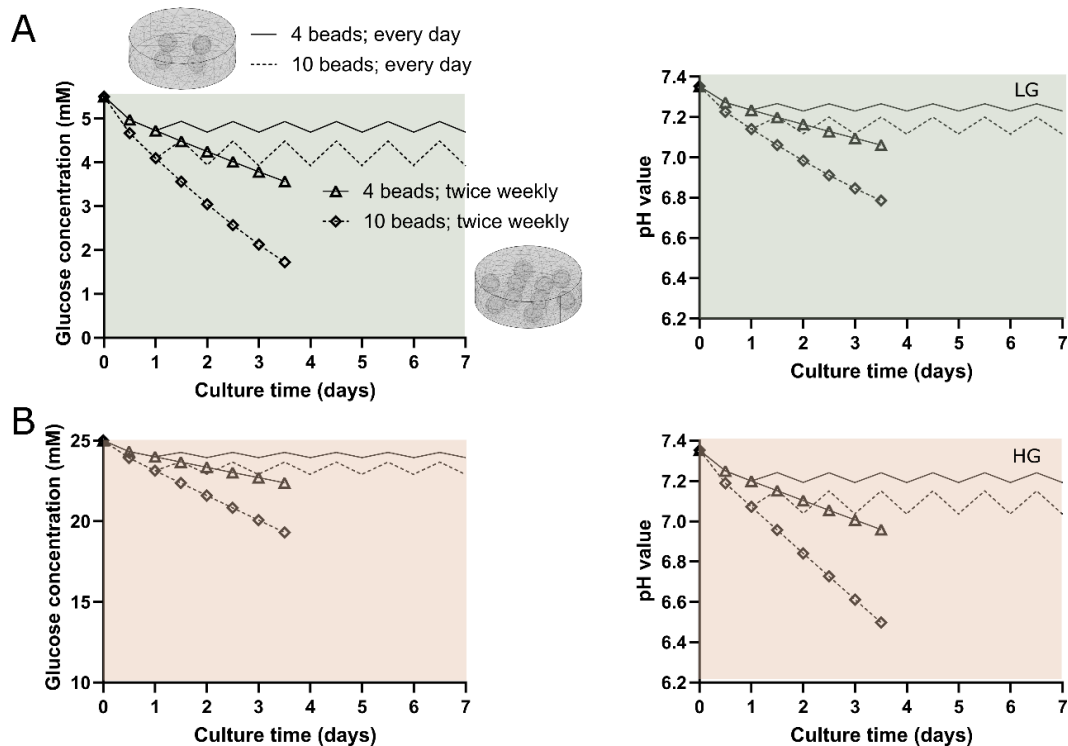


Figure 5.8 Comparing the effect of a standard twice weekly media exchange to a daily media refresh on concentrations within a 4 and 10 bead culture. (A) Minimum glucose and pH values within an arbitrary bead at low glucose (LG) and (B) high glucose (HG).

Figure 5.9(A) presents the oxygen gradients through a quadrant of a cylindrical construct, comparing the effect of construct height and cell seeding density across a NX, PX and HX incubator. Concentrations within a hydrogel containing 20 million cells/mL are significantly lower than those predicted in a 4 million cells/mL hydrogel, while a reduced construct thickness slightly alleviates the reduction in oxygen. Figure 5.9(B) compares the axial profile through the centre of the cylindrical hydrogel. For example, taking the thicker construct (height = 3 mm) and 4 million cells/mL, oxygen concentrations drop to ~ 11.9 %O₂ at NX, ~ 1.4 %O₂ at PX and 0.4 %O₂ at HX, while the same construct with 20 million cells/mL is predicted to drop below 2 %O₂ even at NX conditions and below 0.1 %O₂ at PX and HX conditions. Figure 5.10 shows a transient analysis of the glucose and pH levels within the same constructs over the 7-day period with a media exchange at the midpoint.

Figure 5.10(A), (B) graph the average value of glucose and pH within the constructs cultured in LG, while Figure 5.10(C), (D) graph the average value of glucose and pH within the constructs cultured in HG. The contour plots show the gradients of glucose and pH through the constructs just prior to the media exchange and as expected the glucose and pH increase within the hydrogel following media refresh. All constructs with 4 million cells/mL remain above critical levels of glucose and pH under all culture conditions, with a twice weekly media exchange. However, thicker constructs with 20 million cells/mL start to reach critical levels of glucose and an acidic pH after just two days of culture under LG conditions. Furthermore, even the thinner

construct with 20 million cells/mL is predicted to become acidic prior to the media refresh in HG conditions, with the thicker construct dropping to critically low levels of pH. Figure 5.11 investigates the effect of a daily media refresh on the glucose and pH levels within construct of two different thicknesses, compared to the standard twice weekly media exchange. The results predict that glucose drops, and pH builds up substantially over three days within the thicker construct and suggest that more frequent media refresh may be necessary to maintain a homogeneous nutrient microenvironment throughout the culture period.

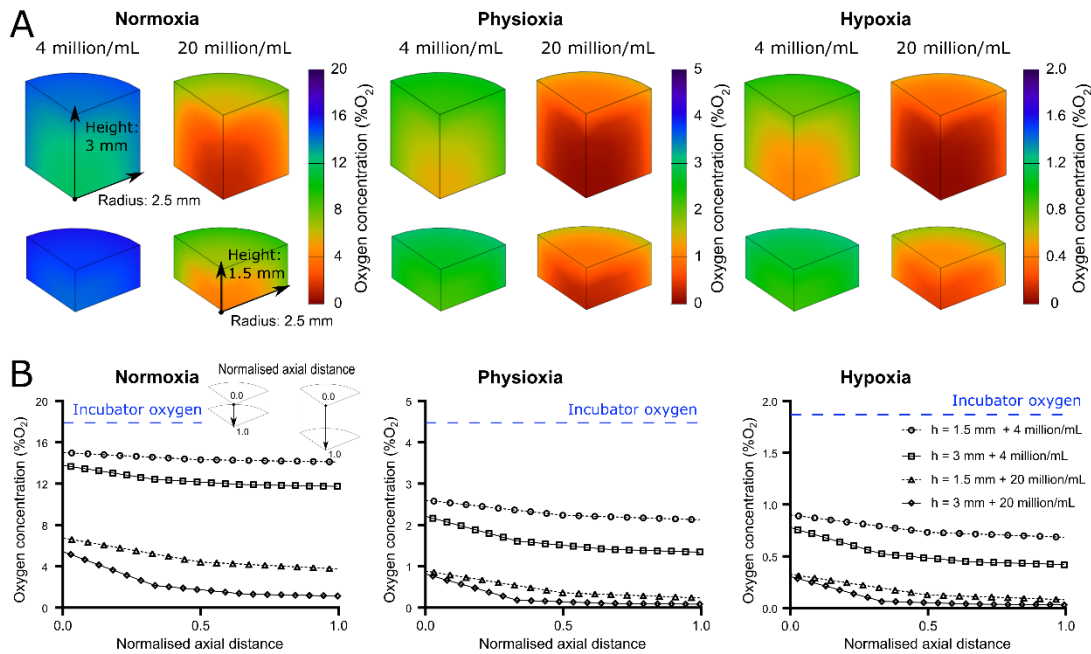


Figure 5.9 Investigating the oxygen microenvironment within a cylindrical construct (radius: 2.5 mm, height: 3 mm, or 1.5 mm) containing a seeding density of either 4 or 20 million cells/mL. Oxygen gradients through a quadrant of a cylindrical construct cultured at normoxia, physioxia or hypoxia. Cells are assumed to have the lower animal metabolic rates. **(B)** Corresponding axial profile of oxygen through the constructs. As indicated, the axial profile runs from the top surface of the hydrogel to the base at the bottom of the culture plate and is normalised to account for investigating two different construct heights.

Figure 5.12 presents the results for pellet culture. Two different types of pellet culture were investigated: conventional pellet culture of ~ 250,000 cells and more recently established micro-aggregate models of ~ 35,000 cells. Pellet cultures were modelled either cultured in an Eppendorf with 1 mL of media or in a 96-well with 200 μ L of media, while micro-aggregates were modelled in a 96-well with 50 μ L of media. Figure 5.12(A) presents the gradients of metabolites in the mid-plane through the culture system on day three, just prior to a standard media exchange. Figure 5.12(B) presents the average concentration across the culture media and within the cell aggregates at the corresponding timepoint. For oxygen, it was predicted that even at NX conditions the concentration within the pellet drops down to almost 1 %O₂ when cultured

in an Eppendorf. When culturing in a 96-well with reduced media height for oxygen diffusion, the oxygen is predicted to be $\sim 4\% \text{O}_2$. In addition, using smaller pellets or micro-aggregates reduces the oxygen demand and produces quite a constant gradient throughout the cellular mass with the average concentration increasing to $\sim 13\% \text{O}_2$, only $\sim 5\% \text{O}_2$ lower than the external boundary condition. For glucose, there is almost a 25% reduction in the concentration within the standard pellet from the initial media concentration (25 mM) and no difference in pellet concentration was predicted even when the media volume is reduced from 1 mL to 200 μL , as HG still provides a surplus of glucose when performing a media exchange twice weekly. The micro-aggregate predicts a concentration very close to the media concentration, with $< 3\text{ mM}$ reduction in media concentration prior to media exchange. However, pH drops substantially within the conventional pellets (~ 6.5). Although a reduced media volume will intensify the effect of lactate accumulation and the resulting pH of the media, the acidity within the conventional pellet remained similar in both configurations. The media of the micro-aggregate is predicted to stay just above pH 7 while the cell aggregate itself drops just below pH 7 with a twice weekly media exchange.

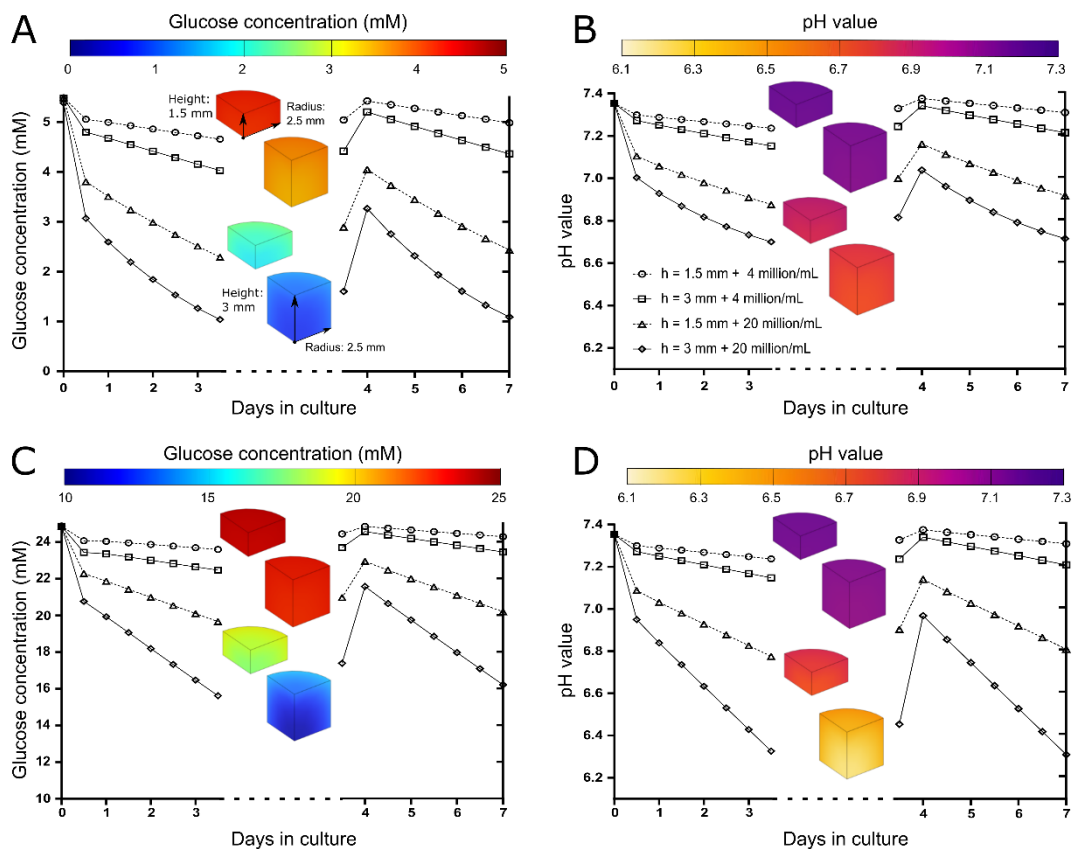


Figure 5.10 Transient analysis of glucose concentration and pH values within a cylindrical construct (radius: 2.5 mm, height: 3 mm, or 1.5 mm) containing a seeding density of either 4 or 20 million cells/ml with a media exchange performed at the midpoint. (A) Glucose concentrations and (B) pH values under low glucose (5.5 mM) media. (C) Glucose concentrations and (D) pH values under high glucose (25 mM) media. The graph represents the average values within the hydrogel and the inset contour plot represents the gradient just prior to media refresh.

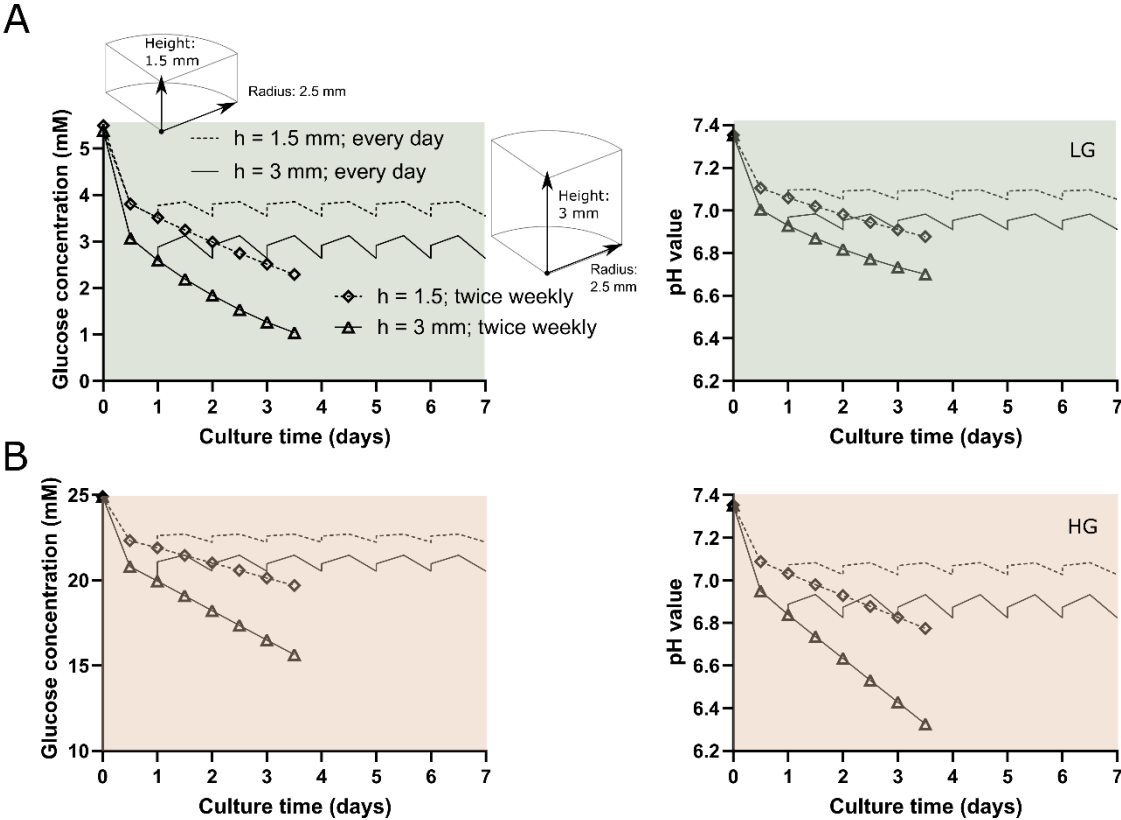


Figure 5.11 Comparing the effect of a standard twice weekly media exchange to a daily media refresh on concentrations within a 4 million cells/mL hydrogel construct. (A) Minimum glucose and pH values within a hydrogel cultured at low glucose (LG) and (B) high glucose (HG).

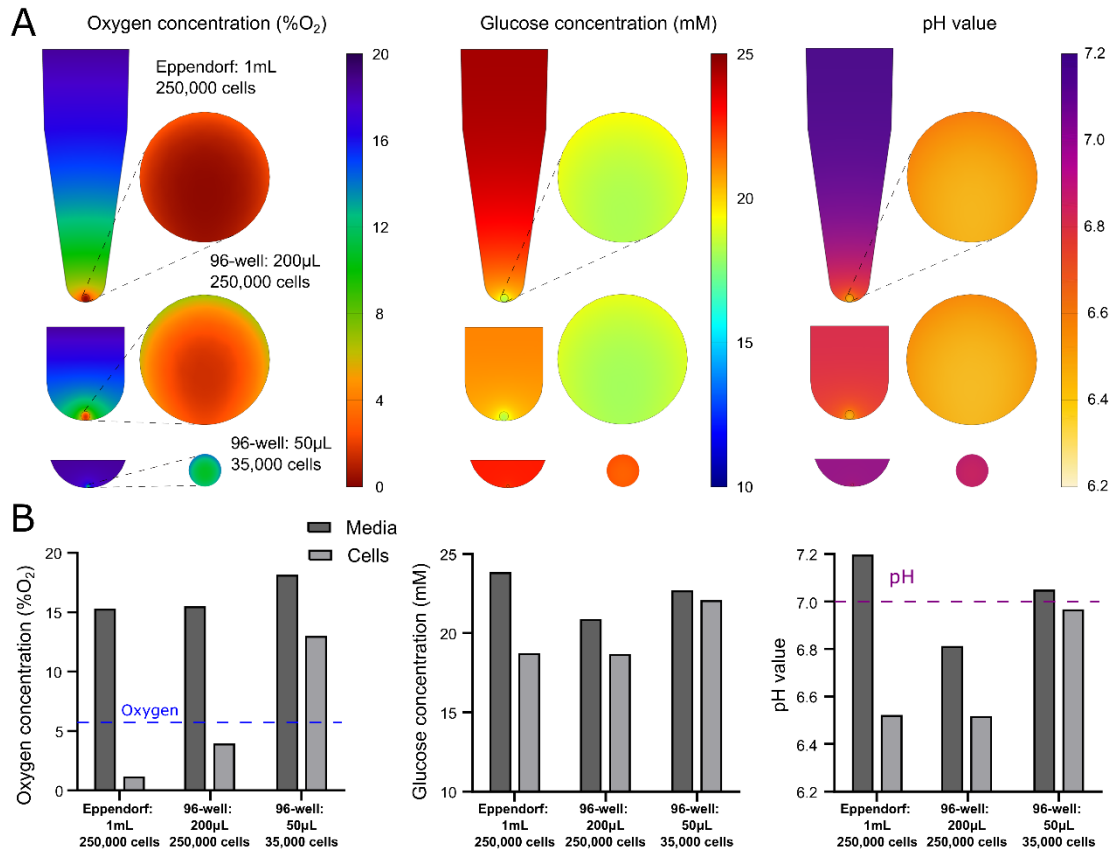


Figure 5.12 Comparing the nutrient microenvironment of a 250,000-cell pellet in 1 mL (Eppendorf) or 200 µL (96-well) of media and a 35,000-cell microaggregate in 50 µL (96-well) of media. (A) Contour plots of oxygen, glucose, and pH gradients through both the culture media and the cell aggregate. (B) Corresponding values for the average concentration of oxygen, glucose and pH in the media and the cell aggregate prior to a media exchange in each of the three culture configurations. The dashed lines indicate the *in vivo* concentrations from the previous chapter. Glucose is not indicated as it is below 3 mM.

5.4 Discussion

IVD research has been challenged with heterogeneous results in term of the regenerative potential and matrix synthesis of promising new therapies or treatments for disc degeneration. Consequently, harmony and standardisation are currently a hot topic across the research field to advance reproducibility and accelerate clinical translation.²³⁴ The overall aim of this work was to characterise the local nutrient microenvironment of 2D cell monolayers and commonly used 3D *in vitro* culture systems, elucidating discrepancies in nutrition between these systems and to ascertain their physiological relevance.

Looking first at 2D cell culture, the majority of NP cell culture work report 6-well plates, followed by T-25 flasks. This appears to be more typical in studies working with species such as rat and human,^{96,254–256} possibly due to limited tissue availability and lower cell yields, while groups working with bovine and porcine cells were more likely to report larger T-75 and T-175 flasks.⁹⁸ Favourably, this work predicted that the choice of culture vessels does not have a significant effect on the metabolite concentrations during monolayer culture. The greatest effect is the total cell number within the culture vessel, providing a microenvironment which changes with time due to proliferation kinetics. As the cells multiply, the rate at which glucose reduces and lactate accumulates increase. Despite this, standard media volumes together with twice weekly media exchanges are predicted to be sufficient, with glucose exhaustion and lactate acid build-up of no significant concern, even at high levels of confluency. However, the drop in glucose and increase in pH between media exchanges will be dependent on how metabolically active the cells are and their specific glycolytic rates. This is highlighted in the case of oxygen, by comparing the “lower” animal and healthy human rates to the “higher” degenerated human rates of OCR available from the literature. While there is no major difference in the oxygen at the cell surface over time for cells with a lower OCR rate, the local cellular oxygen concentration does change over time for cells with higher rates of respiration and may need to be considered in highly oxygen dependent studies.

Oxygen is a key parameter in cell culture, as its diffusion and delivery to cells *in vitro* is very different to haemoglobin transportation *in vivo*.^{180,181,233,236,257} The level experienced by the cells reflects a balance of oxygen diffusion through the media from the surrounding incubator oxygen and OCR together with the total number of cells. While this reduction in oxygen may not be significant at NX levels, the oxygen gradient may still need to be considered if culturing particularly active cells under PX and HX conditions. Diffusion through the tissue culture plastic and flask filters was neglected, with only the media geometry modelled. This assumption was justified by diffusivity through typical culture plastic being ~ 4 orders of magnitude slower than media, while diffusion through the air in the filter is so rapid that a boundary condition at the media surface is sufficient.²⁵⁸

Several studies across a number of different research areas have attempted to measure oxygen concentrations within monolayer cultures.^{259–264} A study using cardiac rat cells under NX conditions measured oxygen concentrations as low as ~ 14.9 %O₂ at the confluent cell surface using an oxygen glass microsensor.²⁶⁴ Another study investigating neutrophils under 4 %O₂ external oxygen measured concentrations of < 1 %O₂ at the cell surface using an OxoProbe.²⁶³ Furthermore, temporal experimental measurements support the transient results in this work, with a study investigating dermal fibroblasts reporting concentrations of ~ 13.7 %O₂ at 10,000 cells/cm² and ~ 10.4 %O₂ at a density of 90,000 cells/cm².²⁵⁹ Although these cell types may be conditioned to very different microenvironmental niches and as a result have distinctly different metabolic rates compared to disc cells, they highlight that if not predicted or measured, the local cellular oxygen concentration may deviate substantially from the external oxygen boundary condition of the gas phase.²⁶¹

When moving towards 3D cell culture systems, the majority of disc research groups performing alginate bead culture use a 30 µL bead.^{223,265–270} Although the current work did not predict large oxygen gradients within the beads themselves, the minimum concentrations were heavily dependent on cell number and external concentrations. Furthermore, external oxygen concentrations of NX, PX and HX are used among these studies, thus making the local oxygen concentration a confounding factor, and not allowing for a true comparison of results between studies. Comparing different seeding densities demonstrates that cell numbers must be considered very carefully and that it is challenging to compare between samples with varying cell densities without considering that the local microenvironments will be different. When culturing a single bead in a well, a surplus of glucose was predicted to remain between feeds, thus questioning the use of supraphysiological HG media, something which has already been experimentally examined at the larger scale of *ex vivo* disc organ culture.²⁴¹ In addition, research groups have reported culturing multiple beads in a single well.^{269,271,272} In this scenario, it was predicted that more frequent media exchanges may be necessary to replenish glucose (particularly in the case of 10 beads in LG) and to circumvent the detrimental accumulation of lactate and subsequent drop in pH. The effect of refreshing the media daily is presented for alginate beads (Figure 5.8) and cylindrical hydrogel cultures (Figure 5.11) and demonstrate that more frequent media exchange may be necessary depending on sample number/size in order to maintain a relatively constant level of glucose and pH throughout the culture period.

The second most popular 3D culture system are cylindrical hydrogel constructs, with the majority of studies using bovine,^{273,274} porcine,^{98,133,219,275} and goat cells.²⁷⁶ As a result, only the “lower” animal metabolic rates were modelled. In terms of the geometry, construct diameters are typically 4 or 5 mm, while the thickness appears to range from 1.5 – 3 mm.^{133,273,274,276,277} The results showed that reducing the construct thickness from 3 mm to 1.5 mm only slightly alleviates the nutrient demands, while cell seeding density and external boundary conditions remain the

driving forces for determining the local microenvironment. Although the current work focused on comparing the thicknesses typically used in the disc field, a previous cartilage study has shown greater effects of construct size on the oxygen gradient when investigating constructs up to a diameter of 8 mm and a thickness of 4.5 mm.²⁷⁸

Confidence in the *in-silico* construct models can be provided by looking towards a recent cartilage study which measured oxygen levels of 3.0 – 7.6 %O₂ (depending on cell type) in the centre of hydrogel constructs (diameter = 5 mm, thickness = 3 mm and 20 million cell/mL) cultured at external NX conditions.²⁷⁹ Furthermore, when comparing external boundary concentration, the authors measured central concentrations of ~ 4.3 %O₂ at NX and ~ 1.1 %O₂ at PX. Although the above study used different cell types (stem cells and chondrocytes) with inherently different metabolic rates and a hydrogel susceptible to greater oxygen diffusion (2% agarose), the measurements are within good agreement with predicted concentrations for 20 million cells/mL under both NX and PX conditions. Nonetheless, these experimental measurements together with the predicted results, elucidate oxygen as the critical nutrient with respect to gradients through the constructs. Thus, *in vitro* cell culture results must be considered in the context of the local microenvironmental niche rather than the external oxygen concentration. Alternatively, the external boundary oxygen concentration could be manipulated based on the parameters of the specific system to establish the desired physiologically relevant concentrations locally. For example, culturing high cell densities at HX or even PX levels of oxygen were predicted to yield a markedly lower oxygen concentration compared to the average *in vivo* human microenvironment which is believed to be closer to ~ 6 %O₂.^{10,280} The results of this study suggest that high cell density constructs may be best suited to culturing at external NX conditions, while lower or more native cell densities require “PX” incubator levels in the disc field to be raised from ~ 5 %O₂ to ~ 10 %O₂ to create more physiologically relevant oxygen niches, in an attempt to reduce the heterogeneity across studies in terms of the oxygen environment.

Like the alginate bead, the cylindrical hydrogels also bring into question the physiological relevance of culturing in HG, particularly when assessing the suitability or effectiveness of cells as a therapy for IVD regeneration. Not only is the glucose supraphysiological for both low and high cell densities, but the models predict greater acidity in the HG constructs (particularly the 20 million cells/mL constructs). Despite explicitly implementing a significant reduction in LPR, based on experimental measurements as pH reduces below 6.7,⁹ it does not appear to be sufficient to offset the lactate accumulation. From these predictions, it is speculated that construct cultures with plentiful nutrient availability (NX and HG) may still develop necrotic cores due to substantial lactic acid build-up and that this may help explain histological results from a study by Buckley *et al.* (2010).²⁸¹ The authors saw reduced collagen type II staining within the core of a chondrocyte

seeded construct (15 million cell/mL) despite superior accumulation through the annulus at NX compared to throughout the whole construct at PX conditions.

Lastly, when investigating cell pellet culture and smaller micro-aggregate systems, it is evident that the conventional pellet configuration of ~ 250,000 cells is not a good representative of the IVD nutrient microenvironment. The model of pellet culture was derived from the cartilage field with high cell numbers, low oxygen conditions and supraphysiological levels of glucose. Although the disc field appears to gravitate towards NX conditions, the current work highlights that despite the high external boundary concentration, the local cellular oxygen is still predicted to reach HX conditions which are not comparable to *in vivo* disc oxygen measurements.^{10,280} HG media appears to provide a surplus of glucose even within the cell aggregate, suggesting that glucose is not the critical nutrient for viability within these configurations. However, the modelling predicts a high build-up of lactic acid within the pellets within three days of culture. Therefore, it is speculated that HX and acidity could be the trigger for necrotic cores and poor viability despite adequate glucose levels.

This work highlights that smaller microaggregates provide a 3D culture microenvironment which is far more tuneable, by selecting appropriate boundary concentrations and eliminating any effect of metabolite gradients. This has been readily contemplated in recent years, with the cartilage field moving towards micro-spheroids or organoids as building blocks rather than large cartilaginous pellets associated with the restricted delivery of nutrients and the removal of waste metabolites.^{282,283} Additionally, in the context of disc research, microaggregates are particularly convenient due to the relatively low cell yield of disc tissue and the limited matrix-synthesis capacity of culture expanded NP cells.^{174,207,254} Recent studies have used disc cells in the range of 1,000 – 35,000 cells per aggregate.^{284–286} Also a previous *in-silico* model,²⁸⁴ together with the current work, suggests that NP aggregates at both ends of this range create homogeneous nutrient microenvironments, circumventing limitations such as intrinsic heterogeneity in cell phenotype and matrix synthesis due to diffusional gradients within larger pellets.

It is recommended to use a hydrogel or ECM scaffold structure where cells are in a physiologically relevant 3D microenvironment using a seeding density close to native tissue i.e. the lower range of 1- 3 million cells/mL. The rationale for this is that native NP tissue is sparsely populated with cells accounting for less than 1% of the disc volume. Furthermore, based on this study it is recommended to use more physiologically relevant LG media for such 3D disc culture within a physioxenic incubator with an external oxygen of 5 %O₂. Although this is contrary to previous findings which measured glucose concentration in “spent” HG media revealing significant drops in glucose from ~ 25 mM to ~ 5 mM within three days,²⁸⁷ it is important to note that these constructs had half the media volume of those modelled in this study and contained bone marrow derived stem cells (20 million cells/mL) stimulated by TGF-β3 compared to growth factor free NP cells. Furthermore, Farrell *et al.* (2015) reported “spent” LG media dropped to ~ 1

mM in the absence of TGF- β 3 which is comparable to the concentrations predicted for a thicker construct containing 20 million cells/mL. This addresses the need to further elucidate differences in the metabolic profile and rates of IVD cells under additional factors such as anabolic stimulation, the presence of inflammatory cytokines or co-culture with stem cell populations. Further experimental insight would be necessary to predict these scenarios *in-silico* in addition to direct measurements for full characterisation. Nonetheless, with a drive for harmonisation and a recent study seeking to standardise the isolation and expansion of NP cells,²³⁴ the field can work towards full characterisation of consistent species-specific NP metabolic rates. Lower and more physiologically relevant glucose concentrations can be implemented in disc research by ensuring an adequate media volume and incorporating more frequent media exchanges, particularly for higher cell density cultures, to circumvent the glucose dropping below critical levels and curbing the build-up of acidity.

This study is an idealised representation of culture microenvironments and thus is not definitive or without limitations. For example, proliferation kinetics were not considered within the 3D models. The rationale for this is that the local microenvironment itself will influence the rate of proliferation and the transient analysis was only performed up until the first media exchange (approx. three days). Traditional pellet cultures under both NX and PX (5 % O₂) have shown reduced DNA content from day 1 – 14, while microaggregates under both conditions have exhibited a reduction from day 14 – 28 making it challenging to quantify cell proliferation within this system.^{288,289} Furthermore, a species-specific proliferation rate of cell aggregates may need to be considered.²⁹⁰ In terms of the hydrogel constructs, constant diffusion coefficients were assumed for each solute. However, substantially increasing the seeding density has been speculated to act as a form of diffusion barrier and any reduction in diffusion was not taken into account in the 20 million cell/mL models.²³⁸

Although this work sought to capture the range of metabolic experiments on disc cells available in the literature, the rates used in the models are not without caveats. There was an assumption that rates were not influenced by culture time or biomaterial type. Jaworski *et al.* (2019) investigated the changes in metabolism during prolonged culture (up to 21 days) and reported differences in GCR between day 1 and day 5 at both NX and PX, with GCR significantly reducing over 21 days at NX.⁹⁴ Additionally, stem cells used in the cartilage field have shown significantly reduced OCR after just 24 hours in a pellet culture configuration and indicating a shift towards predominant glycolysis with long-term culture. The majority of metabolism experiments on animal cells embedded freshly isolated cells in a hydrogel to maintain their 3D phenotype, justifying their use in the 3D bead and construct models.^{9,90,91,94} However, it is likely that there are intrinsic differences in metabolic rates between 2D and 3D cell configurations which have not been taken into account in this work due to a limited availability of appropriate literature. Despite this, it is believed that by capturing a “low” and “high” OCR rate this work has accounted

for any large deviation which may be present between configurations, particularly with oxygen being the more limiting nutrient within 2D systems. Furthermore, rates for human cells are unfortunately limited to just one study where healthy and degenerated cells underwent identical monolayer expansion (HG + NX) for more than three weeks before measurement within a cell suspension.⁹³ Cisewski *et al.* (2018) reported that degenerated cells had a significantly higher OCR (three to five times greater) and a unique glucose response compared to healthy human cells, suggesting a distinct pathological phenotype. An alternative study looking at the bioenergetic effect of *in vitro* induced senescence, found senescent cells exhibited increased mitochondrial ATP-linked respiration and taken together, results suggest a metabolic alteration is necessary to meet the degenerative energy demand for the production and secretion of inflammatory and catabolic factors.²¹³

The large range in rates of disc cells reported may reflect differences in isolation procedures, expansion, measurement configuration and the difficulty of obtaining reproducible interlaboratory measurements.^{234,260} This large variability between studies, in addition to limited availability of literature resulted in averaged or idealised glycolytic rates (GCR + LPR) being used within the *in-silico* models based on the external boundary conditions, rather than modelling each specific cell type. However, it has been reported that notochordal IVD cells are more metabolically active and more sensitive to nutrient deprivation.⁹¹ In some studies, high oxygen has been observed to reduce the rate of glycolysis which is known as a positive Pasteur effect.^{28,58} However, a number of other studies have shown a negative Pasteur or no effect for NP cells.^{9,95} Despite IVD cells preferring a more prevalent glycolytic pathway for energy in its harsh microenvironmental conditions, the reasons for differences in observed phenomenon under varying nutrient concentrations remain unclear. When explicitly modelling the averaged glycolytic rates (Table 5.1), it is apparent that a positive Pasteur is not captured throughout the compiled literature, with PX conditions appearing to have the lowest rates and thus predict the highest concentrations of glucose and pH within the 3D models. To address these potential limitations, a sensitivity analysis was performed using the lowest and highest metabolic rates (Figure 5.3).

Taken together, this work highlights the importance of considering the metabolic demands of the specific cell type being utilised (animal vs. human, notochordal vs. chondrocyte-like, healthy vs. degenerated) in conjunction with their specific culture configuration (2D, 3D). Depending on the choice of culture vessel, geometry, external concentrations, and cell seeding density, different and distinct local nutrient microenvironments will be created. Furthermore, these resulting nutrient concentration gradients have been shown to be important in regulating cell viability, gene expression and matrix synthesis. Understanding the local cellular nutrient concentrations of *in vitro* culture regimes may help advance the disc field towards designing and developing more homogeneous and physiologically relevant systems.

5.5 Conclusion

Primarily, the work in this chapter seek to illustrate the effect that parameters such as external boundary conditions and cell seeding densities have on the local nutrient microenvironment. It highlights that large variation and gradients in metabolite concentrations are easily established without careful consideration of these key parameters and that this diversity currently exists across the disc research field. As a result, this work calls for greater attention to the specific local microenvironment when trying to understand heterogeneity in results between studies. While one external concentration may be suitable for one culture configuration, they may not be appropriate for another. External conditions need to be tailored to the specific cells and culture system to establish homogeneous and physiologically relevant microenvironments. With more deliberate consideration of the external boundary concentrations and *in vitro* culture design, harmony and standardisation of a physiologically relevant microenvironment will push towards greater reproducibility and more successful translation of findings across the field.

Chapter 6. Investigating the Physiological Relevance of *Ex Vivo* Disc Organ Culture Nutrient Microenvironments using *In-Silico* Modelling and Experimental Validation

A significant amount of this Chapter has been published previously in **McDonnell, E. E.** and Buckley, C. T. (2021) ‘Investigating the physiological relevance of ex vivo disc organ culture nutrient microenvironments using in-silico modeling and experimental validation’, *JOR Spine*, 4(2), doi: <https://doi.org/10.1002/jsp2.1141>

Contribution: Substantial contribution to study design, data acquisition and computational modelling, data analysis and presentation, interpretation of data, drafting of the article, revising it critically and final approval.

6.1 Introduction

While *in-silico* modelling has been used extensively to investigate nutrient transport in the human IVD,^{64,104–111} a similar approach has never been applied to *ex vivo* disc organ culture systems. Chapter 5 showed that an *in vivo* disc nutrient microenvironment can be implemented simply *in vitro* through 3D construct geometry, cell seeding density and external nutrient conditions. However, ensuring a nutrient-deprived ECM in whole disc culture may require more consideration and sophistication. The popularity of *ex vivo* disc organ culture has grown over the past decade (Figure 6.1(A)) with the focus being either the development of bioreactor systems^{154,157,158,291–295} or their utilisation to investigate degeneration processes^{122–130} or regeneration strategies.^{131,132,141,133–140} A number of recent *ex vivo* disc organ studies have combined mechanical loading with low glucose culture medium to induce a catabolic niche and pro-inflammatory cell response.^{132,135,148,291} Another used short-term glucose deprivation before refreshing the medium with a higher concentration of glucose.¹⁵⁰ Pfannkuche *et al.* (2019) stated that the major challenge in the setup of organ culture is the maintenance of the anatomical integrity of the disc through retaining the CEP and adjacent vertebral bone, while still allowing adequate nutrition.²⁹⁶ This is important as several studies suggest that the central region of the CEP is the predominant pathway for nutrient diffusion into the NP and inner AF, while more minor molecules are supplied via the AF.^{41,58,59} However, the nutrient and metabolite concentrations within *ex vivo* models have never been measured and the assessment of adequate nutrition has typically been based on cell viability.

In terms of standardising *ex vivo* disc organ culture, it has been acknowledged that it is necessary to optimise parameters such as the loading force and frequency needed to model a physiological or degenerative impact on discs of different scales from different species.²⁹⁷ Bovine caudal discs have become a widely accepted model for *ex vivo* disc organ culture as reflected by

their popularity in published works (Figure 6.1(B)). However, it may also be necessary to refine the culturing medium based on disc parameters such as species and disc size. For example, 70% of published *ex vivo* discs are cultured in HG medium (4.5 g/L or 25 mM) (Figure 6.1(C)), yet these discs range in scale from mouse to human lumbar IVDs and have significantly different disc heights and lateral widths.¹⁵⁹ As a result, the diffusional distance to the central NP cells would be significantly different between these models, and the local glucose concentration has never been measured in order to establish whether culturing in HG medium creates a physiologically relevant nutrient microenvironment. Less diversity is seen in the oxygen culturing conditions (Figure 6.1(D)), with the majority of research groups culturing in normoxia. However, a few studies have cultured in hypoxic or physioxic conditions.^{134,141} Like glucose, the resulting oxygen level in the disc centre has never been quantifiably measured. Therefore, it is unknown whether these systems truly represent a physiologically relevant niche to test potential regenerative therapies based on nutritional demands.

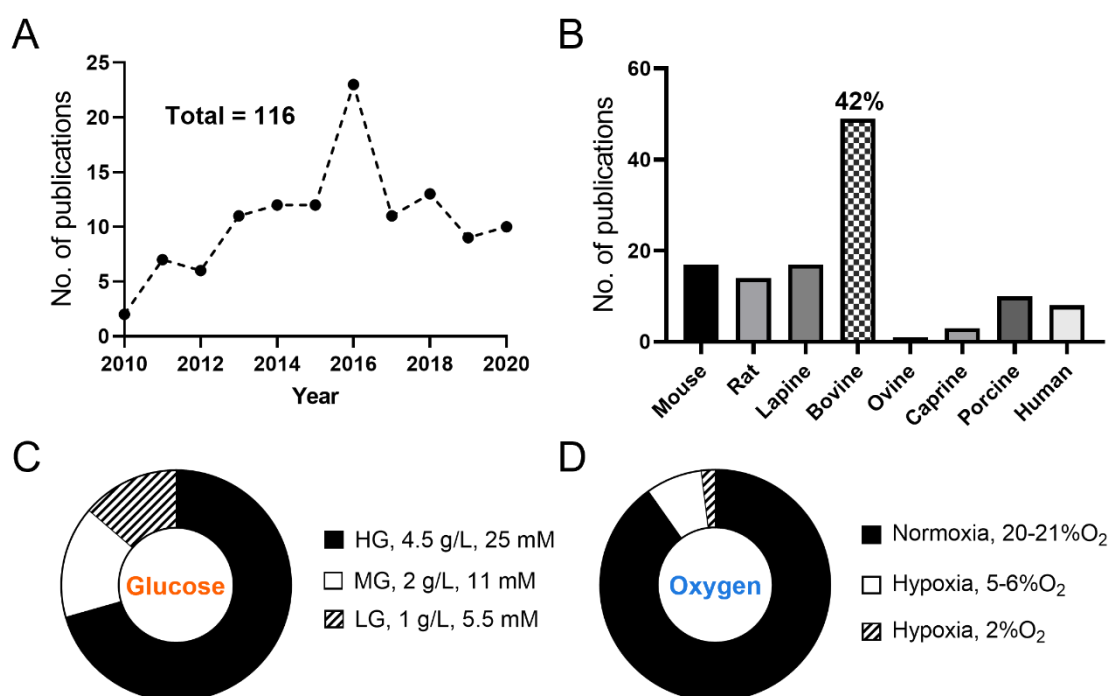


Figure 6.1 Capturing the popularity of bovine *ex vivo* disc organ culture systems and their typical external nutrient conditions. (A) *Ex vivo* culture models have become an important platform in the disc research field with 116 papers published over the last decade. (B) Despite a variety of species being used, almost half of the publications used bovine caudal discs. (C) 70% of *ex vivo* discs are cultured in high glucose (HG), while 16% are cultured in medium glucose (MG) and 14% are cultured in low glucose (LG) medium. (D) 90% of *ex vivo* discs are cultured under normoxic conditions (20-21 %O₂).

This chapter aims to characterise the nutrient microenvironment of the most common *ex vivo* disc organ culture, bovine caudal discs cultured in HG medium and normoxia. *In-silico* models of cultured discs were created using COMSOL Multiphysics®. These models were governed by

coupled reaction-diffusion equations, considering geometrical differences between caudal level and a metabolically active cell density. Metabolic rates were dependent on local oxygen and pH levels by employing equations derived previously.^{9,116} Experimental verification of these models was performed by measuring the metabolite concentrations of oxygen, glucose and pH in discs cultured for seven days.

6.2 Materials & Methods

6.2.1 Geometrical characterisation of disc caudal level

Caudal discs were excised from six skeletally mature bovine tails (30 – 48 months). All bovine animal tissue used in this study was obtained from a local abattoir and did not require ethical approval. The discs were removed from the vertebral bone using the Mitre saw to cut proximally and distally to the EP retaining as little of the bony component as possible (Figure 6.2(A)). The discs were halved through the sagittal plane using a custom-made guillotine. Dimensions of the key diffusional distances (disc diameter, central NP thickness and overall disc height including bony EP) were measured for each caudal level (presented in Figure 6.4 (B)).

6.2.2 Disc isolation and organ culture setup

For organ culture, bovine tissue was obtained from a local abattoir within four hours of sacrifice. Discs were isolated as described above, under sterile conditions. Blood clots and bone debris were removed from the EP by flushing with PBS containing 100 U/mL penicillin, 100 µg/mL streptomycin and 0.25 µg/mL amphotericin B (all Sigma-Aldrich,). Discs were placed into experimental groups based on their caudal level. The largest discs, Cd1-2 to Cd3-4, were placed into Group 1, Cd4-5 and Cd5-6 into Group 2 and the smallest discs, Cd6-7 and Cd7-8 into Group 3. To account for donor variance, each group consisted of three caudal discs from three different tails. Discs were cultured in 80 mL of HG-DMEM (4.5 g/L or 25 mM, Thermo Fisher Scientific) supplemented with 10% FBS, 100 U/mL penicillin, 100 µg/mL streptomycin, 0.25 µg/mL amphotericin B, 1.5 g/mL bovine serum albumin (BSA) and 40 µg/mL L-proline (all Sigma-Aldrich) and 0.1 mg/mL Primocin (InvivoGen). Media was adjusted to ~ 400 mOSm using 150 mM sucrose (S0389, Sigma-Aldrich). The constraining effect on *ex vivo* disc organ culture systems has previously been described.¹⁴¹ As a result, a custom-made bioreactor containing a compression spring with a rate of 8.92 N/mm (751-641, Radionics) was used to achieve ~ 0.4 MPa static loading (Figure 6.2(C)). The individual bioreactors were placed on an orbital shaker under gentle agitation (25 r.p.m) in a NX incubator (37°C, ~ 20 %O₂ and ~ 5 %CO₂). The culture

period was seven days, with a complete media exchange performed halfway through the culture period.

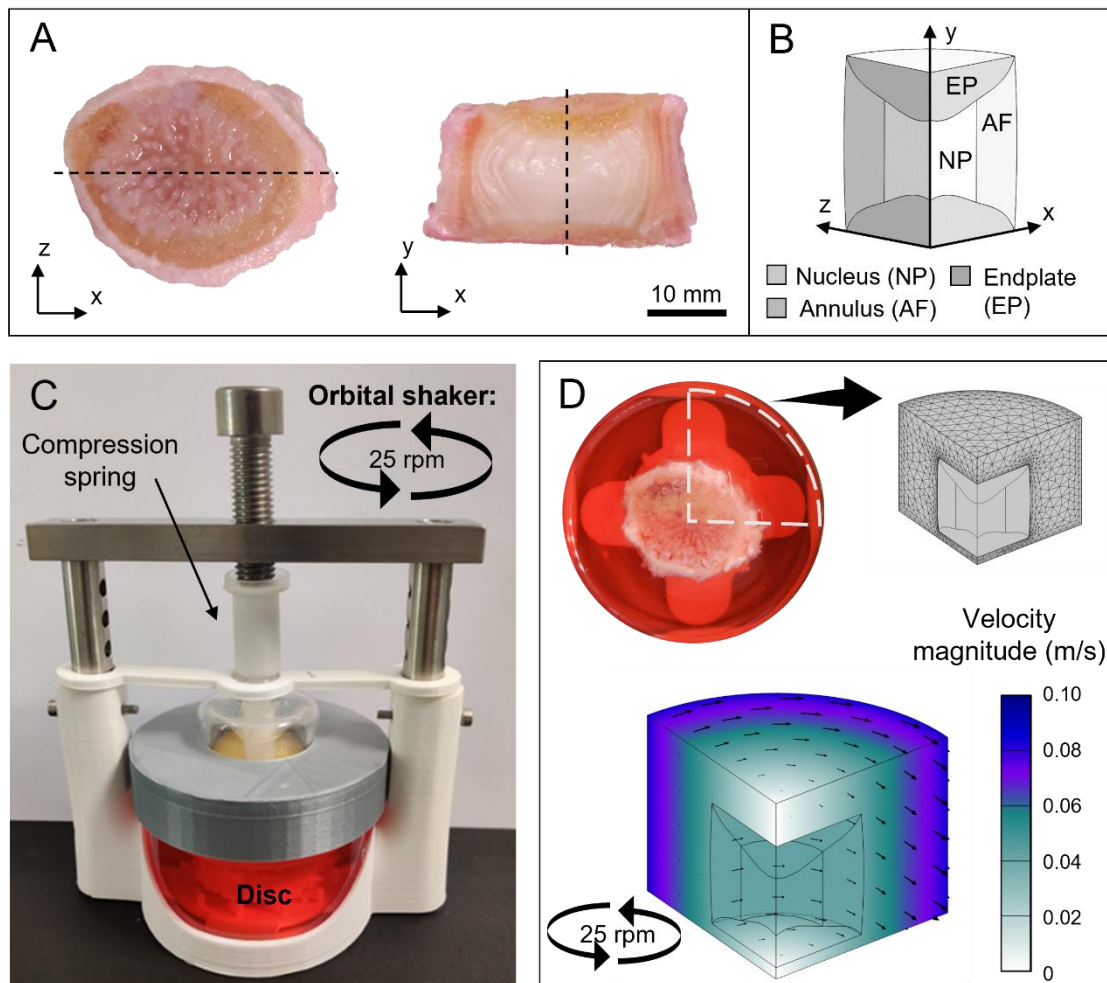


Figure 6.2 Establishing an *in-silico* and *ex vivo* disc organ culture model. (A) Geometry of a bovine caudal disc from Group 2 (Cd4-5). (B) Assuming perfect symmetry, a disc quadrant was used for the *in-silico* simulations. (C) A custom-made bioreactor containing a screw and a compression spring was developed which applies a physiologically relevant static load of ~ 0.4 MPa to the cultured disc. The bioreactor is placed on an orbital shaker at a speed of 25 r.p.m. (D) Each disc was cultured in 80 mL of media. The rotational flow in the media domain was modelled to mitigate any oxygen gradient and ensure mixing of glucose/lactate throughout the media.

6.2.3 Determining metabolically active cell density

A metabolically active cell density at day 0 and day 7 was determined using MTT deposition and DAPI counter staining. Freshly isolated and cultured discs were cut in half along the sagittal plane and an approximate 3 mm thick section was taken across the full diameter of the disc. The sections were incubated in MTT solution as described in Chapter 0. Briefly, tissue was washed, embedded in OCT compound, and stored at -80°C until sectioning on a cryotome. For cell density analysis, $10\ \mu\text{m}$ slices were cut and mounted using fluoroshield with DAPI. Slides

were examined under both brightfield, to capture active MTT+ cells, and fluorescence, to capture the total number of DAPI stained cell nuclei. More detail on the quantitative analysis can be found in Chapter 3. Images for the NP and AF regions at day 0 and day 7 can be found in Appendix D.

6.2.4 Experimental measurements of oxygen, pH and glucose

Following culture, the metabolite concentrations (oxygen, glucose and pH) were measured in the centre of each disc. The intradiscal oxygen and pH levels were measured using fibre-optical fluorescent microsensors (PreSens, Regensburg, Germany). To ensure confidence in the measurement techniques, both microsensors were calibrated and the accuracy of the glucose assay tested before use. The oxygen microprobe underwent a two-point calibration at 0% and 100% air saturation. These calibration points were created by saturating the medium with nitrogen gas and compressed air, respectively. The resolution of the oxygen sensor was $\pm 0.01\% \text{O}_2$ and $\pm 0.09\% \text{O}_2$ at $0.21\% \text{O}_2$ and $20.9\% \text{O}_2$, respectively. The pH sensor is pre-calibrated by the manufacturer from pH 4 to pH 8. The pH probe was also validated over a range of pH 6 to 8 and has a resolution of ± 0.001 pH. During measurements, the sensor probe was placed into pH 7 buffer before and between each disc measurement to ensure accurate and consistent measurement throughout. The discs were maintained in their culture medium at 37°C during the analysis, with the attached temperature sensor placed in the medium (Figure 6.3(A)). Discs were rotated onto their sides to enable the insertion of a needle, containing the microsensor tip, into the disc centre (Figure 6.3(B)). Oxygen measurements were taken until the concentration changed by $< 0.1\%$ between sampling times for a two-minute period. This was established as an acceptable equilibrium criterion while limiting the measuring time to less than ten minutes for each disc. Glucose was measured biochemically by taking 2 mm biopsies from the centre of the NP ($\sim 12.5 \text{ mm}^3$). To determine the water content/hydration, wet and dry tissue weights were recorded before and after lyophilisation.

$$\textit{Hydration} = \frac{\textit{wet weight} - \textit{dry weight}}{\textit{wet weight}} \quad (6-1)$$

Samples were papain digested and assessed using an enzymatic-colorimetric assay as specified in Section 3.6.1. Glucose concentration and pH level of the culture media were also determined.

6.2.5 *In-silico* model of nutrient concentration profiles

A 3D anatomical disc model was created for each of the three experimental groups based on the results of the geometrical characterisation (Figure 6.4(A-B)). Symmetry was assumed in the x- and y-plane (Figure 6.2(A)) to simplify the model to a quadrant of the full disc with three distinct tissue domains: NP, AF and EP (Figure 6.2(B)). In order to simulate the transport of metabolites between the culture media and the disc, a quadrant of the surrounding media was incorporated. An *in-silico* model, governed by reaction-diffusion equations and metabolic rates coupled to the local nutrient concentrations, was created using COMSOL Multiphysics as detailed in Chapter 3. The key input parameters such as the metabolically active cell density and metabolite diffusion coefficients for each tissue domain can be found in Table 6.1. Additionally, the media domain incorporated a pseudo-stationary rotational flow (Computational Fluid Dynamics Module) to capture the mixing from the orbital shaker (Figure 6.2(D)). The *in-silico* model was performed as a time dependent study to capture the full 7-day culture period and the full media exchange at the mid-point. However, models were first run as steady-state studies with *in vivo* boundary conditions to determine the initial nutrient concentrations within the caudal disc prior to culture. These boundary conditions were assumed to be bovine blood concentrations of glucose and lactate and an oxygen concentration of 9.5kPa measured in canine vertebral bodies close to the EP.^{58,298}

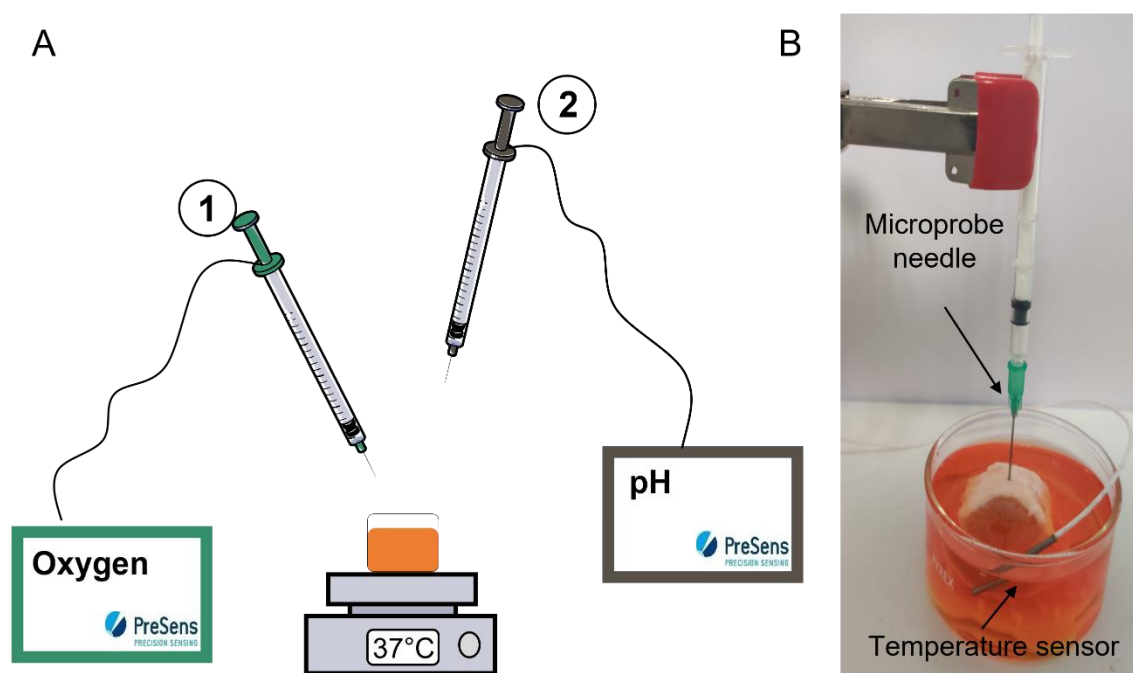


Figure 6.3 Schematic of the PreSens oxygen and pH probe measurement setup. (A) The discs were kept at 37°C in their culture dish and media during the analysis. The oxygen probe was used first to avoid the measurement being compromised by any air which might enter the disc after the needle is withdrawn. (B) The disc was turned onto its side so that the insertion point of the needle was above the surface of the media and the needle was inserted into the middle of the disc (half the disc diameter). Both the oxygen and the pH sensor have a coupled temperature sensor which was placed into the media during the analysis.

6.3 Results

6.3.1 Geometrical variation of bovine discs as a function of caudal level

Discs were categorised into groups based on their caudal level (Figure 6.4(A)). Significant differences were found between the disc diameters of all groups ($p = 0.0072$), with this dimension decreasing with increasing caudal level (Figure 6.4(B)). The overall disc height incorporated the thickness of the bony EP above and below the disc tissue. This distance was 27.5 ± 1.9 mm for Group 1, 21.1 ± 1.8 mm for Group 2 and 17.2 ± 0.8 mm for Group 3 ($n = 6$). Differences were also observed between the central NP thickness of each group (12.6 ± 0.5 mm for Group 1, 9.9 ± 0.5 mm for Group 2 and 8.3 ± 1.0 mm for Group 3 ($n = 6$)) (Figure 6.4(B)).

6.3.2 Metabolically active cell density of *ex vivo* disc organ cultures is an important input parameter for *in-silico* modelling

The metabolically active cell density of the NP and AF regions was determined using MTT with a DAPI counterstain (Figure 6.4((C), (D))). The total cell density (DAPI) and metabolically active cell density (MTT+) in the NP showed no significant differences across the control and experimental groups ($n = 3$). The NP control (day 0) had a metabolically active cell population of approximately 93%, while this value ranged from 78 – 81% across the groups at day 7 (Figure 6.4(E)) shows the total and MTT+ cell densities, calculated positive percentage is not presented). However, as no statistical significance was determined compared to the native control ($p = 0.2738$ for Group 1, $p = 0.1292$ for Group 2 and $p = 0.1522$ for Group 3), a change in the total number of metabolically active cells in the NP domain was not considered in the *in-silico* model. The AF control (day 0) had a lower metabolically active cell population of approximately 86%, which appeared to reduce dramatically across the groups by day 7 (Figure 6.4(F)), with a significant difference determined between the total and active cell density in Group 2 ($p = 0.0483$). The metabolically active cell density of the AF appeared to decline to a baseline comparable with the active cell density of the NP. As a result, the metabolically active cell density in the AF domain of the *in-silico* model was not assumed to be constant and changed in line with the experimental results (Table 6.1). In addition, no significant difference in total or active cell density was found between the experimental groups based on caudal level. A sensitivity analysis was performed to assess AF viability as a key parameter. The results in Figure 6.5 showed that for a 70% reduction in metabolically active cells, the central oxygen concentration increased by $\sim 1\% \text{O}_2$, while the central glucose concentration only increased by ~ 2 mM. However, a higher metabolically active cell population predicted a notably more acidic pH in the disc centre.

Table 6.1 Input parameters and boundary conditions used in the in-silico models for nucleus pulposus (NP), annulus fibrosus (AF), endplates (EP) and media.

		NP	AF	EP	Media
Active cell density (cells/mm ³)	<i>Day 0</i>	5,500 ^a	17,000 ^a	-	-
	<i>Day 7</i>	5,500 ^a	4,200 ^a	-	-
Michaelis-Menten constants	<i>Vmax</i>			-	-
	(<i>nmol/million cells/hr</i>)	5 ^b	6 ^c		
	<i>Km</i> (μ M)	40 ^c	40 ^c	-	-
Effective diffusion coefficient (mm ² /hr)	<i>D_{glucose}</i>	1.35 ^d	0.9 ^d	0.76 ^e	2.22 ^f
	<i>D_{oxygen}</i>	5 ^d	3.78 ^d	2.18 ^e	9.36 ^g
	<i>D_{lactate}</i>	2.28 ^e	1.45 ^e	1.13 ^e	4.32 ^h
Boundary (culturing) conditions	<i>Glucose</i> (mM)	-	-	-	20.9 ^a
	<i>Oxygen</i> (%O ₂)	-	-	-	18.6 ⁱ
	<i>Lactate</i> (mM)	-	-	-	1.6 ^a

^a Values determined experimentally in this work.

^b Experimentally determined for freshly isolated gel encapsulated bovine NP cells⁹.

^c Experimentally determined for freshly isolated gel encapsulated porcine AF cells⁹⁰.

^d Values used previously in the literature^{104,106,107}.

^e Values used previously in the literature¹¹⁰.

^f Experimentally measured glucose diffusion in culture medium²³⁹.

^g Experimentally calculated oxygen diffusion in culture medium²³⁸.

^h Experimentally calculated lactose diffusion in aqueous solution²⁴⁰.

ⁱ True oxygen concentration in a normoxic incubator at sea level²⁵⁷.

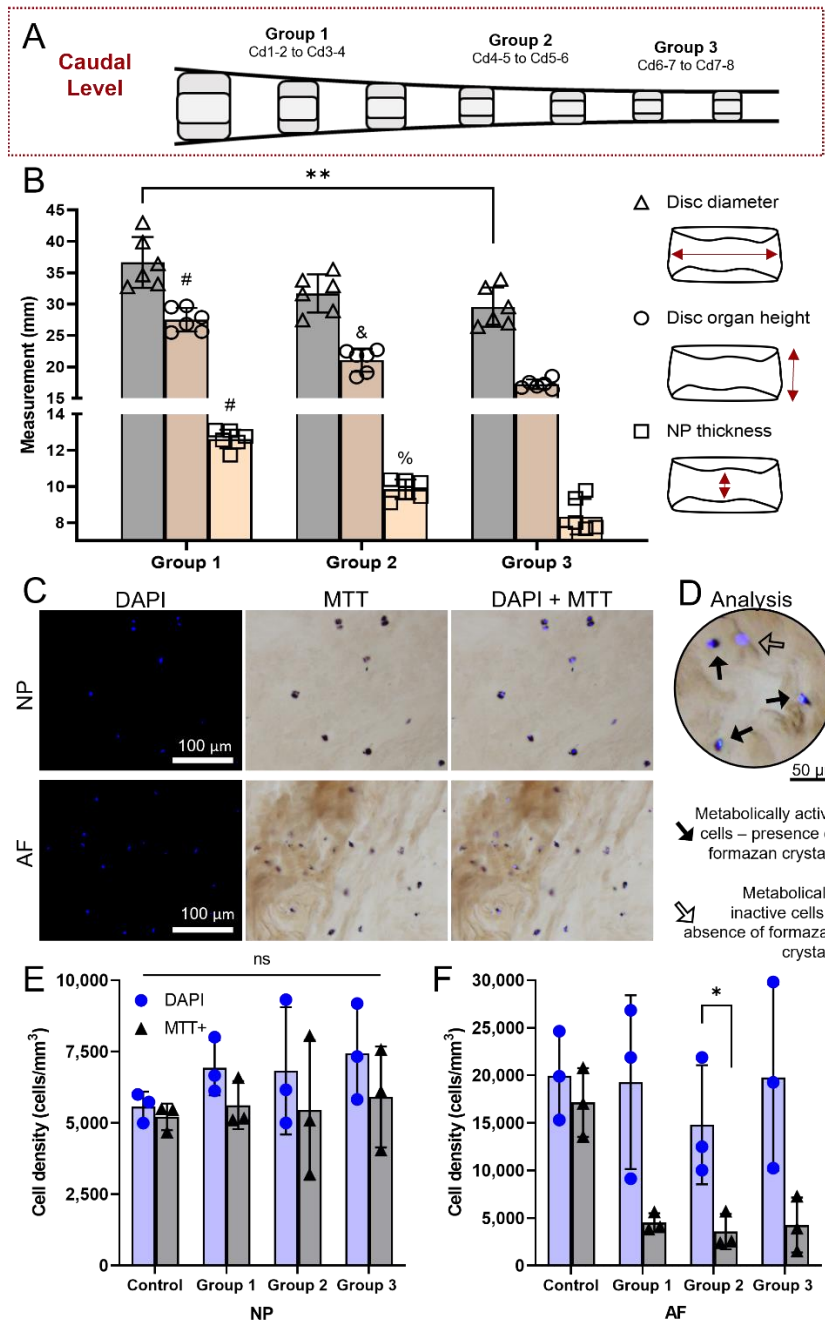


Figure 6.4 Experimental characterisation of key parameters needed to establish the *in-silico* disc organ culture model. (A) Discs were categorised into three experimental groups based on bovine caudal disc level. Group 1: Cd1-2 to Cd3-4, Group 2: Cd4-5 and Cd5-6, Group 3: Cd6-7 and Cd7-8. (B) Key dimensions relating to nutrient transport distances across the three groups (n = 6). ** (p = 0.0072). # (p < 0.0001) indicates significance as compared to the same parameter in both Group 2 and Group 3 and & (p = 0.0020) and % (p = 0.0058) indicates significance as compared to corresponding parameter in Group 3. (C) DAPI images identifying the fluorescing blue nuclei of all cells in the NP and AF regions. MTT brightfield images show deposited formazan crystals around metabolically active cells. (D) Merging of the fluorescence and bright field images enabled identification of metabolically active and inactive cells. (E) The total cell density (DAPI) and metabolically active cell density (MTT+) determined in the NP of native (control) and Groups 1-3 after seven days of culture (n = 3). No significance (ns) was found for NP regions. (F) The total cell density (DAPI) and metabolically active cell density (MTT+) determined in the AF of native (control) and Groups 1-3 after seven days of culture (n = 3). * (p = 0.0483).

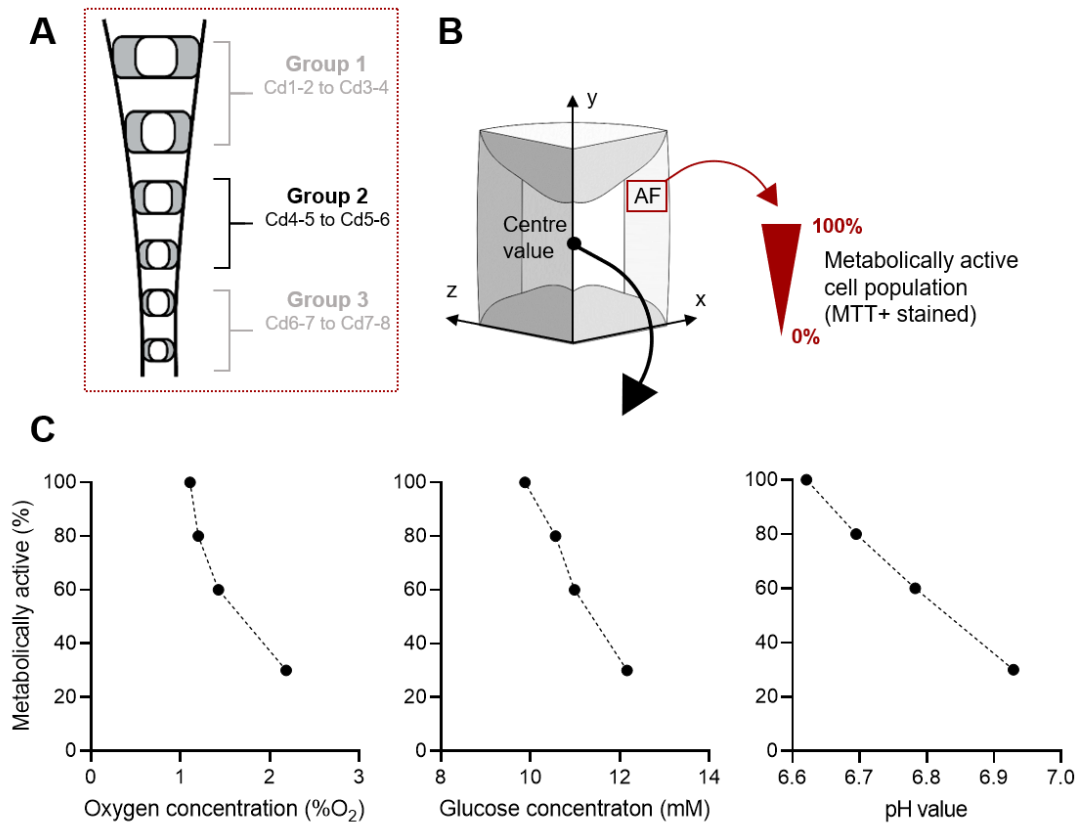


Figure 6.5 A sensitivity analysis was performed to assess the active cell density of annulus fibrosus (AF) as an influential parameter on the central metabolite concentrations. (A) The *in-silico* model for Group 2 (Cd4-5 and Cd5-6) was used to assess AF cell density as a key parameter (B) As the experimental results only revealed a reduction in the metabolically active cell density of the AF, a sensitivity analysis was performed for this domain only. (C) The central oxygen concentration increased by ~ 1 %O₂, while the central glucose concentration only increased by ~ 2 mM for a 70% reduction in metabolically active cells. However, a higher metabolically active cell population predicted a notably more acidic pH in the disc centre.

6.3.3 Predicted and experimentally determined metabolite concentrations in *ex vivo* bovine caudal discs

As expected, oxygen decreased with distance from the boundary of the EP and periphery of the AF (Figure 6.6(A), (B)). The steepest oxygen gradient was observed for the largest caudal disc (Group 1), which had the lowest oxygen concentration in the NP. The *in-silico* model predicted central oxygen concentrations were 1.4 %O₂ for Group 1, 2.5 %O₂ for Group 2 and 4.6 %O₂ for Group 3 (Figure 6.6(B)). The predicted central oxygen concentration for each group was compared with those determined experimentally within cultured caudal discs (Figure 6.6(C)). The experimentally measured values of oxygen were 2.6 ± 1.2 %O₂ for Group 1, 2.6 ± 0.3 %O₂ for Group 2 and 6.5 ± 4.6 %O₂ for Group 3 (n = 3), with no statistical difference between the groups. However, there was a trend of increasing oxygen concentration within discs of decreased disc volume (i.e. Group 3 compared to Group 1), and the predicted values lie within the standard

deviation of those determined experimentally. Overall, there was a 70% reduction from the oxygen level of the culture media to the centre of the *ex vivo* disc organ culture.

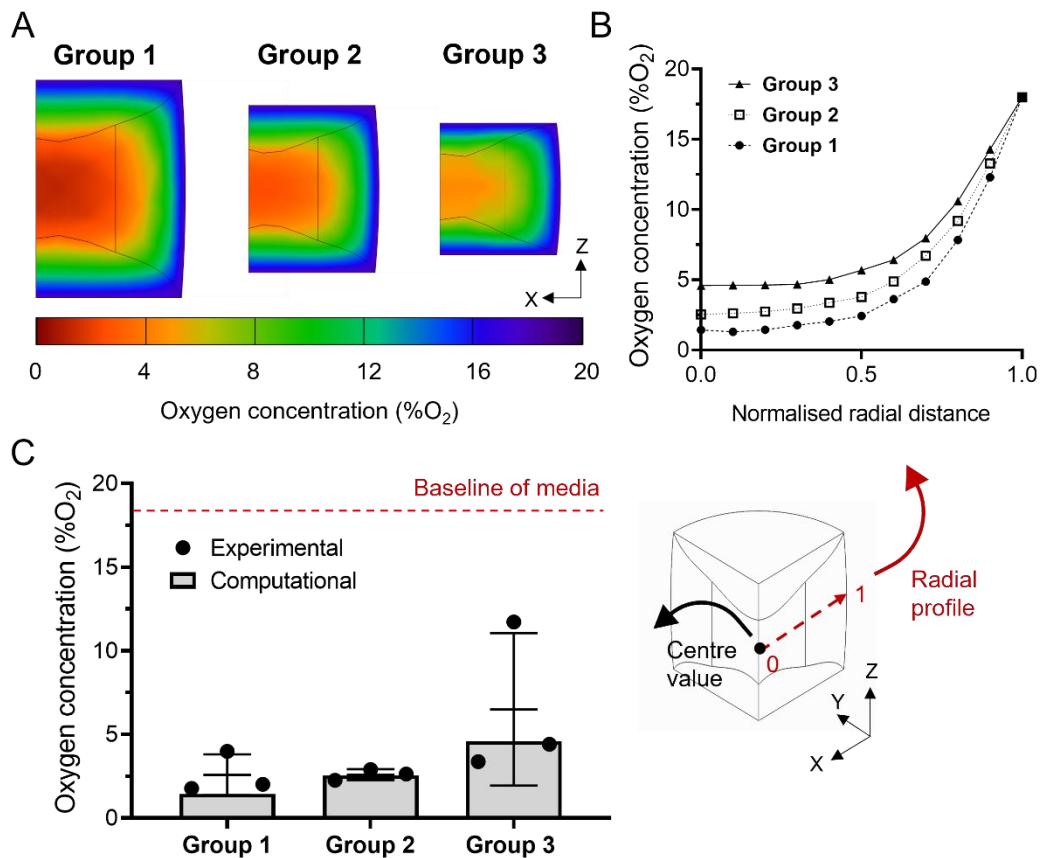


Figure 6.6 Predicted and experimentally determined oxygen concentrations in *ex vivo* bovine caudal discs. (A) Oxygen contour plots in the sagittal plane through the disc centre of each of the three groups. (B) Radial oxygen profile for the different groups. Starting in the disc centre (0.0) and ending at the disc periphery (1.0) (bottom right schematic). The radial distance was normalised by the disc diameter of each group. (C) Comparison of predicted *in-silico* model oxygen concentrations in the disc centre to experimentally measured values ($n = 3$). No statistical significance was found between the experimental groups.

The steepest gradient in glucose concentration was observed for Group 1, which had the lowest glucose concentration in the disc centre, while Group 3 had the highest concentration (Figure 6.7(A), (B)). Predicted central values of glucose were 9.8 mM, 12.6 mM and 15.5 mM for Groups 1, 2 and 3, respectively (Figure 6.7(B)). The experimentally measured values of glucose were 8.0 ± 3.1 mM for Group 1, 10.6 ± 4.5 mM for Group 2 and 12.0 ± 4.3 mM for Group 3 ($n = 3$) (Figure 6.7(C)) and compared favourably with the *in-silico* model predictions. No statistical significance was found between the groups. However, as was the case for oxygen, there was a strong trend of increasing glucose concentration within discs of decreased disc volume, with the initial culturing concentration of glucose reducing approximately 62% in the NP of discs from Group 1 and approximately 25% in the NP of discs from Group 3. The predicted values were found to lie within the standard deviation of those determined experimentally.

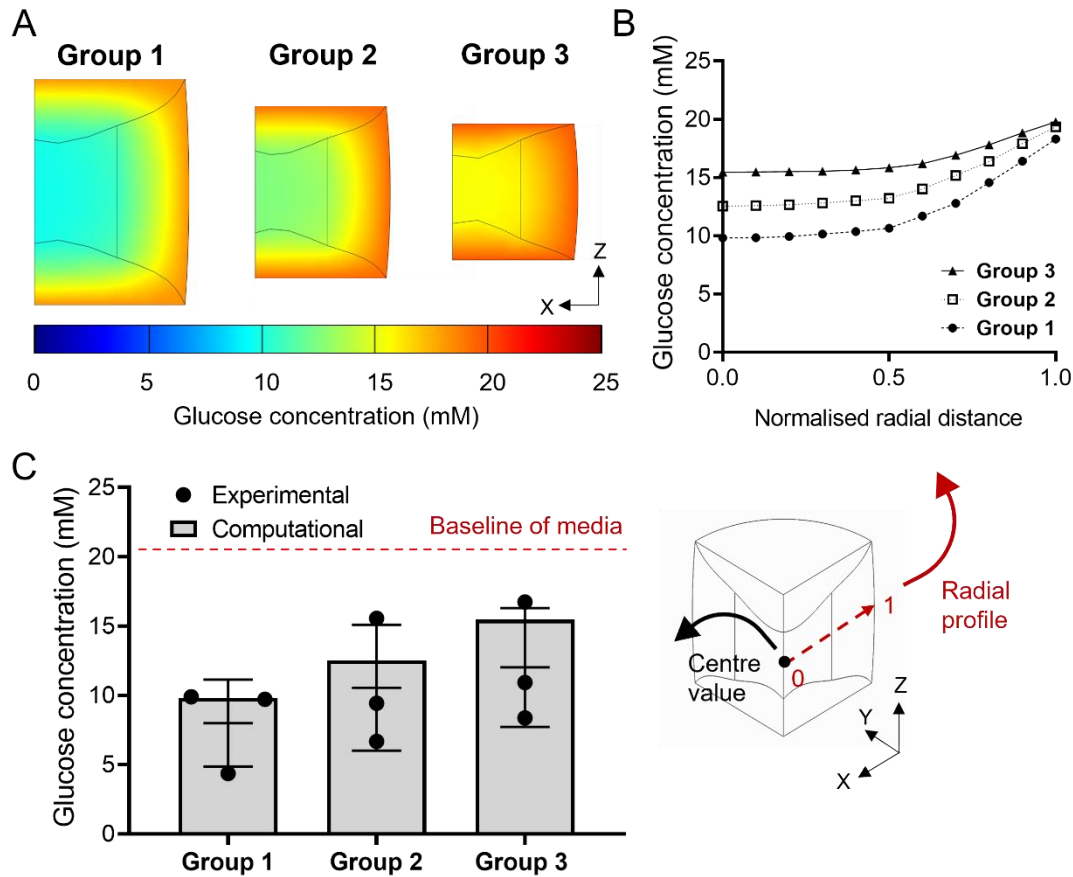


Figure 6.7 Predicted and experimentally determined glucose concentrations in *ex vivo* bovine caudal discs. (A) Glucose contour plots in the sagittal plane through the disc centre of each of the three groups. (B) Radial glucose profile for the different groups. Starting in the disc centre (0.0) and ending at the disc periphery (1.0) (bottom right schematic). The radial distance was normalised by the disc diameter of each group. (C) Comparison of predicted *in-silico* model glucose concentrations in the disc centre to experimentally measured values ($n = 3$). No statistical significance was found between the experimental groups.

In terms of pH, Group 1 had the highest build-up of acidity, while Group 3 exhibited the least acidic NP region with predicted central pH values of 6.75, 6.89 and 6.97 for Groups 1, 2 and 3, respectively (Figure 6.8(A), (B)). The experimentally measured values of pH were 6.72 ± 0.01 for Group 1, 6.83 ± 0.10 for Group 2 and 6.91 ± 0.03 for Group 3 ($n = 3$) (Figure 6.8(C)). A significant difference was found between the experimentally measured pH value in the centre of Group 1 and Group 3 ($p = 0.0221$). The predicted value for Group 2 lay within the standard deviation of the experimental results. Like the oxygen and glucose results, there was good agreement between the *in-silico* and experimental pH measurements.

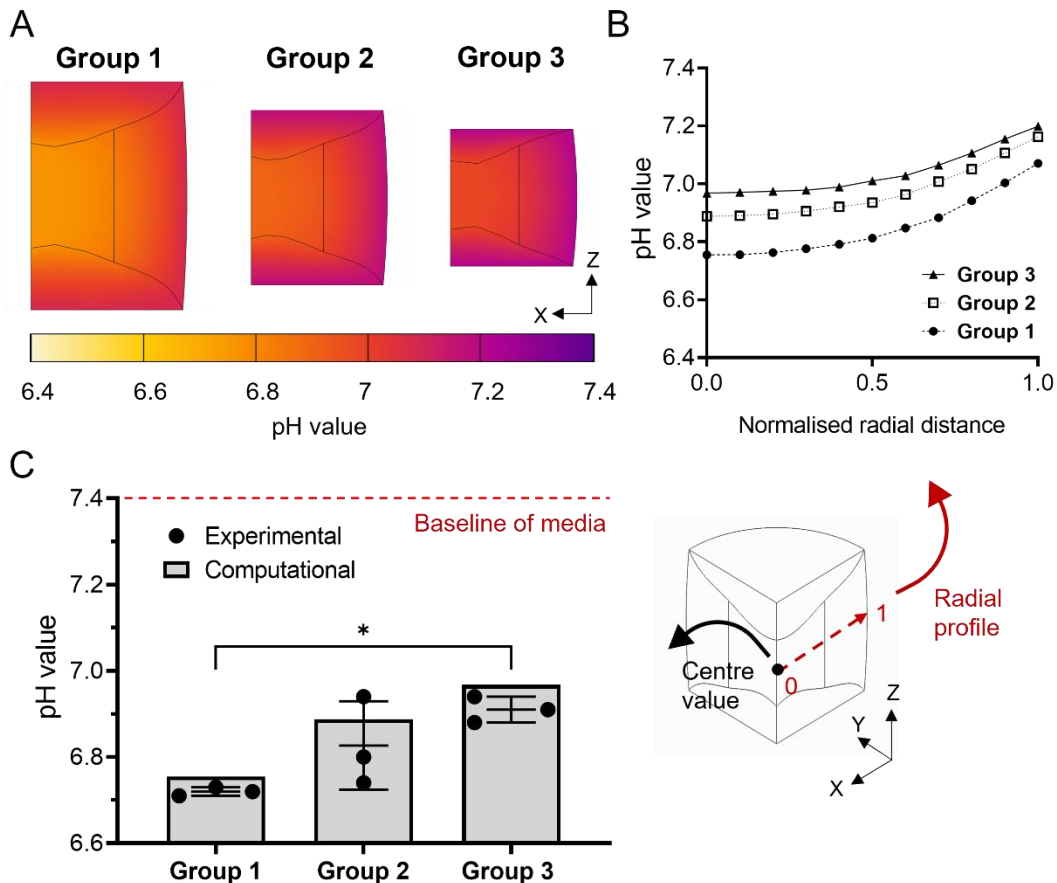


Figure 6.8 Predicted and experimentally determined pH in *ex vivo* bovine caudal discs. (A) pH contour plots in the sagittal plane through the disc centre of each of the three groups. **(B)** Radial pH profile for the different groups. Starting in the disc centre (0.0) and ending at the disc periphery (1.0) (bottom right schematic). The radial distance was normalised by the disc diameter of each group. **(C)** Comparison of predicted *in-silico* model pH values in the disc centre to experimentally measured values ($n = 3$). * ($p = 0.0221$) indicates significance between Group 1 and Group 3.

6.3.4 Additional validation of the *in-silico* model through media analysis

To further validate the *in-silico* model and strengthen the confidence in the predicted results, the glucose concentrations and pH levels in the culture media at day seven were also analysed (Figure 6.9). Experimentally determined glucose concentrations in the media (Group 1: 16.4 ± 1.4 mM, Group 2: 17.6 ± 1.2 mM and Group 3: 17.6 ± 1.1 mM, $n=3$) were found to compare favourably with the *in-silico* model predictions (Figure 6.9(A), (B)). Similarly, experimentally determined pH values of the media were 7.02 ± 0.06 , 7.13 ± 0.06 and 7.17 ± 0.05 for Group 1, Group 2 and Group 3, respectively ($n = 3$) (Figure 6.9(C), (D)). Overall, the results of the media analysis revealed very close agreement between the *in-silico* models and experimental measurements.

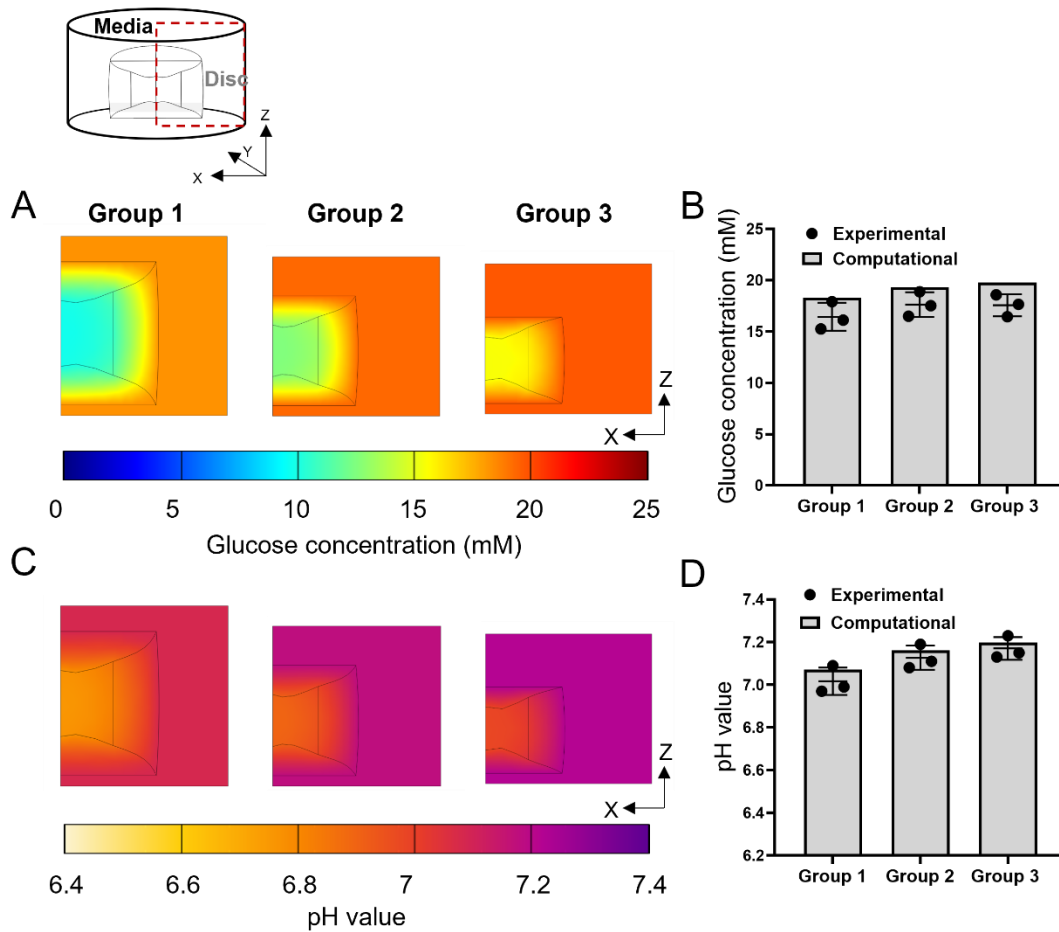


Figure 6.9 Predicted and experimentally determined glucose and pH levels in the culture media. (A) Glucose contour plots in the sagittal plane through the disc centre and the surrounding media of each of the three groups. (B) Comparison of predicted glucose concentration in the culture media compared to experimentally measured values at day 7 ($n = 3$). (C) pH contour plots in the sagittal plane through the disc centre and the surrounding media of each of the three groups. (D) Comparison of predicted pH values in the culture media compared to experimentally measured values at day 7 ($n = 3$).

6.4 Discussion

It has been well established that the harsh nutrient microenvironment of a degenerating IVD provides a significant barrier for the survival and regenerative potential of implanted cell treatments.^{9,11,83,96,98} However, despite the attractiveness of *ex vivo* disc organ culture for the testing and evaluation of potential cell- and biomaterial-based strategies,^{132–135,150} the nutrient microenvironment has never been quantitatively measured and, as a result, their clinical and physiological relevance to the human condition, based on nutrient demands, has not been established. Therefore, this study aimed to characterise the metabolite microenvironments within *ex vivo* disc organ culture using the first experimentally validated *in-silico* nutrient transport model.

While HG medium is most commonly used for culturing *ex vivo* disc organ models,^{127,130,302–306,132,138,149,151,270,299–301} the results of this study suggests that HG culturing creates supraphysiological levels in the disc centre (8 – 12 mM) when compared to predicted *in vivo* glucose concentrations of 0.2 – 1.9 mM under degenerative conditions.^{64,104–111} An important distinction between *in vivo* and *ex vivo* nutrition is the pathway of nutrient transport. While the EP transport route appears to be the more predominant supply route for the NP physiologically, in *ex vivo* culture the blood vessels surrounding the AF and penetrating the EP have been removed and instead the disc is fully submerged in nutrient-rich medium. Thus, it is speculated that more radial nutrient diffusion occurs than exists *in vivo*, contributing further to the supraphysiological levels of glucose measured. This study measured an average oxygen concentration ~ 2.5 %O₂ in larger discs and ~ 6 %O₂ in smaller discs. In terms of hypoxia, these values could be considered markedly different, particularly when low oxygen is essential for NP cells to maintain their phenotype and disc-specific ECM production.²⁸ However, it is important to note that Bartels *et al.* (1998) measured considerable variation, with oxygen values ranging from 3.8 – 13.2 %O₂ in the L3-L4 and L4-L5 IVDs of patients suffering from LBP.¹⁰ The current study found a correlation between disc height and pH level, with the largest discs having a significantly lower pH (~ 6.7) than the smallest (~ 6.9) (p = 0.0221). This is shown for both the predicted and the experimental results, with the predicted contour plots highlighting the gradient of acidity in the larger discs. This correlation is important to note as several studies have used bovine discs of different sizes and caudal levels under the same culturing conditions.^{138,270,303} An early study by Nachemson (1969) measured pH values of ~ 6.9 in lumbar IVDs of patients suffering from less severe levels of back pain and ~ 6.7 in patients suffering from severe backpain.⁷⁷ Therefore, the current *ex vivo* disc organ culture model appears to create a physiologically relevant central pH microenvironment. However, the disc size may need to be carefully considered based on the severity of the model desired in order to achieve the most appropriate acidic niche. Ultimately, it is imperative that the metabolite microenvironment established in culture is matched to the *in vivo*

microenvironment at a stage of human degeneration where the regenerative therapy is being considered an appropriate strategy in a clinical context.

This chapter further highlights that there is a need for standardisation of culturing conditions in order to reduce the *in vitro* to *in vivo* gap and realise more successful clinical translation based on nutritional demands. This is particularly important for interpretation of results when investigating the effect of cell-based therapies.^{132,138} Hence, based on the results of this study, it could be conceivably hypothesised that differences in the microenvironment of *ex vivo* organ cultures may account for the mixed results in terms of cell survival and regenerative capacity of potential treatments. Some studies have utilised short term nutrient deprivation to elicit a degenerative response.¹⁵⁰ However, if there is diminished cell viability it is speculated that nutrient concentrations will most likely rise above physiological levels when returned to HG medium due to a subsequently reduced glycolytic metabolism. This study suggests that in order to achieve physiologically relevant levels of glucose in the centre of *ex vivo* disc organ systems, there is a need to reduce the culturing concentration, while central oxygen and pH levels appear to be more comparable to the *in vivo* human condition. However, Jünger *et al.* (2009) observed significant reduction in the viability of bovine *ex vivo* discs due to limited glucose when cultured with an external glucose concentration of 2 g/L (11 mM) compared to HG media.³⁰⁷ Although the current study showed no significant difference in the active NP cell density at day 7, the local glucose concentration was suprphysiological (~ 10 mM) and not comparable to the effect of a 'lower' glucose concentration. Therefore, there is an additional challenge of balancing a physiologically relevant glucose microenvironment while maintaining viability of *ex vivo* discs for long term culture. As this study observed a diminished metabolically active cell population in the AF region after culture, a sensitivity analysis was performed to assess AF viability as a key parameter. The results showed that even if the proportion of metabolically active cells remains high, the oxygen and glucose levels do not significantly reduce, and importantly the central glucose concentration remains suprphysiological (Figure 6.5). However, a higher proportion of metabolically active cells predicted an increased acidity in the centre of the disc. Therefore, it is important to bear in mind that not only will the species disc size impact the local microenvironment and concentration gradients established, but also, the metabolically active cell density and specific metabolic rates.

Tissue composition such as the species-specific bone density and EP thickness and calcification will affect the solute transport in and out of the IVD.^{24,41,46,64} However, this model of bovine caudal discs were absent of calcification and good agreement between experimental and predicted results suggest that the diffusion coefficients used, to capture transport through the bovine EP with vertebral bone attached, were sufficiently representative of the physical organ culture. As mentioned previously, due to the culturing regime of *ex vivo* systems there is a shift in the supply routes. This may lessen the impact of solute transport effects due to variations in

species-specific bone density, EP thickness, calcification or the presence of growth plate which can be found in young animal disc organs. Despite different species having varying PG content, nutrients such as glucose and oxygen are uncharged molecules and should diffuse into the IVD at their route specific diffusion rates regardless of PG concentration.^{161,308} This is supported by relatively similar glucose diffusion coefficients having been measured in both bovine and human disc tissue which have different PG content.^{67,74} Additionally, sensitivity analysis of the *in-silico* model showed the effective diffusion coefficients to be the least influential parameter, with cell density and cell demand playing the most important role in establishing the nutrient concentration gradients.

The geometrical analysis matched results of a previous study investigating the effect of bovine caudal disc height on NP cell density (calculated from DNA level) of freshly isolated discs.³⁰⁹ Similarly, Boubriak *et al.* (2013) also found no significance between the cell density of different caudal levels or sagittal disc height. However, the authors stated large variation in absolute cell density from tail to tail, which was also reflected in the large standard deviation of the AF cell density of the current study. A study investigating age- and degeneration-related variation in cell density demonstrated human AF cell density decreasing from ~ 38,500 cells/mm³ in the first year of life to ~ 1,600 cells/mm³ by 30 to 60 years. Similarly, the degeneration effect highlights an AF cell density of ~ 25,500 cells/mm³ at Grade I (infant) and ~ 5,000 cells/mm³ at Grade IV.²⁵ Therefore, the higher bovine cell densities determined in this study appear to be more comparable to young and healthy or non-degenerated human IVDs. However, an unanticipated finding was the significant reduction in metabolically active cells in the AF after seven days of culture, while the cells of the NP exhibited no significant difference compared with the native density. The bioreactor used was a relatively simple static compression system compared with some of the more established bioreactors across the research field which use dynamic-loading and physiological diurnal loading.^{142,296} A possible explanation for the poor metabolic activity in the AF region may be due to constant compression of the disc, where the pressure created in the NP is balanced by tensile stresses in the lamella of the AF. A recent study, providing support for this hypothesis, found a significant reduction in viable cells (lactate dehydrogenase staining) in the inner and outer AF after severe static compressive loading.³¹⁰ However, the effects of dynamic loading and fluid flow on solute transport in avascular tissues and constructs have not been fully elucidated. A key early *in vivo* study looking at the effects of physiological loads and fluid transport on tracer concentrations found that fluid “pumping” during movement had an insignificant effect on small solutes such as oxygen and glucose.⁵⁹ However, due to the shift in nutrient supply routes this may be different for *ex vivo* bioreactor systems and warrants further investigation.

As with any *in-silico* model, there are certain limitations and assumptions. Within the scope of this study, it was not possible to experimentally determine metabolic rates for bovine tissue.

While OCRs have been reported for bovine NP cells,⁹ none have been reported for AF cells. Therefore, it was assumed that the Michaelis-Menten constants for bovine AF cells were comparable with those reported for porcine AF cells.⁹⁰ Cell density and metabolism rates will significantly impact the nutrient concentration profiles and are dependent on the species. For the purposes of accurately predicting nutrient concentration profiles, it is important to determine the metabolically active cell population (using the MTT method or similar) as opposed to conventional Live/Dead indicators. The metabolism rates of cells appear to vary between species and degeneration. For example, rat and rabbit NP cells have been shown to exhibit higher LPR compared to non-notochordal bovine NP cells.³¹¹ In addition degenerated human cells exhibit 3 – 5 times greater OCR than non-degenerated cells.⁹³ Unfortunately, due to the mechanics of MTT staining it is only possible to capture a binary indication of cell activity. However, several studies have investigated disc cell metabolism at a range of physiological and supraphysiological glucose concentrations.^{9,90,91,93,98,103} In general, significant cell death appears to occur below a glucose threshold of 0.5 mM (for more than three days) and disc cells have shown little difference in GCR between 1 and 5 mM.^{9,27,49} Additionally, previous work has typically shown higher GCR and lower OCR at supraphysiological glucose levels.^{90,93,98,103}

Taken together, it is critically important to understand the species-specific metabolically active cell density and metabolism rates to achieve a physiologically relevant microenvironmental niche through optimising the nutrient boundary conditions of *ex vivo* organ culture. However, given the good agreement between the *in-silico* concentrations and those measured experimentally, any computational simplifications and assumptions appear justified. As a result of successful validation, the current model could be used to predict the culturing conditions necessary to tailor a desired nutrient microenvironment using key input parameters such as species-specific rates of metabolism, metabolically active cell density and disc geometry. Additionally, it could be developed further to model the impact of delivering cells into a degenerated disc model, as well as identifying an optimal cell number to sustain viability without adversely affecting the local nutrient microenvironment. Despite promising characterisation of the metabolite microenvironment of a relatively straightforward *ex vivo* disc organ culture system, more work is needed to experimentally characterise the effect of introducing pro-inflammatory cytokines on the nutrient microenvironment and cellular metabolism.^{291,312} A recent agent-based model has shown promising advancement in *in-silico* modelling by developing an inflammation and mRNA expression sub-model to capture cellular behaviour in a more multifactorial, biochemical environment.¹¹⁹ Significant advancements in *ex vivo* disc organ culture have also identified optimal loading force and frequency of more complex bioreactor systems.²⁹⁷ Importantly, it has been acknowledged that such parameters must be identified and optimised between discs of different species and scale.²⁹⁶ The findings of this work suggest that a similar

approach is needed in terms of optimising the nutrition of *ex vivo* disc organ culture systems based on geometrical differences.

Moreover, the physiological relevance of the native nutrient microenvironment within the discs of different species of animals may be questioned due to naturally lower blood glucose levels in animals (3.33 – 3.95 mM in rat, goat and bovine) compared to values closer to 5 mM in humans.^{204,298,313,314} While discs from a variety of different animal including mouse^{143,144}, rat^{145,146}, lapine^{122,147}, bovine^{148–151}, ovine^{152,153}, caprine^{154,155} and porcine^{156,157}, a system which employs *ex vivo* degenerate discs from human donors may be the ultimate platform.^{124,139} However, human material is difficult to obtain due to ethical and government regulatory restrictions, making it unfeasible for many research labs. Even after overcoming such challenges, supply may be intermittent without protocols to cryofreeze and bank the tissue and there may be limited control over stage of degeneration of the available tissue. Therefore, in the meantime the majority of the research field resort to the unparalleled advantages of high throughput and easily accessible tissue such as bovine caudal disc which can ultimately be optimised to the nutrition of different stages of human degeneration through predictive modelling and metabolite measurement, as presented throughout this work.

Combining advanced *in-silico* modelling with experimental validation offers a powerful tool for the standardisation of *ex vivo* disc organ culture systems and refinement of animal models. Taken together, this approach offers the ability to better predict the *in vivo* human events and outcomes accelerating the development of cell-based therapeutics towards clinical translation.

6.5 Conclusion

Organ culture systems offer unparalleled advantages for the development and preclinical testing of new regenerative strategies. However, the findings of this chapter suggest that further optimisation and standardisation of *ex vivo* disc organ culture is needed to recapitulate the *in vivo* microenvironmental niche of a degenerating human IVD. Although HG and NX conditions are the most commonly used culturing conditions across all species of *ex vivo* disc organ culture, this study found supraphysiological levels of glucose exist in the centre of bovine caudal discs under these conditions. While the choice of species may be dependent on the specific scientific question, if the nutrient microenvironment is relevant to the study aim, then the culturing parameters may need to be optimised based on disc geometry, metabolically active cell density and species-specific metabolism. Once standardised, it is anticipated that these systems will provide a more powerful and reliable platform to test new treatments and accelerate innovative therapeutics for clinical translation.

Chapter 7. Preclinical to Clinical Translation: Effects of Species-Specific Scale, Metabolism and Matrix Synthesis Rates on Cell-Based Regeneration

A limited amount of this Chapter has been published previously in Barcellona, M. N., **McDonnell, E. E.**, Samuel, S., and Buckley, C. T. (2022) ‘Rat tail models for the assessment of injectable nucleus pulposus regeneration strategies’, *JOR Spine*, 5(3), doi: <https://doi.org/10.1002/jsp2.1216>

Contribution: Contribution to the conception and design of the work. Formed the acquisition, analysis, and interpretation of literature data. Performed the pilot rat study, acquisition, analysis, presentation, and interpretation of results, drafting of the article, revising it critically and final approval.

7.1 Introduction

The ultimate challenge for regenerating the IVD has been focused on developing an easily injectable cell-based strategy to replenish the diseased tissue with viable and functional cells. It is believed that these implanted healthy autologous or allogenic cells would augment ECM anabolism and subsequently restore tissue function. After showing promise *in vitro*, these potential new therapies must demonstrate efficacy and that the benefits of the treatment outweigh its risks under pre-clinical assessment before progressing to clinical evaluation. Pre-clinical animal studies are not only crucial for understanding the progression of degeneration, how risk factors initiate, promote, or otherwise regulate degenerative changes, but also how potential therapeutics alleviate, ameliorate, or inhibit further degeneration. Moreover, animal work has been leveraged to uncover challenges likely to be encountered in a clinical setting, such as injecting cells into the disc with or without hydrogel carriers, retaining the cells *in situ* and maintaining their cell viability and functionality.^{315,316} Nonetheless, animal studies are expensive, labour intensive and important ethical considerations limit their widespread use. In recent years there has been a significant drive to reduce the number of experiments being performed on living animals through the guiding principles of Replacement, Reduction and Refinement (the “Three Rs”). The Three Rs is a systematic framework for performing more humane animal research and is a highly relevant topic across the biomedical field. Furthermore, even after demonstrating safety and efficacy in animals, many cell-based therapies for DDD do not appear to work to the same extent in humans. Therefore, there is a pressing need to ascertain the clinical relevance of different animal models, not only for important scientific and ethical merit but to further accelerate the prospects of more successful clinical translation.

Profound differences between animal species include cell population, both in terms of cell type and cell density, and the scale of the disc geometry and structure.³¹⁷ Large animal models

have been accepted as good models for studying disc structure, geometry, biochemistry and biomechanics.^{164,165,318} Larger animals have a disc structure analogous to humans and they tend to undergo degeneration slowly. Examples include dogs, pigs, goats, sheep and non-human-primates.^{121,166,319,320} Alternatively, small animal models such as mice, rats, and rabbits undergo degenerative changes rapidly and their popularity likely reflects their more cost-effective and higher throughput nature.^{167,318,320} While large animal studies are not consistently conducted, it has been suggested that a large animal without persisting notochordal cells (i.e. goat or sheep) is an important aspect before preceding to human clinical trials.³¹⁵ As mentioned previously, vacuolated notochordal cells disappear rapidly after birth in humans and this may have implications for regenerative potential compared to species which retain their notochordal cells into adulthood (i.e. rabbit, rat and pig).^{315,317}

The human IVD consists of a sparse population of cells and an abundant ECM, which varies in matrix composition radially through the AF (mostly type I collagen) and into the central NP (predominantly type II collagens and GAG). While the GAG and collagen contents have been comprehensively compared across the NP and AF of several animal species,^{161,195} the regional variation in cell density between animals has not been quantified to the same extent. Early work has reported variation in disc cell density between some animal species,^{58,311} with an inverse relationship between disc cell density across the NP and disc height.²⁰⁷ However, no study has directly investigated the cell density of both the NP and AF regions of both a small and large animal, as well as comparing them with respect to the sparsely populated human IVD.

Due to the low oxygen conditions of the IVD, disc cells are believed to primarily obtain their energy through glycolysis.^{28,58} A number of studies have directly measured nutrient consumption (OCR and GCR) and metabolite production (LPR) rates of NP cells as shown in Chapter 2 (Table 2.2 – Table 2.4). However, these investigations have been limited to bovine, porcine and human cells and few studies have made a direct comparison between NP and AF cells.^{9,20,90,91,93–95,98,102,103} While it is less experimentally challenging to measure metabolic rates in 2D culture, monolayer expansion has been shown to shift chondrocytes from a glycolytic to an oxidative energy metabolism within seven days *in vitro*.³²¹ Some studies have encapsulated cells in hydrogels to maintain phenotype stability during culture.^{9,91,94,103} However, challenges remain in limiting bead or construct size, in order to mitigate gradients forming, while still maintaining sufficient cell numbers to establish detectable changes in the metabolite levels within a specified timeframe. Changes in glucose or lactate have been simply measured by sampling culture media using diabetic glucose meters or biochemical assays.^{91,94,95,98,322} Meanwhile, custom-made or commercial metabolic chambers have been used to measure reduction in oxygen or multiple metabolites simultaneously.^{9,90,93} These chambers have been reported to range from 175 μ L – 4 mL in volume. Alternative more advanced Seahorse Flux Analyser methods with greater sensitivity have been employed for rat, rabbit and human disc cells.^{213,323–325} Typically, these

studies (Appendix E.4) are used to investigate the effect of a substrate or inhibition of a pathway and present results in terms of OCR and extracellular acidification rate (ECAR) normalised to protein content. Unfortunately this does not facilitate comparison with the rates measured using the aforementioned methods.

Since GAGs play an important role in both the formation and function of the disc, they are considered fundamental to functional repair through regenerative strategies. As a result, cell-based therapies need to be characterised by their matrix synthesising abilities and in terms of pre-clinical to clinical translation, variation in the anabolic metabolism of different species needs to be considered. For example, a study by Miyazaki *et al.* (2009) demonstrated marked differences in PG production of notochordal (rat and rabbit) and non-notochordal cells (bovine) in an early attempt to delineate the most suitable animal model for the study of biological repair.³¹¹

In order to further ascertain the clinical relevance of both a small and large animal model, this work focuses on comparing rat caudal and goat lumbar studies to human clinical trial parameters (e.g. cell injection number and study duration). Firstly, this chapter will experimentally investigate and compare these animal models to human from the perspective of anatomical scale and their cellular metabolic and regenerative potential. Secondly, *in-silico* modelling, will be employed to predict the subsequent regeneration timeline of animal models compared to clinical trials. These models are governed by the aforementioned experimental parameters and can further predict the ensuing nutrient microenvironment as a result of injecting varying cell numbers into different species. Overall, this work aims to provide a path towards understanding “time to regeneration” within pre-clinical animal models and the stunted success of cell-based clinical trials.

7.2 Materials & Methods

7.2.1 Pre-clinical literature and registered clinical trials of cell-based disc regeneration

A literature search for rat models was performed in the databases PubMed (102), Scopus (90), and Embase (127) in March 2022 using the search terms “intervertebral” AND “disc” AND “degeneration” AND “rat” AND (“needle puncture” OR “stab”). A literature search for goat models was performed in the databases PubMed (48), Scopus (60), and Embase (70) in August 2022 using the search terms “intervertebral” AND “disc” AND “degeneration” AND “goat”. Both pre-clinical literature searches were refined according to Figure 7.1 and a full table of the 80 rat tail studies and 15 goat models can be found in Appendix Table E.1 and E.2, respectively. A clinical search was performed in November 2022 using the clinicaltrials.gov database, a resource provided by the U.S. National Library of Medicine. The search consisted of “intervertebral disc degeneration” as the condition or disease, “cell” as a key search term and the study type was limited to “interventional studies”, which provided 50 search results. Following close inspection of each study (excluding spinal fusion interventions, cervical spine studies and biomechanical/traction studies) the results were refined to 26 cell-based interventions for lumbar disc degeneration. A full list of these trials can be found in Appendix B.

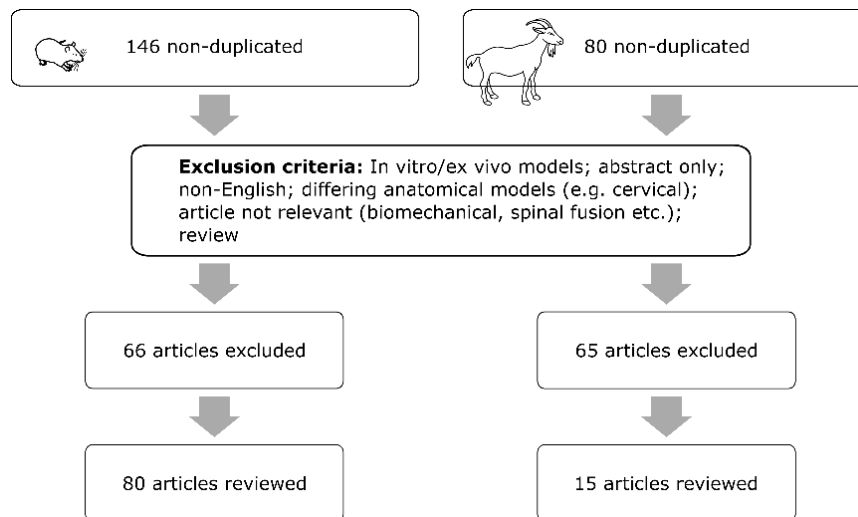


Figure 7.1 Preferred Reporting Items for Systematic Reviews and Meta-Analysis (PRISMA) diagram indicating screening process and exclusion criteria. 80 articles were reviewed for rat tail models and 15 articles for goat lumbar models.

From the rat models which investigated cell-injection, four key studies were identified as relatively comparable in their assessment of the efficacy for a cell source delivered in a hydrogel carrier.^{326–329} The criteria which deemed them appropriate included induced degeneration prior to treatment (at a later time point), provided details on the total number of cells injected in an

appropriate injection volume (< 10 μ l). Additionally, these studies provided clear timepoint results where improvement or significant difference to an injured control was assessed via histology and/or MRI. Through a similar review of the goat studies, only two key articles were identified. Compiled parameters on injected cell number and study duration (from treatment) can be found in Figure 7.2(A) and (B) for rat and goat, respectively. For comparison, Figure 7.2(C) presents 16 of the registered clinical trials which provided details to the same extent e.g. total cell number of a distinct cell source (i.e. exclusion of bone marrow concentrates or platelet rich plasma) and clinical follow up time points which involve MRI for functional regeneration assessment.

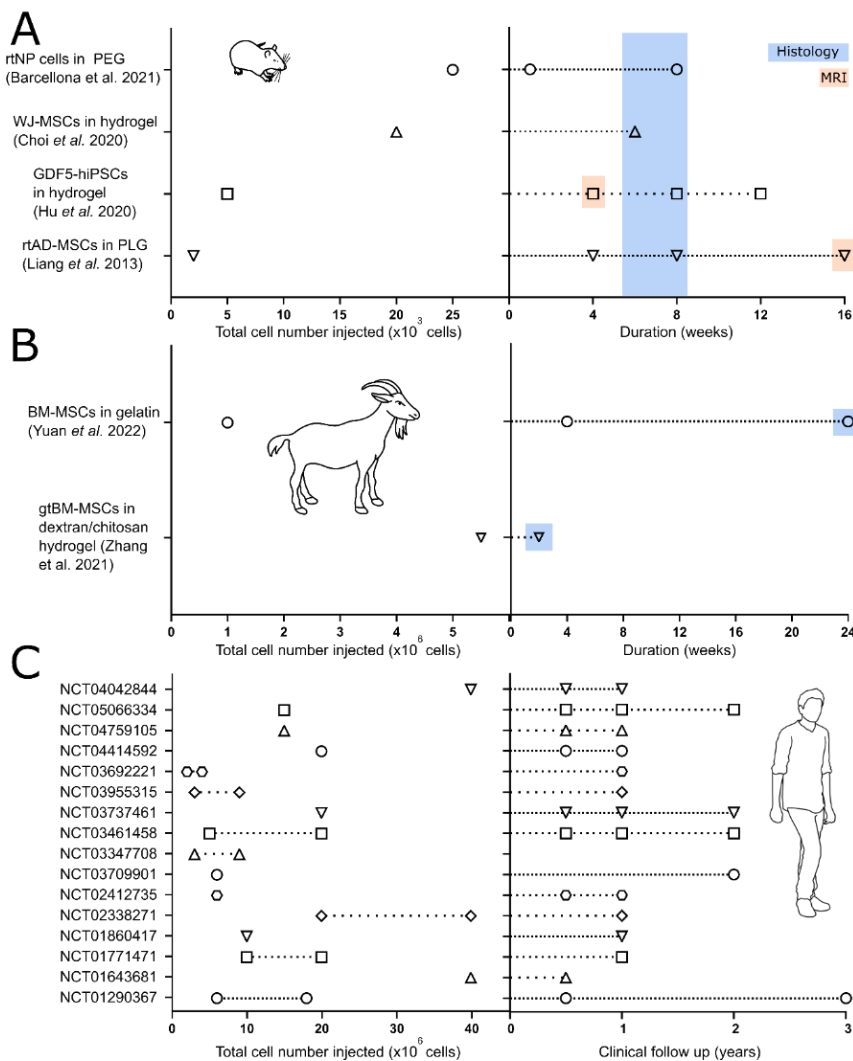


Figure 7.2 Experimental parameters gathered from key pre-clinical animal models in the literature and registered clinical trials for cell-based disc regeneration. (A) Total number of cells injected and study duration for four published rat studies, highlighting the timeframe when differences were reported in histological evaluation and MRI assessment. **(B)** Total number of cells injected and study duration for two published goat studies, again highlighting the timeframe when differences were reported in histological evaluation. **(C)** Total number of cells injected across 16 registered clinical trials, with several trials using a lower and higher cell dose as indicated with dashed lines. Clinical follow up time points refer to functional assessment only using MRI.

7.2.2 Establishing species-specific *in-silico* models using experimentally determined geometries and cell densities

To accurately create a 3D geometry for *in-silico* models of rat caudal and goat lumbar discs, a geometrical analysis of all caudal and lumbar levels was first performed. Additionally, a literature search was carried out to identify the most used anatomical level within animal studies. For the goat, the lumbar section was excised using the last rib for anatomical reference and the L1-2 to L5-6 discs were isolated, dissected, photographed and macroscopic image analysis was performed using ImageJ in the sagittal and transverse reference plane (N = 3). A schematic for reference is shown in Figure 7.3(A) and images for each lumbar level can be found in Appendix E.3 together with a table of all dimensions measured. For the rat, disc levels were identified by digital palpation following the removal of the skin, with the last set of palpable processes reportedly found on the fifth caudal vertebra (i.e., level Cd5) and then counting towards the sacrum to locate Cd1.^{330,331} A section containing Cd1 to Cd10 was prepped for histology as outlined in Chapter 3 and stained with H&E and a dichrome stain consisting of AB and PSR (N = 6). Microscopic image analysis was then performed using ImageJ as depicted in Figure 7.3(B).

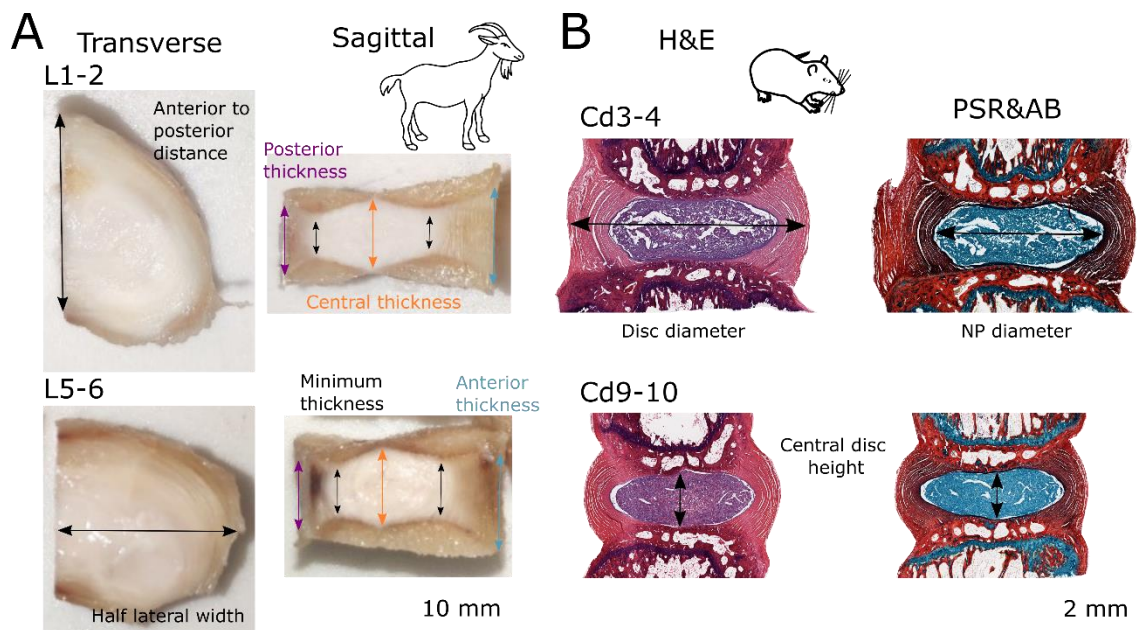


Figure 7.3 Geometrical analysis of goat lumbar and rat caudal disc using macroscopic and microscopic image analysis, respectively. (A) Goat lumbar discs L1-2 to L5-6 were dissected in the transverse and sagittal plane to determine the anterior to posterior distance, lateral width, and disc heights across the midsection. (B) Rat caudal discs Cd3-4 to Cd9-10 were micro-sectioned in the sagittal plane and histologically stained (H&E: hematoxylin and eosin; PSR&AB: picrosirius red and alcian blue) to evaluate the full disc diameter, nucleus pulposus (NP) diameter and the central disc height.

An idealised 3D geometry was created based on the measured dimensions using SOLIDWORKS® for rat caudal level Cd7-8, as it is the most frequently used level in rat studies. Although typical pre-clinical studies use more than one disc per goat, only a 3D model for L3-4 was created in COMSOL Multiphysics. An idealised 3D geometry for a grade III human lumbar disc was created using dimensions previously determined by a member of our research group through image segmentation from MRI, graded by an expert using the Pfirrmann grading system.³³² Full rat, goat and human IVDs with a separate NP and AF domain can be seen in Figure 7.4(A). However, for simplification only a quadrant of the discs is modelled *in-silico*, Figure 7.4(B).

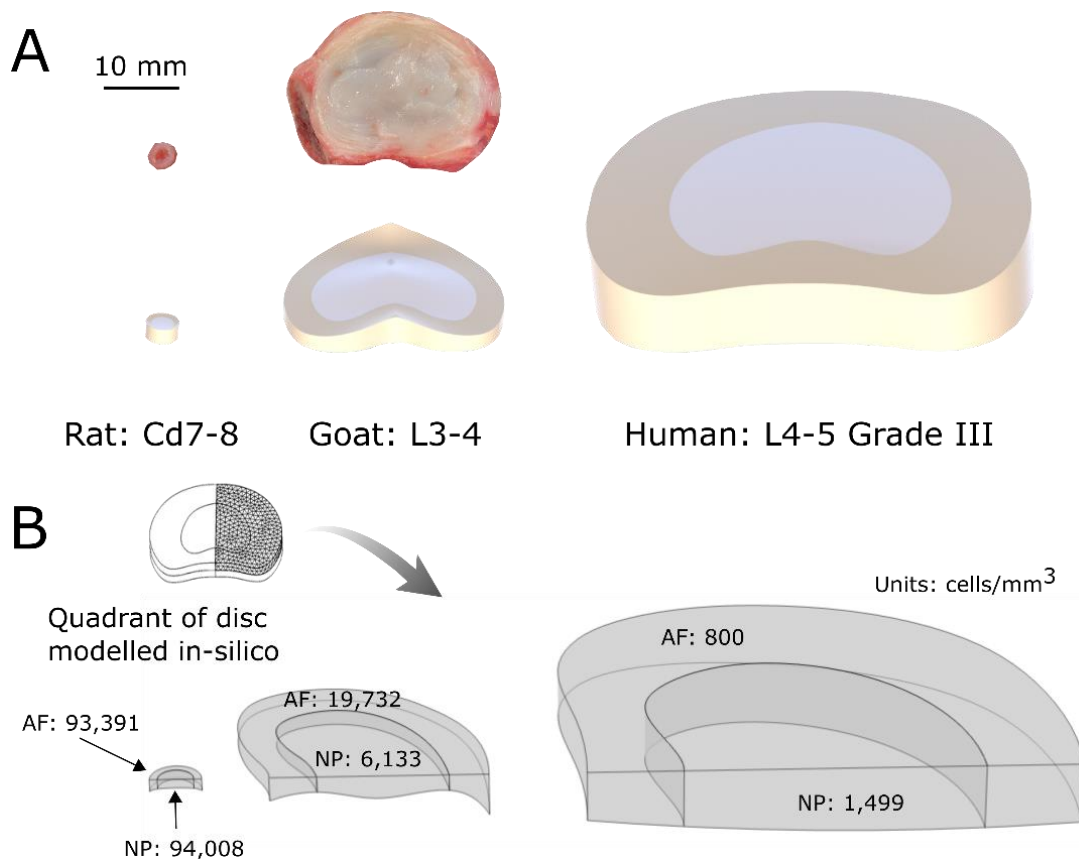


Figure 7.4 Rat caudal (Cd7-8), goat lumbar (L3-4) and human lumbar (L4-5 at Grade III) discs presented in scale to one another. (A) Transverse image of a freshly isolated rat and goat disc together with 3D renderings created using the measured dimensions. (B) Due to symmetry, only a quadrant of the rat, goat and human discs were modelled *in-silico*. The distinct nucleus pulposus (NP) and annulus fibrosus (AF) domains are highlighted together with their modelled native cell densities. Rat and goat cell densities were determined experimentally within this work, while human data was obtained from the literature and is specific to Grade III degeneration.²⁸⁰

The species-specific metabolically active cell density for the NP and AF was determined using MTT and a DAPI counterstain as presented in Chapter 3. For goat, three discs were assessed per donor, with at least six slices analysis per disc (N = 6). Due to the consistency (high gelatinous

nature) of the rat NP, it was not possible to retain the formazan crystals within the tissue and co-localisation with the nuclear DAPI staining was not feasible. Troubleshooting involved attempting to reinforce the tissue with a gelatin or alginate component but allowing these to diffuse into the tissue causes a change in tissue volume and thus confounded the cell density calculation.

7.2.3 Establishing a spheroid culture system for rat, goat, and human disc cells

Positive mould stamps were designed using SOLIDWORKS® CAD software and the individual microwell design was based on recent microwell literature.^{283,333} The microwells had a diameter of 1 mm and a total depth of 1.5 mm, comprising a cylindrical section (1 mm) and a domed end (0.5 mm), Figure 7.5(A). An array of microwells were patterned across the circular base of a stamp designed to fit into either a 12-well plate (145 microwells per well) or a 24-well plate (69 microwells per well). A STL file for the part was prepared on Preform 3.22.0 software (Formlabs, Massachusetts, United States) with a 25 µm print layer thickness for high resolution. The positive mould stamp was fabricated using a Form 2 stereolithography printer and V2 high temperature resin (Formlabs). Post-printing, the stamp was washed in propan-2-ol (Sigma-Aldrich) before curing with UV light (405 nm, 9.1 W) (Form cure, Formlabs) for two hours at 80 °C in accordance with the manufacturer's guidelines. High temperature resin was chosen to allow for autoclave sterilisation.

To fabricate the negative hydrogel microwells under sterile conditions, 2 mL or 1 mL of molten agarose (2% (w/v) at approximately 80 °C, Sigma-Aldrich) was pipetted into the wells of a 12- or 24-well plate, respectively. After the agarose had cooled and solidified, the stamp was carefully removed, leaving behind the hydrogel microwell array at the base of the well plate as shown in Figure 7.5(B). Expanded NP and AF cells were trypsinised, counted using trypan blue staining and the cells were seeded into the microwell array by pipetting an appropriate density into each 12- or 24-well. After seeding, the plates were placed in the incubator to allow the cells to accumulate into the individual microwells (~ 20 mins) before centrifuging at 850 × g for five minutes to condense the cells at the bottom of each well (Figure 7.5(C)). Spheroids were then cultivated in LG-DMEM supplemented with 10% FBS and 2% Pen-Strep (all Gibco) with a daily media exchange for five to seven days (37 °C in a humidified atmosphere with 5 %CO₂ and 10 %O₂). The external incubator oxygen, media glucose concentration and regularity of the media exchange was informed through the predictive *in-silico* models as set out in Chapter 5, in order to retain a relatively stable and physiologically relevant microenvironment within the micro-spheroids.

Cell viability of the spheroids was established using a live/dead assay kit (Invitrogen, Bioscience). Media was aspirated and the hydrogel microwells were gently rinsed with PBS

before incubation for one hour in a phenol free DMEM (Sigma) solution containing $2\ \mu\text{M}$ calcein AM and $4\ \mu\text{M}$ of ethidium homodimer-1 (EthD-1). Following incubation, the hydrogel microwells were rinsed again. By applying a gentle aspirate and dispense motion, the spheroids were dislodged from their individual microwells and transferred to a 35 mm diameter confocal dish (81156, Ibidi). Samples were imaged on a Leica SP8 scanning confocal microscope (485 nm and 530 nm excitation and 530 nm and 645 nm emission for calcein and EthD-1, respectively). All images are presented as maximum projection z-stack reconstructions qualitatively analysing cell viability.

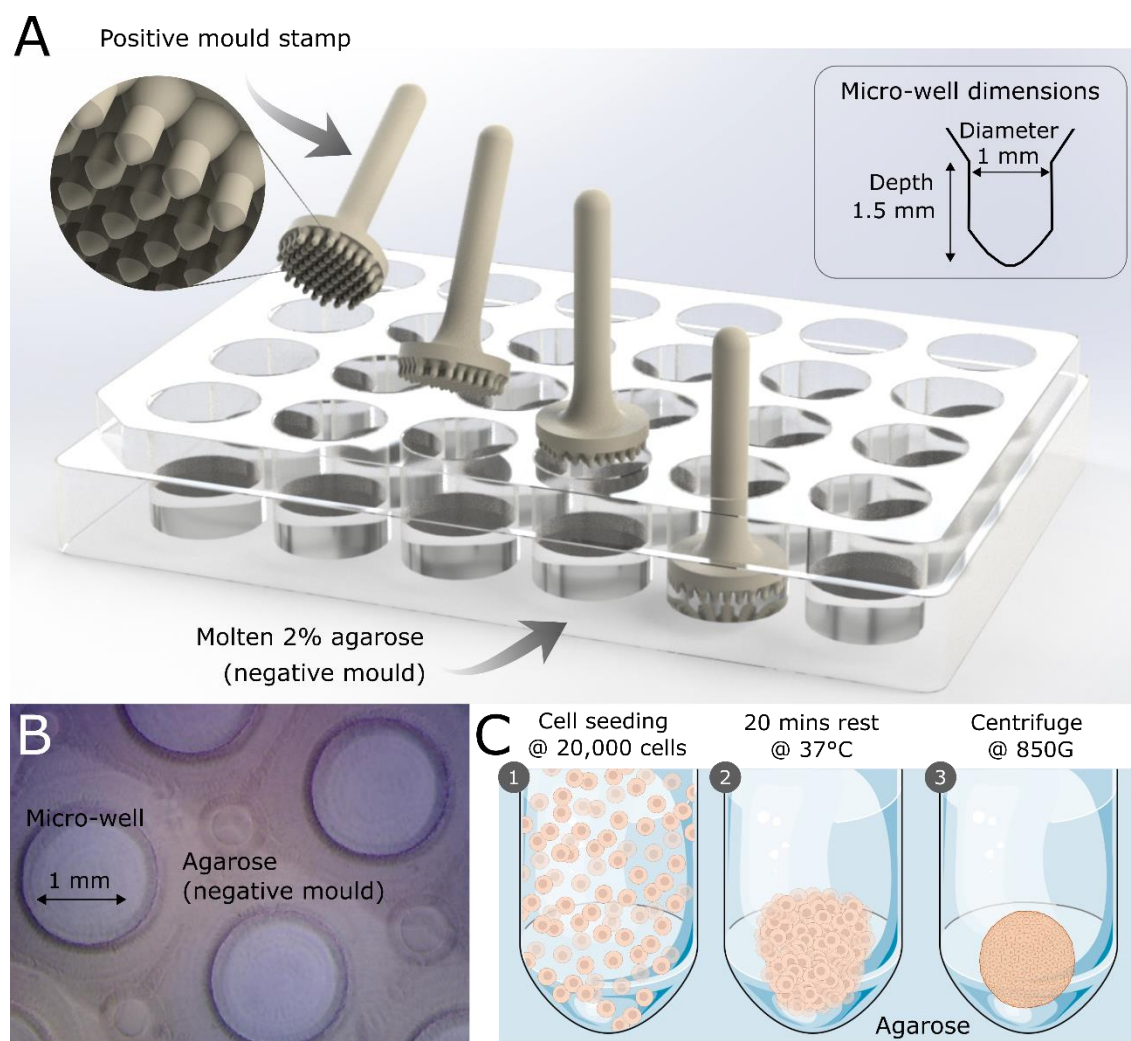


Figure 7.5 Agarose microwell array fabrication and the formation of disc spheroids. **(A)** Geometry of a 3D printed stamp and the process to be used to create 69 micro-wells array in molten 2% agarose in each well of a 24-well plate. The cross-section sketch highlights the dimensions of each individual microwell. **(B)** Microscope image of the negative mould left in the solidified agarose after the removal of the stamp. **(C)** Schematic of the steps involved in creating the disc spheroids within the agarose microwell array.

7.2.4 Metabolic flux analysis for experimentally determined nutrient consumption and lactate production rates

The Seahorse XFe96 analyser, together with the Spheroid FluxPak (Agilent Technologies), simultaneously measures in real time the reduction in oxygen level, a measure of the OCR and pH level, a measure of extracellular acidification rate (ECAR) in the medium directly surrounding a single cell spheroid. The Seahorse cartridge plate was hydrated with sterile DI water and incubated in a non-CO₂ incubator at 37°C for a minimum of 8 hours prior to use. The water was then exchanged for XF calibrant fluid (Agilent Technologies) 45 – 60 mins before running the assay.

Disc cell spheroids were cultured for five to seven days in their agarose microwell arrays prior to being transferred to the Seahorse 96-well spheroid microplates and allowed to rest for at least one hour prior to running the assay. In brief, the spheroid microplates were first coated with 100 µg/mL poly-D-lysine (Sigma), rinsed twice with sterile DI water and air dried for 30 mins prior to loading 175 µL of assay media to each well. Complete unbuffered XF assay medium consisted of Seahorse XF DMEM supplemented with 5.5 mM glucose, 1 mM sodium pyruvate and 2 mM L-glutamine (all Agilent Technologies). Media was made up fresh, pH adjusted to 7.4 and warmed to 37°C in the waterbath. Spheroids were transferred by allowing them to float out of a P200 pipette tip, to the bottom of the well by gravity alone, without ejection of any additional media and to attach to the cell adhesive at the bottom of the well. Blank wells (XF assay medium only) were prepared without spheroids for subtracting the background OCR and ECAR during analysis. Extracellular flux measurements were performed six times at twenty-minute intervals under basal conditions i.e. no injection of inhibitor/stimulator treatments. Following the Seahorse assay, metabolic rate samples were removed from the 96-well microplate and transferred into Eppendorf's together with the assay media, before then aspirating off the media and storing the samples at -80°C until papain digestion.

The raw measurements of oxygen level (mmHg) and pH, as shown in Figure 7.6, were extracted from the Wave software (Agilent Technologies) and the data analysis was performed in Excel. In short, metabolic rates were calculated over the linear/plateaued region of the data set (after 10 mins for oxygen) and pH measurements were converted to lactate concentration using a standard curve which had been created using the Seahorse XFe96 analyser system and the same assay medium in Section 3.7.2 (Figure 3.4). OCR and LPR calculations were normalised by cell number per well i.e. spheroid. The cell number of each spheroid was established through biochemical DNA quantification and interpolation using the purpose made standard curve from Section 3.6.2 (Figure 3.3). For biochemical assessment, individual spheroids were papain digested in 60 µL. As the ECAR is a measure of glycolysis, GCR was estimated based on the assumption

that ~ 2 moles of lactate are produced for every mole of glucose consumed by highly glycolytic disc cells.³³⁴

At least three biological repeats were performed for each species with prep/donor matched NP and AF cells (N = 3). The human cells in this work were isolated from a 43-year-old female, 44-year-old male, a 33-year-old female and a 40-year-old female (N = 4). Technical replicates were analysed for outliers using the ROUT method. A minimum of 25 replicates passed the outlier test with an average of two outliers removed per dataset.

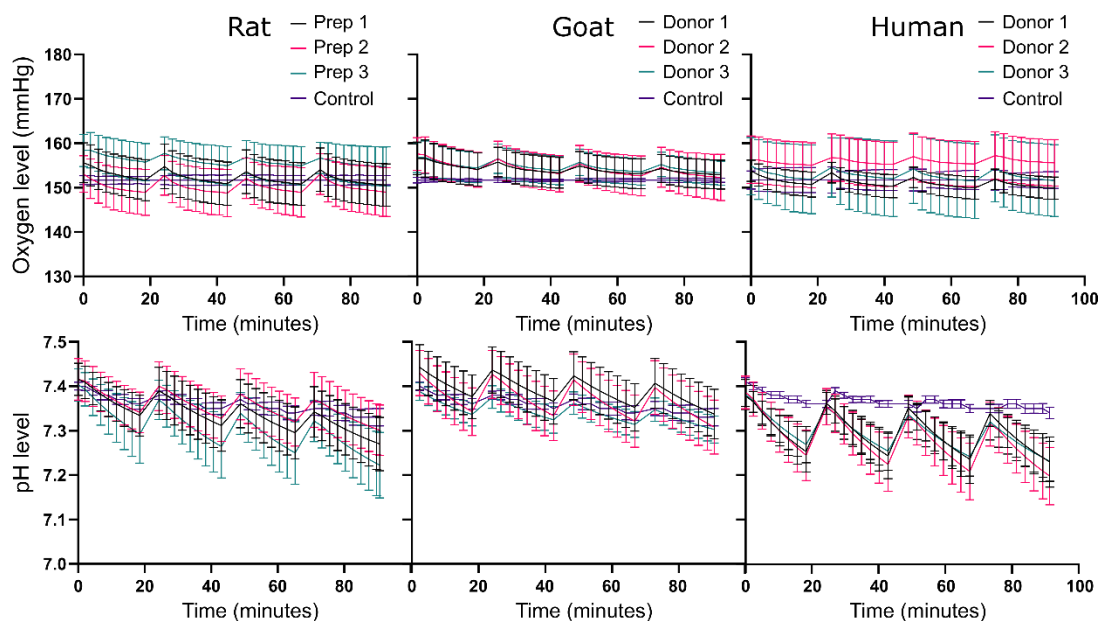


Figure 7.6 An example of raw measurements from the Seahorse XFe96 analyser showing simultaneous measurement in real time of the reduction in oxygen and pH level for rat, goat, and human nucleus pulposus cells. Levels reduce over a 30 min. measurement period, before the sensor cartridge rises to allow oxygen to re-infiltrate and fresh media exchange (causing the pH to rise). The graphs show four repeated measurement periods for more than 25 spheroids per prep/donor prior to normalisation for cell number.

7.2.5 Towards experimental validation of *in-silico* nutrient transport models

The *in-silico* nutrient transport model was created using COMSOL Multiphysics as outlined in Section 3.1. The steady-state nutrient microenvironment was governed by the species-specific metabolically active cell densities determined in Section 7.2.2 and metabolic rates determined in Section 7.2.4. Briefly, the experimentally measured OCR was implemented into the coupled reaction-diffusion equations dependent on local oxygen and pH concentration, as used in previous chapters (Equation 7-1). Glycolysis was measured as LPR; thus an assumption was made on a 2:1 ratio of lactate to glucose, and GCR was extrapolated. GCR was modelled as rate limited to local glucose concentration, as explained in Chapter 5. Additional input parameters such as metabolite diffusion coefficients for each tissue domain are presented in Table 7.1. The

parameters for diffusion in human tissue are those used previously for Grade III degeneration in Chapter 4. With limited data available for species-specific diffusion rates, values measured in bovine tissue was considered to be the most appropriate for the animal models.

Table 7.1 Effective diffusion coefficients (mm²/hr) used *in-silico* for the nucleus pulposus (NP) and annulus fibrosus (AF) domains of rat, goat, and human discs.

	Rat		Goat		Human	
	NP	AF	NP	AF	NP	AF
D_{gluc}	1.22 ^a	axial: 0.7 radial: 0.52 ^c	1.22 ^a	axial: 0.7 radial: 0.52 ^c	1.17 ^f	axial: 0.45 radial: 0.37 ^g
D_{o_2}	5 ^b	3.78 ^d	5 ^b	3.78 ^d	4.81 ^f	axial: 3.08 radial: 2.20 ^g
D_{lac}	1.62 ^a	1.2 ^e	1.62 ^a	1.2 ^e	1.56 ^f	axial: 0.61 radial: 0.50 ^h

^a Glucose measurements, lactate derived from glucose.¹⁸³

^b Theoretical values from the literature.⁵⁸

^c Experimentally determined in axial and radial direction for bovine tissue under 10% strain.⁶⁷

^d Experimentally determined axially for bovine tissue under 15% strain.⁷³

^e Derived from glucose.²⁴

^f Experimentally measured in the literature and hydration adjusted as set out in Chapter 4.

^g Literature values for human tissue under 10% strain and temperature adjusted as set out in Chapter 4.

^h Derived from glucose values in Chapter 4.

Uncertainty remains regarding the metabolite concentrations surrounding the disc boundary, particularly in the case of rat caudal and goat lumbar discs. Similar to previous numerical models, it was assumed that glucose concentrations and pH levels at the periannular boundary are that of blood plasma in the surrounding blood vessels.^{104–106} Concentrations at the NP boundary, underneath the EP, were estimated based on the reduction in concentration through the EP modelled in Chapter 4. Oxygen values from $< 1\% \text{O}_2$ to $6\% \text{O}_2$ have been used as boundary conditions throughout the literature.²² In an attempt to refine the boundary concentrations and improve confidence, models were first run for “healthy” conditions, with native cell densities and geometries. Healthy or uninjured rat caudal discs and goat lumbar discs were then probed experimentally using the methods established in Chapter 6. These experimentally measured values for oxygen and pH were then compared to the predicted profiles in order to iteratively determine the boundary concentrations and enhance confidence in the modelling capabilities. The results of this partial validation are presented in Figure 7.7 and the finalised boundary concentrations are presented in Table 7.2. Undoubtedly the nutrient microenvironments will change with degeneration or induced injury due to factors such as alterations in cell number and distribution. This will be addressed further in Section 7.2.6.

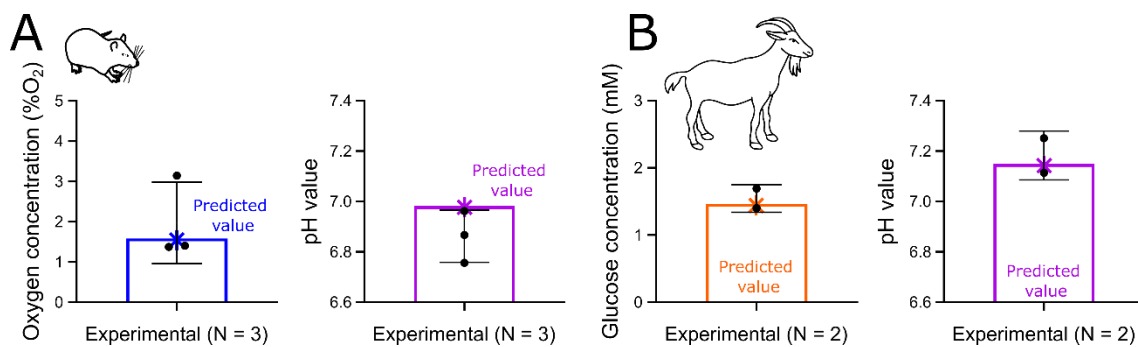


Figure 7.7 Towards experimental validation of in-silico modelling of the nutrient microenvironment in pre-clinical animal models. (A) Preliminary experimental measurement of oxygen and pH values in the centre of rat caudal discs (N = 3) using probing technology and compared to predicted *in-silico* results. **(B)** Preliminary experimental measurement of glucose and pH values in the centre of goat lumbar discs (N = 2) using biochemical and probing technology, respectively. Measured values (black) are compared to predicted *in-silico* results for each metabolite (coloured).

Table 7.2 Boundary concentrations used *in-silico* at the nucleus pulposus (NP)/cartilage endplate (CEP) interface and the periannular surface of the annulus fibrosus (AF) for rat, goat, and human.

	Rat		Goat		Human	
	NP	AF	NP	AF	NP	AF
<i>Gluc (mM)</i>	3.50 ^a	3.95 ³¹³	2.90 ^a	3.90 ³¹⁴	3.04 ^a	4.75 ²⁰⁴
<i>O₂ (%O₂)^b</i>	2.22	5.92	1.85	5.92	1.48	5.92
<i>Lac (mM)</i>	3.30 ^d	1.98 ^c	3.30 ^d	1.98 ^c	3.30 ^d	1.98 ^c

^a Concentrations at the NP-EP interface were estimated based on the reduction in glucose through the EP modelled in Chapter 4.

^b Periannular oxygen concentration was approximated from the literature and iteratively adjusted according to preliminary experimental validation of the models. Concentrations at the NP-EP interface were estimated based on reduction through the EP and iterative experimental validation.

^c Periannular lactate concentration assumed to be that of typical blood plasma (pH 7.35 – 7.45).

^d Concentrations at the NP-EP interface were estimated based on the reduction in lactate through the EP modelled in Chapter 4 together with iterative experimental validation.

7.2.6 Experimentally determining species-specific GAG synthesis rates to compare animal and human cell-based regeneration *in-silico*

NP cell spheroids for the assessment of GAG production were formed as individual spheroids in a flat bottomed 96-well plate, which was coated with a thin layer of 2% agarose to prevent cell attachment. This was similar to off the shelf low-adherence cell-repellent surface 96-well plates which have been used previously to form canine and human disc micro-aggregates.^{289,290} The rationale for this was that a higher throughput system was not required and media sampling per individual spheroid was pertinent and not possible within the microwell array system. Each spheroid was cultured in 200 μ l of phenol-free LG-DMEM supplemented with 10% FBS and 2% Pen-Strep (all Gibco), with a media exchange performed every three days for two weeks (37 °C in a humidified atmosphere with 5 %CO₂ and 10 %O₂). The aspirated media was retained at every feed, as on termination of culture the spheroid specific-media and spheroid sample were combined and stored at -80°C until lyophilization under a standard drying protocol (0.200 mBar, -10°C, 16 – 18h). To ensure sufficient GAG accumulation, for detection through biochemical analysis, 3 – 5 spheroids were pooled per technical replicate (together with their media) and dried samples were subsequently papain digested in 100 μ l/spheroid.

A transient GAG regeneration model was created based on the conservation of mass for GAG theory established previously by Gu *et al.* for the human IVD:^{113,335}

$$\frac{\partial(c^{GAG})}{\partial t} + \nabla(c^{GAG}v^s) = Q^{GAG} \quad (7-1)$$

where c^{GAG} is the molar concentration of GAG (per tissue volume) and v^s is the velocity of solid matrix. Q^{GAG} is the synthesis/degeneration rate of GAG (per tissue volume) i.e. the rate of GAG content change and was simply modelled in this work as the balance between GAG synthesis rate (Q^{syn}) and GAG degradation rate (Q^{deg}):

$$Q^{GAG} = Q^{syn} - Q^{deg} \quad (7-2)$$

The GAG synthesis rate was assumed to be dependent on the viable cell density, ρ^{cell} , and GAG degradation rate is proportionally related to the local GAG content (c^{GAG}):

$$Q^{GAG} = \lambda_1\rho^{cell} - \lambda_2c^{GAG} \quad (7-3)$$

where λ_1 is the GAG synthesis rate per cell and λ_2 is the GAG degradation rate. Under the condition of a healthy disc, degeneration is not occurring and as a result Q^{GAG} is assumed to be zero. Therefore, the above equation becomes:

$$\lambda_1 = \frac{\lambda_2 c_0^{GAG}}{\rho_0^{cell}} \quad (7-4)$$

where c_0^{GAG} is the GAG content prior to degeneration and ρ_0^{cell} is the viable cell density at a healthy state. The GAG synthesis rate per cell (λ_1) used in the model were those experimentally determined in this work for each species and were assumed to be invariant with time. The GAG degeneration rate (λ_2) was also assumed to remain constant and has previously been calculated based on the half-life of GAG:^{113,335}

$$\lambda_2 = \frac{\ln 2}{\tau} \quad (7-5)$$

where τ is the half-life of GAG turnover and has been reported to be 11 years.³³⁶ This value has been used in a previous model where the predictions were consistent with measured results.^{113,194,336}

Species-specific GAG content was acquired from the literature and are presented in Table 7.3.^{161,193,195} In the case of human, the initial value set in the model is a disc with Grade III degeneration deemed suitable for treatment with cell-injection. For the animal models, native healthy GAG content was adjusted according to qualitative histological staining following puncture injury or chondroitinase ABC (chABC) injection for rat and goat, respectively. In rat, this corresponded to a 100% reduction in GAG based on Safranin-O staining by Barcellona *et al.* (2021) for caudal discs punctured with a 27 G needle and left two weeks prior to treatment.³²⁶ In goat, this corresponded to a 50% reduction in GAG based on AB staining of lumbar discs injected with 1U of chABC and left twelve weeks prior to treatment.³³⁷ Similarly according to the literature, it can be assumed that establishing an injury model significantly disrupts the cellularity. As a result, a 75% and a 50% reduction in cellularity was employed for rat and goat, respectively.^{338,339} Furthermore, $\mu\text{g}/\text{mg}$ dry weight (DW) of GAG was converted to $\mu\text{g}/\text{tissue}$ volume for input into the *in-silico* model using a species-specific $\text{mg DW}/\text{mm}^3$ conversion factor which was determined experimentally.

Table 7.3 Glycosaminoglycan (GAG) parameters used *in-silico* for the nucleus pulposus (NP) and annulus fibrosus (AF) domains of rat, goat, and human discs.

	Rat		Goat		Human	
	NP	AF	NP	AF	NP	AF
<i>Healthy/native</i>						
<i>GAG content</i> ($\mu\text{g}/\text{mg DW}$)	95.2 ^a	37.5 ^b	335 ^c	95 ^b	537.8 ^d	153 ^d
<i>Degenerated</i>						
<i>GAG content</i> ($\mu\text{g}/\text{mm}^3$)	0	10.6	47.4	26.9	80.7 ^e	30.3 ^e
<i>GAG synthesis</i>						
<i>rate</i> ($\text{pg}/\text{cell}/\text{day}$)	6.19 ^f	-	9.08 ^f	-	8.48 ^f	-

^a Cd9-10 of 12-month male Sprague Dawley rats.¹⁶¹

^b Averaged for inner and outer AF.^{161,195}

^c L4-5 of 2.5 – 3.5 year male goats.¹⁹⁵

^d Grade II human tissue, AF averaged over inner/outer and anterior/posterior region.¹⁹³

^e Grade III human tissue, AF averaged over inner/outer and anterior/posterior region.¹⁹³

^f Experimentally determined in this study.

7.3 Results

7.3.1 Experimentally determined species-specific parameters

To compare the IVD scale-effect between species, the geometry of rat and goat discs was first assessed with respect to caudal and lumbar level, respectively. From Figure 7.8(A) it appears that only one or two caudal discs are used per rat and there is a strong inclination towards using levels Cd6-7 to Cd8-9, with ~ 30% of studies using Cd7-8. Importantly, Cd7-8 was found to be not significantly different from all other investigated levels in terms of disc height (Figure 7.8(B)). Additionally, only discs outside the commonly used range (Cd6-7 to Cd8-9) had a disc diameter significantly larger (Cd3-4 at $p = 0.0007$ and Cd4-5 at $p = 0.0012$) and smaller (Cd9-10 at $p = 0.0467$) than Cd7-8, Figure 7.8(C). Similarly, only Cd3-4 ($p = 0.0096$) and Cd4-5 ($p = 0.0259$) had an NP diameter significantly larger than Cd7-8. For the goat models in Figure 7.8(D), it appears less common to use only one level per animal than to use all five lumbar discs, with no clear predominant level of choice. Despite this, L5-6 is selected half as frequently as L1-2 to L4-5 and although the disc height appears to vary down the lumbar spine, only the central disc height of L2-3 was found to be significantly different to L5-6 ($p = 0.0255$), Figure 7.8(E). The results in Figure 7.8(F) show that as the discs progress down the lumbar section they widen laterally, and the A-P width shortens. The lateral width of L5-6 was significantly larger than L1-2 ($p = 0.0137$), L2-3 ($p = 0.0094$) and L4-5 ($p = 0.0240$), while only the A-P width of L1-2 was significantly larger than L5-6 ($p = 0.0257$).

Figure 7.9(A) presents the native cell density of rat tissue, with separate AF and NP regions fluorescently stained with DAPI, while MTT brightfield images, showing the co-localised formazan crystals, is only presented for AF, as it was indeterminable in the NP matrix as mentioned in Section 7.2.2. Similarly, Figure 7.9(B) presents the native cell density of goat tissue, with a clear distinction between the fibrous lamella of the AF and sparser cell distribution in the NP matrix. Figure 7.9(C) presents the percentage of cells quantified as MTT positive, with rat AF tissue determined as significantly higher than goat AF ($p = 0.013$) and NP ($p = 0.004$) while no significant difference was determined between goat AF and NP ($p = 0.849$). MTT+ visualisation within the rat NP was not feasible due to the highly gelatinous composition. Figure 7.9(D) presents the quantified species-specific metabolically active cell density. It was assumed that the percentage of MTT positive cells in the rat NP would be similar to the AF, as no significant difference was determined between the NP and AF in goat. No significance was found between the cell density of rat NP (94×10^3 cells/mm³) and AF (93×10^3 cells/mm³) tissue ($p = 0.999$), while goat AF (16×10^3 cells/mm³) had a significantly higher cell density than the NP (6×10^3 cells/mm³) ($p = 0.026$). Additionally, it was determined that rat tissue has a significantly greater cell population than the corresponding region of goat tissue ($p < 0.0001$).

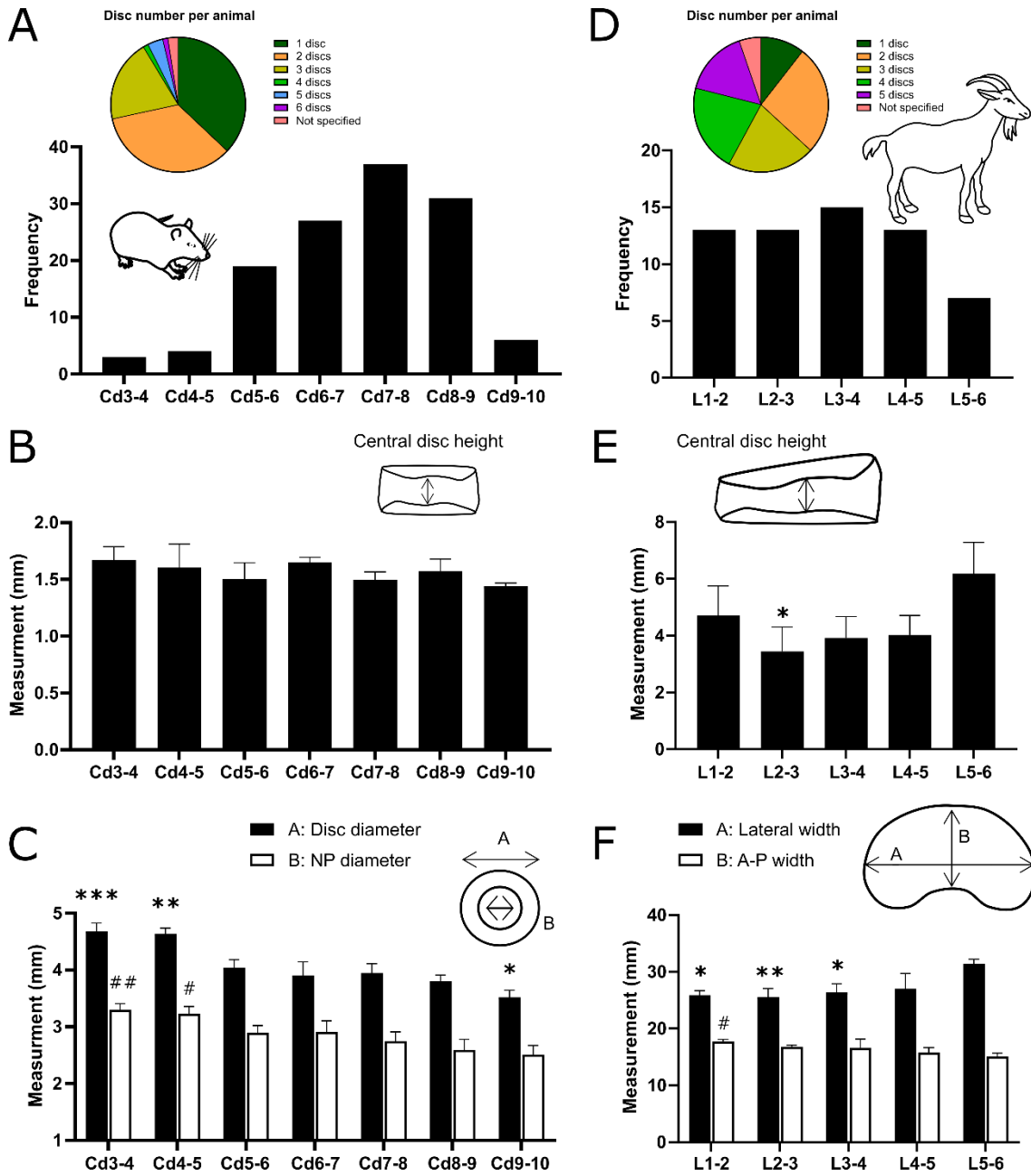


Figure 7.8 Geometrical analysis of rat caudal level Cd3-4 to Cd9-10 and goat lumbar level L1-2 to L5-6. (A) Literature search results for the number of discs per animal and frequency of caudal levels used in published rat tail studies. (B) Experimentally measured central disc height for 8-week-old Wistar rats (N = 6), with no statistical significance found between Cd7-8 (most frequently used) and all other levels within this range. (C) Corresponding external disc diameter and internal nucleus pulposus (NP) diameter. Statistics indicate a significant difference to Cd7-8 full disc (*) and NP (#) diameter with $p < 0.05$. (D) Literature search results for the number of discs per animal and frequency of lumbar levels used in published goat studies. (E) Experimentally measured central disc height for skeletally mature Saanen goats (N = 3), a significant difference was only found between L2-3 and L5-6 (least frequently used). (F) Corresponding lateral and anterior to posterior (A-P) width. Statistics indicate a significant difference to L5-6 lateral (*) and A-P (#) width.

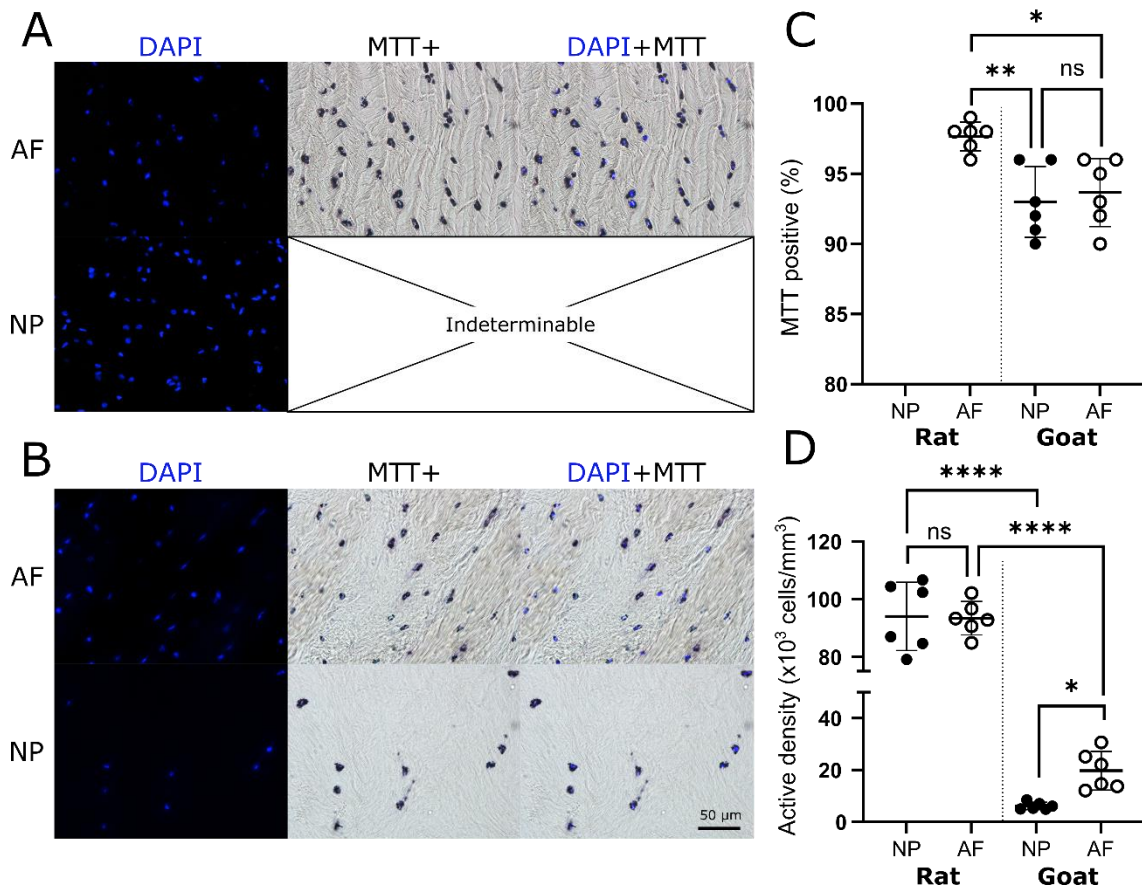


Figure 7.9 Experimentally determined metabolically active cell density for the nucleus pulposus (NP) and annulus fibrosus (AF) of rat caudal and goat lumbar discs. (A) Native rat and **(B)** goat tissue fluorescently DAPI stained to indicate the nuclei of all cells and MTT brightfield imaged to identify co-localised formazan crystals deposition around metabolically active cells. **(C)** The percentage of cells quantified as MTT positive, with rat AF tissue determined as significantly higher than goat AF ($p = 0.013$) and NP ($p = 0.004$) while no significant difference was determined between goat AF and NP ($p = 0.849$). MTT+ visualisation within the rat NP was not feasible due to the highly gelatinous composition. **(D)** Species-specific metabolically active cell density, assuming a similar percentage of MTT positive cells in the rat NP as determined in the AF. No significance was found between the rat NP and AF cell density ($p = 0.999$), while goat AF had a significantly higher cell density than the NP ($p = 0.026$). Additionally, it was determined that rat tissue has a significantly greater cell population than the corresponding region of goat tissue ($p < 0.0001$).

The species-specific disc spheroids were assessed daily in order to ensure that both cell types (NP and AF) from each species (rat, goat, and human) were capable of forming stable cellular-aggregates within the designed culture system over a seven day period. Figure 7.10(A) consists of representative daily microscopic images showing rat NP spheroids within the agarose microwell array. Figure 7.10(B) and Figure 7.10(C) present diameters for rat, goat, and human NP and AF spheroids, respectively. The spheroid diameters were quantified daily to assess condensation and identify when stable spheroids are formed based on the plateau of the temporal graph. The results showed no significant difference in diameters between consecutive days, except for Day 1 and Day 2 in rat AF, human NP and human AF. In general, all spheroids

condensate with diameters decreasing over the first few days. Rat and human spheroids plateau fastest with diameters becoming consistent day 4 – 5, while goat spheroids continue to condensate only beginning to at day 6 – 7. Figure 7.10(D) consists of representative microscopic images of both NP and AF spheroids from rat, goat, and human after seven days.

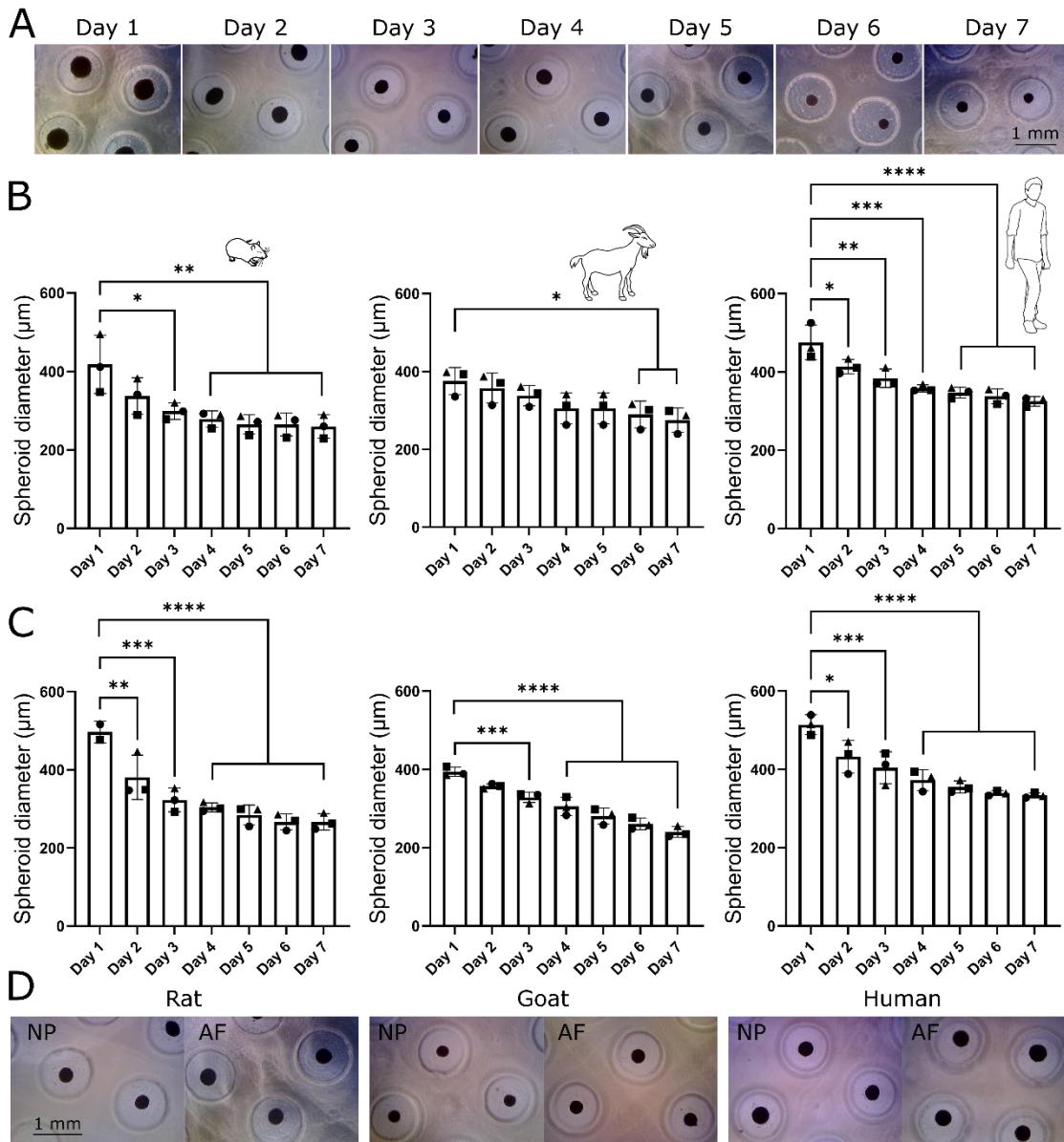


Figure 7.10 Temporal assessment of disc spheroids (nucleus pulposus: NP and annulus fibrosus: AF) from rat, goat, and human over a 7-day culture period. (A) Example of daily microscopic images showing rat NP spheroids within the agarose microwell array. (B) Quantification of spheroid diameters for rat, goat, and human NP cells. Rat spheroids became statistically different to Day 1 at Day 3 ($p = 0.012$), goat at Day 6 ($p = 0.045$) and human at Day 2 ($p = 0.024$). (C) Quantification of spheroid diameters for rat, goat, and human AF cells. Rat spheroids became statistically different to Day 1 at Day 2 ($p = 0.005$), goat at Day 3 ($p = 0.0007$) and human at Day 2 ($p = 0.0101$). (D) Microscopic images of both NP and AF spheroids from rat, goat, and human after seven days.

Prior to carrying out the metabolic flux analysis, the cell viability of the spheroids was qualitatively assessed to ensure an acceptable level of cell viability (> 80%) to later perform normalisation of the consumption and production rates. Due to the 3D and compact cell nature of the spheroids, an exact quantitative assessment was not feasible. Figure 7.11(A) presents representative images indicating a high viability of both NP and AF spheroids for all species within the agarose microwell array culture system. Figure 7.11(B) shows that in 3D spheroid form, human NP cells have a significantly lower OCR than rat NP cells ($p = 0.0005$) and goat NP cells ($p = 0.0031$), while human AF was only significantly lower than goat AF ($p = 0.0352$). Furthermore, Figure 7.11(C) shows that rat NP cells had a significantly higher LPR than both goat NP cells ($p = 0.0068$) and human NP cells ($p = 0.0119$), while no significant differences were detected among AF cells across the different species.

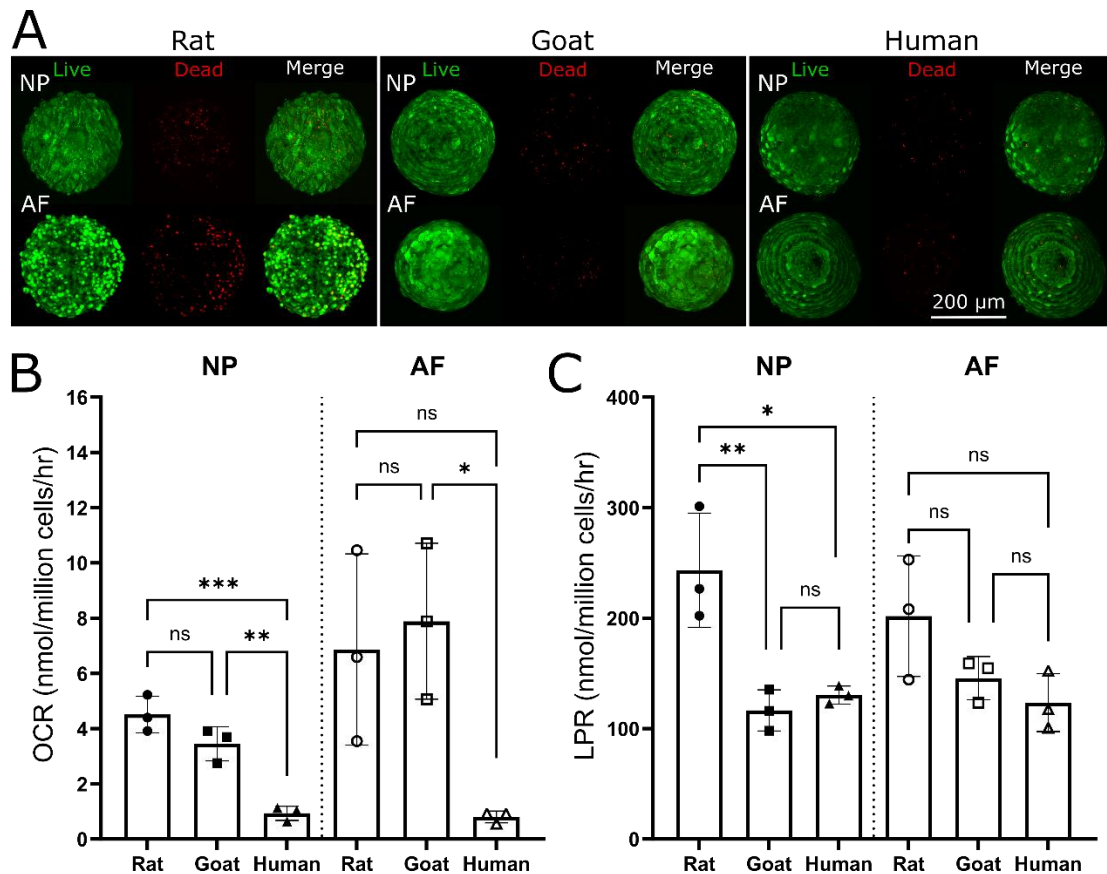


Figure 7.11 Viability assessment and measured metabolic rates of nucleus pulposus (NP) and annulus fibrosus (AF) spheroids from rat, goat, and human. (A) Spheroids were assessed using Live/Dead staining to ensure viability remained high prior to carrying out metabolic rate measurements. (B) Oxygen consumption rates (OCR) and (C) lactate production rates (LPR) for disc cells assessed in a 3D spheroid configuration ($N = 3$). Human NP cells had a significantly lower OCR than rat NP ($p = 0.0005$) and goat NP ($p = 0.0031$), while human AF was only significantly lower than goat AF ($p = 0.0352$). Rat NP cells had a significantly higher LPR than goat NP ($p = 0.0068$) and human NP ($p = 0.0119$), while no significant differences were detected for AF cells.

Figure 7.12 presents the species-specific matrix synthesis rates calculated over a two-week culture period and normalised by the DNA content/cell number per micro-spheroid. Furthermore, histological evaluation is included, highlighting the GAG and collagen distribution within the micro-spheroids using AB and PSR staining, respectively. The GAG synthesis rates of rat NP cells were found to be significantly lower than goat NP cells ($p = 0.0385$). However, no significant difference was detected between the human NP cells and the two animal species. Nonetheless, human NP cells had significantly lower collagen synthesis rates than both rat ($p = 0.0093$) and goat ($p = 0.0033$) NP cells, while no significant difference was detected between the two animal species.

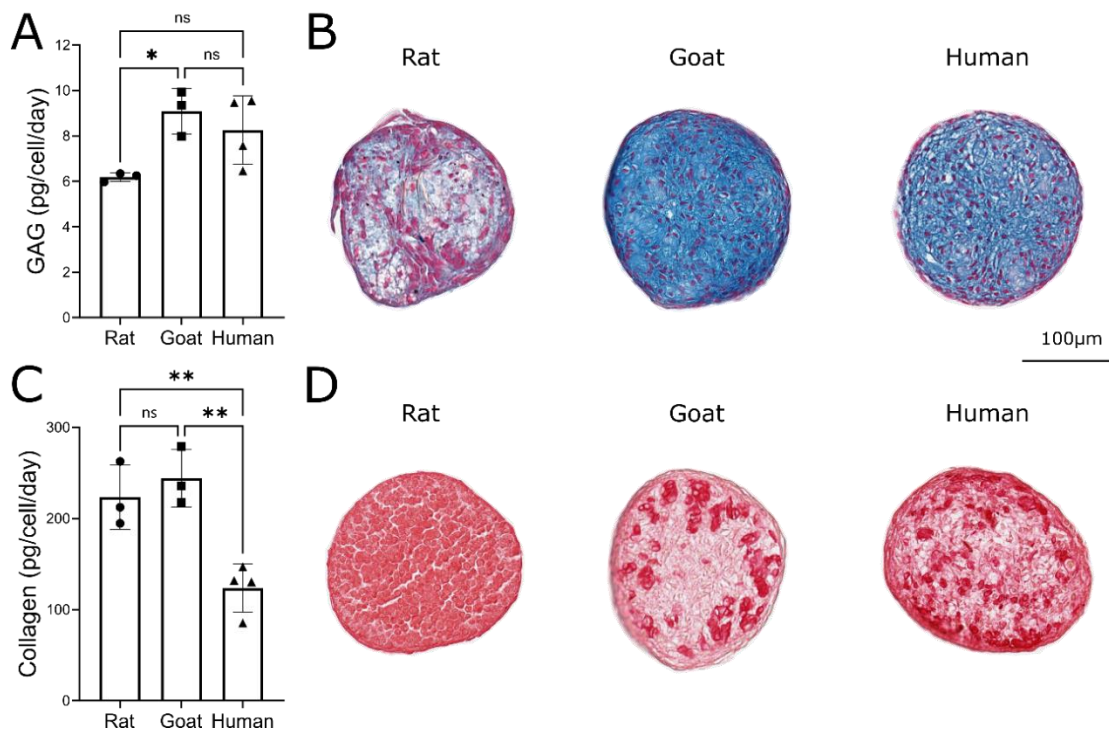


Figure 7.12 Species-specific matrix synthesis rates and histological evaluation of nucleus pulposus (NP) micro-spheroids. (A) Glycosaminoglycan (GAG) production rates for rat ($N = 3$), goat ($N = 3$), and human NP cells ($N = 4$) over a two-week period. Rat NP cells had a significantly lower production rate than goat NP cells ($p = 0.0385$). (B) Corresponding histological evaluation using alcian blue (AB) to stain for GAG. (C) Collagen production rates for rat ($N = 3$), goat ($N = 3$), and human NP cells ($N = 4$) over a two-week period. Collagen production rates for human NP cells were significantly lower than both rat ($p = 0.0093$) and goat ($p = 0.0033$) NP cells. (D) Corresponding histological evaluation using picrosirius red (PSR) to stain for collagen.

7.3.2 Predicted differences in regeneration capacity and nutrient microenvironments between species.

As mentioned previously, *in-silico* modelling was used to inform the external boundary condition of the microwell culture system, in order to cultivate and retain a relatively stable and physiologically relevant microenvironment within the individual micro-spheroids. Figure 7.13 presents the results of this iterative process, where the experimentally measured species-specific metabolic rates and spheroid diameters were implemented to predict the metabolite concentrations within the micro-spheroids. Figure 7.13(A) shows that the micro-spheroids should be cultured in LG and that the culture system needs to undergo a daily media refresh in order to maintain relatively stable levels of glucose and pH within the spheroids. If the system is maintained for three days, as is typically cell culture standard practice, the glucose and pH levels drop significantly lower compared to the baseline levels. Furthermore, these *in-silico* models aided in the initial design of the culture system and the selection of an optimum cell seeding density. An optimum cell number was defined as sufficient cells to elicit detectable changes in metabolism, within a specific timeframe, while ensuring that metabolite gradients are not forming within the micro-spheroids (Figure 7.13(B)). Inevitable experimental variation in spheroid diameter and cell number were accounted for by modelling three microwells of the agarose array for each species. Figure 7.13(C) presents the average concentrations predicted within the spheroids with the standard deviation accounting for these experimental diversities. Glucose concentration and pH levels were predicted to be relatively comparable between species, at approximately 3.5 mM and pH 7. However, oxygen was predicted to be higher within the human spheroids compared to the animal spheroids, despite a consistent external boundary concentration to the culture systems, this was due to significantly lower OCR measured for human (Figure 7.11(B)).

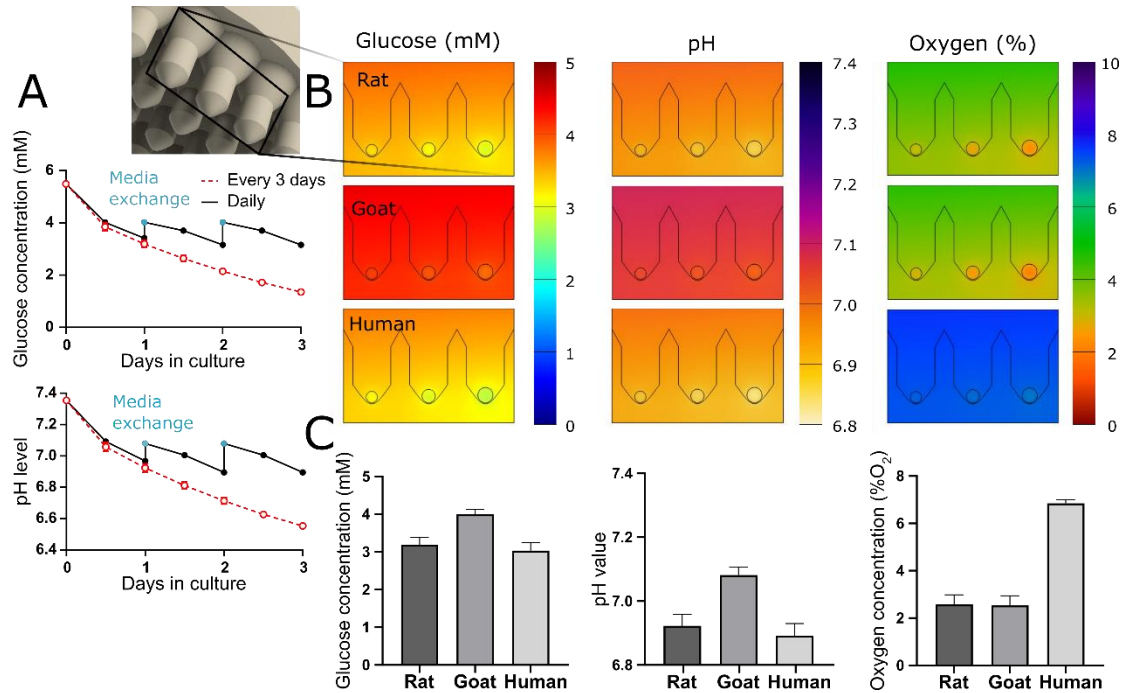


Figure 7.13 *In-silico* modelling of the microwell culture system to inform the external boundary concentrations necessary to create a physiologically relevant microenvironment within the spheroids. Predicted average glucose and pH concentrations within spheroids which underwent a culture media exchange every three days or a daily media exchange. (B) Contour plots of glucose, pH and oxygen distributions within three microwells of the agarose array for rat, goat and human (top to bottom). (C) Average concentrations predicted within the spheroids presented above, with the standard deviation accounting for the minor variation in diameter of the three spheroids presented for each species.

Figure 7.14 presents the predicted GAG matrix regeneration in the NP of a pre-clinical rat and goat model compared to predicted regeneration within human clinical trials for cell-based therapies. As detailed previously, all investigated parameters were selected based on what has been reported in the literature for these specific animal models or registered publicly for clinical trials. Figure 7.14(A) predicts that based on the experimentally determined rat matrix synthesis rates, substantial regeneration is feasible in rat caudal models within a 12-week timeframe. Injection delivery of 2,000 or 25,000 cells accounts for only 0.2% or 3% of the healthy species-specific NP cell density, respectively. Despite these relatively low cell treatment numbers, the literature has reported MRI signal to be significantly higher than punctured controls as early as four weeks and superior histological staining for GAG at around 6 – 8 weeks, as highlighted in the graph (Figure 7.14(A)).^{326–329}

Figure 7.14(B) predicts that based on the experimentally determined goat matrix synthesis rates, substantial regeneration is feasible in goat lumbar models within a 12-month timeframe. Injecting 1 million or 5.5 million cells accounts for 30% or 165% of the healthy species-specific NP cell density, respectively. It has been reported in the literature that cell treatments showed significantly higher aggrecan expression and histological staining compared to injured control and performed superior to acellular treatments around six months, as highlighted in the graph.³⁴⁰ Figure 7.14(C) predicts that based on the experimentally determined human matrix synthesis rates, together with the substantially larger scale of the human IVD, the timeframe for functional GAG regeneration is a matter of years and it is highly dependent on the number of cells injected clinically. With no cell injection degeneration is predicted to continue from Grade III toward Grade IV over ten years. A low dose of 1 million cells fails to prevent further degeneration, while a dose of 5 million cell is predicted to maintain the GAG levels at those of Grade III, without further degeneration. A treatment dose of 10 million cells is predicted to be capable of initiating regeneration. Nonetheless, GAG matrix recovery is predicted to be only 65% of Grade II levels after 10 years. Doubling this dose to 20 million cells predicts recovery to Grade II levels of GAG at ~ 10 years, while quadrupling the dose to 40 million predicts recovery to Grade II levels of GAG within 4 years. Figure 7.14(D) presents an example of the *in-silico* contour plots for rat (25×10^3 cells), goat (5.5×10^6 cells), and human models of GAG regeneration. Predicted GAG results are normalised to the native/healthy NP content for rat and goat and Grade II content for human and the geometries are presented to scale to emphasise the scale-effect and the timeframe predicted for animal model regeneration compared to the trajectory of human clinical trials.

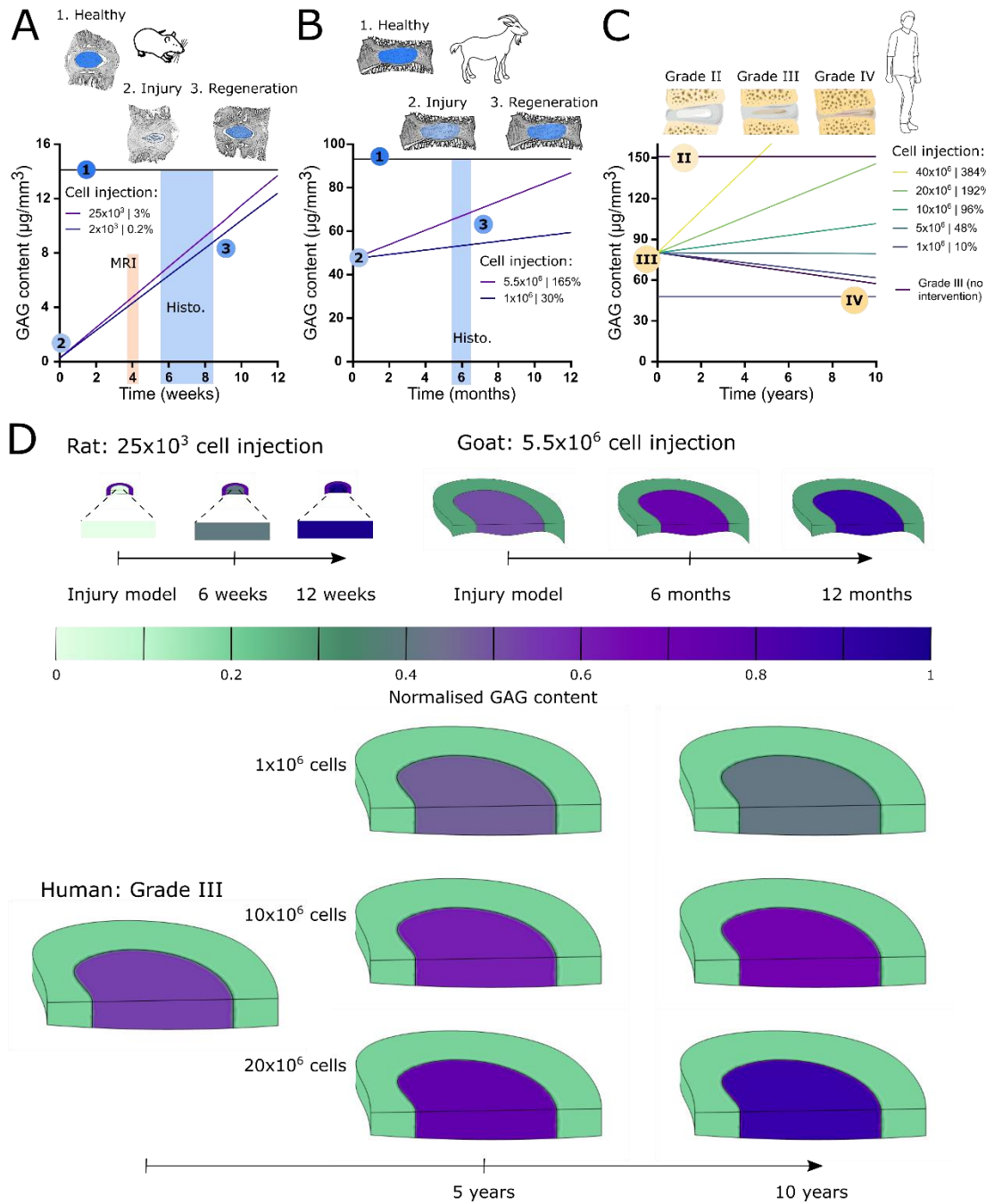


Figure 7.14 Predicted glycosaminoglycan (GAG) matrix regeneration in the nucleus pulposus (NP) of a pre-clinical rat model, goat model and human clinical trials for cell-based therapies. (A) Predicted GAG regeneration in a rat degeneration model injected with 2×10^3 (0.2% of healthy NP cell population) or 25×10^3 (3% of healthy NP cell population) cells over a 12-week study. The shaded regions either indicate when MRI signal has been reported as significantly higher or histological GAG staining significantly stronger compared to an injured control, in the literature. (B) Predicted GAG regeneration in a goat degeneration model injected with 1×10^6 (30% of healthy NP cell population) or 5.5×10^6 (165% of healthy NP cell population) cells over a 12-month study. (C) Predicted GAG regeneration in a clinical trial injected with 1×10^6 – 40×10^6 cells (10-383% of Grade III NP cell population). (D) A sample of corresponding contour plots for *in-vitro* rat (25×10^3 cells), goat (5.5×10^6 cells), and human models of GAG regeneration (geometries presented to scale). GAG is normalised to the native/healthy NP content for rat and goat and Grade II content for human.

Figure 7.15 presents the nutrient microenvironments predicted within pre-clinical rat and goat models. Figure 7.15(A) highlights the predicted glucose distribution within a healthy rat and goat disc compared to an injury model injected with the upper range of 25,000 and 5.5 million cells, respectively. Figure 7.15(B) presents the A-P profile of glucose through the disc, further incorporating the lower range of cell injection and the effect of injury (without cell injection). Similarly, Figure 7.15(C) highlights the predicted pH distribution, Figure 7.15(D) the corresponding A-P profile of pH, Figure 7.15(E) highlights the predicted oxygen distribution and Figure 7.15(F) the corresponding A-P profile of oxygen through the disc. In summary, it is predicted that a Cd7-8 disc in rat has an approximate central microenvironment of 2 mM glucose, pH of 6.9 and oxygen level of 1.5 %O₂, while a L3-4 disc in goat has an approximate central microenvironment of 1.4 mM glucose, pH of 6.9 and oxygen level of 2 %O₂. In both animal models, inducing an injury results in disrupted cell density within the NP and thus predicts higher levels of nutrients and less acid build-up than a fully functioning healthy disc. Injecting either 2,000 or 25,000 cells into an injured rat model is not predicted to alter the injured microenvironment as these cell numbers represent only 0.24% and 3% of the native/healthy NP cell population. However, injecting 1 million cells (30% of the native/healthy NP cell population) into the injured goat model is predicted to restore the nutrient microenvironment to that of a healthy state, while injecting 5.5 million cells (165% of the native/healthy NP cell population) is predicted to slightly reduce nutrient concentrations and pH below the healthy levels.

Figure 7.16 presents the predicted nutrient microenvironment within a Grade III human IVD undergoing clinical assessment for a range of injected cell numbers. Firstly, Figure 7.16(A-C) presents the distribution of glucose, pH and oxygen across the IVD with either no cell treatment or a high cell dose of 10, 20 or 40 million cells and Figure 7.16(D) presents the corresponding A-P profile of glucose, oxygen and pH for all investigated doses from 1 million to 40 million cells. As expected, increasing the cell dose further exacerbates the nutrient microenvironment. Secondly, Figure 7.16(E) compares the resulting central NP concentrations across the pre-clinical animal models and the clinical human models. An important finding is that the typical ranges of cell injection in rat and goat models do not appear to significantly alter the nutrient microenvironment from its healthy steady-state levels. However, different nutrient microenvironments are predicted to be established clinically depending on the number of cells being implanted. For example, at the highest dose of 40 million cells, glucose is predicted to drop below 1 mM, pH to 6.8 and oxygen below 1 %O₂.

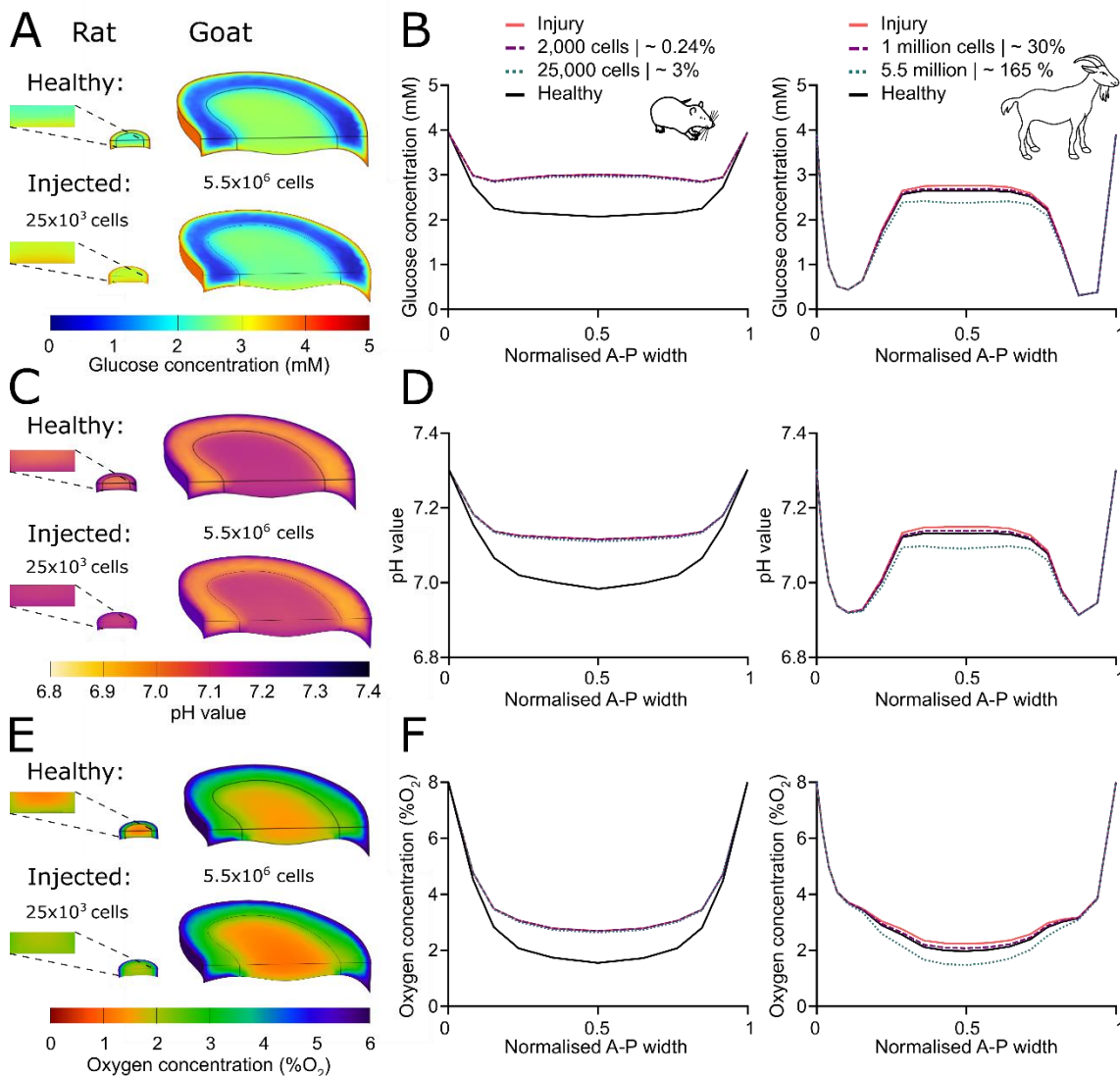


Figure 7.15 Predicted nutrient microenvironments within pre-clinical rat and goat animal models assessing cell-based therapies. (A) Predicted glucose distribution across a healthy rat and goat disc compared to an injury model injected with cells. (B) Anterior to posterior (A-P) profile for glucose, at mid-height, through the corresponding *in-silico* models for rat and goat. (C) Predicted pH distribution across a healthy rat and goat disc compared to an injury model injected with cells. (D) A-P profile for pH, at mid-height, through the corresponding *in-silico* models for rat and goat. (E) Predicted oxygen distribution across a healthy rat and goat disc compared to an injury model injected with cells. (F) A-P profile for oxygen, at mid-height, through the corresponding *in-silico* models for rat and goat.

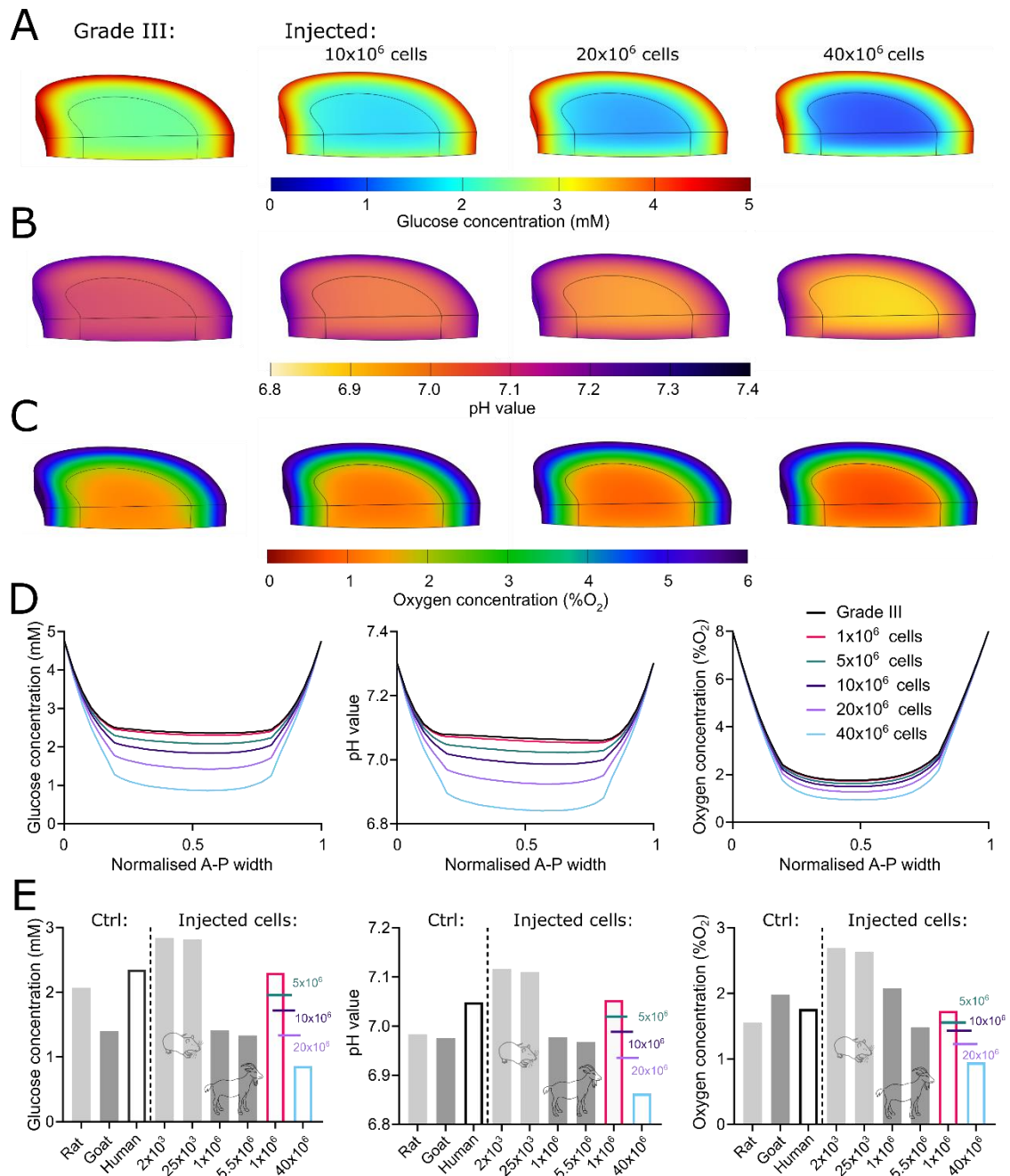


Figure 7.16 Predicted nutrient microenvironments within a Grade III human intervertebral disc (IVD) undergoing clinical assessment for a range of injected cell numbers. (A) Predicted glucose, **(B)** pH and **(C)** oxygen distribution across a Grade III human IVD with no treatment or with an injection of 10x10⁶, 20 x10⁶ or 40 x10⁶ cells. **(D)** Corresponding anterior to posterior (A-P) profile of glucose, pH, and oxygen at mid-height, through each of the *in-silico* models. **(E)** Minimum metabolite (glucose, pH and oxygen) concentrations within the NP for both pre-clinical animal models and clinical human models, under control (ctrl) conditions i.e. healthy animal and Grade III human, compared to the investigated ranges of cell numbers for each species.

7.4 Discussion

A significant hurdle for potential cell-based therapies is the subsequent survival and regenerative capacity of the implanted cells.^{9,11,83,96,98} While many exciting developments have demonstrated promise in this regard pre-clinically, cell-based therapies for DDD fail to translate equivalent clinical efficacy.⁵⁻⁷ As a result, the urgency to ascertain the clinical relevance of different animal models has not only ethical merit but also important scientific value for the acceleration of successful translation. This work investigated both a small and large animal model, comparing them to the human IVD from the perspective of anatomical scale, cellular metabolism and regenerative potential. Importantly, this work highlights the power of *in-silico* modelling, not only to predict the regeneration timeframe of animal models compared to the more stunted success of human clinical trials, but to inform the design of pre-clinical assessment and manage the expectations of clinical evaluation.

With regard to LBP, there is a clinical consensus that short-term pain should be treated conservatively. However, when interventions are considered to combat degeneration, a therapy would ideally need to be minimally invasive, delivered in a single operation and as easily adopted by clinicians as standard operating procedures such as microdiscectomy. Given that the degenerative cascade has been characterised by a loss of viable and functional cells, regenerative medicine or tissue engineering approaches propose minimally invasively replenishing the IVD with an injection of active cells. The overall objective is to restore tissue structure and preserve spinal motion. As a result, the implanted cells must produce a sufficient amount of disc-specific ECM and inhibit or retard further degeneration *in vivo*. While no animal studies completely restore the IVD structure, pre-clinical results suggest cause for optimism.³¹⁵ However, as mentioned extensively in the previous chapters, the effect of a challenging biochemical microenvironment on viability and normal cell function will undoubtedly impact the degree of subsequent regeneration. Therefore, it is imperative to determine (i) how many cells are needed to restore the NP matrix, (ii) in what timeframe functional results are to be expected, (iii) how this may vary across species and (iv) whether the microenvironment can sustain such a cell dose without further exacerbating the challenging biochemical niche.

From reviewing pre-clinical literature for DDD, there is a strong preference for the rat caudal model over a large animal model such as goat, both from the perspective of feasibility and affordability. The lower financial and animal husbandry burden is reflected in the high number of rats per study and an inclination towards using only one or two caudal levels per animal, as opposed to fewer goats and the use of almost all lumbar levels per study.^{329,337,341,342} According to the geometrical analysis there is no major concern that caudal level could be a confounding factor on the nutrient microenvironment between Cd5 to Cd9, as no significant difference in geometry was identified. As a consequence, it may be advised to remain within this most commonly used

range. Similarly, goat lumbar level geometry is not significantly different between L1 to L5. However, L5-6 should be considered different to other lumbar levels in terms of disc height and width (both lateral and A-P). The profound importance of disc geometry and scale comes into its own when comparing species. For example, it is estimated that a single human NP is almost 800 times the volume of a rat NP and 12 times that of a goat NP. Furthermore, this study highlights the astronomically higher cell density of the smaller animal models, with the rat having a 60-fold higher and goat a 4-fold higher NP cell density than the sparse human densities measured previously.^{24,25} As mentioned earlier, it is often hypothesised that the diffusion distances across a disc will determine the central metabolite concentrations along with the cellular density, with an inverse relationship between disc height and cell density.²⁰⁷ This is reflected throughout the current work with the scale-effect on both geometry and cell density balancing out to establish relatively similar nutrient concentrations within healthy rat, goat and human discs. Although no other study has attempted to quantify and compare the metabolically active cell density of both NP and AF tissue across different species, the values can be compared to individual rat and goat studies which have assessed cell density in some manner.^{311,343} While the mean cell densities determined within this work are slightly higher, values reported in the literature lay within the standard deviation of the current findings.

In addition to the differences in cell density between species, an appreciation needs to be afforded to the number of cells to be injected into the disc in terms of how these cell doses compare to the resident cell population and how this translates from a pre-clinical animal model to a human. From reviewing the clinical trial parameters it has been reported that total cell numbers ranging from 1 to 40 million cells are being used (excluding bone marrow concentrates).^{176,344} Furthermore, it appears that just as much variation exists among pre-clinical studies, with rat models receiving a range of 2 – 25 thousand cells and goat typically receiving 1 – 5.5 million cells.^{326–329,337,340} For the first time this work sought to contemplate how these ranges compare to the native NP density of the respective species. It has often been postulated that the injection of a significantly large number of cells may exacerbate the biochemical microenvironment, due to competing nutrient demands, and thus the precise cell number being delivered needs to be carefully considered.^{6,207} However, prior to this work the exact number of cells required for functional regeneration was unclear. Many cell therapy development studies focus on showing that cells can produce the desired disc-specific ECM, but it is imperative to identify the timeframe within which these cells can lay down this matrix and subsequently regenerate the IVD.

It was initially hypothesised that animal cells would have higher matrix synthesis rates compared to human cells. However, this was not detected across all ECM components in the current study. While the collagen production rates for animal cells were significantly higher than human, it was surprising that rat cells had the lowest GAG synthesis rates among the species and

no significant difference was found between goat and human. Nonetheless, GAG synthesis rates on a per cell basis were relatively low across all species and on average were only ~ 4% of that of collagen. Not only is this particularly important for the regenerative potential of these cells but compared to collagen and elastin, IVD aggrecan displays a more rapid turnover as it is more susceptible to proteolysis due to its less compact structure.³⁴⁵ Therefore, overall matrix synthesis and turnover needs to be balanced to have a net regenerative effect. A previous *in-silico* study investigated the effect of increasing GAG synthesis rate and decreasing the GAG degradation rate of resident NP cells without further cell injection. In both cases mildly degenerated discs were predicted to repair effectively but neither could circumvent severely degenerated discs.³³⁵ Nonetheless, this study was theoretically based and biological treatments to alter the synthesis and degradation rates of GAG *in vivo* need further exploration. The half-life of GAG turnover used in the current work was derived from experimental literature and had been used in the aforementioned work, together with a previous model by the same authors, where the predictions were consistent with experimental measurements.^{113,194,336} However, a caveat of this work is consistent degradation between species, whereas the half-life of aggrecan is an increasing function of age and may be consistently lower for degenerate human IVD tissue compared to animal.³⁴⁵

Nonetheless, the current work showed that based on experimentally determined native GAG synthesis rates, substantial regeneration is feasible in rat within a 12-week timeframe despite the injected cell numbers being < 5% of the native NP population. Regeneration is also predicted to be feasible in goat within a 12-month timeframe. However, substantially higher cell doses are necessary. A dose of less than half the NP cell population will only slightly regenerate the GAG matrix, whereas a cell dose of over 1.5 times the NP population was predicted to be necessary to restore GAG to levels close to a healthy goat disc. Meanwhile, the human results predict further deterioration of a mildly degenerated Grade III disc over ten years without a curative cell injection, while a dose of five million cells is necessary to prevent GAG content diminishing further in the substantially larger human IVD. Nonetheless, a higher treatment dose of 10 – 40 million cells is predicted to be capable of initiating regeneration, with the substantial timeframe for functional GAG restoration being years and highly dependent on the number of cells injected clinically (4 – 10 years).

The IVD develops embryologically from the mesenchyme, with the NP formed by the highly specialised notochordal cells which produce the primary matrix components. These cells eventually die off into adulthood being replaced by NP cells when the avascular tissue has thickened and fully formed.^{19,173} Injected cell-based NP or MSC therapies are not these highly specialised notochordal cells which have developed in the unique disc microenvironment. While cell therapies may be sufficient to synthesise adequate amounts of GAG in the thinner discs of pre-clinical animal models, there are significant hurdles for these therapies clinically. For

instance, repair using NP transplantation in a small rat model indicated that cell implantation had a significantly greater disc height index (DHI) compared to the puncture control at just eight weeks and demonstrated increased central matrix composition through Safranin-O staining.³²⁶ Similar follow up studies have been performed in clinical trials on the human IVD.^{230,346-348} Despite positive results such as increased disc fluid content in treated patients reported at 1- and 2-year follow-up, there is an overall scarcity in the literature on clinical trials and published reports tend to be vague in their shortcomings and no tremendous breakthroughs have been reported.^{230,349}

It appears that follow up assessments are typically from six months to three years, whereas the results of this work predict a longer timeframe for detectable functional regeneration which may contribute to ineffective clinical outcomes and conclusions. Furthermore, many studies only report on pain and disability (VAS and ODI) at follow up.^{350,351} Linking to clinical results which are available using functional MRI assessment, the predicted inefficacy of one million cells is reflected in a study which revealed only a single patient had a mild improvement at three years after a dose of one million activated NP cells.²⁵⁴ Furthermore, the predicted requisite of at least ten million cells for functional regeneration is reflected in a study which reported elevated water content at twelve months after a dose of ten million BM-MSCs, but no recovery in disc height, which according to the predictions of this current work is not unsurprising at such an early stage.²²⁷ Similar promise was reported for eight patients after an injection of ten million juvenile chondrocytes at an early time point of twelve months.²²⁸ However, the fundamental question remains whether the microenvironment can sustain the cell doses being delivered. For example, a study reporting cell doses ranging from 15 – 52 million revealed mixed results in a long term feasibility study (4 – 6 year follow up).³⁵² While a positive correlation between the overall improvement and the total number of cells injected was reported, the ~ 52 million cells were administered to a 24 year old patient who exhibited maintenance of disc height while ~ 28 million cells were administered to a 53 year old patient who exhibited mild progression of DDD. Therefore, it has been postulated that the inherent microenvironment and thus the optimal cell dose may vary significantly on a patient to patient basis as reported for *in vivo* disc measurements.^{10,77}

This work does not imply that cell-based therapies are inevitably “doomed” clinically and that they are not worthy of further pursuit or exploration. More exactly, this work suggests a need to manage expectations in terms of the timeframes needed to achieve successful clinical outcomes while balancing the maximum number of cells which can be injected without detrimentally perturbing the nutrient microenvironment. Within the pre-clinical models, it was predicted that inducing injury causes the nutrient concentrations to increase (due to disrupted cell density), which has been experimentally measured in goat models (Dr Lachlan Smith, University of Pennsylvania, USA; personal communication of unpublished data Nov 2022). As a result, when

cells are then injected, the microenvironmental niche is not exacerbated to the same extent as the larger degenerating human IVD. It is speculated that this may explain DiscGenics Inc. moving from ten million cells in their pre-clinical rabbit model, to a low dose of three million and a high dose of six million cells in their ongoing clinical trials (NCT03347708).¹⁷⁵ While this work predicts that a clinical dose of at least 40 million cells is necessary to achieve healthy Grade II levels of regeneration within five years, it also predicts that 40 million cells will adversely affect the nutrient microenvironment with glucose reducing below 1 mM, pH below 6.9 and oxygen below 1 %O₂. As a result, the models in this work predict ten million cells to be the upper limit for cell-based regeneration. In particular, this is due to the build-up of lactate, as the detrimental effect of acidity on cells has been well established in the literature, reporting increased cell death, decreased proliferation and inhibited anabolic gene expression resulting in decreased matrix accumulation.^{97,99,322} These predictions correlate with our earlier models (Chapter 4), and as mentioned previously, may reflect the clinical shift from early trials using 20 – 60 million cells per disc to Mesoblast Ltd. progressing with a lower dose of six million cells in Phase 3 trials (NCT02412735) following the comparison of a low and high dose in Phase 2 trials (NCT01290367).^{227–230,280}

The comparison of metabolic rates between species in this work found that human cells (both NP and AF) had significantly lower OCRs than animal disc cells, signifying lower respiration in the human cells. This supports previous evidence that disc cells acquire most of their energy from glycolysis due to the large human IVD being a challenged oxygen environment.^{28,58} Meanwhile, animal AF cells having a higher OCR than their corresponding NP cells may be a result of an oxygen gradient through the tissue *in vivo*, with more aerobic respiration occurring under higher oxygen levels. A positive Pasteur effect describes the phenomenon where glycolysis (in this case LPR measurement) is suppressed by high oxygen concentrations and subsequently results in an increase in respiration. While this was detected for rat with NP cells having higher LPR than AF cells, goat NP cells did not appear to have higher rates of LPR than AF cells despite their lower OCR. However, this must be approached with some caution as this study did not directly investigate the effect of nutrient concentrations on metabolic rates for NP and AF cells. As mentioned in Section 2.3.3, several studies have observed a positive Pasteur effect in NP and AF cells (canine, porcine and bovine),^{28,58,91,94} while a recent study with porcine cells observed a positive Pasteur effect in AF cells but not NP cells.⁹⁵ Additionally, below 8 %O₂, oxygen has been shown to decrease the rate of LPR, while above 10 %O₂ the effect of oxygen was insignificant (i.e. a negative Pasteur effect).⁹ It is speculated that the large standard deviation in the AF rates measured may be due to not separating the AF into inner and outer regions. Furthermore, it has been demonstrated that human NP and AF cells have different GLUT expression profiles suggesting regional differences in the metabolic nature of the human IVD.¹¹ However, the current study was unable to detect a significant difference between the human NP

and AF in particular. Together, this may be due to challenging identification of the distinct tissue regions in samples from microdissection surgeries. The lack of specific markers for AF cells has hampered protocols to confirm distinct NP and AF cell populations. However, new markers such as CD146 and Mohawk (MKX) have been identified to characterise AF phenotype and provide opportunities to identify more distinct cell populations.¹⁹⁰

When compared to the literature for human disc cells, OCR measured in this study is significantly lower. Cisewski *et al.* (2018) culture expanded healthy and degenerated human disc cells in monolayer to achieve a sufficient number of cells to carry out investigations into OCR on a cell suspension.⁹³ However, culture expansion has been shown to shift chondrocytes from a glycolytic to an oxidative energy metabolism within seven days *in vitro*.³²¹ The current study is the first to measure the metabolic rate of disc cells in a 3D spheroid configuration where cell to cell interaction and pericellular matrix deposition enhance cell attachment, proliferation, matrix production and phenotype expression.³⁵³ Additionally, this micro-spheroid culture system was favoured as it can be used with low seeding densities, which minimises nutrient gradients and reduces the need for culture expansion, thus limiting alterations to the cell metabolism and loss of disc cell phenotype. One limitation of these rates is that viability was not quantitatively assessed to adjust the normalisation by total DNA content and may result in rates being calculated to a lower level. Nonetheless, the use of the Seahorse analyser results in a high-throughput and significantly more sensitive system, with a 2.3 μL micro-chamber created around each individual spheroid as opposed to the 175 μL – 4 mL metabolic chambers used previously.^{9,90,93} In order to calculate the GCR of disc cells for the *in-silico* modelling, an assumption of 2:1 glycolysis was made. Although there is literature to suggest this ratio can change, it does not alter significantly enough to invalidate this assumption. Overall, the higher glycolytic rates for disc cells, measured in terms of LPR in this work, indicate a less efficient pathway of energy production. Despite similar rates of GAG production between species, higher OCR in animal cells indicate more efficient energy production, with aerobic respiration producing thirty-six ATP molecules per molecule of substrate compared to two ATP through anaerobic glycolysis.

Taken together, this work provides insight into the cell number capable of surviving and initiating repair without exacerbating the microenvironmental niche. It has previously been implied that the impoverished nutrient levels impose an upper limit on the cell number which can be implanted.^{5,7,227,280,348} However, this is the first work to theoretically propose a cell dose which attempts to balance both the biochemical microenvironment and sufficient matrix synthesis for functional repair. Furthermore, this study informs the timeline within which positive changes could be expected and detected clinically. The main findings of this chapter is that these *in-silico* models compare favourably to the pre-clinical literature in terms of the capabilities of animal regeneration. However, they predict very long timeframes (of the order of years) for regeneration in the large human IVD. It is speculated that this may explain the variable results emerging from

trials and the failure of cell-based regeneration to be adopted clinically.^{174,176,344,354–357} Despite the important insights provided in this work, it is important to bear in mind that cell-based therapies first and foremost initiate matrix deposition and compositional change to the disc and this is the extent of the predictions within this work. However, DDD and its associated spinal pain is a complex multifactorial process and in order to be clinically viable, therapeutic strategies need to alleviate pain perception. Currently there is no direct measurement of pain, only of the perceived disability it causes clinically, while pre-clinical animal models are also unable to communicate accurately the level of ongoing pain which they are suffering.¹²¹ Nonetheless, in order to prevent occurrences which lead to pain, the regeneration and preservation of a healthy functional IVD is important.³⁵⁸ While this work enables the research field and clinicians to manage expectations on cell-based regeneration, it suggests our credulousness that cells alone will be sufficient to establish de novo GAG matrix and bring about “functional change” to a degenerating disc. Perhaps cell therapies are better placed as a preventative rather than curative therapy, where a successful outcome is simply impeding further degeneration in the long term. As a result of elucidating the temporal and scale limitations of relying solely on cells, this work advocates the prospects of alternative therapeutic strategies such as re-programming cells through microRNA and gene engineering approaches or preconditioning and priming strategies.^{7,322,359} Moreover, combining cell approaches with biomimetic biomaterials may be a more potent therapy to restore or recreate the structural and biochemical composition of the damaged tissue within an expedited timeframe.³⁶⁰

7.5 Conclusion

For the first time this work corroborates what has long been postulated, that the scale-effect of cell-based human IVD regeneration is not trivial. The IVD is the largest avascular structure in the body with significant diffusional distances which hamper the nutrient supply to both inherent disc cells and injected therapeutic cells. This work presents *in-silico* models which correlate favourably to pre-clinical literature in terms of the capabilities of animal regeneration and predicts that compromised nutrition is not a significant challenge in small animal discs. On the contrary, this chapter highlights a very fine clinical balance between an adequate cell dose for sufficient repair, through de novo matrix deposition, without exacerbating the human microenvironmental niche. While these findings help to explain the failed translation of promising pre-clinical data and the stunted results emerging from clinical trials at present, they also enable the research field and clinicians to manage expectations on cell-based regeneration. Furthermore, these results may inform the design of clinical trials in terms of more long term follow up assessment (over a number of years) for positive functional change. Additionally, as computing power and software capabilities increase, it is conceivable that the future holds the generation of patient-specific models which could be used for patient assessment, as well as pre- and intraoperative planning.

Chapter 8. Final Discussion

LBP is a major global socio-economic concern, with the primary cause believed to be disc degeneration, which may lead to nerve ingrowth, facet joint arthritis and obstructions such as disc herniation or osteophyte formation, which can impinge on nerve roots and the spinal cord. Despite its prevalence and debilitating consequences, current clinical treatment for LBP primarily aims to alleviate pain rather than treat the underlying degeneration. With the burden of an aging and increasingly sedentary population, significant research into regenerative therapies has been undertaken in an attempt to halt the degenerative process or initiate repair within a degenerated IVD. Ultimately, these potential therapies aim to prevent occurrences, which lead to pain by preserving a healthy functional structure.³⁵⁸ This is particularly important when compared to conventional surgical treatments, such as spinal fusion, which do not restore the normal biomechanics and can even exacerbate degeneration in adjacent IVDs.⁴ Encouragingly, the spine field is filled with a growing body of basic research with many promising therapies demonstrating potential pre-clinically, thus many exciting developments are anticipated in the next few decades.¹⁷⁷ Nonetheless, as mentioned throughout this work, the IVD is a large avascular structure, hampered by significant diffusion distances, giving rise to metabolite gradients throughout. Therefore, its unique biochemical microenvironment and limited supply of nutrients have been postulated to be the greatest obstacle to overcome on the path towards disc regeneration,^{207,361} with the weak outcomes of prospective studies commonly linked to the microenvironment niche.⁵⁻⁷ Moreover, poor nutrition of the resident disc cells is believed to be one of the main contributors to degeneration,^{26,27,41,42} with the microenvironment confounded further by pathological features such as EP calcification, sclerosis of the vertebral bone and factors affecting blood supply, such as atherosclerosis and sickle cell anaemia.^{8,61} Subsequently, this thesis focused on the importance of the nutrient microenvironment throughout the full development and assessment process, in order to maximise the translation endeavours of emerging cell therapies all the way from “bench to bedside”.

As regenerative approaches advance rapidly there is urgency for a more thorough understanding of the exact metabolite concentrations present in the human IVD and how they govern the behaviour of potential cell therapies. Moreover, there is discussion surrounding the optimal timing of cell-based intervention.^{6,190} Therefore, it is imperative to more thoroughly characterise how the microenvironment changes with degeneration. Given the intrinsic difficulty and ethical constraints in obtaining accurate *in vivo* human measurements of the nutrient microenvironment, the spine field relies heavily on early seminal work and *in-silico* modelling as a complementary approach in providing valuable insight into the physiological or pathophysiological microenvironment. As a result, Chapter 4 sought to consolidate glucose, pH and oxygen levels previously measured or predicted within the NP, with the aim of re-evaluating the microenvironment at stages of degeneration, which are clinically relevant for cell-based regeneration.

As discussed previously, *in-silico* studies from the literature have investigated effects such as reducing nutrient supply^{104,109} and altering tissue diffusivity^{104,106,107} by reducing CEP permeability or porosity through parametric analysis.^{64,108,111} Despite significant advances interrelating metabolic rates^{9,116} and incorporating cell death with nutrient deprivation,^{107,210} modelling remains limited by availability of experimental data, both as input parameters and for subsequent validation of predictions.²⁸⁰ Rather than taking a similar parametric approach or solely focusing on the influence of different geometric or physical parameters on the metabolite concentrations, this work sought to characterise degeneration grade-specific parameters such as metabolically active cell densities,³¹ tissue hydration,^{191,193–201} diffusion parameters^{24,67,73,74,183–187} and calcification.²⁵ Therefore, it is believed that the multivariate models presented in this work advance the research field through pooled experimental data for more accurate modelling parameters of a dehydrated NP, anisotropic AF and calcified CEP at specific degeneration grades.

Taken together, pre-existing measurements and the results predicted in this work suggest that metabolite concentrations may not be as critically low as commonly believed.^{207–209} In fact, nutrient concentrations may increase due to reduced disc height and vasculature ingrowth. A recent review reported on the prevalence of vascular ingrowths which extend into the inner AF through degenerative fissures and may explain shifts in cell density and distribution with degeneration.^{25,35,36} Furthermore, it predicted that calcification does not appear to have a detrimental effect at earlier stages of degeneration when cell therapies are deemed an appropriate treatment. However, as with any *in-silico* model, there are assumptions and limitations which have been addressed within the specific chapter discussions. A limitation in the discussion of these *in-silico* models is the lack of a robust sensitivity analysis within this work, which could provide greater insight into identifying the most dominant parameters. While this work assessed the effect of a range of physiological and experimentally determined parameters, input parameters were not systematically increased/decreased by a fold change. Nonetheless, a recent study by Shalash *et al.* (2022) employed a similar nutrient-transport model and changed variables by \pm 50% of their baseline. The authors reported that geometry, solute-specific reaction rates and diffusivity dominate over cell density.⁶⁵

Although this work consolidated what has previously been measured by key experimental studies *in vivo* and used this information to help validate the predictive models, the overarching perception throughout this work is the need for more quantitative measurements of nutrient and metabolite concentrations. Not just intradiscal measurements but also nutrient supply and IVD boundary concentrations are needed to instil confidence in nutrient-transport models and may need to be assessed in a patient-specific manner. For example, human disc histopathology studies have revealed that not all degenerated discs exhibit calcification of the CEPs.²²⁶ To overcome this, this work sought to capture models of each grade with and without calcification. However, as addressed in Section 4.4, this results in generic models at each degeneration grade, with mean parameters rather than a range of plausible bounds to the mean and emphasises the requirement of more patient-specific models which

will be addressed further in Section 8.1. Furthermore, insight from a more thorough sensitivity analysis, will provide greater insight on which parameters to prioritise on a patient-specific basis.

Whether through predictive modelling, direct measurement or advanced imaging modalities, further insight into the specific nutrient microenvironments established *in vivo* will enable the design of cell culture experiments to recapitulate a range of unique, yet all physiologically relevant, niches *in vitro*. This will lead to the development of more effective therapies with greater potential for reversing or slowing down degeneration in patient-specific microenvironments. As discussed previously, the research field has been challenged by heterogeneous results in terms of the regenerative potential and matrix synthesis of different cell sources and subsequent therapies. Consequently, harmony and standardisation are currently a very popular topic in advancing reproducibility and subsequently accelerating clinical translation.²³⁴ As a result, it is believed that there is a commitment to standardise the practice of recapitulating the targeted microenvironmental niche *in vitro*.³⁶²

While resident NP cells have been shown to adapt to their harsher microenvironment, it has been demonstrated that these conditions may adversely affect the survival and regenerative potential of injected cell therapies.^{11,12,98} A number of studies have investigated the effect of challenging metabolite concentrations on potential cell sources. For example, porcine BM-MSCs and NP cells cultured under 1, 5 and 25 mM of glucose and reported NP cells had a lower GCR compared to MSCs. Furthermore BM-MSCs exhibited a higher GCR under HX conditions thus implying that native NP cells are more suitably adapted to sustaining the harsh microenvironmental conditions of the IVD than potential BM-MSC cell treatments.⁹⁸ Several published studies have looked at the effect of oxygen on articular chondrocytes (AC), nasal chondrocytes (NC) and BM-MSCs for tissue engineering purposes.^{98,221,222,363} It has been demonstrated that anoxia ($< 0.1\% \text{O}_2$) had detrimental effects on ECM accumulation of bovine ACs, whereas 5 – 10 $\% \text{O}_2$ resulted in increased matrix synthesis followed by decreasing synthesis at NX conditions.²²² Similarly, Scotti *et al.* (2012) demonstrated enhanced synthesis of sGAG and collagen type II for human ACs under 5% oxygen conditions,²²¹ while Malda *et al.* observed enhanced matrix synthesis and viability of human NCs in 3D culture at 2 $\% \text{O}_2$.³⁶³ In terms of the effect of pH on cell strategies, acidic conditions strongly decreased cell proliferation, reduced cell viability and inhibited anabolic gene expression and proliferative activity of young and mature rat BM-MSC and porcine BM-MSCs.^{96,99} However, unless studies, like those mentioned above, are specifically investigating the effect of microenvironmental conditions, there is an under appreciation of the effect of culturing conditions. Furthermore, a disconnect often occurs between the external incubator or media concentrations and the actual local concentrations experienced by the cells. This may even have occurred within these studies, by each using different configurations such as pellet culture or alginate beads.^{98,221,222,363}

To this extent, Chapter 5 aimed to characterise the local nutrient microenvironment of 2D cell monolayers and commonly used 3D *in vitro* culture systems, in order to highlight the effect of culturing parameters and to place “standard practice” culturing conditions into context in terms of physiological

relevance. The results revealed that large variations and gradients in metabolite concentrations are easily established without the careful consideration of key parameters and that this diversity currently exists across the disc research field. Although this work initially sought to provide specific guidelines for culture conditions, every culture system is unique and while one external concentration may be suitable for one culture configuration, it may not be appropriate for another. For example, depending on the choice of culture vessel, geometry, external concentrations and cell seeding density, different and distinct local nutrient microenvironments will be created. As a result, this work calls for greater attention to be given to the combined effects of these culturing parameters on the local microenvironment and the confounding downstream influences on gene expression and matrix synthesis, particularly when trying to understand heterogeneity in results between studies. Ultimately, predictive modelling is an invaluable tool to all in the design of *in vitro* experiments to ensure a relevant and stable local microenvironment. However, it would also be critically important to understand the species-specific metabolic rates within the configuration being investigated.²⁴¹ Alternatively, advanced metabolite measuring or monitoring technology would need to be incorporated.^{259–264,279} Nonetheless, it is strongly believed that with careful deliberation of the external boundary concentrations and *in vitro* culture design, harmony and standardisation of the local microenvironment will push towards the identification of an optimal cell source, greater reproducibility and more successful translation of findings across the field.

Following *in vitro* characterisation, *ex vivo* organ culture systems offer unparalleled advantages for the development and preclinical testing of new regenerative strategies. The popularity of *ex vivo* disc organ culture has grown over the past decade with the focus being on either the development of bioreactor systems^{154,157,158,291–295} or their utilisation to investigate degeneration processes^{122–130} or regeneration strategies.^{131,132,141,133–140} In terms of standardising *ex vivo* culture systems, it has been acknowledged that it is necessary to optimise parameters such as the loading force and frequency needed to model a physiological or degenerative impact on discs of different scales from different species.²⁹⁷ However, despite the cells being in their native 3D environment and highly specialised ECM, prior to this thesis the nutrient and metabolite concentrations within *ex vivo* models had never been measured and the assumption of adequate nutrition has typically been based on cell viability assessment. As a result, Chapter 6 aimed to characterise the nutrient microenvironment of common *ex vivo* bovine caudal disc culture systems using *in-silico* models incorporating geometrical differences between caudal levels and a metabolically active cell density.

Although HG and NX are the most commonly used culturing conditions across all species of *ex vivo* disc organ culture, this work found that supraphysiological levels of glucose exist in the centre of relatively large bovine caudal discs under these conditions. Therefore, this work suggests that further optimisation and standardisation of *ex vivo* disc organ culture is needed to recapitulate the *in vivo* microenvironmental niche of a degenerating human IVD. While the choice of species may be dependent on the specific scientific question, if the nutrient microenvironment is relevant to the study aim such as

investigating a regenerative cell therapy, then the culturing parameters may need to be optimised based on disc geometry, metabolically active cell density and species-specific metabolism. Additionally, as mentioned previously, these parameters may need to be experimentally determined for each system if *in-silico* models are to be employed to inform the culture regime. Alternatively, as was carried out in this work for the first experimental validation of IVD nutrient-transport models, experimental measurements could be made to determine the concentration of glucose and oxygen, as well as the pH level in the centre of *ex vivo* organ culture, in order to confirm the physiological relevance of the system. Once standardised, it is anticipated that these systems will provide a more powerful and reliable platform to test new treatments and accelerate innovative therapeutics for clinical translation.

In terms of the progress of clinical translation, these promising therapies typically undergo pre-clinical assessment in an *in vivo* animal model. However, even after demonstrating safety and efficacy in animals, many of these therapies enter into a critical period between preclinical validation and clinical evaluation, where their efficiency is stunted in humans. There are currently twenty-six clinical trials registered using cell-based regeneration for DDD and while a number of published follow up studies have demonstrated safety and promise for alleviating LBP, clinical success remains in its infancy.^{227,228,230,254} Many hurdles remain in terms of the measurable clinical outcomes and variable results on functional regeneration.^{6,177,190,319} This work took a commonly used small (rat caudal) and large (goat lumbar) animal model and sought to explore differences in metabolic activity and regenerative capacity between species in an attempt to ascertain their clinical relevance. These experimentally determined parameters on geometric scale, native cell densities, nutrient demands and regenerative GAG synthesis rates were then modelled *in-silico* to elucidate species-specific nutrient microenvironments and predict differences in temporal regeneration between animal models.

For the first time Chapter 7 presents *in-silico* models which compare favourably to the pre-clinical literature in terms of the capabilities of animal regeneration histologically and via MRI. However, they predict prolonged timeframes, of the order of years, for cell-based regeneration in human. This is the first work to propose a specific upper limit cell dose (10 million) which is capable of initiating functional repair without exacerbating the microenvironmental niche, something which does not appear to be a pertinent issue pre-clinically, due to the difference in geometrical scale and cell density between animal and human discs. Together, this work provides a path towards understanding “time to regeneration” within commonly used pre-clinical animal models compared to human. Moreover, the results of this work may help to explain the variable results emerging from clinical trials which use a range of cell numbers and shorter term follow up assessment, as well as the limited translation compared to their promising pre-clinical models.¹⁷⁶ Moreover, by informing the timeline within which positive changes can be expected, this work could further inform the design of clinical trials in terms of follow up assessment based on cell dose and the management of patient expectations.

Overall, this thesis highlights the value of *in-silico* modelling as a tool to help design for success all the way from *in vitro* and *ex vivo* development to pre-clinical and clinical assessment. In general, *in-*

silico modelling can provide a wealth of information on the degenerating IVD, a relatively complex and challenging structure to access and assess *in vivo*. It reduces our dependence on animal experiments, surgical or cadaveric samples and has the potential to be an invaluable complementary aid to clinical studies. Furthermore, as computing power and software capabilities increase, it is conceivable that the future holds the generation of patient-specific models, which could be used to better define patient assessment and outcome targets, as well as pre- and intraoperative planning.

8.1 Limitations and Future Perspectives

While promising and highly informative to the research field, the findings presented throughout this thesis are not without limitation. This section not only aims to address the caveats within the current work but also to address the significant hurdles, which still face cell-based regeneration elucidated throughout this work.

As previously discussed, *in-silico* modelling remains limited by the availability of robust experimental data, both as input parameters and for subsequent validation of predictions.²⁸⁰ Combining advanced *in-silico* modelling with experimental validation offers a more powerful tool for the further standardisation of both *in vitro* and *ex vivo* disc organ culture systems and the refinement of animal models. While experimental validation protocols were established and performed for intact animal discs both following *ex vivo* culture (Chapter 6) and in freshly euthanised rat and goat discs (Chapter 7), the 2D and 3D cell culture models in Chapter 5 are short of experimental accompaniment. To overcome these limitations and advance the standardisation of physiologically relevant microenvironments *in vitro*, monitoring systems such as multi-well sensor plates (PreSens, Regensburg, Germany) could be employed to simultaneously measure oxygen and pH via a sensor at the bottom of the well combined with media sampling for glucose and lactate levels as carried out later in Chapter 6. More advanced detection of spatial concentrations or metabolite mapping could be performed by developing techniques such as nanoparticle sensors or quantitative bioluminescence single photon imaging.³⁶⁴⁻³⁶⁶

A limitation of the nutrient-transport models predicting the *in vivo* nutrient microenvironment was the assumption of pure diffusion, while mechanical loading could enhance nutrition through forced solute convection. However, it is generally believed that diffusion is the main mechanism of transport for these small solutes such as nutrients through the ECM of the disc,^{24,59,62} while convection plays a role transporting the larger solutes.^{24,62,63} Nonetheless, the causal link between degeneration and transport inadequacy remains complicated and nutrient transport properties may be particularly important in aging and degeneration with the CEP becoming less porous, less hydrated and the presence of calcification impeding diffusion.²³¹ Furthermore, studies have reported increased porosity, due to osteoporosis and osteochondral remodelling, and speculate this to be linked to degenerative features such as the loss of NP osmotic pressure, antigen exposure and immune inflammation.²³² Therefore, the significance of convection due to dynamic loading may vary significantly from patient to patient

depending on individual matrix composition and porosity. Additionally, the models within this work may appear relatively simplistic when compared to multiphase mechano-electrochemical models which exist in the literature. These theoretically advanced modelling techniques couple the biology (cell viability, metabolic rates, synthetic rates) and mechanics, including the solid deformation, fluid flow and solutes transport (diffusion, convection, and binding).^{22,113,335} However, any theoretical simplification was justified by the focus being placed on advancing *in-silico* modelling through a strong foundation of experimentally determined input parameters such as grade-specific diffusion coefficients, cell density, tissue hydration, disc height and CEP calcification in Chapter 4. Furthermore, given the strong agreement between the *in-silico* predictions and those measured experimentally in Chapter 6, any computational simplifications and assumptions appear justified.

Additional limitations exist within the degenerated *in-silico* animal models. Firstly, caveats are inherent to animal experiments as degeneration are typically induced by spontaneous injury or enzymatic induction and do not capture the natural, pathological progression of degeneration and the importance of genetics.^{168,169} Secondly, from a modelling perspective, caveats include the degenerated animal models being represented by (i) a reduction in initial GAG content and (ii) a disruption to the native cell density of the NP. Although these parameters are informed by qualitative histological staining and literature grading of cellularity changes with degeneration,^{326,337-339} they are not the only degenerative changes to occur and additional factors such as reduction in disc height were not taken into account in this model. Within both the animal and human models, there is an assumption that there is no change in nutrient supply or waste removal with degeneration. However, the relationship between the surrounding microvasculature and transport is not straightforward. Additionally, subchondral bone sclerosis and occlusion of marrow contact channels may affect the vertebral supply route, with a correlation reported between functional capillary bud density and diffusion.^{214,215} This may contribute to lower nutrient availability through the EP route,^{57,216-218} which could create a shift in the predominance of the transport routes. Thus, more quantitative measurements of nutrient supply and metabolite concentrations at the boundary of the IVD are needed and may need to be assessed in both a species and a patient specific manner.

Throughout this work NP cells remained the focus of any potential cell therapy. For example, Chapter 5 focused on the *in vitro* culture of NP cells characterised by metabolic rates which have previously been measured for NP cells across different species and Chapter 7 focused on experimentally determining rat, goat and human NP metabolic and matrix synthesis rates. Furthermore, the *in-silico* models in Chapter 7 elucidate the “time to regeneration” between species assuming that the injected cells are homogeneously distributed throughout the NP, remain viable after delivery and possess a discogenic phenotype. Accordingly, it is assumed that they maintain similar metabolic and synthesis rates as those measured for the native NP cells in 3D spheroid configuration, where cell to cell interaction and pericellular matrix deposition enhance cell attachment, proliferation, matrix production and phenotype expression.³⁵³ Despite this assumption, the *in-silico* models assessing the effect of

culturing parameters on *in vitro* microenvironments in Chapter 5 highlighted the importance of determining and considering the metabolic demands of the specific cell type being utilised (animal vs. human, notochordal vs. chondrocyte-like, healthy vs. degenerated) in conjunction with their specific culture configuration (2D, 3D). Therefore, with cell sources and cell-engineering approaches still being investigated in order to identify the most suitable cell population and enhance the survival and effectiveness of transplanted cells,¹⁹⁰ the methods throughout this work can easily be applied to an alternative cell type, in order to predict and compare its effect on the nutrient microenvironment and capacity for timely regeneration. It is postulated that the cell dose to be injected will depend on the potential cell-type, in particular its metabolic activity and its expected survival after delivery.

Likewise, given the varying stages of human IVD degeneration and the variation in microenvironments *in vivo*,^{10,77} it is further believed that it will be important to design individual-specific treatments and cell doses unique to the clinical condition of the patient.^{65,190} A recent *in-silico* model has explained the advantages of developing a patient-specific platform to study nutrient transport, highlighting the importance for incorporating patient-specific data and generating unique models where the disc size and measured diffusivities had significant effect on metabolite distributions in the IVD.⁶⁵ The authors reported distinct diffusion behaviour between patients and importantly even between discs of the same Pfirrmann grade. Therefore, there is a compelling urgency for patient-specific models to help researchers to design and clinicians to select personalised therapies (such as cell dose/type or additional anabolic factors) to suit unique microenvironments and furthermore based on this work, predict patient outcomes. Diffusion weighted imaging (DWI) is a specialised type of MRI which can be used to create images of the movement of water molecules within living tissues and be processed to generate apparent diffusion coefficient (ADC) maps of solutes as recently presented for IVD tissue.⁶⁵ Although this technique may reflect diffusivity in patient-specific discs it is a measure of water molecules in tissues and not a direct measure of the solutes or metabolites of interest. Nonetheless, such *in vivo* data is a valuable input for models and may be particularly insightful to assess the effects of CEP calcification on nutrient transport.

Despite the field advancing towards more extensive clinical trials, there is still a clear need to identify suitable patients and non-invasive characterisation of an IVD biochemical microenvironment could help stratify patient cohorts e.g. using sophisticated MRI techniques such as chemical exchange saturation transfer (CEST) proving to be the most indicative methodology for quantitative surrogates for composition such as sGAG content and pH within the IVD.^{367–369} Alternatively, magnetic resonance spectroscopy is another non-invasive imaging technique that allows for the detection and measurement of certain metabolites in living tissue and has been used to provide information about various aspects of tissue metabolism such as lactate concentrations.³⁷⁰ However, it is a relatively complex and specialised technique and like many developing imaging modalities its use in a clinical setting is somewhat limited due to technical and practical considerations. Furthermore the spatial resolution is limited compared to conventional MRI, which will challenge the precise localisation of metabolite

signals within the tissue. Other relatively experimental techniques for determining key metabolites include oxygen-sensitive MRI which has been developed to more directly measure tissue oxygenation levels compared to blood oxygen level dependent (BOLD) imaging.³⁷¹

In terms of prioritising input parameters within future work, it would be most advantageous for the field to advance imaging modalities to determine oxygen, glucose and pH/lactate concentrations at the disc boundary (supply) and within the patient-specific discs. This *in vivo* data, together with information on diffusivity through the different tissue domains, and an extensively characterised (in terms of their metabolic profile) therapeutic cell source would provide substantial information in order to predict suitable patient-specific cell doses and regeneration capacity. Needless to say, *in vivo* metabolite concentrations and gradients, measured through non-invasive imaging, are also needed in order to provide confidence in the predictive modelling.

As mentioned previously, while this work enables the research field and clinicians to manage expectations on cell-based regeneration, it suggests significant challenges for cell-based therapies to produce sufficient *de novo* GAG matrix and bring about “functional change” to a degenerating disc. However, successful translation to clinic not only relies on science and innovation but also on planning and the awareness of the hurdles to overcome with the efforts of a multidisciplinary team.³¹⁹ The IVD is the largest avascular structure in the body and the microenvironment within it remains the biggest challenge to overcome for injected therapeutic cells. A number of studies have investigated pH priming or buffering as a strategy to support survival and enhanced ECM deposition under harsher microenvironments.^{288,322,372} These studies are preliminary *in vitro* investigations and *in vivo* studies must be performed to further consolidate their efficacy. Another method is preconditioning to improve cell differentiation into native phenotypes within the diseased microenvironment.⁷ Hypoxic preconditioning of MSCs demonstrated promising results pre-clinically,^{373,374} while human NP cells preconditioned at 2 %O₂ in a proprietary cocktail have progressed clinically to phase I/II trials (NCT03347708).^{175,375} Nonetheless, cell-based regeneration remains contingent on cells remaining viable and maintaining their regenerative response under an exacerbated nutrient deficit.^{5,7,190,208} Therefore, as discussed previously, this work advocates the prospects of alternative therapeutic strategies such as re-programming cells through microRNA and gene engineering approaches combined with biomimetic biomaterials as a more potent therapy to restore the biochemical and structural composition of the damaged tissue within an expedited timeframe.^{359,360} Additionally, perhaps cell therapies are better placed as a preventative rather than curative therapy, where a successful outcome is simply limiting further degeneration in the long term.

Chapter 9. Concluding Remarks

The fundamental goal of this thesis was to elucidate the nutrient microenvironment throughout all stages of cell-based therapy development, from “bench to bedside”. Together this work aimed to reinforce the importance of the nutrient microenvironment in an attempt to reduce the *in vitro* to *in vivo* gap and maximise potential for successful clinical translation based on nutritional demands. The key contributions to the biomedical field emanating from the research are summarised below:

- I consolidated and re-evaluated the human disc nutrient microenvironment by thoroughly reviewing the literature and reflecting on early measurements from seminal studies.
- I employed *in-silico* models underpinned by more recent experimentally determined parameters of degeneration and nutrient transport, with the objective of re-evaluating the current knowledge in terms of grade-specific stages of degeneration.
- I characterised the local nutrient microenvironment of 2D cell monolayers and commonly used 3D *in vitro* NP culture systems using *in-silico* modelling, in order to highlight the effect of culturing parameters such as diffusion rate, media volume and cell density. This work calls for greater attention to the combined effects of these parameters, particularly when attempting to understand the heterogeneity of results between studies.
- This work placed “standard practice” culturing conditions into context in terms of physiological relevance and found that specific guidelines for *in vitro* culture conditions could not be established; every system is unique and while one external concentration may be suitable for one configuration, it may not be appropriate for another.
- I characterised the nutrient microenvironment of common *ex vivo* bovine caudal disc culture systems using *in-silico* models, incorporating geometrical differences between caudal level and a metabolically active cell density, and provided the first experimental validation of these nutrient-transport models through experimental measurement of glucose, oxygen and pH within a disc cultured for seven days.
- I experimentally investigated species-specific geometrical scale, native cell density, nutrient metabolism and matrix synthesis rates for rat, goat and human disc cells.
- I employed these experimentally determined parameters *in-silico* in order to elucidate species-specific nutrient microenvironments and predict differences in temporal regeneration between animal models.
- For the first time this work provided a path towards understanding “time to regeneration” between commonly used pre-clinical animal models and the stunted success or expectations of cell-based clinical trials.

References

1. Dieleman JL, Baral R, Birger M, et al. US Spending on Personal Health Care and Public Health, 1996-2013. *JAMA*. 2016;316(2627).
2. Tavares WM, de França SA, Paiva WS, Teixeira MJ. A systematic review and meta-analysis of fusion rate enhancements and bone graft options for spine surgery. *Sci Rep*. 2022;12(1). doi:10.1038/s41598-022-11551-8
3. Upfill-Brown A, Policht J, Sperry BP, et al. National trends in the utilization of lumbar disc replacement for lumbar degenerative disc disease over a 10-year period, 2010 to 2019. *J Spine Surg*. 2022;8(3):343-352. doi:10.21037/JSS-22-4/COIF
4. Global Industry Analysts Inc. *Spinal Surgery - A Global Business Strategic Report*.; 2011.
5. Sakai D, Andersson GBJ. Stem cell therapy for intervertebral disc regeneration: Obstacles and solutions. *Nat Rev Rheumatol*. 2015;11(4):243-256. doi:10.1038/nrrheum.2015.13
6. Smith LJ, Silverman LI, Sakai D, et al. Advancing cell therapies for intervertebral disc regeneration from the lab to the clinic: Recommendations of the ORS spine section. *JOR Spine*. 2018;(July):e1036. doi:10.1002/jsp2.1036
7. Farhang N, Silverman LI, Bowles RD. Improving Cell Therapy Survival and Anabolism in Harsh Musculoskeletal Disease Environments. *Tissue Eng - Part B Rev*. 2020;26(4):348-366. doi:10.1089/ten.teb.2019.0324
8. Grunhagen T, Shirazi-Adl A, Fairbank JCT, Urban JPG. Intervertebral Disk Nutrition: A Review of Factors Influencing Concentrations of Nutrients and Metabolites. *Orthop Clin North Am*. 2011;42(4):465-477. doi:10.1016/j.ocl.2011.07.010
9. Bibby S, Jones D a, Ripley RM, Urban JPG. Metabolism of the intervertebral disc: effects of low levels of oxygen, glucose, and pH on rates of energy metabolism of bovine nucleus pulposus cells. *Spine (Phila Pa 1976)*. 2005;30(5):487-496;
10. Bartels EM, Fairbank JCT, Winlove PC, Urban JPG. Oxygen and lactate concentrations measured in vivo in the intervertebral discs of patients with scoliosis and back pain. *Spine (Phila Pa 1976)*. 1998;23(1):1-8;
11. Richardson SM, Knowles R, Tyler J, Mobasher A, Hoyland JA. Expression of glucose transporters GLUT-1, GLUT-3, GLUT-9 and HIF-1 α in normal and degenerate human intervertebral disc. *Histochem Cell Biol*. 2008;129(4):503-511. doi:10.1007/s00418-007-0372-9
12. Agrawal A, Guttapalli A, Narayan S, Albert TJ, Shapiro IM, Risbud M V. Normoxic stabilization of HIF-1 α drives glycolytic metabolism and regulates aggrecan gene expression in nucleus pulposus cells of the rat intervertebral disk. *Am J Physiol - Cell Physiol*. 2007;293(2):621-631. doi:10.1152/ajpcell.00538.2006

13. Marchand F, Ahmed AM. Investigation of the Laminate Structure of Lumbar Disc Anulus Fibrosus. *Spine (Phila Pa 1976)*. 1990;15(5):402-410;
14. Ayad S, Weiss JB. Biochemistry of the intervertebral disc. In: Jayson, ed. *The Lumbar Spine and Back Pain*. London: Churchill Livingstone; 1986:100-137;
15. Lotz JC, Fields AJ, Liebenberg E. The role of the vertebral end plate in low back pain. *Glob Spine J*. 2013;3(3):153-164;
16. Roberts S, Menage J, Urban JPG. Biochemical and structural properties of the cartilage end-plate and its relation to the intervertebral disc. *Spine (Phila Pa 1976)*. 1989;14(2):166-174;
17. Rodriguez AG, Slichter CK, Acosta FL, et al. Human Disc Nucleus Properties and Vertebral Endplate Permeability. *Spine (Phila Pa 1976)*. 2011;36(7):512-520;
18. Smith LJ, Nerurkar NL, Choi K-S, Harfe BD, Elliott DM. Degeneration and regeneration of the intervertebral disc: lessons from development. *Dis Model Mech*. 2011;4(1):31-41;
19. Urban JPG, Roberts S. Development and degeneration of the intervertebral discs. *Mol Med Today*. 1995;1(7):329-335;
20. Wu Y. Integrating Biomechanics and Cell Physiology to Understanding IVD Nutrition and Cell Homeostasis. 2013;(May).
21. Rufai A, Benjamin M, Ralphs JR. The development of fibrocartilage in the rat intervertebral disc. *Anat Embryol*. 1995;192(1):53-62;
22. Zhu Q. Numerical Modeling of Intervertebral Disc Degeneration and Repair. 2016.
23. Errington RJ, Puustjarvi K, White IRF, Roberts S, Urban JPG. Characterisation of cytoplasm-filled processes in cells of the intervertebral disc. *J Anat*. 1998;192(3):369-378. doi:10.1046/j.1469-7580.1998.19230369.x
24. Maroudas A, Stockwell R, Nachemson A, Urban JPG. Factors involved in the nutrition of the human lumbar intervertebral disc: cellularity and diffusion of glucose in vitro. *J Anat*. 1975;120(1):113-130;
25. Liebscher T, Haefeli M, Wuertz K, Nerlich AG, Boos N. Age-Related Variation in Cell Density of Human Lumbar Intervertebral Disc. *Spine (Phila Pa 1976)*. 2011;36(2):153-159;
26. Bibby S, Fairbank JCT, Urban MR, Urban JPG. Cell viability in scoliotic discs in relation to disc deformity and nutrient levels. *Spine (Phila Pa 1976)*. 2002;27(20):2220-2228;
27. Horner HA, Urban JPG. 2001 Volvo Award Winner in Basic Science Studies: Effect of nutrient supply on the viability of cells from the nucleus pulposus of the intervertebral disc. *Spine (Phila Pa 1976)*. 2001;26(23):2543-2549;
28. Ishihara H, Urban JPG. Effects of low oxygen concentrations and metabolic inhibitors on proteoglycan and protein synthesis rates in the intervertebral disc. *J Othopaedic Res*. 1999;17(6):829-835;
29. Oshima H, Ishihara H, Urban JPG, Tsuji H. The use of coccygeal discs to study intervertebral disc metabolism. *J Orthop Res*. 1993;11(3):332-338;

30. Stairmand JW, Holm S, Urban JPG. Factors influencing oxygen concentration gradients in the intervertebral disc. A theoretical analysis. *Spine (Phila Pa 1976)*. 1991;16(4):444-449;
31. Martins D, Medeiros VP De, Wajchenberg M, et al. Changes in human intervertebral disc biochemical composition and bony end plates between middle and old age. *PLoS One*. 2018;13(9):1-17. doi:10.1371/journal.pone.0203932
32. Tomaszewski KA, Walocha JA, Mizia E, Gładysz T, Głowacki R, Tomaszewska R. Age- and degeneration-related variations in cell density and glycosaminoglycan content in the human cervical intervertebral disc and its endplates. *Polish J Pathol*. 2015;66(3):296-309. doi:10.5114/pjp.2015.54964
33. Sivan SS, Wachtel E, Roughley PJ. Structure, function, aging and turnover of aggrecan in the intervertebral disc. *Biochim Biophys Acta - Gen Subj*. 2014;1840(10):3181-3189. doi:10.1016/j.bbagen.2014.07.013
34. Ohnishi T, Novais EJ, Risbud M V. Alterations in ECM signature underscore multiple sub-phenotypes of intervertebral disc degeneration. *Matrix Biol Plus*. 2020;(xxxx):100036. doi:10.1016/j.mbplus.2020.100036
35. Fournier DE, Kiser PK, Shoemaker JK, Battié MC, Séguin CA. Vascularization of the human intervertebral disc: A scoping review. *JOR Spine*. 2020;(August):1-13. doi:10.1002/jsp2.1123
36. Fields AJ, Liebenberg EC, Lotz JC. Innervation of pathologies in the lumbar vertebral endplate and intervertebral disc. *Spine J*. 2014;14(3):513-521. doi:10.1016/j.spinee.2013.06.075. Innervation
37. Murata M, Morio Y, Kuranobu K. Lumbar disc degeneration and segmental instability: a comparison of magnetic resonance images and plain radiographs of patients with low back pain. *Arch Orthop Trauma Surg*. 1994;113(6):297-301;
38. Pfirrmann CW a., Metzdorf A, Zanetti M, Hodler J, Boos N. Magnetic Resonance Classification of Lumbar Intervertebral Disc Degeneration. *Spine (Phila Pa 1976)*. 2001;26(17):1873-1878;
39. Thompson JP, Pearce RH, Schechter MT, Adams MA, Tsang IK, Bishop PB. Preliminary evaluation of a scheme for grading the gross morphology of the human intervertebral disc. *Spine (Phila Pa 1976)*. 1990;15(5):411-415;
40. Wilke HJ, Rohlmann F, Neidlinger-Wilke C, Werner K, Claes LE, Kettler A. Validity and interobserver agreement of a new radiographic grading system for intervertebral disc degeneration: Part I. Lumbar spine. *Eur Spine J*. 2006;15(6):720-730; doi:10.1007/s00586-005-1029-9
41. Nachemson A, Lewin T, Maroudas A, Freeman MAR. In vitro diffusion of dye through the endplates and the annulus fibrosus of human lumbar inter-vertebral discs. *Acta Orthop*. 1970;41(6):589-607. doi:10.3109/17453677008991550
42. Holm S, Selstam G, Nachemson A. Carbohydrate metabolism and concentration profiles of solutes in the canine lumbar intervertebral disc. *Acta Physiol Scand*. 1982;115(1):147-156;

43. Chandraraj S, Briggs CA, Opeskin K. Disc herniations in the young and end-plate vascularity. *Clin Anat*. 1998;11(3):171-176;
44. Roberts S, Menage J, Eisenstein SM. The cartilage end-plate and intervertebral disc in scoliosis: Calcification and other sequelae. *J Orthop Res*. 1993;11(5):747-757;
45. Bernick S, Cailliet R. Vertebral end-plate changes with aging of human vertebrae. *Spine (Phila Pa 1976)*. 1982;7(2):97-102. doi:10.1097/00007632-198203000-00002
46. Roberts S, Urban JPG, Evans H, Eisenstein SM. Transport Properties of the Human Cartilage Endplate in Relation to Its Composition and Calcification. *Spine (Phila Pa 1976)*. 1996;21(4):415-420.
47. Grant MP, Epure LM, Bokhari R, Roughley PJ, Antoniou J, Mwale F. Human cartilaginous endplate degeneration is induced by calcium and the extracellular calcium-sensing receptor in the intervertebral disc. *Eur Cells Mater*. 2016;32(514):137-151. doi:10.22203/eCM.v032a09
48. Fields AJ, Ballatori A, Liebenberg EC, Lotz JC. Contribution of the Endplates to Disc Degeneration. *Curr Mol Biol Reports*. 2018;4(4):151-160. doi:10.1007/s40610-018-0105-y
49. Bibby S, Urban JPG. Effect of nutrient deprivation on the viability of intervertebral disc cells. *Eur Spine J*. 2004;13(8):695-701;
50. Ohshima H, Urban JPG. The effect of lactate and ph on proteoglycan and protein synthesis rates in the intervertebral disc. *Spine (Phila Pa 1976)*. 1992;17(9):1079-1082. doi:10.1097/00007632-199209000-00012
51. Boos N, Wallin A, Gbedegbegnon T, Aebi M, Boesch C. Quantitative MR imaging of lumbar intervertebral disks and vertebral bodies: influence of diurnal water content variations. *Radiology*. 1993;188(2):351-354;
52. Trout JJ, Buckwalter JA, Moore KC. Ultrastructure of the human intervertebral disc: II. Cells of the nucleus pulposus. *Anat Rec*. 1982;204(4):307-314;
53. Wong J, Sampson SL, Bell-Briones H, et al. Nutrient supply and nucleus pulposus cell function: effects of the transport properties of the cartilage endplate and potential implications for intradiscal biologic therapy. *Osteoarthr Cartil*. 2019;27(6):956-964. doi:10.1016/j.joca.2019.01.013
54. Dolor A, Sampson SL, Lazar AA, Lotz JC, Szoka FC, Fields AJ. Matrix modification for enhancing the transport properties of the human cartilage endplate to improve disc nutrition. *PLoS One*. 2019;14(4):1-18. doi:10.1371/journal.pone.0215218
55. Jackson AR. Transport and Metabolism of Glucose in Intervertebral Disc. 2010.
56. Galbusera F, Van Rijbergen M, Ito K. Ageing and degenerative changes of the intervertebral disc and their impact on spinal flexibility. *Eur Spine J*. 2014;23(SUPPL. 3).
57. Benneker LM, Heini PF, Alini M, Anderson SE, Ito K. 2004 Young investigator award winner: Vertebral endplate marrow contact channel occlusions and intervertebral disc degeneration. *Spine (Phila Pa 1976)*. 2005;30(2):167-173; doi:10.1097/01.brs.0000150833.93248.09

58. Holm S, Maroudas A, Urban JPG, Selstam G, Nachemson A. Nutrition of the Intervertebral Disc: Solute Transport and Metabolism. *Connect Tissue Res.* 1981;8(2):101-119;
59. Urban JPG, Holm S. Nutrition of the intervertebral disc: effect of fluid flow on solute transport. *Clin Orthop Relat Res.* 1982;(170):296-302;
60. Urban JPG, Maroudas A. The measurement of fixed charged density in the intervertebral disc. *Biochim Biophys Acta - Gen Subj.* 1979;586(1):166-178. doi:10.1016/0304-4165(79)90415-X
61. Kauppila LI. Prevalence of stenotic changes in arteries supplying the lumbar spine. A postmortem angiographic study on 140 subjects. *Ann Rheum Dis.* 1997;56(10):591-595;
62. Urban JPG, Holm S, Maroudas A. Diffusion of small solutes into the intervertebral disc: An in vivo study. *Biorheology.* 1978;15(3-4):203-223. doi:10.3233/BIR-1978-153-409
63. O'Hara BP, Urban JPG, Maroudas A. Influence of cyclic loading on the nutrition of articular cartilage. *Ann Rheum Dis.* 1990;49(7):536-539;
64. Jackson AR, Huang C-YC, Gu WY. Effect of endplate calcification and mechanical deformation on the distribution of glucose in intervertebral disc: a 3D finite element study. *Comput Methods Biomech Biomed Engin.* 2011;14(2):195-204;
65. Shalash W, Ahrens SR, Bardanova LA, Byvaltsev VA, Giers MB. Patient-specific apparent diffusion maps used to model nutrient availability in degenerated intervertebral discs. *JOR Spine.* 2021;4(4). doi:10.1002/jsp2.1179
66. Allhands R V, Torzilli PA, Kallfelz FA. Measurement of diffusion of uncharged molecules in articular cartilage. *Cornell Vet.* 1984;74(2):111-123;
67. Jackson AR, Yuan T-Y, Huang C-YC, Travascio F, Gu WY. Effect of Compression and Anisotropy on the Diffusion of Glucose in Annulus Fibrosus. *Spine (Phila Pa 1976).* 2008;33(1):1-7;
68. Maroudas A. Physicochemical Properties of Cartilage in the Light of Ion Exchange Theory. *Biophys J.* 1968;8(5):575-595;
69. Torzilli PA, Dethmers DA, Rose DE, Schryuer HF. Movement of interstitial water through loaded articular cartilage. *J Biomech.* 1983;16(3).
70. Torzilli PA, Adams T, Mis RJ. Transient solute diffusion in articular cartilage. *J Biomech.* 1987;20(2):203-214;
71. Torzilli PA, Grande DA, Arduino JM. Diffusive properties of immature articular cartilage. *J Biomed Mater Res.* 1998;40(1):132-138;
72. Jackson AR, Gu WY. Transport Properties of Cartilaginous Tissues. *Curr Rheumatol Rev.* 2009;5(1):40-50;
73. Yuan T-Y, Jackson AR, Huang C-YC, Gu WY. Strain-Dependent Oxygen Diffusivity in Bovine Annulus Fibrosus. *J Biomech Eng.* 2009;131:074503. doi:10.1115/1.3127254
74. Jackson AR, Yuan T-Y, Huang C-YC. Nutrient Transport in Human Annulus Fibrosus is Affected by Compressive Strain and Anisotropy. *Ann Biomed Eng.* 2012;40(12):1-8;

75. Holm S, Nachemson A. Nutritional changes in the canine intervertebral disc after spinal fusion. *Clin Orthop Relat Res.* 1982;169:243-258. <http://www.embase.com/search/results?subaction=viewrecord&from=export&id=L12021038>.
76. Holm S, Selstam G. Oxygen tension alterations in the intervertebral disc as a response to changes in the arterial blood. *Ups J Med Sci.* 1982;87(2):163-174. doi:10.3109/03009738209178421
77. Nachemson A. Intradiscal measurements of pH in patients with lumbar rhizopathies. *Acta Orthop.* 1969;40(1):23-42. doi:10.3109/17453676908989482
78. Diamant B, Karlsson J, Nachemson A. Correlation between lactate levels and pH in discs of patients with lumbar rhizopathies. *Experientia.* 1968;24(12):1195-1196. doi:10.1007/BF02146615
79. Mirza SK, White AA. Anatomy of intervertebral disc and pathophysiology of herniated disc disease. *J Clin Laser Med Surg.* 1995;13(3):131-142;
80. Kofoed H, Levander B. Respiratory gas pressures in the spine: Measurements in goats. *Acta Orthop.* 1987;58(4):415-418. doi:10.3109/17453678709146369
81. Rajpurohit R, Risbud M V., Ducheyne P, Vresilovic EJ, Shapiro IM. Phenotypic characteristics of the nucleus pulposus: Expression of hypoxia inducing factor-1, glucose transporter-1 and MMP-2. *Cell Tissue Res.* 2002;308(3):401-407. doi:10.1007/s00441-002-0563-6
82. Windhaber R a J, Wilkins RJ, Meredith D. Functional characterisation of glucose transport in bovine articular chondrocytes. *Pflügers Arch Eur J Physiol.* 2003;446(5):572-577;
83. Mwale F, Ciobanu I, Giannitsios D, Roughley PJ, Steffen T, Antoniou J. Effect of Oxygen Levels on Proteoglycan Synthesis by Intervertebral Disc Cells. *Spine (Phila Pa 1976).* 2011;36(2):131-138. doi:10.1097/BRS.0b013e3181d52b9e
84. Razaq S, Wilkins RJ, Urban JPG. The effect of extracellular pH on matrix turnover by cells of the bovine nucleus pulposus. *Eur Spine J.* 2003;12(4):341-349;
85. Gilbert HTJ, Hodson NW, Baird P, Richardson SM, Hoyland JA. Acidic pH promotes intervertebral disc degeneration: Acid-sensing ion channel -3 as a potential therapeutic target. *Sci Rep.* 2016;6(1):37360. doi:10.1038/srep37360
86. Johnson ZI, Schoepflin ZR, Choi H, Shapiro IM, Risbud M V. Disc in flames: Roles of TNF- α and IL-1 β in intervertebral disc degeneration. *Eur Cells Mater.* 2015;30:104-117. doi:10.22203/eCM.v030a08
87. Uchiyama Y, Cheng CC, Danielson KG, et al. Expression of Acid-Sensing Ion Channel 3 (ASIC3) in nucleus pulposus cells of the intervertebral disc is regulated by p75NTR and ERK signaling. *J Bone Miner Res.* 2007;22(12):1996-2006. doi:10.1359/jbmr.070805
88. Minogue BM, Richardson SM, Zeef LAH, Freemont AJ, Hoyland JA. Characterization of the human nucleus pulposus cell phenotype and evaluation of novel marker gene expression to define adult stem cell differentiation. *Arthritis Care Res.* 2010;62(12):3695-3705. doi:10.1002/art.27710

89. Gilbert HTJ, Hoyland JA, Richardson SM. Stem cell regeneration of degenerated intervertebral discs: Current status (Update). *Curr Pain Headache Rep.* 2013;17(12).
90. Huang C-YC, Yuan T-Y, Jackson AR, Hazbun L, Fraker C, Gu WY. Effects of Low Glucose Concentrations on Oxygen Consumption Rates of Intervertebral Disc Cells. *Spine (Phila Pa 1976)*. 2007;32(19):2063-2069;
91. Guehring T, Wilde G, Sumner M, et al. Notochordal intervertebral disc cells: Sensitivity to nutrient deprivation. *Arthritis Rheum.* 2009;60(4):1026-1034;
92. Jaworski LM, Kleinhans KL, Jackson AR. Effects of Long-Term Nutrient Deprivation on the Activity and Viability of Notochordal Nucleus Pulposus Cells of the Intervertebral Disc. In: *ORS 2014 Annual Meeting.* ; 2014. doi:10.1186/ar629
93. Cisewski SE, Wu Y, Damon BJ, Sachs BL, Kern MJ, Yao H. Comparison of Oxygen Consumption Rates of Nondegenerate and Degenerate Human Intervertebral Disc Cells. *Spine (Phila Pa 1976)*. 2018;43(2):E60-E67. doi:10.1097/BRS.0000000000002252
94. Jaworski LM, Kleinhans KL, Jackson AR. Effects of Oxygen Concentration and Culture Time on Porcine Nucleus Pulposus Cell Metabolism : An in vitro Study. 2019;7(April):1-12. doi:10.3389/fbioe.2019.00064
95. Yin X, Motorwala A, Vesvoranan O, Levene H, Gu WY. Effects of Glucose Deprivation on ATP and Proteoglycan Production of Intervertebral Disc Cells under Hypoxia. *Sci Rep.* 2020:1-12. doi:10.1038/s41598-020-65691-w
96. Wuertz K, Godburn K, Neidlinger-Wilke C, Urban J, Iatridis JC. Behavior of mesenchymal stem cells in the chemical microenvironment of the intervertebral disc. *Spine (Phila Pa 1976)*. 2008;33(17):1843-1849. doi:10.1097/BRS.0b013e31817b8f53
97. Wuertz K, Godburn K, Iatridis JC. MSC response to pH levels found in degenerating intervertebral discs. *Biochem Biophys Res Commun.* 2009;379(4):824-829. doi:10.1016/j.bbrc.2008.12.145
98. Naqvi SM, Buckley CT. Extracellular matrix production by nucleus pulposus and bone marrow stem cells in response to altered oxygen and glucose microenvironments. *J Anat.* 2015;227(6):757-766. doi:10.1111/joa.12305
99. Naqvi SM, Buckley CT. Bone marrow stem cells in response to intervertebral disc-like matrix acidity and oxygen concentration implications for cell-based regenerative therapy. *Spine (Phila Pa 1976)*. 2016;41(9):743-750. doi:10.1097/BRS.0000000000001314
100. Borrelli CM, Buckley CT. Synergistic effects of acidic pH and pro-inflammatory cytokines il-1 β and tnf- α for cell-based intervertebral disc regeneration. *Appl Sci.* 2020;10(24):1-17. doi:10.3390/app10249009
101. Lee RB, Wilkins RJ, Razaq S, Urban JPG. The effect of mechanical stress on cartilage energy metabolism. *Biorheology.* 2002;39(1-2):133-143;
102. Cisewski SE. Nutrient Related Mechanisms of Intervertebral Disc Degeneration. 2016.

103. Salvatierra JC, Yuan T-Y, Fernando H, et al. Difference in energy metabolism of annulus fibrosus and nucleus pulposus cells of the intervertebral disc. *Cell Mol Bioeng*. 2011;4(2):302-310;
104. Sélard E, Shirazi-Adl A, Urban JPG. Finite element study of nutrient diffusion in the human intervertebral disc. *Spine (Phila Pa 1976)*. 2003;28(17):1945-1953;
105. Magnier C, Boiron O, Wendling-Mansuy S, Chabrand P, Deplano V. Nutrient distribution and metabolism in the intervertebral disc in the unloaded state: A parametric study. *J Biomech*. 2009;42(2):100-108;
106. Soukane DM, Shirazi-Adl A, Urban JPG. Investigation of solute concentrations in a 3D model of intervertebral disc. *Eur Spine J*. 2009;18(2):254-262;
107. Shirazi-Adl A, Taheri M, Urban JPG. Analysis of cell viability in intervertebral disc: Effect of endplate permeability on cell population. *J Biomech*. 2010;43(7):1330-1336;
108. Jackson AR, Huang C-YC, Brown MD, Gu WY. 3D Finite Element Analysis of Nutrient Distributions and Cell Viability in the Intervertebral Disc: Effects of Deformation and Degeneration. *J Biomech Eng*. 2011;133(9). doi:10.1115/1.4004944
109. Zhu Q, Jackson AR, Gu WY. Cell viability in intervertebral disc under various nutritional and dynamic loading conditions: 3d Finite element analysis. *J Biomech*. 2012;45(16):2769-2777;
110. Galbusera F, Mietsch A, Schmidt H, Wilke HJ, Neidlinger-Wilke C. Effect of intervertebral disc degeneration on disc cell viability: a numerical investigation. *Comput Methods Biomech Biomed Engin*. 2013;16(3):328-337;
111. Wu Y, Cisewski SE, Sachs BL, Yao H. Effect of cartilage endplate on cell based disc regeneration: a finite element analysis. *Mol Cell Biomech*. 2015;10(2):159-182;
112. Schmidt H, Galbusera F, Rohlmann A, Shirazi-Adl A. What have we learned from finite element model studies of lumbar intervertebral discs in the past four decades? *J Biomech*. 2013;46(14):2342-2355;
113. Gu WY, Zhu Q, Gao X, Brown MD. Simulation of the Progression of Intervertebral Disc Degeneration Due to Decreased Nutritional Supply. *Spine (Phila Pa 1976)*. 2014;39(24):1411-1417;
<http://content.wkhealth.com/linkback/openurl?sid=WKPTLP:landingpage&an=00007632-201411150-00005>.
114. Soukane DM, Shirazi-Adl A, Urban JPG. Analysis of Nonlinear Coupled Diffusion of Oxygen and Lactic Acid in Intervertebral Discs. *J Biomech Eng*. 2005;127(12):1121-1126;
115. Soukane DM, Shirazi-Adl A, Urban JPG. Computation of coupled diffusion of oxygen, glucose and lactic acid in an intervertebral disc. *J Biomech*. 2007;40(12):2645-2654;
116. Huang C-YC, Gu WY. Effects of mechanical compression on metabolism and distribution of oxygen and lactate in intervertebral disc. *J Biomech*. 2008;41(6):1184-1196;
117. Boos N, Weissbach S, Rohrbach H, Weiler C, Spratt KF, Nerlich AG. Classification of age-

- related changes in lumbar intervertebral discs: 2002 Volvo award in basic science. *Spine (Phila Pa 1976)*. 2002;27(23):2631-2644;
118. Johnson WEB, Caterson B, Eisenstein SM, Roberts S. Human intervertebral disc aggrecan inhibits endothelial cell adhesion and cell migration in vitro. In: *Spine*. ; 2005. doi:10.1097/01.brs.0000162624.95262.73
 119. Baumgartner L, Reagh JJ, González Ballester MA, Noailly J. Simulating intervertebral disc cell behaviour within 3D multifactorial environments. *Bioinformatics*. 2020:0-1. doi:10.1093/bioinformatics/xxxxx
 120. Tendulkar G, Chen T, Ehnert S, Kaps HP, Nüssler AK. Intervertebral disc nucleus repair: Hype or hope? *Int J Mol Sci*. 2019;20(15). doi:10.3390/ijms20153622
 121. Alini M, Eisenstein SM, Ito K, et al. Are animal models useful for studying human disc disorders/degeneration? *Eur Spine J*. 2008;17(1):2-19;
 122. Zhan JW, Wang SQ, Feng MS, et al. Constant compression decreases vascular bud and VEGFA expression in a rabbit vertebral endplate ex vivo culture model. *PLoS One*. 2020. doi:10.1371/journal.pone.0234747
 123. Choi H, Chaiyamongkol W, Doolittle AC, et al. COX-2 expression mediated by calcium-TonEBP signaling axis under hyperosmotic conditions serves osmoprotective function in nucleus pulposus cells. *J Biol Chem*. 2018. doi:10.1074/jbc.RA117.001167
 124. Krock E, Rosenzweig DH, Currie JB, Bisson DG, Ouellet JA, Haglund L. Toll-like receptor activation induces degeneration of human intervertebral discs. *Sci Rep*. 2017;7(1):1-12. doi:10.1038/s41598-017-17472-1
 125. Pang L, Li P, Zhang R, Xu Y, Song L, Zhou Q. Role of p38–MAPK pathway in the effects of high-magnitude compression on nucleus pulposus cell senescence in a disc perfusion culture. *Biosci Rep*. 2017. doi:10.1042/BSR20170718
 126. Li P, Gan Y, Wang H, et al. Role of the ERK1/2 pathway in osmolarity effects on nucleus pulposus cell apoptosis in a disc perfusion culture. *J Orthop Res*. 2017. doi:10.1002/jor.23249
 127. Walter BA, Likhitpanichkul M, Illien-Jünger S, Roughley PJ, Hecht AC, Iatridis JC. TNF α transport induced by dynamic loading alters biomechanics of intact intervertebral discs. *PLoS One*. 2015;10(3):1-16. doi:10.1371/journal.pone.0118358
 128. Krock E, Rosenzweig DH, Chabot-Doré AJ, et al. Painful, degenerating intervertebral discs up-regulate neurite sprouting and CGRP through nociceptive factors. *J Cell Mol Med*. 2014. doi:10.1111/jcmm.12268
 129. Markova DZ, Kepler CK, Addya S, et al. An organ culture system to model early degenerative changes of the intervertebral disc II: Profiling global gene expression changes. *Arthritis Res Ther*. 2013. doi:10.1186/ar4301
 130. Purmessur D, Walter BA, Roughley PJ, Laudier DM, Hecht AC, Iatridis JC. A role for TNF α in intervertebral disc degeneration: A non-recoverable catabolic shift. *Biochem Biophys Res*

- Commun.* 2013;433(1):151-156. doi:10.1016/j.bbrc.2013.02.034
131. Richards J, Tang S, Gunsch G, et al. Mast cell/proteinase activated receptor 2 (PAR2) mediated interactions in the pathogenesis of discogenic back pain. *Front Cell Neurosci.* 2019;13(July):1-14. doi:10.3389/fncel.2019.00294
 132. Wangler S, Menzel U, Li Z, et al. CD146/MCAM distinguishes stem cell subpopulations with distinct migration and regenerative potential in degenerative intervertebral discs. *Osteoarthritis Cartil.* 2019;27(7):1094-1105. doi:10.1016/j.joca.2019.04.002
 133. Naqvi SM, Gansau J, Gibbons D, Buckley CT. In Vitro Co-culture and Ex Vivo Organ Culture Assessment of Primed and Cryopreservation Stromal Cell. *Eur Cells Mater.* 2019;37:134-152.
 134. Teixeira GQ, Pereira CL, Ferreira JR, et al. Immunomodulation of Human Mesenchymal Stem/Stromal Cells in Intervertebral Disc Degeneration. *Spine (Phila Pa 1976).* 2018;43(12):E673-E682. doi:10.1097/BRS.0000000000002494
 135. Peroglio M, Douma LS, Caprez TS, et al. Intervertebral disc response to stem cell treatment is conditioned by disc state and cell carrier: An ex vivo study. *J Orthop Transl.* 2017;9:43-51. doi:10.1016/j.jot.2017.03.003
 136. Anderson DG, Markova D, An HS, et al. Human Umbilical Cord Blood Y Derived Mesenchymal Stem Cells in the Cultured Rabbit Intervertebral Disc A Novel Cell Source for Disc Repair. *Am J Phys Med Rehabil.* 2013;92(5):420-429. doi:10.1097/PHM.0b013e31825f148a
 137. Illien-Jünger S, Pattappa G, Peroglio M, et al. Homing of mesenchymal stem cells in induced degenerative intervertebral discs in a whole organ culture system. *Spine (Phila Pa 1976).* 2012;37(22):1865-1873. doi:10.1097/BRS.0b013e3182544a8a
 138. Chan SCW, Gantenbein-Ritter B, Leung VY, Chan D, Cheung KMC, Ito K. Cryopreserved intervertebral disc with injected bone marrow-derived stromal cells: a feasibility study using organ culture. *Spine J.* 2010;10(6):486-496. doi:10.1016/j.spinee.2009.12.019
 139. Rosenzweig DH, Gawri R, Moir J, et al. Dynamic loading, matrix maintenance and cell injection therapy of human intervertebral discs cultured in a bioreactor. *Eur Cells Mater.* 2016;31:26-39. doi:10.22203/eCM.v031a03
 140. Mwale F, Wang HT, Roughley PJ, Antoniou J, Haglund L, Link N and mesenchymal stem cells can induce regeneration of the early degenerate intervertebral disc. *Tissue Eng - Part A.* 2014;20(21-22):2942-2949. doi:10.1089/ten.tea.2013.0749
 141. Teixeira GQ, Boldt A, Nagl I, et al. A Degenerative/Proinflammatory Intervertebral Disc Organ Culture: An Ex Vivo Model for Anti-inflammatory Drug and Cell Therapy. *Tissue Eng Part C Methods.* 2016;22(1):8-19. doi:10.1089/ten.tec.2015.0195
 142. Gantenbein B, Illien-Jünger S, Chan SCW, et al. Organ culture bioreactors-platforms to study human intervertebral disc degeneration and regenerative therapy. *Curr stem cell Res Ther.* 2015;10(4):339-352.

<http://www.pubmedcentral.nih.gov/articlerender.fcgi?artid=4437861&tool=pmcentrez&render type=abstract>.

143. Xing Y, Zhang P, Zhang Y, et al. A multi-throughput mechanical loading system for mouse intervertebral disc. *J Mech Behav Biomed Mater*. 2020. doi:10.1016/j.jmbbm.2020.103636
144. Dai J, Xing Y, Xiao L, et al. Microfluidic Disc-on-a-Chip Device for Mouse Intervertebral Disc - Pitching a Next-Generation Research Platform to Study Disc Degeneration. *ACS Biomater Sci Eng*. 2019. doi:10.1021/acsbiomaterials.8b01522
145. Wu X, Liao Z, Wang K, et al. Targeting the IL-1 β / IL-1Ra pathways for the aggregation of human islet amyloid polypeptide in an ex vivo organ culture system of the intervertebral disc. *Exp Mol Med*. 2019. doi:10.1038/s12276-019-0310-7
146. Koerner JD, Markova DZ, Schroeder GD, et al. The effect of substance P on an intervertebral disc rat organ culture model. *Spine (Phila Pa 1976)*. 2016;41(24):1851-1859. doi:10.1097/BRS.0000000000001676
147. McKee C, Beeravolu N, Brown C, Perez-Cruet M, Chaudhry GR. Mesenchymal stem cells transplanted with self-assembling scaffolds differentiated to regenerate nucleus pulposus in an ex vivo model of degenerative disc disease. *Appl Mater Today*. 2020. doi:10.1016/j.apmt.2019.100474
148. Li Z, Gehlen Y, Heizmann F, et al. Preclinical ex-vivo Testing of Anti-inflammatory Drugs in a Bovine Intervertebral Degenerative Disc Model. *Front Bioeng Biotechnol*. 2020;8(June):1-23. doi:10.3389/fbioe.2020.00583
149. Zhou Z, Zeiter S, Schmid T, et al. Effect of the CCL5-Releasing Fibrin Gel for Intervertebral Disc Regeneration. *Cartilage*. 2020;11(2):169-180. doi:10.1177/1947603518764263
150. Rosenzweig DH, Fairag R, Mathieu AP, et al. Thermoreversible hyaluronan-hydrogel and autologous nucleus pulposus cell delivery regenerates human intervertebral discs in an ex vivo, physiological organ culture model. *Eur Cells Mater*. 2018;36:200-217. doi:10.22203/eCM.v036a15
151. Frauchiger DA, Chan SCW, Benneker LM, Gantenbein B. Intervertebral disc damage models in organ culture: a comparison of annulus fibrosus cross-incision versus punch model under complex loading. *Eur Spine J*. 2018. doi:10.1007/s00586-018-5638-5
152. Illien-Jünger S, Gantenbein-Ritter B, Grad S, et al. The combined effects of limited nutrition and high-frequency loading on intervertebral discs with endplates. *Spine (Phila Pa 1976)*. 2010;35(19):1744-1752. doi:10.1097/BRS.0b013e3181c48019
153. Gantenbein B, Grunhagen T, Lee CR, Van Donkelaar CC, Alini M, Ito K. An in vitro organ culturing system for intervertebral disc explants with vertebral endplates: A feasibility study with ovine caudal discs. *Spine (Phila Pa 1976)*. 2006;31(23):2665-2673. doi:10.1097/01.brs.0000244620.15386.df
154. Rustenburg CME, Snuggs JW, Emanuel KS, et al. Modelling the Catabolic Environment of the

- Moderately Degenerated Disc with a Caprine Ex Vivo Loaded Disc Culture System. *Eur Cells Mater.* 2020;40:21-37. doi:10.22203/eCM.v040a02
155. Peeters M, Van Rijn S, Vergroesen PPA, et al. Bioluminescence-mediated longitudinal monitoring of adipose-derived stem cells in a large mammal ex vivo organ culture. *Sci Rep.* 2015;5(1):1-12. doi:10.1038/srep13960
 156. Shi J, Pang L, Jiao S. The response of nucleus pulposus cell senescence to static and dynamic compressions in a disc organ culture. *Biosci Rep.* 2018;38(2). doi:10.1042/BSR20180064
 157. Li P, Gan Y, Wang H, et al. A Substance Exchanger-Based Bioreactor Culture of Pig Discs for Studying the Immature Nucleus Pulposus. *Artif Organs.* 2017. doi:10.1111/aor.12834
 158. Jim B, Steffen T, Moir J, Roughley PJ, Haglund L. Development of an intact intervertebral disc organ culture system in which degeneration can be induced as a prelude to studying repair potential. *Eur Spine J.* 2011;20(8):1244-1254;
 159. O'Connell GD, Vresilovic EJ, Elliott DM. Comparison of Animals Used in Disc Research to Human Lumbar Disc Geometry. *Spine (Phila Pa 1976).* 2007;32(3):328-333;
 160. Shapiro IM, Risbud M V. *The Intervertebral Disc - Molecular and Structural Studies.* Wien: Springer-Verlag; 2014.
 161. Beckstein JC, Sen S, Schaer TP, Vresilovic EJ, Elliott DM. Comparison of animal discs used in disc research to human lumbar disc: Axial compression mechanics and glycosaminoglycan content. *Spine (Phila Pa 1976).* 2008;33(6):166-173. doi:10.1097/BRS.0b013e318166e001
 162. Pattappa G, Li Z, Peroglio M, Wismer N, Alini M, Grad S. Diversity of intervertebral disc cells: Phenotype and function. *J Anat.* 2012. doi:10.1111/j.1469-7580.2012.01521.x
 163. Tang SN, Bonilla AF, Chahine NO, et al. Controversies in spine research: Organ culture versus in vivo models for studies of the intervertebral disc. *JOR Spine.* 2022. doi:10.1002/JSP2.1235
 164. Melrose J, Smith S, Ghosh P. Differential expression of proteoglycan epitopes by ovine intervertebral disc cells. *J Anat.* 2000;197(2):189-198;
 165. Wang J cheng, Kabo J, Tsou P, Halevi L, Shamie A. The effect of uniform heating on the biomechanical properties of the intervertebral disc in a porcine model. *Spine J.* 2005;5(1):64-70;
 166. Fusellier M, Clouet J, Gauthier O, Tryfonidou MA, Le Visage C, Guicheux J. Degenerative lumbar disc disease: in vivo data support the rationale for the selection of appropriate animal models. *Eur Cells Mater.* 2020;39:18-47. doi:10.22203/eCM.v039a02
 167. Iatridis JC, Mente PL, Stokes IAF, Aronsson DD, Alini M. Compression-Induced Changes in Intervertebral Disc Properties in a Rat Tail Model. *Spine (Phila Pa 1976).* 1999;24(10):996-1002;
 168. Sambrook PN, MacGregor AJ, Spector TD. Genetic influences on cervical and lumbar disc degeneration: A magnetic resonance imaging study in twins. *Arthritis Rheum.* 1999;42(2):366-372;

169. Battié M, Videman T, Parent E. Lumbar Disc Degeneration Epidemiology and Genetic Influences. *Spine (Phila Pa 1976)*. 2004;29(23):2679-2690;
170. O'Connell GD, Johannessen W, Vresilovic EJ, Elliott DM. Human internal disc strains in axial compression measured noninvasively using magnetic resonance imaging. *Spine (Phila Pa 1976)*. 2007. doi:10.1097/BRS.0b013e31815b75fb
171. Y P, X Q, H S, et al. Proper animal experimental designs for preclinical research of biomaterials for intervertebral disc regeneration. *Biomater Transl*. 2021;2(2):91-142. doi:10.12336/BIOMATERTRANSL.2021.02.003
172. Hunter C, Matyas J, Duncan NA. The Notochordal Cell in the Nucleus Pulposus: A Review in the Context of Tissue Engineering. *Tissue Eng*. 2003;9(4):667-677;
173. McCann MR, Séguin CA. Notochord Cells in Intervertebral Disc Development and Degeneration. *J Dev Biol*. 2016;4(1). doi:10.3390/JDB4010003
174. Sakai D, Schol J. Cell therapy for intervertebral disc repair: Clinical perspective. *J Orthop Transl*. 2017;9:8-18. doi:10.1016/j.jot.2017.02.002
175. Silverman LI, Dulatova G, Tandeski T, et al. In Vitro and In Vivo Evaluation of Discogenic Cells, An Investigational Cell Therapy for Disc Degeneration. *Spine J*. 2019. doi:10.1016/j.spinee.2019.08.006
176. Schol J, Sakai D. Comprehensive narrative review on the analysis of outcomes from cell transplantation clinical trials for discogenic low back pain. *North Am Spine Soc J*. 2023;13:100195. doi:10.1016/j.xnsj.2022.100195
177. Binch ALA, Fitzgerald JC, Growney EA, Barry F. Cell-based strategies for IVD repair: clinical progress and translational obstacles. *Nat Rev Rheumatol*. 2021. doi:10.1038/s41584-020-00568-w
178. Walter BA, Korecki CL, Purmessur D, Roughley PJ, Michalek AJ, Iatridis JC. Complex loading affects intervertebral disc mechanics and biology. *Osteoarthr Cartil*. 2011;19(8):1011-1018. doi:10.1016/j.joca.2011.04.005
179. Walter BA, Illien-Jünger S, Nasser P, Hecht AC, Iatridis JC. Development and validation of a bioreactor system for dynamic loading and mechanical characterization of whole human intervertebral discs in organ culture. *J Biomech*. 2014;47(9):2095-2101;
180. Keeley TP, Mann GE. Defining physiological normoxia for improved translation of cell physiology to animal models and humans. *Physiol Rev*. 2019;99(1):161-234. doi:10.1152/physrev.00041.2017
181. Place TL, Domann FE, Case AJ. Limitations of oxygen delivery to cells in culture: An underappreciated problem in basic and translational research. *Free Radic Biol Med*. 2017;113(October):311-322. doi:10.1016/j.freeradbiomed.2017.10.003
182. Kobayashi S, Baba H, Takeno K, Miyazaki T, Meir A, Urban JPG. Physical Limitations to Tissue Engineering of Intervertebral Disc Cells. *Tissue Eng*. 2010:247-281.

183. Boubriak OA, Lee RB, Urban JPG. Nutrient supply to cells of the intervertebral disc; effect of diurnal hydration changes. In: *49th Annual Meeting of the Orthopaedic Research Society*. Vol Poster #11. ; 2003:1127.
184. Wu Y, Cisewski SE, Wegner N, et al. Region and strain-dependent diffusivities of glucose and lactate in healthy human cartilage endplate. *J Biomech.* 2016;49(13):2756-2762. doi:10.1016/j.jbiomech.2016.06.008
185. Haselgrove JC, Shapiro IM, Silverton SF. Computer modeling of the oxygen supply and demand of cells of the avian growth cartilage. *Am J Physiol - Cell Physiol.* 1993. doi:10.1152/ajpcell.1993.265.2.c497
186. Burstein D, Gray ML, Hartman AL, Gipe R, Foy BD. Diffusion of small solutes in cartilage as measured by nuclear magnetic resonance (NMR) spectroscopy and imaging. *J Orthop Res.* 1993;11(4):465-478. doi:10.1002/jor.1100110402
187. Obradovic B, Meldon JH, Freed LE, Vunjak-Novakovic G. Glycosaminoglycan deposition in engineered cartilage: Experiments and mathematical model. *AIChE J.* 2000. doi:10.1002/aic.690460914
188. Wu Y, Cisewski SE, Sachs BL, et al. The region-dependent biomechanical and biochemical properties of bovine cartilaginous endplate. *J Biomech.* 2015;48(12):3185-3191. doi:10.1016/j.jbiomech.2015.07.005
189. Malda J, Rouwkema J, Martins D, et al. Oxygen Gradients in Tissue-Engineered PEGT/PBT Cartilaginous Constructs: Measurement and Modeling. *Biotechnol Bioeng.* 2004;86(1):9-18;
190. Buckley CT, Hoyland JA, Fujii K, Pandit A, Iatridis JC, Grad S. Critical aspects and challenges for intervertebral disc repair and regeneration-Harnessing advances in tissue engineering. *JOR Spine.* 2018;(July):e1029. doi:10.1002/jsp2.1029
191. Delucca JF, Peloquin JM, Smith LJ, Wright AC, Vresilovic EJ, Elliott DM. MRI Quantification of Human Spine Cartilage Endplate Geometry : Comparison With Age , Degeneration , Level , and Disc Geometry. *J Orthop Res.* 2016;(August):1410-1417. doi:10.1002/jor.23315
192. Higgins J, Li T, Deeks JJ. Chapter 6: Choosing effect measures and computing estimates of effect. In: *Cochrane Handbook for Systematic Reviews of Interventions Version 6.2.* ; 2021.
193. Antoniou J, Steffen T, Nelson F, et al. The Human Lumbar Intervertebral Disc Evidence for Changes in the Biosynthesis and Denaturation of the Extracellular Matrix with Growth, Maturation, Ageing, and Degeneration. *J Clin Invest.* 1996;98(4):996-1003.
194. Iatridis JC, MacLean JJ, O'Brien M, Stokes IAF. Measurements of proteoglycan and water content distribution in human lumbar intervertebral discs. *Spine (Phila Pa 1976).* 2007;32(14):1493-1497. doi:10.1097/BRS.0b013e318067dd3f
195. Showalter BL, Beckstein JC, Martin JT, et al. Comparison of animal discs used in disc research to human lumbar disc: Torsion mechanics and collagen content. *Spine (Phila Pa 1976).* 2012;37(15). doi:10.1097/BRS.0b013e31824d911c

196. Lyons G, Eisenstein SM, Sweet MBE. Biochemical changes in intervertebral disc degeneration. *Biochim Biophys Acta*. 1981;673:443-453. doi:10.1016/0304-4165(81)90476-1
197. Gu WY, Mao XG, Foster RJ, Weidenbaum M, Mow VC, Rawlins BA. The anisotropic hydraulic permeability of human lumbar annulus fibrosus: Influence of age, degeneration, direction, and water content. *Spine (Phila Pa 1976)*. 1999;24(23):2449-2455. doi:10.1097/00007632-199912010-00005
198. Acaroglu ER, Iatridis JC, Setton LA, Foster RJ, Mow VC, Weidenbaum M. Degeneration and Aging Affect the Tensile Behavior of Human Lumbar Annulus Fibrosus. *Spine (Phila Pa 1976)*. 1995.
199. Antoniou J, Goudsouzian NM, Heathfield TF, et al. The human lumbar endplate. Evidence of changes in biosynthesis and denaturation of the extracellular matrix with growth, maturation, aging, and degeneration. *Spine (Phila Pa 1976)*. 1996;21(10):1153-1161;
200. Bishop PB, Pearce RH. The proteoglycans of the cartilaginous end-plate of the human intervertebral disc change after maturity. *J Orthop Res*. 1993;11(3):324-331. doi:10.1002/jor.1100110303
201. Bishop PB. Changes in the proteoglycans of the intervertebral disc cartilaginous endplate with aging and degeneration. 1989;(July 1989).
202. Costi JJ, Stokes IA, Gardner-Morse M, Laible JP, Scoffone HM, Iatridis JC. Direct measurement of intervertebral disc maximum shear strain in six degrees of freedom: Motions that place disc tissue at risk of injury. *J Biomech*. 2007. doi:10.1016/j.jbiomech.2006.11.006
203. Heuer F, Schmidt H, Wilke HJ. The relation between intervertebral disc bulging and annular fiber associated strains for simple and complex loading. *J Biomech*. 2008. doi:10.1016/j.jbiomech.2007.11.019
204. Wang Y, Xu W, Zhang Q, et al. Follow-up of blood glucose distribution characteristics in a health examination population in Chengdu from 2010 to 2016. *Med (United States)*. 2018;97(8). doi:10.1097/MD.00000000000009763
205. Feng G, Li L, Liu H, et al. Hypoxia differentially regulates human nucleus pulposus and annulus fibrosus cell extracellular matrix production in 3D scaffolds. *Osteoarthr Cartil*. 2013;21(4):582-588. doi:10.1016/j.joca.2013.01.001
206. Chen JW, Li B, Yang YH, Jiang SD, Jiang LS. Significance of hypoxia in the physiological function of intervertebral disc cells. *Crit Rev Eukaryot Gene Expr*. 2014;24(3):193-204. doi:10.1615/CritRevEukaryotGeneExpr.2014010485
207. Bendtsen M, Bunker C, Colombier P, et al. Biological challenges for regeneration of the degenerated disc using cellular therapies. *Acta Orthop*. 2016;87:39-46. doi:10.1080/17453674.2017.1297916
208. Vadalà G, Ambrosio L, Russo F, Papalia R. Interaction between Mesenchymal Stem Cells and Intervertebral Disc Microenvironment : From Cell Therapy to Tissue Engineering. *Stem Cells*

- Int.* 2019.
209. Guerrero J, Häckel S, Croft A, Hoppe S, Albers CE, Gantenbein B. The nucleus pulposus microenvironment in the intervertebral disc: the fountain of youth? *Eur Cells Mater.* 2021;41:707-738. doi:10.22203/ecm.v041a46
 210. Wills CR, Foata B, González Ballester MA, Karppinen J, Noailly J. Theoretical explorations generate new hypotheses about the role of the cartilage endplate in early intervertebral disk degeneration. *Front Physiol.* 2018;9(SEP):1-12. doi:10.3389/fphys.2018.01210
 211. Bue M, Hanberg P, Thomassen MB, et al. Microdialysis for the Assessment of Intervertebral Disc and Vertebral Cancellous Bone. *In Vivo (Brooklyn).* 2020;34(2):527-532. doi:10.21873/invivo.11804
 212. Wang Y. Enhancement of Nutrient Transport and Energy Production of the Intervertebral Disc by the Implantation of Polyurethane Mass Transfer Device. 2017.
 213. Patil P, Falabella M, Saeed A, et al. Oxidative stress-induced senescence markedly increases disc cell bioenergetics. *Mech Ageing Dev.* 2019;180(April):97-106. doi:10.1016/j.mad.2019.04.006
 214. Van Der Werf M, Lezuo P, Maissen O, Van Donkelaar CC, Ito K. Inhibition of vertebral endplate perfusion results in decreased intervertebral disc intranuclear diffusive transport. *J Anat.* 2007;211(6):769-774. doi:10.1111/j.1469-7580.2007.00816.x
 215. Gullbrand SE, Peterson J, Mastropolo R, et al. Drug-induced changes to the vertebral endplate vasculature affect transport into the intervertebral disc in vivo. *J Orthop Res.* 2014;32(12):1694-1700. doi:10.1002/jor.22716
 216. Laffosse JM, Accadbled F, Molinier F, Bonnevalle N, De Gauzy JS, Swider P. Correlations between effective permeability and marrow contact channels surface of vertebral endplates. *J Orthop Res.* 2010;28(9):1229-1234. doi:10.1002/jor.21137
 217. Krug R, Joseph GB, Han M, et al. Associations between vertebral body fat fraction and intervertebral disc biochemical composition as assessed by quantitative MRI. *J Magn Reson Imaging.* 2019. doi:10.1002/jmri.26675
 218. Montazel JL, Divine M, Lepage E, Kobeiter H, Breil S, Rahmouni A. Normal Spinal Bone Marrow in Adults: Dynamic Gadolinium-enhanced MR Imaging. *Radiology.* 2003. doi:10.1148/radiol.2293020747
 219. Naqvi SM, Buckley CT. Differential response of encapsulated nucleus pulposus and bone marrow stem cells in isolation and coculture in alginate and chitosan hydrogels. *Tissue Eng - Part A.* 2015;21(1-2):288-299. doi:10.1089/ten.tea.2013.0719
 220. Li H, Liang C, Tao Y, et al. Acidic pH conditions mimicking degenerative intervertebral discs impair the survival and biological behavior of human adipose-derived mesenchymal stem cells. *Exp Biol Med.* 2012;237(7):845-852. doi:10.1258/ebm.2012.012009
 221. Scotti C, Osmokrovic A, Wolf F, et al. Response of human engineered cartilage based on

- articular or nasal chondrocytes to interleukin-1 β and low oxygen. *Tissue Eng - Part A*. 2012;18(3-4):362-372. doi:10.1089/ten.tea.2011.0234
222. Grimshaw MJ, Mason RM. Bovine articular chondrocyte function in vitro depends upon oxygen tension. *Osteoarthr Cartil*. 2000;8(5):386-392. doi:10.1053/joca.1999.0314
223. Gantenbein B, Calandriello E, Wuertz-Kozak K, Benneker LM, Keel MJB, Chan SCW. Activation of intervertebral disc cells by co-culture with notochordal cells, conditioned medium and hypoxia. *BMC Musculoskelet Disord*. 2014;15(1):1-15. doi:10.1186/1471-2474-15-422
224. Le Maitre CL, Freemont AJ, Hoyland JA. The role of interleukin-1 in the pathogenesis of human intervertebral disc degeneration. *Arthritis Res Ther*. 2005;7(4):732-745. doi:10.1186/ar1732
225. Wuertz K, Vo N, Kletsas D, Boos N. Inflammatory and catabolic signalling in intervertebral discs: The roles of NF-KB and map kinases. *Eur Cells Mater*. 2012. doi:10.22203/ecm.v023a08
226. Le Maitre CL, Dahia CL, Giers MB, et al. Development of a standardized histopathology scoring system for human intervertebral disc degeneration: an Orthopaedic Research Society Spine Section Initiative. *Jor Spine*. 2021;(June):1-29. doi:10.1002/jsp2.1150
227. Orozco L, Soler R, Morera C, Alberca M, Sánchez A, García-Sancho J. Intervertebral disc repair by autologous mesenchymal bone marrow cells: A pilot study. *Transplantation*. 2011;92(7):822-828. doi:10.1097/TP.0b013e3182298a15
228. Coric D, Pettine K, Sumich A, Boltz MO. Prospective study of disc repair with allogeneic chondrocytes. *J Neurosurg Spine J Neurosurg Spine*. 2013;18(18):85-95. doi:10.3171/2012.10.SPINE12512
229. Comella K, Silbert R, Parlo M. Effects of the intradiscal implantation of stromal vascular fraction plus platelet rich plasma in patients with degenerative disc disease. *J Transl Med*. 2017;15(1):4-11. doi:10.1186/s12967-016-1109-0
230. Kumar H, Ha DH, Lee EJ, et al. Safety and tolerability of intradiscal implantation of combined autologous adipose-derived mesenchymal stem cells and hyaluronic acid in patients with chronic discogenic low back pain: 1-year follow-up of a phase i study. *Stem Cell Res Ther*. 2017;8(1):1-14. doi:10.1186/s13287-017-0710-3
231. Sampson SL, Sylvia M, Fields AJ. Effects of dynamic loading on solute transport through the human cartilage endplate. *J Biomech*. 2019;83:273-279. doi:10.1016/j.jbiomech.2018.12.004
232. Xiao ZF, He JB, Su GY, et al. Osteoporosis of the vertebra and osteochondral remodeling of the endplate causes intervertebral disc degeneration in ovariectomized mice. *Arthritis Res Ther*. 2018;20(1):207. doi:10.1186/s13075-018-1701-1
233. Al-ani A, Toms D, Kondro D, Thundathil J, Id YY, Id MU. Oxygenation in cell culture : Critical parameters for reproducibility are routinely not reported. *PLoS One*. 2018:1-13.
234. Basatvat S, Bach FC, Barcellona MN, et al. Harmonization and standardization of nucleus pulposus cell extraction and culture methods. 2023. doi:10.1002/jsp2.1238
235. Bambrick LL, Kostov Y, Rao G. In vitro Cell Culture pO₂ is Significantly Different from

- Incubator pO₂. *Biotechnol Prog.* 2011;1-5. doi:10.1002/btpr.622
236. Allen CB, Schneider BK, White CW, et al. Limitations to oxygen diffusion and equilibration in in vitro cell exposure systems in hyperoxia and hypoxia. *Am J Physiol Lung Cell Mol Physiol.* 2001;(281):1021-1027.
237. Refresh cell culture. *Nat Biomed Eng.* 2021;5(8):783-784. doi:10.1038/S41551-021-00790-1
238. Figueiredo L, Pace R, D'Arros C, et al. Assessing glucose and oxygen diffusion in hydrogels for the rational design of 3D stem cell scaffolds in regenerative medicine. *J Tissue Eng Regen Med.* 2018;12(5):1238-1246. doi:10.1002/term.2656
239. Suhaimi H, Wang S, Das DB. Glucose diffusivity in cell culture medium. *Chem Eng J.* 2015. doi:10.1016/j.cej.2015.01.130
240. Ribeiro ACF, Ortona O, Simões SMN, et al. Binary mutual diffusion coefficients of aqueous solutions of sucrose, lactose, glucose, and fructose in the temperature range from (298.15 to 328.15) K. *J Chem Eng Data.* 2006;51(5):1836-1840. doi:10.1021/je0602061
241. McDonnell EE, Buckley CT. Investigating the physiological relevance of ex vivo disc organ culture nutrient microenvironments using in silico modeling and experimental validation. *JOR Spine.* 2021;4(2):e1141. doi:10.1002/jsp2.1141
242. Sakai D, Mochida J, Iwashina T, et al. Regenerative effects of transplanting mesenchymal stem cells embedded in atelocollagen to the degenerated intervertebral disc. *Biomaterials.* 2006;27(3):335-345. doi:10.1016/j.biomaterials.2005.06.038
243. Hulst AC, Hens HJH, Buitelaar RM, Tramper J. Determination of the effective diffusion coefficient of oxygen in gel materials in relation to gel concentration. *Biotechnol Tech.* 1989. doi:10.1007/BF01875620
244. Ju LK, Ho CS. The measurement of oxygen diffusion coefficients in polymeric solutions. *Chem Eng Sci.* 1986. doi:10.1016/0009-2509(86)87040-3
245. Zhao W, Zhang Y, Liu Y, et al. Oxygen diffusivity in alginate/chitosan microcapsules. *J Chem Technol Biotechnol.* 2013;88(3):449-455. doi:10.1002/jctb.3845
246. Ehsan SM, George SC. Nonsteady state oxygen transport in engineered tissue: Implications for design. *Tissue Eng - Part A.* 2013. doi:10.1089/ten.tea.2012.0587
247. Estapé D, Gòdia F, Solà C. Determination of glucose and ethanol effective diffusion coefficients in Ca-alginate gel. *Enzyme Microb Technol.* 1992. doi:10.1016/0141-0229(92)90009-D
248. Weng L, Liang S, Zhang L, Zhang X, Xu J. Transport of glucose and poly(ethylene glycol)s in agarose gels studied by the refractive index method. *Macromolecules.* 2005. doi:10.1021/ma047337w
249. Hartig D, Hacke S, Ott L, et al. Diffusion Studies of Glucose and Sucrose in Chitosan Membranes and Beads for Enzymatic Production Processes. *Chem Eng Technol.* 2018. doi:10.1002/ceat.201800075
250. Dembczynski R, Jankowski T. Characterisation of small molecules diffusion in hydrogel-

- membrane liquid-core capsules. *Biochem Eng J*. 2000;6(1):41-44. doi:10.1016/S1369-703X(00)00070-X
251. Gabardo S, Rech R, Ayub MAZ. Determination of lactose and ethanol diffusion coefficients in calcium alginate gel spheres: Predicting values to be used in immobilized bioreactors. *J Chem Eng Data*. 2011. doi:10.1021/je101288g
 252. Bassi AS, Rohani S, Macdonald DG. Measurement of effective diffusivities of lactose and lactic acid in 3% agarose gel membrane. *Biotechnol Bioeng*. 1987. doi:10.1002/bit.260300614
 253. Øyaas J, Storrø I, Svendsen H, Levine DW. The effective diffusion coefficient and the distribution constant for small molecules in calcium-alginate gel beads. *Biotechnol Bioeng*. 1995;47(4):492-500. doi:10.1002/bit.260470411
 254. Mochida J, Sakai D, Nakamura Y, Watanabe T, Yamamoto Y, Kato S. Intervertebral disc repair with activated nucleus pulposus cell transplantation: a three-year, prospective clinical study of its safety. *Eur Cells Mater*. 2015;29:202-212. doi:10.22203/ecm.v029a15
 255. Sakai D, Nakai T, Hiraishi S, et al. Upregulation of glycosaminoglycan synthesis by Neurotrophin in nucleus pulposus cells via stimulation of chondroitin sulfate N-acetylgalactosaminyltransferase 1: A new approach to attenuation of intervertebral disc degeneration. *PLoS One*. 2018;13(8):1-19. doi:10.1371/journal.pone.0202640
 256. Cherif H, Bisson DG, Jarzem P, Weber MH, Ouellet JA, Haglund L. Curcumin and o-Vanillin Exhibit Evidence of Senolytic Activity in Human IVD Cells In Vitro. *J Clin Med*. 2019;8(4):433. doi:10.3390/jcm8040433
 257. Wenger R, Kurtcuoglu V, Scholz C, Marti H, Hoogewijs D. Frequently asked questions in hypoxia research. *Hypoxia*. 2015;(3):35-43. doi:10.2147/hp.s92198
 258. Chapman JD, Sturrock J, Boag JW, Crookall JO. Factors Affecting the Oxygen Tension around Cells Growing in Plastic Petri Dishes. *Int J Radiat Biol Relat Stud Physics, Chem Med*. 1970;17(4):305-328.
 259. Tokuda Y, Crane S, Yamaguchi Y, Zhou L, Falanga V. The levels and kinetics of oxygen tension detectable at the surface of human dermal fibroblast cultures. *J Cell Physiol*. 2000;182(3):414-420.
 260. Mamchaoui K, Saumon G. A method for measuring the oxygen consumption of intact cell monolayers. *Am J Physiol*. 2000;278(4 PART 1). doi:10.1152/AJPLUNG.2000.278.4.L858
 261. Pettersen EO, Larsen LH, Ramsing NB, Ebbesen P. Pericellular oxygen depletion during ordinary tissue culturing, measured with oxygen microsensors. 2005:257-267.
 262. Chen B, Longtine MS, Nelson DM. Pericellular oxygen concentration of cultured primary human trophoblasts. *Placenta*. 2013;34(2):106-109. doi:10.1016/J.PLACENTA.2012.11.011
 263. Campbell EL, Bruyninckx WJ, Kelly CJ, et al. Transmigrating neutrophils shape the mucosal microenvironment through localized oxygen depletion to influence resolution of inflammation. *Immunity*. 2014;40(1):66-77. doi:10.1016/J.IMMUNI.2013.11.020

264. Kagawa Y, Matsuura K, Shimizu T, Tsuneda S. Direct measurement of local dissolved oxygen concentration spatial profiles in a cell culture environment. *Biotechnol Bioeng.* 2015;112(6):1263-1274. doi:10.1002/bit.25531
265. Bucher C, Gazdhar A, Benneker LM, Geiser T, Gantenbein-Ritter B. Nonviral gene delivery of growth and differentiation factor 5 to human mesenchymal stem cells injected into a 3d bovine intervertebral disc organ culture system. *Stem Cells Int.* 2013;2013. doi:10.1155/2013/326828
266. Chan SCW, Tekari A, Benneker LM, Heini PF, Gantenbein B. Osteogenic differentiation of bone marrow stromal cells is hindered by the presence of intervertebral disc cells. *Arthritis Res Ther.* 2015;18(1):11. doi:10.1186/s13075-015-0900-2
267. May RD, Frauchiger DA, Albers CE, Benneker LM, Kohl S, Gantenbein B. Inhibitory effects of human primary intervertebral disc cells on human primary osteoblasts in a co-culture system. *Int J Mol Sci.* 2018;19(4). doi:10.3390/ijms19041195
268. May RD, Frauchiger DA, Albers CE, Hofstetter W, Gantenbein B. Exogenous stimulation of human intervertebral disc cells in 3-dimensional alginate bead culture with bmp2 and 151p: Cyto-compatibility and effects on cell phenotype. *Neurospine.* 2020;17(1):77-87. doi:10.14245/ns.2040002.001
269. Peroglio M, Eglin D, Benneker LM, Alini M, Grad S. Thermoreversible hyaluronan-based hydrogel supports in vitro and ex vivo disc-like differentiation of human mesenchymal stem cells. *Spine J.* 2013;13(11):1627-1639. doi:10.1016/j.spinee.2013.05.029
270. Li Z, Lang G, Karfeld-Sulzer LS, et al. Heterodimeric BMP-2/7 for nucleus pulposus regeneration—In vitro and ex vivo studies. *J Orthop Res.* 2017;35(1):51-60. doi:10.1002/jor.23351
271. Abbott RD, Purmessur D, Monsey RD, Brigstock DR, Laudier DM, Iatridis JC. Degenerative grade affects the responses of human nucleus pulposus cells to Link-N, CTGF, and TGFβ3. *J Spinal Disord Tech.* 2013;26(3):86-94. doi:10.1097/BSD.0b013e31826e0ca4
272. Purmessur D, Schek RM, Abbott RD, Ballif BA, Godburn K, Iatridis JC. Notochordal conditioned media from tissue increases proteoglycan accumulation and promotes a healthy nucleus pulposus phenotype in human mesenchymal stem cells. *Arthritis Res Ther.* 2011;13(3).
273. Kim DH, Martin JT, Elliott DM, Smith LJ, Mauck RL. Phenotypic stability, matrix elaboration and functional maturation of nucleus pulposus cells encapsulated in photocrosslinkable hyaluronic acid hydrogels. *Acta Biomater.* 2015;12(1):21-29. doi:10.1016/j.actbio.2014.10.030
274. Gorth D, Lothstein K, Chiaro J, et al. Hypoxic Regulation of Functional Extracellular Matrix Elaboration by Nucleus Pulposus Cells in Long-Term Agarose Culture. *J Orthop Res.* 2015;33(5):747-754. doi:10.1016/j.physbeh.2017.03.040
275. Korecki CL, Taboas JM, Tuan RS, Iatridis JC. Notochordal cell conditioned medium stimulates mesenchymal stem cell differentiation toward a young nucleus pulposus phenotype. *Stem Cell Res Ther.* 2010;1(2). doi:10.1186/scrt18

276. Gullbrand SE, Schaer TP, Agarwal P, et al. Translation of an injectable triple-interpenetrating-network hydrogel for intervertebral disc regeneration in a goat model. *Acta Biomater.* 2017;60:201-209. doi:10.1016/j.actbio.2017.07.025
277. Zlotnick HM, Stoeckl BD, Henning EA, Steinberg DR, Mauck RL. Optimized Media Volumes Enable Homogeneous Growth of Mesenchymal Stem Cell-Based Engineered Cartilage Constructs. *Tissue Eng Part A.* 2021;27(3-4):214-222. doi:10.1089/ten.tea.2020.0123
278. Buckley CT, Meyer EG, Kelly DJ. The influence of construct scale on the composition and functional properties of cartilaginous tissues engineered using bone marrow-derived mesenchymal stem cells. *Tissue Eng Part A.* 2012;18(3-4):382-396. doi:10.1089/TEN.TEA.2011.0145
279. Carroll S, Buckley CT, Kelly DJ. Measuring and Modeling Oxygen Transport and Consumption in 3D Hydrogels Containing Chondrocytes and Stem Cells of Different Tissue Origins. *Front Bioeng Biotechnol.* 2021;9. doi:10.3389/fbioe.2021.591126
280. McDonnell EE, Buckley CT. Consolidating and re-evaluating the human disc nutrient microenvironment. *JOR Spine.* 2022;5(1):e1192. doi:10.1002/JSP2.1192
281. Buckley CT, Vinardell T, Kelly DJ. Oxygen tension differentially regulates the functional properties of cartilaginous tissues engineered from infrapatellar fat pad derived MSCs and articular chondrocytes. *Osteoarthr Cartil.* 2010;18(10):1345-1354. doi:10.1016/J.JOCA.2010.07.004
282. Burdis R, Kelly DJ. Biofabrication and bioprinting using cellular aggregates, microtissues and organoids for the engineering of musculoskeletal tissues. *Acta Biomater.* 2021;126:1-14. doi:10.1016/j.actbio.2021.03.016
283. Nulty J, Burdis R, Kelly DJ. Biofabrication of Prevascularised Hypertrophic Cartilage Microtissues for Bone Tissue Engineering. *Front Bioeng Biotechnol.* 2021;9:469. doi:10.3389/FBIOE.2021.661989
284. Samuel S, McDonnell EE, Buckley CT. Effects of Growth Factor Combinations TGFβ3, GDF5 and GDF6 on the Matrix Synthesis of Nucleus Pulposus and Nasoseptal Chondrocyte Self-Assembled Microtissues. *Appl Sci.* 2022;12(3):1453. doi:10.3390/APP12031453
285. Bach FC, Laagland LT, Grant MP, et al. Link-N: The missing link towards intervertebral disc repair is species-specific. *PLoS One.* 2017;12(11):1-21. doi:10.1371/journal.pone.0187831
286. Bach FC, de Vries SAH, Riemers FM, et al. Soluble and pelletable factors in porcine, canine and human notochordal cell-conditioned medium: Implications for IVD regeneration. *Eur Cells Mater.* 2016;32:163-180. doi:10.22203/eCM.v032a11
287. Farrell MJ, Shin JI, Smith LJ, Mauck RL. Functional consequences of glucose and oxygen deprivation on engineered mesenchymal stem cell-based cartilage constructs. *Osteoarthr Cartil.* 2015;23(1):134-142. doi:10.1016/j.joca.2014.09.012
288. Peck SH, Bendigo JR, Tobias JW, et al. Hypoxic Preconditioning Enhances Bone Marrow-

- Derived Mesenchymal Stem Cell Survival in a Low Oxygen and Nutrient-Limited 3D Microenvironment. *Cartilage*. 2019. doi:10.1177/1947603519841675
289. Bach FC, de Vries SAH, Krouwels A, et al. The species-specific regenerative effects of notochordal cell-conditioned medium on chondrocyte-like cells derived from degenerated human intervertebral discs. *Eur Cells Mater*. 2015;30:132-147. doi:10.22203/eCM.v030a10
290. Bach FC, Libregts S, Creemers LB, et al. Notochordal-cell derived extracellular vesicles exert regenerative effects on canine and human nucleus pulposus cells. *Oncotarget*. 2017;8(51):88845-88856. doi:10.18632/oncotarget.21483
291. Lang G, Liu Y, Geries J, et al. An intervertebral disc whole organ culture system to investigate proinflammatory and degenerative disc disease condition. *J Tissue Eng Regen Med*. 2018;12(4):e2051-e2061. doi:10.1002/term.2636
292. Li Z, Lezuo P, Pattappa G, et al. Development of an ex vivo cavity model to study repair strategies in loaded intervertebral discs. *Eur Spine J*. 2016;25(9):2898-2908. doi:10.1007/s00586-016-4542-0
293. Grant MP, Epure LM, Salem O, et al. Development of a Large Animal Long-Term Intervertebral Disc Organ Culture Model That Includes the Bony Vertebrae for Grant, M., Epure, L. M., Salem, O., AlGarni, N., Ciobanu, O., Alaqeel, M., Antoniou, J., & Mwale, F. (2016). Development of a Large Animal. *Tissue Eng - Part C Methods*. 2016;22(7):636-643. doi:10.1089/ten.tec.2016.0049
294. Stannard JT, Edamura K, Stoker AM, et al. Development of a whole organ culture model for intervertebral disc disease. *J Orthop Transl*. 2016. doi:10.1016/j.jot.2015.08.002
295. Hartman RA, Bell KM, Debski RE, Kang JD, Sowa GA. Novel ex-vivo mechanobiological intervertebral disc culture system. *J Biomech*. 2012. doi:10.1016/j.jbiomech.2011.10.036
296. Pfannkuche J, Guo W, Cui S, et al. Intervertebral disc organ culture for the investigation of disc pathology and regeneration – benefits , limitations , and future directions of bioreactors. *Connect Tissue Res*. 2019;00(00):1-18. doi:10.1080/03008207.2019.1665652
297. Gantenbein B, Frauchiger DA, May RD, Bakirci E, Rohrer U, Grad S. Developing bioreactors to host joint-derived tissues that require mechanical stimulation. *Encycl Tissue Eng Regen Med*. 2019;1-3(March):261-280. doi:10.1016/B978-0-12-801238-3.65611-8
298. Pawliński, Bartosz Gołębiowski M, Trela M, Witkowska-Piłaszewicz O. Comparison of blood gas parameters, ions, and glucose concentration in polish Holstein-Friesian Dairy cows at different milk production levels. *Sci Rep*. 2023;13(1414). doi:doi.org/10.1038/s41598-023-28644-7
299. Pattappa G, Peroglio M, Sakai D, et al. CCL5/rantes is a key chemoattractant released by degenerative intervertebral discs in organ culture. *Eur Cells Mater*. 2014;27:124-136. doi:10.22203/eCM.v027a10
300. Frauchiger DA, May RD, Bakirci E, et al. Genipin-enhanced fibrin hydrogel and novel silk for

- intervertebral disc repair in a loaded bovine organ culture model. *J Funct Biomater*. 2018;9(3). doi:10.3390/jfb9030040
301. Chan SCW, Walser J, Ferguson SJ, Gantenbein B. Duration-dependent influence of dynamic torsion on the intervertebral disc: an intact disc organ culture study. *Eur Spine J*. 2015;24(11):2402-2410. doi:10.1007/s00586-015-4140-6
 302. Chan SCW, Walser J, Käppeli P, Shamsollahi MJ, Ferguson SJ, Gantenbein-Ritter B. Region Specific Response of Intervertebral Disc Cells to Complex Dynamic Loading: An Organ Culture Study Using a Dynamic Torsion-Compression Bioreactor. *PLoS One*. 2013;8(8):1-11. doi:10.1371/journal.pone.0072489
 303. Li Z, Lang G, Chen X, et al. Polyurethane scaffold with in situ swelling capacity for nucleus pulposus replacement. *Biomaterials*. 2016;84:196-209. doi:10.1016/j.biomaterials.2016.01.040
 304. Walter BA, Purmessor D, Moon A, et al. Reduced tissue osmolarity increases trpv4 expression and pro-inflammatory cytokines in intervertebral disc cells. *Eur Cells Mater*. 2016;32:123-136. doi:10.22203/eCM.v032a08
 305. Illien-Jünger S, Lu Y, Purmessor D, et al. Detrimental effects of discectomy on intervertebral disc biology can be decelerated by growth factor treatment during surgery: A large animal organ culture model. *Spine J*. 2014;14(11):2724-2732. doi:10.1016/j.spinee.2014.04.017
 306. Beatty AM, Bowden AE, Bridgewater LC. Functional Validation of a Complex Loading Whole Spinal Segment Bioreactor Design. *J Biomech Eng*. 2016;138(6):1-4. doi:10.1115/1.4033546
 307. Jünger S, Gantenbein-Ritter B, Lezuo P, Alini M, Ferguson SJ, Ito K. Effect of Limited Nutrition on In Situ Intervertebral Disc Cells Under Simulated-Physiological Loading. *Spine (Phila Pa 1976)*. 2009;34(12):1264-1271;
 308. Urban JPG, Maroudas A. The measurement of fixed charge density in the intervertebral disc. *Biochim Biophys Acta*. 1979;586:166-178;
 309. Boubriak OA, Watson N, Sivan SS, Stubbens N, Urban JPG. Factors regulating viable cell density in the intervertebral disc: Blood supply in relation to disc height. *J Anat*. 2013;222(3):341-348;
 310. Zhou Z, Cui S, Du J, et al. One strike loading organ culture model to investigate the post-traumatic disc degenerative condition. *J Orthop Transl*. 2020;20(26):141-150. doi:10.1016/j.jot.2020.08.003
 311. Miyazaki T, Kobayashi S, Takeno K, Meir A, Urban JPG, Baba H. A Phenotypic Comparison of Proteoglycan Production of Intervertebral Disc Cells Isolated from Rats, Rabbits, and Bovine Tails; Which Animal Model is Most Suitable to Study Tissue Engineering and Biological Repair of Human Disc Disorders? *Tissue Eng Part A*. 2009;15(12):3835-3846. doi:10.1089/ten.tea.2009.0250
 312. Du J, Pfannkuche J, Lang G, et al. Proinflammatory intervertebral disc cell and organ culture models induced by tumor necrosis factor alpha. *JOR Spine*. 2020;3(3):1-12.

- doi:10.1002/jsp2.1104
313. Wang Z, Yang Y, Xiang X, Zhu Y, Men J, He M. Estimation of the normal range of blood glucose in rats. *Wei sheng yan jiu= J Hyg Res.* 2010;39(2):133-137.
 314. Quandt JE, Barletta M, Cornell KK, Giguère S, Hofmeister EH. Evaluation of a point-of-care blood glucose monitor in healthy goats. *J Vet Emerg Crit Care.* 2018;28(1):45-53. doi:10.1111/VEC.12686
 315. Tong W, Lu Z, Qin L, et al. Cell therapy for the degenerating intervertebral disc. *Transl Res.* 2017;181:49-58. doi:10.1016/j.trsl.2016.11.008
 316. Yan C, Wang X, Xiang C, et al. Applications of Functionalized Hydrogels in the Regeneration of the Intervertebral Disc. *Biomed Res Int.* 2021;2021. doi:10.1155/2021/2818624
 317. Daly C, Ghosh P, Jenkin G, Oehme D, Goldschlager T. A Review of Animal Models of Intervertebral Disc Degeneration: Pathophysiology, Regeneration, and Translation to the Clinic. *Biomed Res Int.* 2016;2016.
 318. Malli SE, Kumbhkarn P, Dewle A, Srivastava A. Evaluation of Tissue Engineering Approaches for Intervertebral Disc Regeneration in Relevant Animal Models. *ACS Appl Bio Mater.* 2021;4(11):7721-7737. doi:10.1021/acsabm.1c00500
 319. Thorpe AA, Bach FC, Tryfonidou MA, et al. Leaping the hurdles in developing regenerative treatments for the intervertebral disc from preclinical to clinical. *JOR Spine.* 2018;1(3):e1027. doi:10.1002/jsp2.1027
 320. Poletto DL, Crowley JD, Tanglay O, Walsh WR, Pelletier MH. Preclinical in vivo animal models of intervertebral disc degeneration. Part 1: A systematic review. *JOR Spine.* 2022:e1234. doi:10.1002/JSP2.1234
 321. Heywood HK, Lee DA. Monolayer expansion induces an oxidative metabolism and ROS in chondrocytes. *Biochem Biophys Res Commun.* 2008;373:224-229. doi:10.1016/j.bbrc.2008.06.011
 322. Gansau J, Buckley CT. Priming as a strategy to overcome detrimental PH effects on cells for intervertebral disc regeneration. *Eur Cells Mater.* 2021. doi:10.22203/eCM.v041a11
 323. Hartman R, Patil P, Tisherman R, et al. Age-dependent changes in intervertebral disc cell mitochondria and bioenergetics. *Eur Cells Mater.* 2018;36:171-183. doi:10.22203/eCM.v036a13
 324. Silagi ES, Schoepflin ZR, Seifert EL, et al. Bicarbonate Recycling by HIF-1-dependent Carbonic Anhydrase isoforms 9 and 12 is Critical in Maintaining Intracellular pH and Viability of Nucleus Pulposus Cells. *J Bone Miner Res.* 2018;33(2):338-355. doi:10.1002/jbmr.3293.Bicarbonate
 325. Silagi ES, Novais EJ, Bisetto S, et al. Lactate Efflux From Intervertebral Disc Cells Is Required for Maintenance of Spine Health. *J Bone Miner Res.* 2020;35(3):550-570. doi:10.1002/jbmr.3908

326. Barcellona MN, Speer JE, Jing L, et al. Bioactive in situ crosslinkable polymer-peptide hydrogel for cell delivery to the intervertebral disc in a rat model. *Acta Biomater.* 2021;131:117-127. doi:10.1016/J.ACTBIO.2021.06.045
327. Choi UY, Joshi HP, Payne S, et al. An injectable hyaluronan–methylcellulose (HAMC) hydrogel combined with wharton’s jelly-derived mesenchymal stromal cells (WJ-MSCs) promotes degenerative disc repair. *Int J Mol Sci.* 2020;21(19):1-20. doi:10.3390/ijms21197391
328. Hu A, Xing R, Jiang L, et al. Thermosensitive hydrogels loaded with human-induced pluripotent stem cells overexpressing growth differentiation factor-5 ameliorate intervertebral disc degeneration in rats. *J Biomed Mater Res - Part B Appl Biomater.* 2020;108(5):2005-2016. doi:10.1002/jbm.b.34541
329. Liang C, Li H, Tao YQ, et al. Dual release of dexamethasone and TGF- β 3 from polymeric microspheres for stem cell matrix accumulation in a rat disc degeneration model. *Acta Biomater.* 2013;9(12):9423-9433. doi:10.1016/j.actbio.2013.08.019
330. Barcellona MN, McDonnell EE, Samuel S, Buckley CT. Rat tail models for the assessment of injectable nucleus pulposus regeneration strategies. *JOR Spine.* 2022;5(3):e1216. doi:10.1002/jsp2.1216
331. Than KD, Rahman SU, Wang L, et al. Intradiscal injection of simvastatin results in radiologic, histologic, and genetic evidence of disc regeneration in a rat model of degenerative disc disease. *Spine J.* 2014;14(6):1017-1028. doi:10.1016/j.spinee.2013.11.034. Intradiscal
332. Bagnell J. Development of patient-specific in silico models based on magnetic resonance imaging (MRI) data to predict nutrient microenvironment profiles in human intervertebral discs. 2022.
333. Burdis R, Chariyev-Prinz F, Browe DC, et al. Spatial patterning of phenotypically distinct microtissues to engineer osteochondral grafts for biological joint resurfacing. *Biomaterials.* 2022;289. doi:10.1016/J.BIOMATERIALS.2022.121750
334. Dashty M. A quick look at biochemistry: Carbohydrate metabolism. *Clin Biochem.* 2013;46(15):1339-1352. doi:10.1016/J.CLINBIOCHEM.2013.04.027
335. Zhu Q, Gao X, Temple HT, Brown MD, Gu WY. Simulation of Biological Therapies for Degenerated Intervertebral Discs. *J Orthop Res.* 2016;34(4):699-708. doi:10.1002/jor.23061. Simulation
336. Sivan SS, Tsitron E, Wachtel E, et al. Aggrecan turnover in human intervertebral disc as determined by the racemization of aspartic acid. *J Biol Chem.* 2006. doi:10.1074/jbc.M600296200
337. Zhang C, Gullbrand SE, Schaer TP, et al. Combined Hydrogel and Mesenchymal Stem Cell Therapy for Moderate-Severity Disc Degeneration in Goats. *Tissue Eng - Part A.* 2021;27(1-2):117-128. doi:10.1089/ten.tea.2020.0103
338. Keorochana G, Johnson JS, Taghavi CE, et al. The effect of needle size inducing degeneration

- in the rat caudal disc: Evaluation using radiograph, magnetic resonance imaging, histology, and immunohistochemistry. *Spine J.* 2010;10(11):1014-1023. doi:10.1016/j.spinee.2010.08.013
339. Gullbrand SE, Malhotra NR, Schaer TP, et al. A large animal model that recapitulates the spectrum of human intervertebral disc degeneration. *Osteoarthr Cartil.* 2017;25(1):146-156. doi:10.1016/j.joca.2016.08.006
340. Yuan Q, Du L, Xu H, et al. Autologous Mesenchymal Stromal Cells Combined with Gelatin Sponge for Repair Intervertebral Disc Defect after Discectomy: A Preclinical Study in a Goat Model. *Front Biosci - Landmark.* 2022;27(4):131. doi:10.31083/j.fb12704131
341. Liao J-C, Bustin SA. Cell Therapy Using Bone Marrow-Derived Stem Cell Overexpressing BMP-7 for Degenerative Discs in a Rat Tail Disc Model. *Int J Mol Sci.* 2016;17(2):147. doi:10.3390/IJMS17020147
342. Peeters M, Detiger SEL, Karfeld-Sulzer LS, et al. BMP-2 and BMP-2/7 Heterodimers Conjugated to a Fibrin/Hyaluronic Acid Hydrogel in a Large Animal Model of Mild Intervertebral Disc Degeneration. *Biores Open Access.* 2015;4(1):398-406. doi:10.1089/BIORES.2015.0025/ASSET/IMAGES/LARGE/FIGURE2.JPEG
343. Paul CPL, Schoorl T, Zuiderbaan HA, et al. Dynamic and Static Overloading Induce Early Degenerative Processes in Caprine Lumbar Intervertebral Discs. *PLoS One.* 2013;8(4). doi:10.1371/journal.pone.0062411
344. Schol J, Sakai D. Cell therapy for intervertebral disc herniation and degenerative disc disease: clinical trials. *Int Orthop.* 2019;43(4):1011-1025. doi:10.1007/s00264-018-4223-1
345. Sivan SS, Hayes AJ, Wachtel E, et al. Biochemical composition and turnover of the extracellular matrix of the normal and degenerate intervertebral disc. *Eur Spine J.* 2014;23(SUPPL. 3):344-353. doi:10.1007/s00586-013-2767-8
346. Meisel HJ, Siodla V, Ganey TM, Minkus Y, Hutton WC, Alasevic OJ. Clinical experience in cell-based therapeutics: Disc chondrocyte transplantation. A treatment for degenerated or damaged intervertebral disc. *Biomol Eng.* 2007. doi:10.1016/j.bioeng.2006.07.002
347. Centeno CJ, Markle J, Dodson E, et al. Treatment of lumbar degenerative disc disease-associated radicular pain with culture-expanded autologous mesenchymal stem cells: A pilot study on safety and efficacy. *J Transl Med.* 2017;15(1):1-12. doi:10.1186/s12967-017-1300-y
348. Noriega DC, Ardura F, Hernández-Ramajo R, et al. Intervertebral Disc Repair by Allogeneic Mesenchymal Bone Marrow Cells. *Transplantation.* 2017;101(8):1945-1951. doi:10.1097/tp.0000000000001484
349. Meisel HJ, Ganey T, Hutton WC, Libera J, Minkus Y, Alasevic O. Clinical experience in cell-based therapeutics: Intervention and outcome. *Eur Spine J.* 2006;15(SUPPL. 3). doi:10.1007/s00586-006-0169-x
350. Bae HW, Amirdelfan K, Coric D, et al. A Phase II Study Demonstrating Efficacy and Safety of Mesenchymal Precursor Cells in Low Back Pain Due to Disc Degeneration. *Spine J.*

- 2014;14(11):S31-S32. doi:10.1016/j.spinee.2014.08.084
351. Pang X, Yang H, Peng B. Human umbilical cord mesenchymal stem cell transplantation for the treatment of chronic discogenic low back pain. *Pain Physician*. 2014;17(4):525-530.
 352. Elabd C, Centeno CJ, Schultz JR, Lutz G, Ichim T, Silva FJ. Intra-discal injection of autologous, hypoxic cultured bone marrow-derived mesenchymal stem cells in five patients with chronic lower back pain: A long-term safety and feasibility study. *J Transl Med*. 2016;14(1):1-9. doi:10.1186/s12967-016-1015-5
 353. Hernández RM, Orive G, Murua A, Pedraz JL. Microcapsules and microcarriers for in situ cell delivery. *Adv Drug Deliv Rev*. 2010;62(7-8):711-730. doi:10.1016/j.addr.2010.02.004
 354. Vadalà G, Ambrosio L, Russo F, Papalia R, Denaro V. Stem Cells and Intervertebral Disc Regeneration Overview — What They Can and Can ’ t Do Stem Cells and Intervertebral Disc Regeneration Overview — What They Can and Can ’ t Do. 2021;(April). doi:10.14444/8054
 355. Meisel HJ, Agarwal N, Hsieh PC, et al. Cell Therapy for Treatment of Intervertebral Disc Degeneration: A Systematic Review. *Glob Spine J*. 2019;9(1_suppl):39S-52S. doi:10.1177/2192568219829024
 356. Sun Y, Leung VY, Cheung KM. Clinical trials of intervertebral disc regeneration: current status and future developments. *Int Orthop*. 2019;43(4):1003-1010. doi:10.1007/s00264-018-4245-8
 357. Ju DG, Kanim LE, Bae HW. Is There Clinical Improvement Associated With Intradiscal Therapies? A Comparison Across Randomized Controlled Studies. *Glob Spine J*. 2020. doi:10.1177/2192568220963058
 358. Diwan AD, Melrose | James. Intervertebral disc degeneration and how it leads to low back pain. *JOR Spine*. November 2022:e1231. doi:10.1002/JSP2.1231
 359. Wang C, Cui L, Gu Q, et al. The Mechanism and Function of miRNA in Intervertebral Disc Degeneration. *Orthop Surg*. 2022;14(3):463. doi:10.1111/OS.13204
 360. Borrelli CM, Buckley CT. Injectable Disc-Derived ECM Hydrogel Functionalised with Chondroitin Sulfate for Intervertebral Disc Regeneration. *Acta Biomater*. 2020. doi:10.1016/j.actbio.2020.10.002
 361. Huang Y-C, Urban JPG, Luk KDK. Intervertebral disc regeneration: do nutrients lead the way? *Nat Rev Rheumatol*. 2014;10(9):561-566;
 362. McDonnell EE, Buckley CT. Two- and three-dimensional in vitro nucleus pulposus cultures: An in silico analysis of local nutrient microenvironments. *JOR Spine*. 2022;5(3). doi:10.1002/jsp2.1222
 363. Malda J, van Blitterswijk C, van Geffen M, Martens DE, Tramper J, Riesle J. Low oxygen tension stimulates the redifferentiation of dedifferentiate adult human nasal chondrocytes. *Osteoarthr Cartil*. 2004;12(4):306-313. doi:10.1016/j.joca.2003.12.001
 364. Walenta S, Schroeder T, Mueller-Klieser W. Metabolic mapping with bioluminescence: Basic and clinical relevance. *Biomol Eng*. 2002;18(6):249-262. doi:10.1016/S1389-0344(01)00107-1

365. Walenta S, Doetsch J, Mueller-Klieser W, Kunz-Schughart LA. Metabolic imaging in multicellular spheroids of oncogene-transfected fibroblasts. *J Histochem Cytochem.* 2000;48(4):509-522. doi:10.1177/002215540004800409
366. Taguchi M, Ptitsyn A, McLamore ES, Claussen JC. Nanomaterial-mediated Biosensors for Monitoring Glucose. *J Diabetes Sci Technol.* 2014;8(2):403. doi:10.1177/1932296814522799
367. Müller-Lutz A, Cronenberg T, Schleich C, et al. Comparison of glycosaminoglycan chemical exchange saturation transfer using Gaussian-shaped and off-resonant spin-lock radiofrequency pulses in intervertebral disks. *Magn Reson Med.* 2017;78(1):280-284. doi:10.1002/MRM.26362
368. Wada T, Togao O, Tokunaga C, et al. Glycosaminoglycan chemical exchange saturation transfer in human lumbar intervertebral discs: Effect of saturation pulse and relationship with low back pain. *J Magn Reson Imaging.* 2017;45(3):863-871. doi:10.1002/JMRI.25397
369. Melkus G, Grabau M, Karampinos DC, Majumdar S. Ex vivo porcine model to measure pH dependence of chemical exchange saturation transfer effect of glycosaminoglycan in the intervertebral disc. *Magn Reson Med.* 2014;71(5):1743-1749. doi:10.1002/MRM.24838
370. Isobe T, Matsumura A, Anno I, et al. Lactate quantification by proton magnetic resonance spectroscopy using a clinical MRI machine: A basic study. *Australas Radiol.* 2007;51(4):330-333. doi:10.1111/J.1440-1673.2007.01745.X
371. Chopra S, Foltz WD, Milosevic MF, et al. Comparing oxygen-sensitive MRI (BOLD R2*) with oxygen electrode measurements: a pilot study in men with prostate cancer. *Int J Radiat Biol.* 2009;85(9):805-813. doi:10.1080/09553000903043059
372. Naqvi SM, Gansau J, Buckley CT. Priming and cryopreservation of microencapsulated marrow stromal cells as a strategy for intervertebral disc regeneration Priming and cryopreservation of microencapsulated marrow stromal cells as a strategy for intervertebral disc regeneration. *Biomed Mater.* 2018;13.
373. Chiang ER, Ma HL, Wang JP, et al. Use of Allogeneic Hypoxic Mesenchymal Stem Cells For Treating Disc Degeneration in Rabbits. *J Orthop Res.* 2019;37(6):1440-1450. doi:10.1002/jor.24342
374. Wang W, Wang Y, Deng G, et al. Transplantation of hypoxic-preconditioned bone mesenchymal stem cells retards intervertebral disc degeneration via enhancing implanted cell survival and migration in rats. *Stem Cells Int.* 2018;2018. doi:10.1155/2018/7564159
375. Hiraishi S, Schol J, Sakai D, et al. Discogenic cell transplantation directly from a cryopreserved state in an induced intervertebral disc degeneration canine model. *JOR Spine.* 2018;1(2):e1013. doi:10.1002/jsp2.1013
376. Choi H, Merceron C, Mangiavini L, et al. Hypoxia promotes noncanonical autophagy in nucleus pulposus cells independent of MTOR and HIF1A signaling. *Autophagy.* 2016;12(9):1631-1646. doi:10.1080/15548627.2016.1192753
377. Silagi ES, Batista P, Shapiro IM, Risbud M V. Expression of Carbonic Anhydrase III, a Nucleus

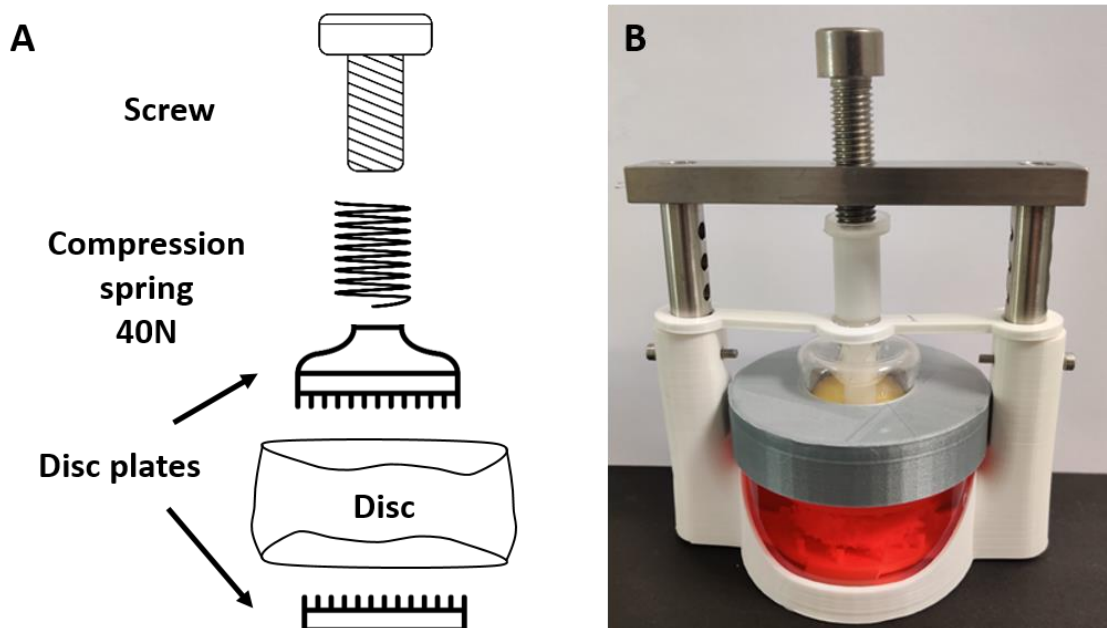
- Pulposus Phenotypic Marker, is Hypoxia-responsive and Confers Protection from Oxidative Stress-induced Cell Death. *Sci Rep.* 2018;8(1):1-13. doi:10.1038/s41598-018-23196-7
378. Pan H, Strickland A, Madhu V, et al. RNA binding protein HuR regulates extracellular matrix gene expression and pH homeostasis independent of controlling HIF-1 α signaling in nucleus pulposus cells. *Matrix Biol.* 2019;77:23-40. doi:10.1016/j.matbio.2018.08.003
379. Madhu V, Boneski PK, Silagi ES, et al. Hypoxic regulation of mitochondrial metabolism and mitophagy in nucleus pulposus cells is dependent on HIF-1 α -BNIP3 axis. *J Bone Miner Res.* 2020. doi:10.1002/acr.22212

Appendices

Appendix A – Standard operating protocols (SOPs) established within this thesis work

A.1 Bovine Disc Organ Culture

The bioreactor design includes a dynamic ball joint comprising of a long shaft and a superior disc plate. The shaft houses the spring and is long enough to enable culture of different disc heights. The superior and inferior disc plates consist of protrusions which facilitate a distributed load across the entire disc EP surface, grip the disc in place and allow the free flow of media above and below the disc organ culture, alleviating any nutritional limitations. A small plunger was designed such that when it is flush with the top of the spring shaft, spring with a rate of 8.92 N/mm (751-641, Radionics) was used to achieve compressive load of 40 N which translates to physiologically relevant static loading ~ 0.4 MPa. The top stainless steel attachment of the bioreactor features six separate pin holes to allow for screw adjustment for variable disc heights, and a centred, threaded hole where the final screw secures the vertical compression of the spring plunger onto the compression spring. To maintain oxygen exchange within culture, 100mL Pyrex crystallising dishes were incorporated with custom-made lids which have slight protrusions, mimicking those of well-plates and allowing the lid to remain raised.



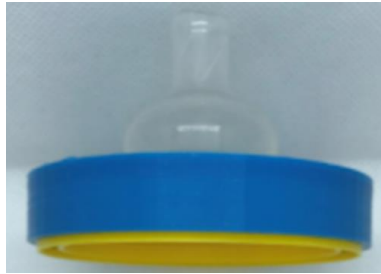
Static compression bioreactor for ex vivo disc organ culture. (A) Highlights some key elements of the bioreactor. The screw applies the vertical compression of the spring, which in turn applies a physiologically relevant load of 40N onto the disc. The superior and inferior disc plates secure the disc in place and allow the free flow of media above and below the disc. **(B)** Full assembly of the custom-made bioreactor with a cultured disc *in situ*.

Sterilisation:

Note: Prep at least 4 bioreactors per experimental group.

- All bioreactor parts which were 3D printed using fused deposition modelling (Ultimaker 2, Ultimaker) and stereolithography (Form 2, FormLabs) modelling were sterilised through ethylene oxide (ETO) sterilisation prior to culture to allow for sufficient out-gassing.
- The Pyrex dishes and other metal components were sterilised via autoclave.

Tip: Sterilise as assembled as possible i.e., the outer and inner lid lids assembled with the baby bottle cap and plunger.



- Dissection equipment: tweezers, pliers, guillotine, Allen keys
Other equipment: Gauze, squeezey bottle, chopping board

Dissection Setup:

- Setup BM hood the night before – mitre saw, tinfoil, waste bucket, hammer, chopping board
- Pin up the blade cover of saw to make sure the saw is exposed to UV
- Soak gauze in PBS + Pen-Strep (HiOsmo) and prepare 6 well plate x 3
- Soak tail in 1:100 Betodeine solution made with warm tap water (15-20 mins)
- Wipe with PBS soaked gauze

PBS prep:

- To create a high osmolarity (HiOsmo) PBS (~ 400 mOSm): add 25.26g of sucrose to 50ml and sterile filter back into the 500 mL bottle
- Add 2% penicillin-streptomycin (Pen-Strep) and 0.2% Primocin (InvivoGen)

Media prep (per 500ml bottle of high glucose (4.5g/L) DMEM):

1. Discard 60 ml of media
2. Add 50 ml of sterile filtered FBS (10%)
3. Add 10 ml of sterile filtered Pen-Strep (2%)
4. Thoroughly mix and discard 31.5 ml
5. Aliquot 50 ml in a 120 ml tube
 - Add the following to the 120 mL tube:
 - 750 mg bovine serum albumin (BSA)
 - 25.26 g sucrose (~ 400 mOSm)
 - Rotate until dissolved
 - 0.5 ml L-Proline (500 µL aliquot)

- 5 ml Sodium pyruvate (fridge)
- 6. Sterile filter back into the stock bottle
- 7. Add 0.2% Primocin (InvivoGen)

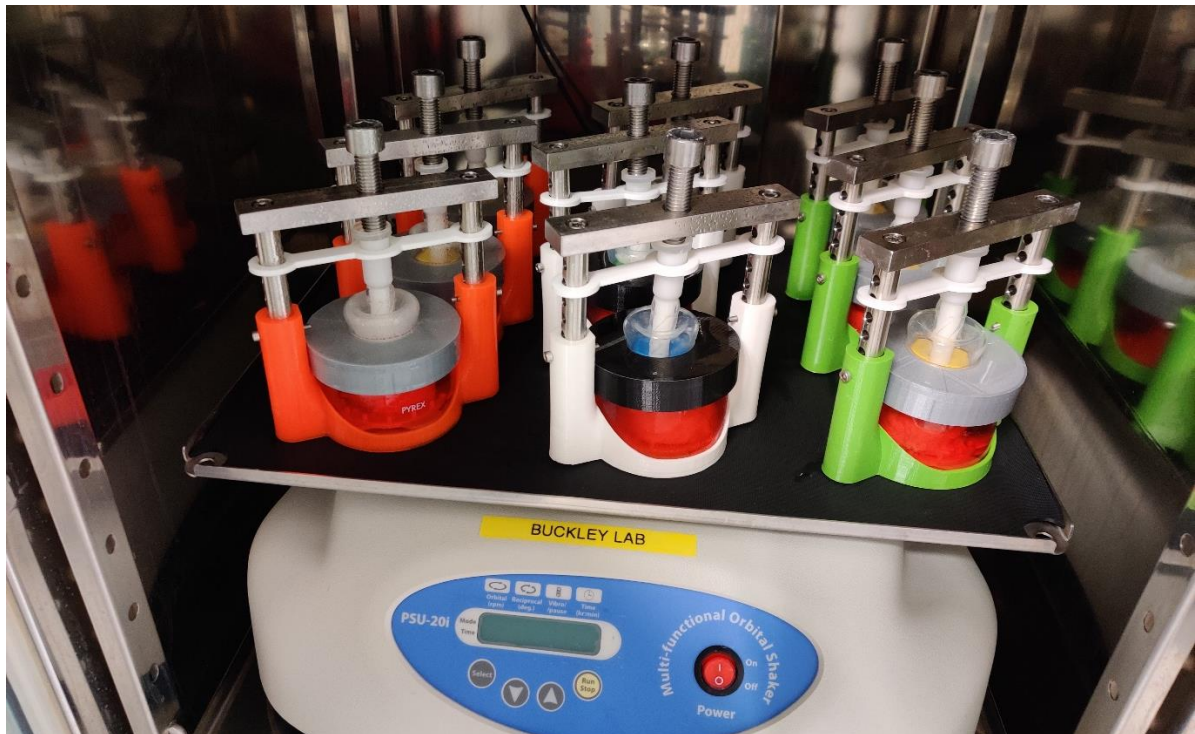
Feeding:

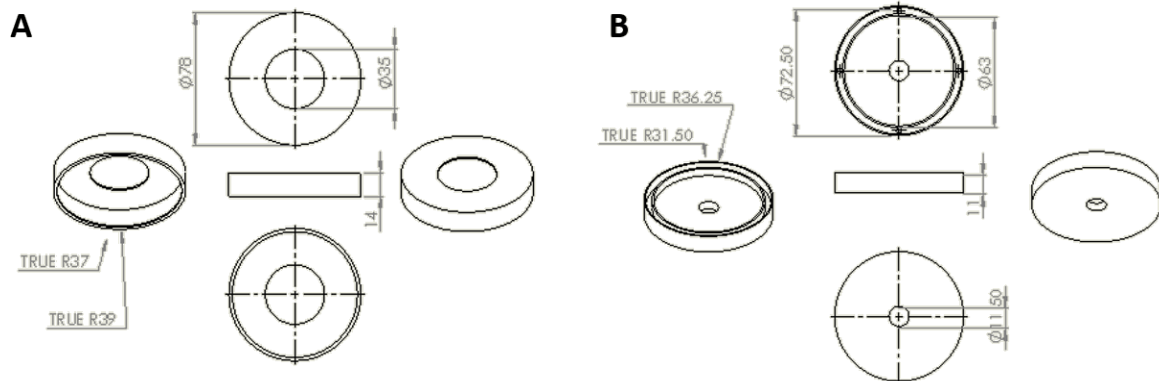
3 groups (n=3) => 720 ml (80 ml x 9)

Note: Prior to a full media exchange media samples were kept for analysis

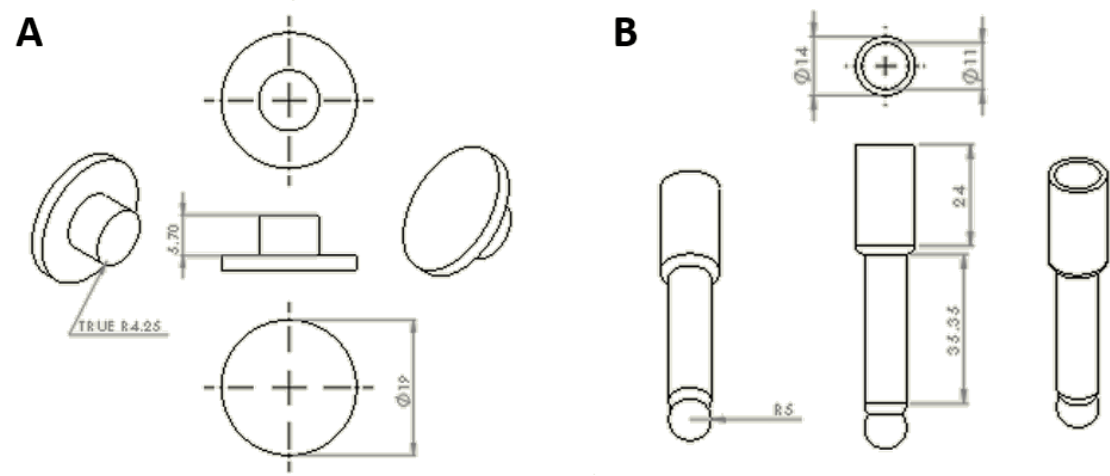


The individual bioreactors were placed on an orbital shaker under gentle agitation (25 rpm) in a normoxia incubator (37°C, ~20 %O₂ and ~5 %CO₂). The culture period was seven days, with a complete media exchange performed halfway through the culture period.

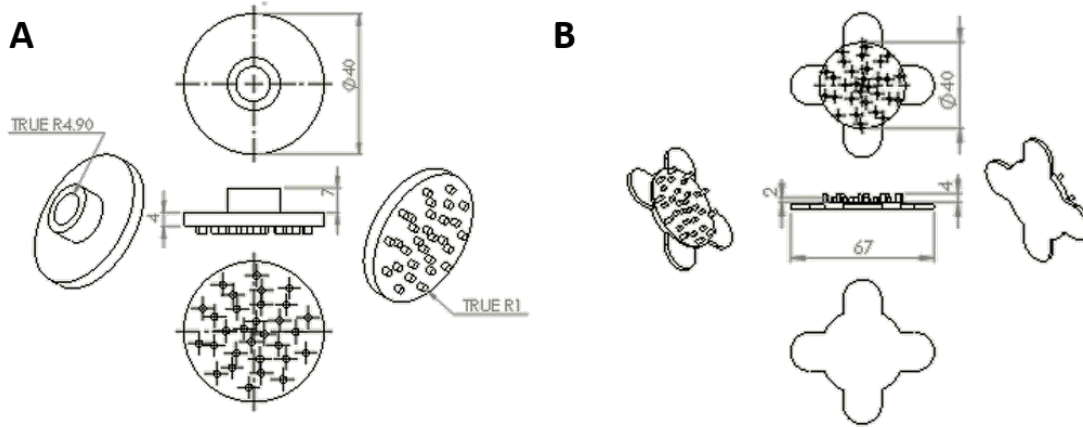




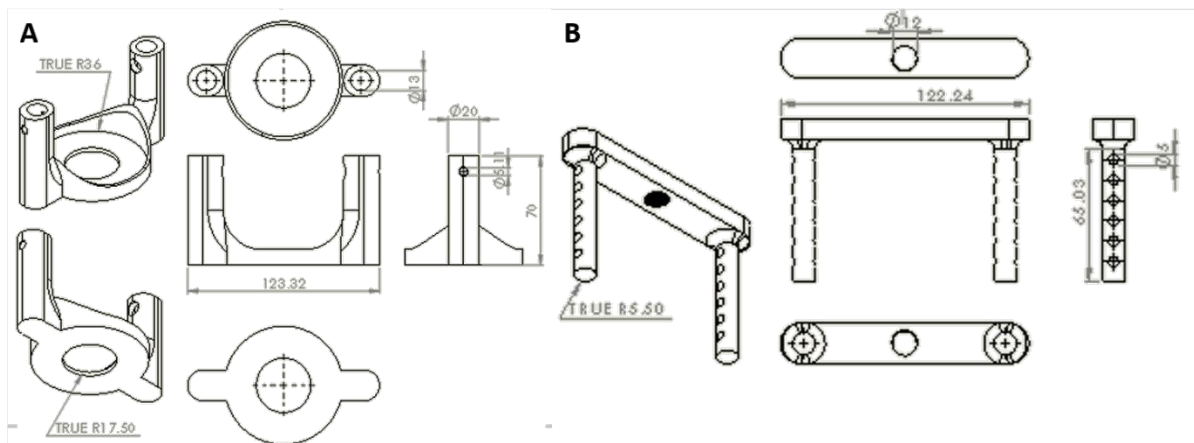
Drawings of bioreactor lids. (A) Outer lid of the bioreactor, which locks into the inner lid. **(B)** The inner lid fits onto the rim of the Pyrex culture dish, while remaining raised to enable exchange of gases.



Drawings of the plunger and shaft of the bioreactor. (A) Plunger which sits on top of the spring shaft. When the top screw is tightened flush with the top of the plunger, it compresses the spring to induce a load of 40N. **(B)** The spring shaft houses the spring and has a dynamic ball joint where it meets the superior disc plate to allow for flat and angled disc endplates.



Drawings of the superior and inferior disc plates. (A) The superior disc plate has a ball socket on its top surface into which the ball of the spring shaft fits. **(B)** The inferior disc plate sits under the cultured disc. Both disc plates have protrusions which help to grip the disc in place and allow fluid flow above and below the disc.



Drawings of the base and top attachments of the bioreactor. (A) The base of the bioreactor holds a 100 mL Pyrex culture dish in the centre. It also has two post-holes opposite each other which hold the posts of the top attachment with a pin joint. **(B)** The top attachment of the bioreactor has a threaded hole in the centre for the top screw to apply the compression. The posts, which slot into the base, have a number of holes to adjust the height of the pin joint based on disc height.

A.2 Determining the Metabolically Active Cell Density of Disc Tissue

⚠️ **Protocol involves use of toxic chemical: Thiazolyl Blue Tetrazolium Bromide (commonly known as MTT). Weight powder form in fume hood and use always use nitrile gloves.**

⚠️ **Cryogenics training required for working with Liquid Nitrogen**

Materials

- MTT or Methylthiazolyldiphenyl-tetrazolium bromide (3-(4,5-Dimethyl-2-thiazolyl)-2,5-diphenyl-2H-tetrazolium bromide) (CAS-No. 298-93-1, Sigma-Aldrich)
- PBS and/or phenol-free media (high osmolarity if applicable)
- OCT (optimal cutting temperature) compound (361603E VWR)
- 2-Methylbutane or often referred to as isopentane (M32631, Sigma-Aldrich)
- Liquid Nitrogen
- Wet or dry ice (preferable dry)
- Fluoroshield with DAPI (F6057, Sigma-Aldrich)

- Large Styrofoam box and lid
- Metal beads (main lab)
- Larger plastic beaker (e.g., 2 L) & smaller glass beaker (e.g., 500 mL)
- Long tweezers
- Histology moulds

Location (general or group-specific)

- MTT powder – L3.30, CTB fridge door in tinfoil (group-specific)
 - MTT stock solution – L3.30, CTB freezer, 2nd drawer, 50mL tube in tinfoil
- OCT – L3.30, long cupboards (group-specific)
- 2-Methylbutane – L.29, fridge, 1L brown bottle (general)
- Fluoroshield with DAPI – L3.30, TB fridge door (group-specific)

MTT staining

1. Stock solution concentration: 5 mg/mL
 - MTT powder dissolved in PBS & stored at -20 for 6 months (see above for location)
2. Working solution: 0.5mg/mL e.g., for 10 mL take 1 mL stock solution & 9 mL phenol free media (high osmolarity if applicable)
3. Incubation time: 3 hours (dependent on tissue thickness) at 37 degrees on a shaker.
4. Colour change to blue will be observed in metabolically active regions
5. Rinse tissue a few times with PBS, removing as much of the yellow solution as possible
6. OCT embed immediately and leave overnight in fridge if tissue is unfixed (see below)

OCT embedding + freezing

1. Fill a histology mould just big enough for tissue sample) with OCT and be careful to avoid bubble formation. Use a Pasteur pipette to remove any bubbles. Place the sample in the mould directly in contact with the bottom.
2. Leave over-night to allow OCT to seep into the tissue. Keep unfixed tissue refrigerated.

When ready to snap freeze – prepare isopentane in **fume hood with any heat or ignition sources removed**:

3. Place glass beaker into the plastic beaker with the metal beads surrounding it as shown below. The beads operate as a weight.
4. In the **fume hood**, pour the isopentane into the glass beaker (**careful**: the bottle will be pressurised when opened). Pour enough isopentane to cover sample when submerged (3-4 cm is enough for histology moulds).
5. Place the beaker system into a Styrofoam box with approximately 5cm of liquid nitrogen in it. Allow to chill for 20-30 mins until ice forms on the beaker and the solution appears very cold.



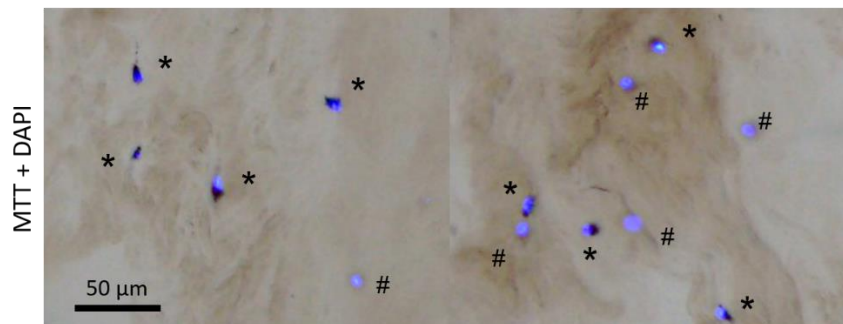
6. Using long tweezers, submerge the moulds containing the sample into the chilled isopentane for 10 - 20 seconds. OCT will turn completely white/opaque. Try to keep the mould level and not let the OCT and sample move.
7. Remove and allow isopentane to drip from sample.
8. Place sample on dry ice until sectioning or storage at -80°C .

Cryo-sectioning

- Contact Gavin McManus (MCMANUG@tcd.ie) for training on cryostat and book via iLabs https://tcd.corefacilities.org/service_center/3268/?tab=equipment (5 euro/hr)
- For cell quantification tissue typically sliced at $10\ \mu\text{m}$

DAPI counterstain and Image analysis

- Use PBS to remove OCT from slides carefully (potential to fix slices at this stage but not recommended)
- Fluoroshield with DAPI, coverslip & seal with nail varnish
- Image immediately (if fixed) using brightfield for MTT and fluorescence for DAPI (e.g. Olympus BX51)
- Using imageJ:
 - Automatic particle counting for DAPI
 - Manually count MTT positive stained cells using combined bright field & DAPI & cell counter plug-in



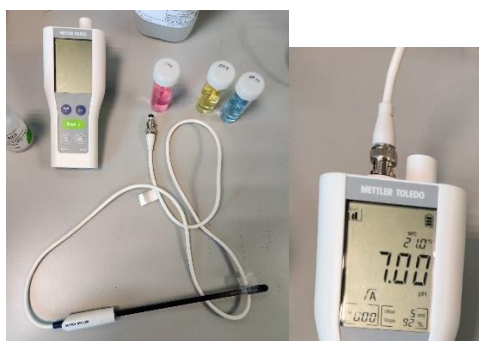
Viability criteria for viable cell density analysis. By merging the MTT brightfield with the DAPI counterstaining, metabolically viable cells can be identified by overlapping formazan crystal deposition and blue fluorescing nuclei (*), while dead cells are identified by blue fluorescence in the absence of black formazan deposition (#).

A.3 Calibration of Resources for Assessing Metabolic Concentrations

pH Sensor Probe Calibration (METTLER TOLEDO)

Stored in long Buckley cupboards in Biomaterial's lab (L3.30)

- pH sensor probe (InLab Expert Pro-ISM)
 - Measuring range: pH 0 – 14
 - Temperature range: 0 - 100°
 - Shaft diameter: 12 mm
- Portable pH meter
- pH buffers: pH 4 (buffer 1), pH 7 (buffer 2) and pH 10 (buffer 3)
- 3 M KCl reference electrode filling solution (Orion 910008 Thermo Scientific)
- Di water & Kimwipes



Calibration

1. Connect the pH probe sensor to the left port of the meter as shown above.
2. Remove the parafilm on probe tip and wetting cap (containing the reference electrode filling solution).
3. Turn meter ON (blue Exit button) and press Calibrate (blue Cal button).
4. Place the probe into buffer 1 (pink pH 4), note "Cal. Lin. 1" in the bottom left of the scene on the meter. Hold probe still until value has stabilise and meter beeps.
5. Rinse electrode with Di water and carefully tap it with a kimwipe to remove excess liquid (never wipe the pH probe)
6. Place the probe into buffer 2 (yellow pH 7), note "Cal. Lin. 2" in the bottom left of the scene on the meter. Hold probe still until value has stabilise and meter beeps.
7. Rinse electrode with Di water and carefully tap it with a kimwipe.
8. Place the probe into buffer 3 (blue pH 10), note "Cal. Lin. 3" in the bottom left of the scene on the meter. Hold probe still until value has stabilise and meter beeps.
9. Rinse electrode with Di water and carefully tap it with a kimwipe.
10. Calibration is complete and probe is ready for measurement.



pH Measurement

1. Place electrode submerged in solution and press Read (green button).
2. Hold probe still until value has stabilise and meter beeps. pH measured will stay displayed on the screen.
3. Rinse electrode with Di water and carefully tap it with a kimwipe between experimental measurements

Probe storage

- Using a transfer pipette, ensure there is some reference electrode filling solution inside the black wetting cap of the pH probe.
- Carefully place the wetting cap onto the electrode tip, wiping away any excess filing solution.
- Gently wrap parafilm around the top of the wetting cap to create a seal and stoppe the electrode from drying out.
-

Oxygen Microsensor Probe Calibration (PreSens)

Materials

- Needle-type oxygen microsensor: NTH-PSt1-L5-TS-NS40/0.8-NOP
 - Needle casing: 40 mm length & 0.8 mm outer diameter (~21G)
 - Measuring rage: 0 – 50%O₂
 - Temperature range: 0 - 50°
 - Sterilisation: EtO
 - Calibration: Two-point with oxygen-free environment (nitrogen, sodium sulfate) and air-saturated environment
 - Cleaning: 3% hydrogen peroxide, Ethanol or soap solution
 - Storage: 60-month stability once stored in the dark at room temp.
- Micro-fibre Optic Oxygen Transmitter: Micro TX3
- Buckley lab XPS laptop with Presens software (password: BuckleyLab2015)
- Yellow capped tubs with holes in lids (as shown below).
- Tubing for compressed air & nitrogen stream with a syringe and 18G needle attached (as shown below)
- Retort stand



Setup

1. Fill the yellow tubs with Di water (approximately $\frac{3}{4}$ full).
2. Attach tubing with syringe and needle attached to the compressed air/nitrogen gas line.
3. Place the temperature sensor into the yellow tub with a single larger hole.
4. Set up the retort stand with the oxygen needle sensor and syringe connected to the air/nitrogen supply entering the same tub (ensure both needles are well submerged into the Di water).
5. The syringe from the air/nitrogen supply is placed into one of the holes in the cluster of holes, while the oxygen sensor goes into the single hole on the other side of the lid (as shown below)



6. Open valve (blue lever) on the compressed air/nitrogen gas line.
7. Turn the knob on the air/nitrogen supply to get a steady stream flowing through the tubing/syringe/needle into the Di water and creating a steady stream of bubbles.
8. Ensure the bubbles are not too close to the oxygen sensor needle as the fibre-optic probes are very fragile and can break easily (see above)

Valve closed

Valve open



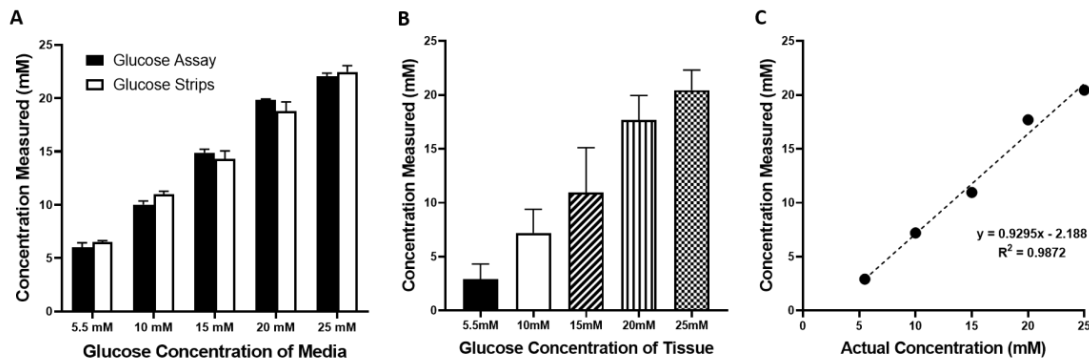
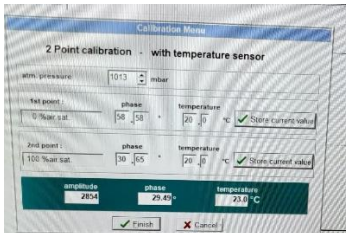
2 Point Calibration (with temperature sensor):

0 %air saturation

- Tubing & syringe attached to **nitrogen gas** supply.
- Following instructions on the software, record the phase and temperature for the 1st point.
- Ensure that the nitrogen gas has successfully purged any oxygen from the Di water by waiting until the phase reading has stabilised.
-

100 %air saturation

- Tubing & syringe attached to **compressed air** supply.
- Following instructions on the software, record the phase and temperature for the 2nd point.
- Ensure that the compressed air has successfully saturated the Di water by waiting until the phase reading has stabilised.



Assessing the accuracy of the biochemical glucose assay. (A) Media samples of known glucose concentration tested using the glucose assay and the glucose sensor strips. **(B)** Results of the measured glucose concentration in tissue samples of a known glucose concentration. **(C)** Standard curve with an equation of the line to be used as a correction factor for the biochemically determined glucose concentration.

A.4 Enzymatic Isolation of Rat, Goat and Human NP and AF Cells

- ⚠ **Protocol involves the use of the hazardous material Trypan blue (Carcinogenic and toxic, use PPE, avoid contact and work inside the culture hood)**
- ⚠ **Protocol involves use of sharps such as scalpel blades.**

Materials:

Name	Conc.	Abb	storage	code	Vendor
Sterile syringe filter (0.2 µm)				10216441	Fisher
Amp B			-20°C		
1x Phosphate buffered Saline (sterile)	1x	PBS	RT		
FBS			-20°C		
Trypan Blue					
Collagenase type II			4°C		Gibco
Pen/Strep		P/S	-20°C		
Dulbecos Modified Eagles Medium		DMEM	4°C		Gibco
Pronase			4°C		Millipore
Primocin	50mg/mL		-20 °C		InvivoGen

Reagents

Washing buffer (keep at room temp.)

Sterile 1x PBS + 2% P/S + AmpB + 0.2% Primocin (product concentration: 50 mg/mL, working concentration 100µg/mL)

Example: For 500mL

1. Take 489 mL sterile PBS
2. Add 10mL P/S (sterile filter)
3. Add 50µL Amp B
4. Add 1 mL primocin

Digestion media (keep in fridge at 4°C)

Low glucose (5.5 mM) DMEM + 2% P/S + 0.2% Primocin

Example: For 500 mL

1. Take 489 mL LG DMEM
2. Add 10mL P/S (sterile filter)
3. Add 50µL Amp B
4. Add 1 mL primocin

Digestion volumes:

Rat: estimate 5 mL per rat tail i.e., 15mL for a batch of 3 donors or 30 mL for a batch of 6 donors; typically, 10-12 discs per tail

Goat: estimate 25 mL per disc (10 mL for the NP, 10 mL for the AF); typically, 4-5 discs per spine

Human: 10 mL/g of tissue

Expansion Media (XPAN) (keep in fridge at 4°C for up to 3 months)

Low glucose (5.5 mM) DMEM + 2% P/S + 10% FBS + AmpB

For 500 mL (full bottle)

1. Remove 60 mL DMEM and discard
2. Add 10 mL sterile PS (sterile filter)
3. Add 50 mL FBS (sterile filter)

Pronase (Millipore Corp MERCK 53702-50KU)

Stored at 4°C (in enzyme box) in biomaterials fridge

Note: activity changes from batch to batch. Check specification and prepare digestion solution accordingly

Working concentrations:

- **Rat:** 70 U/mL of digestion media for NP and AF
- **Goat:** 100 U/mL of digestion media for NP and AF
- **Human:** 100 U/mL of digestion media for NP and AF.

Collagenase Type II (Gibco 17101015)

Stored at 4°C (in enzyme box) in biomaterials fridge

Note: activity changes from batch to batch. Check specification and prepare digestion solution accordingly

Working concentrations:

- **Rat:** 400 U/mL of digestion media for NP and AF.
- **Goat:** 300 U/mL of digestion media for NP and AF.
- **Human:** 300 U/mL of digestion media for NP and AF.

1. Weigh pronase + collagenase and combine with desired volume of digestion media.
2. Place digestion media into a water bath at 37°C to dissolve while performing the tissue isolation.
3. Insure to **sterile filter** (0.2 µm filter) the digestion media prior to adding it to the tissue.

Preparation when tissue isolation day is confirmed:

- Book biomaterials hood for tissue dissection, oven at 37°C and animal lab hood for cell counting/plating/freezing
- **Goat:** transport/containers
- Ensure carcass waste has been emptied in advance
- Ensure there is a good supply of IMS in the lab
- **Goat + Rat AF:** Ensure C-tubes are sterile (EtO at least 2 days prior to allow adequate degassing)
- Ensure you have the necessary tissue culture plastic e.g., appropriate flask (yellow capped for NP cells) and sizes
- Ensure adequate incubator space and correct oxygen level for study/expansion
- Ensure there is a sufficient supply of enzymes, media, supplements, and iodine solution.

Prepare the day before:

- Prepare and/or Sterilize:
- Sterilise equipment: Tweezers (One per person plus a spare)

- Gather scalpels (user dependent but No. 15 may be preferred for rat isolation), sterile petri dishes (animal lab cupboards) etc.
- 500 mL washing buffer
- 500 mL expansion media
- Digestion media
- Weigh enzymes the day before (can combine enzymes but keep dry at 4°C)
- Coat flasks – if appropriate; gelatine coat the flasks the evening before cell isolation
- Weigh sterile tubes for tissue collection and write the weight on the tube (e.g., 50 mL tube per goat donor).

Morning of isolation

1. Prep the biomaterials hood – wipe down surfaces with IMS, spray everting with distal and leave for 10 mins before wiping away and doing a final wipe with IMS. Prepare a square of tinfoil (double layer) in each working area, maximum two people working in the hood at one time. Place tweezers and scalpels on the working area (always spraying everything into the hood)
2. Wash a large waste beaker (particularly important for goat isolations) with soapy water, line with small yellow waste bags, fill a small beaker with 70% IMS for equipment and spray both into the hood.
3. Close hood and put on UV while waiting for the tissue to arrive

Rat tissue harvesting

Tails are likely obtained within an hour of euthanasia

1. Place washing buffer into the water bath at 37°C.
2. Outside of the hood: using a sterile scalpel cut the skin of the tail (proximal to distal) on opposite sides of the tail and pull the skin off the tail.
3. Using the spray bottle of iodine solution (50% iodine solution, 50% water), disinfect the tails thoroughly, spray with 70% IMS and place into the working area of the hood.
 - a. There will be many strings, that can be pulled off the tail
4. Open the IVD by inserting a blade as close as possible to the bounding endplate along the transverse plane, avoiding the central plane of the disc to maintain NP integrity and avoid tissue shearing.
5. Once opened, the disc tissue is exposed. Scoop out the gelatinous NP using needle point tweezers and place into the pre-weighed tubes.
6. For AF isolation: cut along the other bounding endplate to remove the AF tissue in donut-shaped slice. AF tissue will need to be diced into smaller pieces on a sterile petri dish. Place into the pre-weighed tubes.

Tip: To maximise AF surface area, hold the AF with tweezers and shred the tissue with repeated strokes into extremely fine pieces

Tip: Change Scalpel when they get dull

Tip: keep tissue moist using washing buffer. Dry out tissue leads to increasing cell death

7. Proceed to the next disc, working proximal to distal through the tail. Gathering the NP (and AF) at each caudal level until the disc become too small.
8. If sterility is questioned at any point, discard the tissue, it is not worth compromising the entire batch.
9. Continue until all the tails have been incorporated into the batch of NP (and AF). Usually 3-6 tails per batch.
10. Re-weigh the tubes to get the tissue weight. Expected weight is ~ 15-18mg/tail.

Goat tissue harvesting

Spines are likely obtained within 5-6 hours of euthanasia

1. Place washing buffer into the water bath at 37°C.
2. Remove the sacrum/pelvis (if attached) by cutting through and scarifying the final disc, it is harder to clean and is not worth compromising the isolation.
3. First wash the spines thoroughly with lukewarm soapy water, then place into a bucket of iodine solution (10% iodine stock iodine solution, 90% lukewarm water) to disinfect the spines for 5-10mins.
4. Outside of the hood: in a clean area (with a double layer of bin bags covering the bench top), remove as much extraneous tissue as possible using a tweezers and scalpel (avoid touching the exposed under tissue with your hands) until the discs can be clearly identified.
5. Spray with 70% IMS and transfer into the working area of the hood using tinfoil (sprayed with IMS) rather than your hands.
6. Open the IVD by inserting a blade as close as possible to the bounding endplate along the transverse plane, avoiding the central plane of the disc to maintain IVD integrity. Using the spinous processes for grip, 'snap' the disc open.
7. Once opened, the disc tissue is exposed. Cut out the NP using a blade to trace the interface between NP and AF tissue and get under the NP tissue with the blade to separate it from the other bounding EP. Place into the pre-weighed tubes.

Tip: To maximise AF surface area, hold the AF with tweezers and shred the tissue with repeated strokes into extremely fine pieces, changing scalpel as soon as it gets dull

Tip: keep tissue moist using washing buffer. Dry out tissue leads to increasing cell death

8. For AF isolation: cut along the other bounding endplate to remove the AF tissue (probably in sections, hard to remove the AF in a single slice as is the case for rat tissue). AF tissue will need to be diced into smaller pieces on a sterile petri dish. Place into the pre-weighed tubes.
9. Proceed to the next disc. Gathering the NP (and AF) from 4-5 discs per donor.
10. Re-weigh the tubes to get the tissue weight. Expected weight per donor is ~ 1.3g of NP and ~ 1.7g of AF.
11. If sterility is questioned at any point, discard the tissue, it is not worth compromising the entire batch.

Human tissue harvesting

Tissue returned to lab with 2 hours of surgical removal (discectomy), operating in HL only

1. Place washing buffer and digestion media into the water bath at 37°C.
2. Add washing buffer and spin down at 650G for 5 minutes (repeat 3 times using fresh washing buffer each time in order to remove as much blood and debris as possible)
3. Aspirate washing buffer and replace with digestion media (without enzymes) containing kanamycin sulfate at 100 µg/mL (sterile filter) and place in the incubator overnight.

Tissue Dissociation and Cell culture

Clean collection tubes thoroughly, change culture sleeves & gloves and move isolated tissue into AL hood and continue working there.

1. Add equal quantities of washing buffer to all tubes and spin down at 650G for 5 minutes (it is standard to repeat 3 times using fresh washing buffer each time, this is best practice for goat tissue, but one wash may be preferred for rat tissue where there is greater risk of losing tissue each time).

2. **Goat:** Aspirate washing buffer and replace with digestion media (without enzymes) and place in the incubator overnight (this is not only a good way to verify no bacterial growth, but it splits the isolation into 2 more manageable days), ensure that the caps of the tubes are loosely unscrewed in the incubator for oxygen. Continue the following steps the next morning.
3. **Rat/Goat/Human:** Aspirate washing buffer/enzyme-free media.
4. **Human:** Separate the AF and NP on a sterile petri dish using a scalpel and tweezers separate. NP will have swollen overnight while the AF will have retained its structure with visible lamellae structure. Use separate tweezers and mince NP and AF into smaller fragments on separate petri dishes to prevent cross contamination from this point onwards.
5. Ensuring that the digestion media **containing enzymes** was sterile filtered, add the desired volume calculated based dependent on the amount of tissue collected from the relevant species (see guidelines above).
6. Incubate in the oven at 37°C in rotator at 10 r.p.m.
 - a. **Rat NP** – incubate for a period of 5-6 hours checking regularly and triturating with a 18G needle as the tissue starts to break up (after ~ 1-2 hours).
 - b. **Rat AF, Goat NP & AF** – will need further mechanical dissociation using the C-tubes and tissue dissociator (gentleMACS).
 - i. Transfer the tissue and digestion media into the C-tubes (max. 10 mL per tube)
 - ii. Invert the tube and attach to the dissociator, make sure tubes are tightly sealed
 - iii. Select:
 1. Spleen 03.02 (15 sec)
 2. Adipose (50 sec)
 3. Spleen 03.02 (15 sec)
 - iv. Return the digests to 37°C and after 1 hour repeat the tissue dissociator steps, continuing until the tissue has been broken down.
 - c. **Human NP and AF** - incubate for a period of 3-4 hours checking regularly and triturating with a 18G needle as the tissue starts to break up (after ~ 1-2 hours).
7. It is recommended to check the digestion media as the tissue breaks down using trypan blue to have an idea how well the cells are being released and whether they are still in clumps or whether they have reached the level of single cells.
8. Stop the digestion when you have a lot of single cells to avoid cell damage/death, transfer digestion into a fresh 50 mL tube using a 70 µm cell strainer (using several strainers if there remains tissue that will clog the strainer, potentially use a stripette to slowly transfer the digest to avoid spillage or compromising the sterility)
9. Centrifuge cell suspension at 650G for 5 minutes, aspirate the digestion media, add washing buffer, break up the cell pellet and spin down again at 650G for 5 minutes.
10. Resuspend the cells in XPAN media and perform a cell count (relevant SOP)

Do one of the following:

1. Plate cells for cell expansion
2. Use cells for experiment
3. Freeze cells for long-term storage

A.5 Disc Micro-Spheroid Formation using Rat, Goat and Human cells (NP and AF)

NOTE:

- This is an effective method for a 'standardised' protocol that works across both NP and AF cells from different species (rat, goat and human). However, adjustments to the protocol such as settling time and centrifuge step could be refined further to optimise each specific cell type and species separately.

Making the agarose microwell array (typically the day before seeding)

Several size variations of the 'positive' stamps are available (all with 1 mm diameter microwells):

- 6-well plate: 401 microwell array
- 12-well plate: 145 microwell array
- 24 well plate: 69 microwell array

The stamps are best printed with FormLabs High Temperature resin so that they can be sterilised in the autoclave.

Sterile equipment:

- Tweezers, appropriate size spatula or the desired well size, petri dishes and well plates to form the agarose moulds in.
1. Prepare a sterile solution of Agarose (TCBE Chem List #180) in DI water.
 - a. 4% w/v (400 mg in 10 mL or 4 g in 100 L) is best for 6-well moulds
 - b. 2% w/v (200 mg in 10 mL or 2 g in 100 L) is favourable less brittle agarose in the smaller 24-well moulds.

Tip: Autoclave agarose solution ~ 2 hours before planning to make the moulds to have a sterile molten solution. Otherwise keep at 80°C in the oven 3, until needed in the laminar flow hood.

2. Add 6 mL of agarose to each 6-well, 2 mL to each 12-well or 1 mL to each 24-well.

Tip: use the centre most cells of a 12-well and 24-well plate as better spheroids form in these wells than the edge wells, due to the centrifuge.

3. Immediately place the positive stamp into the agarose, ensuring that it is not touching the bottom of the well and that no air bubbles are present.

Tip: Spray the positive microwell surface of the 6-well stamps with sterile DI water prior to inserting it into the agarose, this helps to eliminate bubbles in the larger moulds but is not necessary for the 12- and 24-well stamps.

Tip: Holders can be used to keep the stamp in place and stop it from sinking to the bottom of the well.

4. Allow the agarose to set 5 - 20mins depending on the size of the well and how hot the agarose was.
5. Return the agarose solution to the oven while the agarose in the plate sets.

Tip: Removing the positive stamp successfully will take some practice to perfect. Always practise non-sterile on the benchtop first.

6. Using a flat spatula (size appropriate to the well size) cut the excess agarose away from the top of the positive stamp. Tweezers are helpful if agarose does not come up in one piece.
7. Carefully separate the stamp from the agarose by tilting the handle.

Tip: This is trickier in the smaller wells and a tiny spatula can be used to gently pull the agarose mould down if it lifts with the stamp.

8. Repeat the process for all wells.
9. Add media (typically XPAN but whatever media is appropriate to what your culture condition/experiment will be) to the wells and place in an incubator until seeding time. Approximately ~ 3 mL for a 6-well and ~ 1 mL to a 24-well.

Seeding the micro-spheroids

1. Change the centrifuge to the plate rotor (124mm) and spin each plate (using an appropriate balance) at 850 G for 5 mins to remove any air bubbles and ensure the agarose is settled at the bottom of the well plate.

Tip: G- force is the equivalent of relative centrifugal force (RCF). It is different to the revolutions per minute (RPM) but can be calculated from RPM together with the radius of the rotor (mm).
2. Trypsinise flasks and perform a cell count as standard.
3. Remove the soaking media from the agarose moulds.
4. Seed each well with the appropriate number of cells to achieve the desired 'cells per spheroid'.
 - a. 6-well plate: 401 microwell array using 3 mL cell suspension
 - b. 12-well plate: 145microwell array using 2 mL cell suspension
 - c. 24 well plate: 69 microwell array using 1 mL of cell suspension

Note: range of 1,000 – 60,000 cells/spheroid have been tried in this microwell configuration.
5. Return the plates to the incubator and allow cells to settle for 5 – 20 mins.

Tip: Settling time may need to be optimised exactly for each cell type/species.
6. Spin the plates at 850 x G for 5 minutes to collect all the cells at the bottom of the microwells. Confirm this using the microscope and return the plates to the incubator.

Tip: Centrifuge settling may need to be optimised exactly for each cell type/species.

Culture of the micro-spheroids

In-silico models have informed the culture conditions and feeding schedule of wells seeded at 20,000 cells/spheroid in the 24-well configurations (1.38 million cells/24-well).

For a 'physiologically relevant' micro-niche within this setup:

- Culture in a 10 %O₂ incubator with 1 mL of low glucose XPAN media (5.5mM or 1 g/L).
- Refresh the media daily to prevent pH dropping due to accumulation of lactate with the low media volume of 1 mL.

Note: Cell aggregates tend to form compact spheroids within 1-4 days and have been cultured up to 7 days within this microarray configuration. Compaction time till depend on how happy/healthy the cells are, and a species effect has been evident.

Harvesting the micro-spheroids

- Spheroids can be accessed individually using a P1000 tip on the minimum volume.
- Or harvested all together by flushing the media over the micro-spheroids to help liberate them using a P1000. Remove the media containing the loose spheroids and transfer to the collection pot. Flip the agarose mould upside down into a new well-plate and spin the inverted moulds at 750 x G for 5 min to remove the last of the spheroids. Rinse the agarose thoroughly to aspirate all spheroids.

Tip: ~ 400 µm sieves can be used to strain the spheroid suspension and trap agarose fragments depending on the application of the spheroids.

A.6 Basel Metabolic Rates of Disc Spheroids using Seahorse Analysis

Materials:

Name	Conc.	Abb	storage	code	Vendor
Poly-D Lysine	100µg/mL	PDL	-20°C	P6407	Sigma
XF DMEM			4°C	103575-100	Agilent
Glucose Solution	1M	Gluc	4°C	103577-100	Agilent
Pyruvate Solution	100mM	Py	4°C	103578-100	Agilent
Glutamine Solution	200 mM	Glut	-20°C	103579-100	Agilent

Reagents:

Poly-D-Lysine (Aliquoted at -20°C)

1. Add 50 mL of sterile tissue culture grade water (DI) to a 5 mg bottle.
Working concentration: 100 µg/mL
2. 1mL aliquots can be stored frozen at -20 °C and thawed in a 37 °C water bath prior to coating the spheroid microplate.

Note: Using the recommended 30µl per well a whole 96-well plate would use just less than 3mL.

Seahorse media (made up fresh on the day of the assay)

Note: It is recommended to incubate assay medium at 37°C for no more than 4 hours, as substrates, such as glutamine, can degrade.

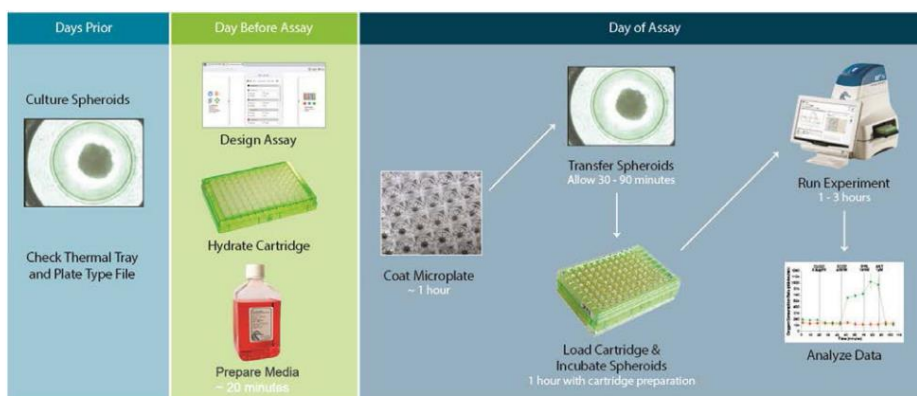
Example: For a full 96-well plate 20 mL is sufficient (175 – 180 µl/well)

1. Take 19.5 mL no glucose XF DMEM
2. Add 200 µL of pyruvate solution (working conc. 1 mM)
3. Add 200 µL of glutamine solution (working conc. 2 mM)
4. For low glucose conditions: add 100 µL of glucose solution (working conc. 5 mM)
5. Adjust to pH 7.4 if necessary and sterile filter using a 0.2 µm filter.
6. Maintain media at 37°C until loading the microplate with 175 µl/well.

Note: Seahorse analysis requires non- or low-buffered assay media. Agilent's' XF DMEM is recommended. No adjustment to the final pH is required when using the recommended the Agilent Seahorse XF Supplements. See Agilent's "Preparation of XF Assay Media" instruction sheet for more details.

Agilent Seahorse XF Supplement	Range of final supplement concentrations recommended for final pH of 7.4 +/- 0.2
Seahorse XF Glucose (1.0 M solution)	0 – 10 mM
Seahorse XF Sodium Pyruvate (100 mM solution)	0 – 1 mM
Seahorse XF L-Glutamine (200 mM solution)	0 – 2 mM

Spheroid Microplate Assay Workflow



Note: The XFe96 analyser on TBSI level 5 (DKF lab) has a thermal tray compatible for the spheroid microplate. However, see Agilent's "XFe96 Spheroid Microplate and Flux Pak" user guide for further information on each step.

Day before assay:

1. Aliquot at least 20 mL of Seahorse XF Calibrant into a 50 mL conical tube.
2. Open the XFe96 Extracellular Flux Assay Kit and remove the contents.
3. Place the sensor cartridge upside down next to the utility plate.
4. Fill each well of the utility plate with 200 μ L of sterile DI water using a multichannel pipette
5. Carefully lower the sensor cartridge onto the utility plate, submerging the sensors in the water.
6. Verify the water level is high enough to keep the sensors submerged.
7. Place assembled sensor cartridge and utility plate together with the tube of calibrant in a non-CO₂ 37°C incubator overnight (incubator beside the Seahorse analyser on TBSI level 5).

Day of assay:

A. Coat the microplate (within a sterile biosafety hood)

1. Add 30 μ L of poly-D-lysine per well, ensuring that the detent in the Agilent Seahorse XFe96 Spheroid Microplate is covered.
 - a. **Tip:** To save time and aliquots only coat as many wells as needed for the assay.
2. Spin the plate in the centrifuge at 650xG for 5 min ensure there are no air bubbles. Ensure you are using an appropriate microplate balance.
3. Leave the plate let sit for 20 minutes in the culture hood.
4. Aspirate poly-D-lysine from the wells.
5. Wash the wells two times with 200 μ L sterile DI water using the multichannel pipette.
6. Aspirate after final wash, and air dry for a minimum of 30 minutes.
 - a. **Tip:** Use this time to make up the seahorse assay media as shown above.
7. Warm the plate for 30 minutes in a 37 °C non-CO₂ incubator.
8. Add 37 °C media and return the plate to a 37 °C non-CO₂ incubator until ready to load spheroids.

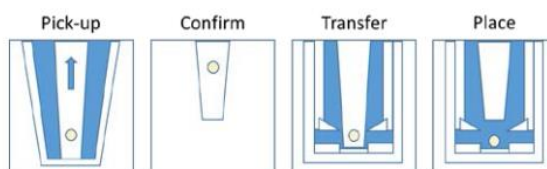
B. Transfer sensor cartridge into Seahorse XF Calibrant

1. Remove the conical tube of calibrant and assembled sensor cartridge with utility plate from the incubator.
2. Place the sensor cartridge upside down next to the utility plate.
3. Remove and discard the water from the utility plate, tap upside down over some tissue to remove any remaining drips.

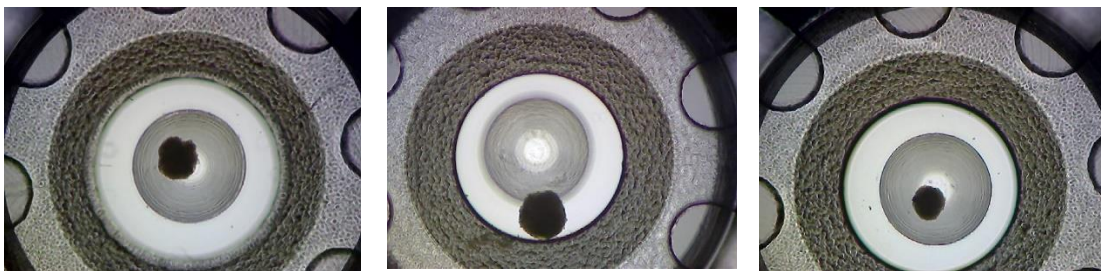
4. Fill each well of the utility plate with 200 μL of the pre-warmed XF Calibrant.
5. Lower the sensor cartridge onto the utility plate, submerging the sensors in calibrant.
6. Place assembled sensor cartridge with utility plate in a non-CO₂ 37°C incubator for 45 – 60 minutes prior to loading the injection ports of the sensor cartridge (if relevant to the specific assay).
 - a. **Tip:** Use this time to transfer the spheroids into the microplate

C. Transferring spheroids into microplate

- a. **Note:** The transfer of individual spheroids (without ejecting solution) is very tedious and practicing the transfer process is strongly recommended prior to running the first assay. Used or expired Microplates can be used for this.
 - b. **Note:** Practicing will significantly reduce the time required for this step. However, the transfer of ~ 30 spheroids may take 45 – 60 mins depending on user experience and spheroid size.
1. Remove culture media and gentle wash the agarose microwells with PBS twice. Replace media with ~ 1mL of seahorse assay media (want to avoid buffered solution getting transferred into the seahorse plate).
 2. Add 175 μL of assay media to each well of the coated Agilent Seahorse XFe96 Spheroid Microplate.
 3. Using a sufficiently large bore pipette tip to accommodate spheroid size, place the tip against the bottom of the agarose well containing the spheroid and aspirate.
 - a. **Tip:** P1000 tips on the minimum volume have generally been sufficient. However, we do have large bore P200 tips available for larger spheroids.
 4. Slowly remove the tip, and visually confirm that you have aspirated the spheroid.
 5. Move the tip containing the spheroid to a well of the Agilent Seahorse XFe96 Spheroid Microplate.
 6. Place the tip against the bottom of the well directly in the centre and hold the pipette steady for approx. 20 seconds.



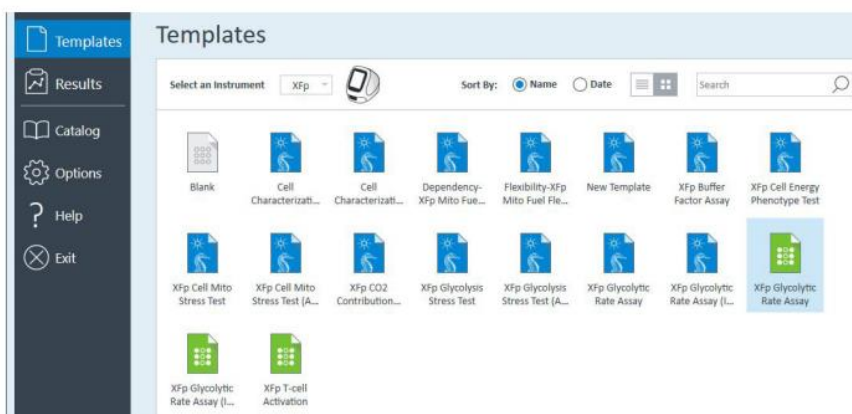
- a. **Note:** The spheroid should float out of the tip, to the bottom of the well by gravity alone, without ejection of media.
 - b. **Tip:** Change tips between each spheroid as it appears to reduce the number of spheroids that get stuck within the tip.
7. Visually confirm that the spheroid is in the centre of the well under a magnifying glass or microscope as shown below. The entire spheroid must be in the circular well for data to be consistent between wells.



8. Spin the plate in the centrifuge at 650xG for 5 min to help the spheroids attach to the base of the well and ensure that there are no air bubbles. Ensure you are using an appropriate microplate balance containing a volume equivalent to the assay media.
9. Warm the microplate and let the spheroids adjust at 37 °C in a non-CO2 incubator for at least 1 hour.
 - a. **Tip:** Preform the calibration 15 - 30mins before the end of this incubation time.

D. Running the assay

1. If running a particular assay (e.g., Mito Stress Test or ATP Rate Assay) or using the injection ports in any other manner, load the desired compounds into the appropriate injector ports in the assay cartridge now.
 - a. **Tip:** Look at the Agilent assay/test kit user guides for component concentrations and how to use the injection ports.
 - b. **Tip:** Concentrations and time between injections need to be optimised between 3D spheroid and 2D monolayer culture. See Agilent's "XFe96 Spheroid Microplate and Flux Pak" user guide for further information.
2. Open the Wave software and select an appropriate template for your assay.



3. The template will prompt you to fill in the "Group Definitions", "Plate Map" and "Protocol".
 - a. **Tip:** For easier data analysis label differences e.g., donors or experimental conditions within the group definitions and highlight the wells on the plate map. You could also highlight wells to exclude (e.g., broken/misplaced spheroids or a well containing an air bubble)
4. Within the "Protocol" tap remove any steps of the template that are not appropriate to this assay by hitting the highlighted "X" as shown below for an oligomycin injection step.



5. Baseline/Basal measurement cycle is the starting point for every Seahorse assay and consists of three measurements before the first injection. If deleting the injection steps the baseline measurement can be edited to suit the specific aim of the assay.
 - a. **Note:** The default measurement cycle times for a Seahorse XFe96 Analyzer: 3 minutes Mix; 0 minutes Wait; 3 minutes Measure
 - b. **Tip:** The number of cycles can be edited (increased or decreased) during the assay. However, the duration of the mix/wait/measure step must be finalised before starting the assay.
6. The standard cycle used for 7-day old disc spheroids initially seeded at ~ 20,000 cells: 3 minutes Mix; 0 minutes Wait; 20 minutes Measure
 - a. **Note:** The number of cycles used have ranged from 1 – 9 depending on the aim of the assay.
7. When ready to start the calibration, click “Run Assay” and a tab comes up with editable fields for project and plate information, or other important notes related to the assay.
 - a. **Note:** Any information entered on this view is saved in the assay result excel file.
 - b. **Note:** A User folder can be found on the Desktop containing a “BioEng” folder.
8. Any errors or warnings will be displayed on the right side of the Run Assay step.
 - a. **Note:** A typical error message is the notification that some assay wells have not been assigned to a group on the Plate Map. If a template is designed correctly, Wave displays an “All Set” confirmation message.

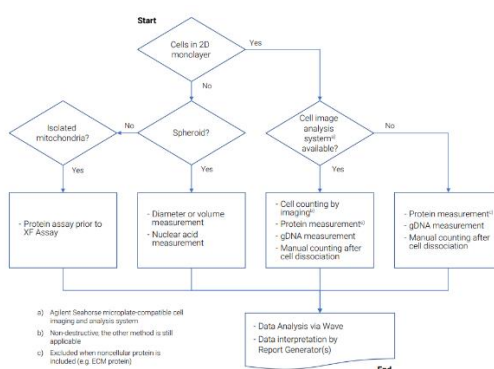


9. When prompted by software, place the utility plate and sensor cartridge **WITHOUT THE LID** onto the thermal tray.
 - a. **Tip:** The A-H labels on the plate will be closest to you, with the barcode of the sensor cartridge facing away, otherwise there will be a read failure. For further details on read failures and how to manually input barcode information see the Wave user guide.
10. After double checking that the lid has been removed and that the orientation is correct, click “I’m ready”. Calibration takes approximately 15 - 30 mins.
11. When prompted, replace the utility plate in the thermal tray with the spheroid microplate **WITHOUT THE LID.**
 - a. **Tip:** Again, the A-H labels on the plate will be closest to you, but there is a barcode on both sides of the Microplate.

12. After double checking that the lid has been removed and that the plate orientation is correct, click “Load cell plate”. Initialisation can take 12 – 15 mins to equilibrate before the first measurement cycle begins.

E. Completing the assay

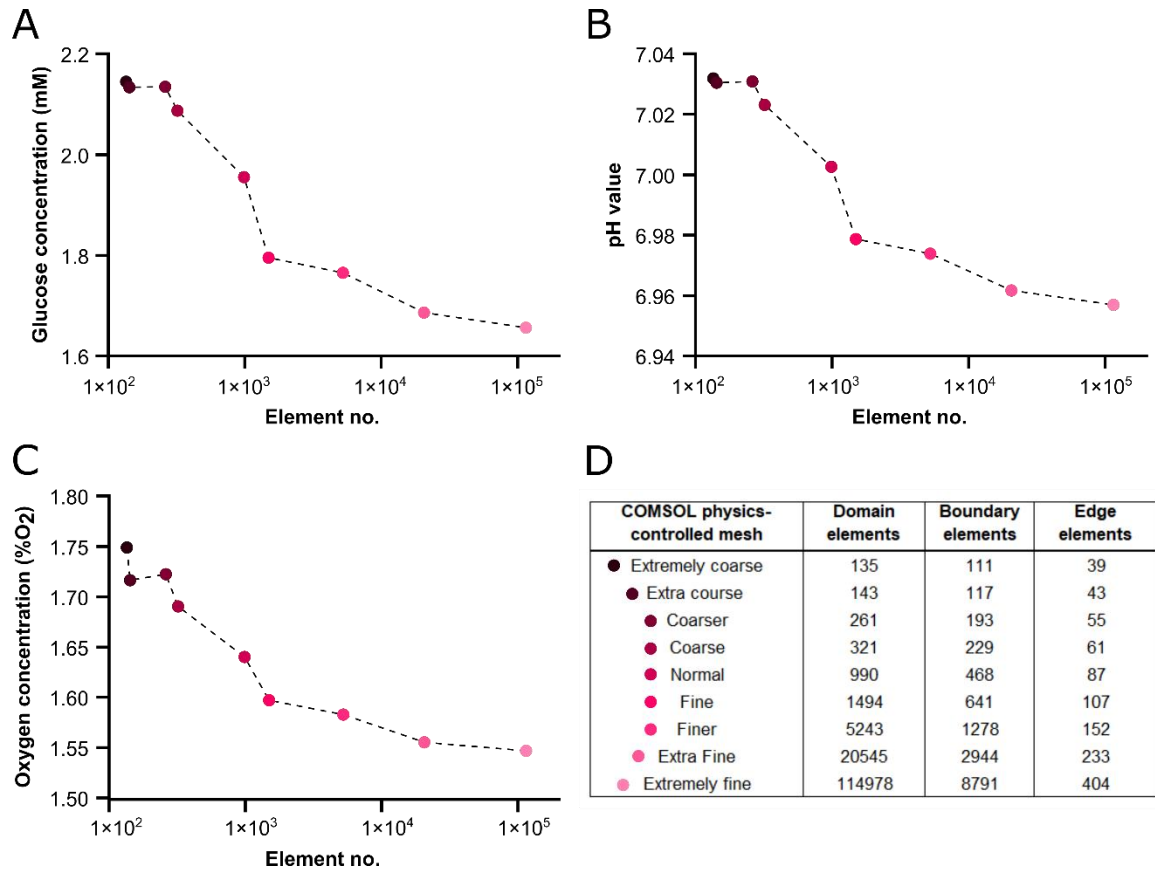
1. At the completion of the assay, ensure that you have removed the microplate and sensor cartridge from the analyser.
2. Export the results from Wave as an excel file and close your experiment tab within Wave.
3. Do not turn off the machine or close the Wave software.
4. After the assay, examine the position of the spheroids in each well using a dissecting or inverted microscope. This is to confirm that all spheroids remained in the centre of the well during the assay and within correct proximity of the sensor. Exclude any wells with compromised spheroids or visible bubbles.
 - a. **Note:** The importance of the spheroid position in data analysis is discussed in “Technical Considerations” of Agilent’s “XFe96 Spheroid Microplate and Flux Pak” user guide.
5. Normalization of Seahorse data is a key component in the workflow for performing and/or subsequent analysis of raw data to ensure accurate and consistent interpretation of results between wells.
 - a. **Note:** See Agilent’s Technical Overview on “Methods and strategies for normalizing XF metabolic data to cellular parameters”



6. Normalisation of disc spheroids with an initial seeding density of ~20,000 cells has been performed successfully using the Picogreen DNA assay.
7. Remove the individual spheroids (with the assay media) from the Seahorse plate and into screw cap Eppendorf’s.
 - a. **Tip:** Use the light magnifying glass to ensure that the spheroid has been transferred successfully and has not broken or gotten stuck in the pipette tips.
 - b. **Tip:** Pre-label the Eppendorf’s with the corresponding well ID.
8. Aspirate the assay media, leaving the spheroid dry to be stored frozen or immediately digested.
9. For papain digestion, follow the standard protocol using 50 μ L per spheroid.
10. For picogreen DNA quantification, use 10 μ L of digest in triplicate with the normal DNA standards in the SOP.

Appendix B – Chapter 4 (Human microenvironment)

B.1 Mesh convergence study



Effect of element number on **(A)** glucose concentration **(B)** pH value and **(C)** oxygen concentration in the centre of the nucleus pulposus (NP) of a 3D human disc model. **(D)** The coloured data points correspond to the setting of the COMSOL physics-controlled meshes. Presented are the number of elements for each element type within the modelled quadrant of the disc, for each mesh setting.

B.2 List of reviewed clinical trials involving cell injection of the treatment of intervertebral disc degeneration

Start Date	NCT Number	Expected completion	Status	Enrolment	Age	Interventions	Cells		Volume/carrier	Timeframe (MRI)	Locations	Last update
Aug-11	NCT01290367	2015	Completed	100	18+ yrs	Biological: Single Dose MPCs Injection Procedure: Single injection of saline solution Procedure: Single injection of hyaluronic acid	MPCs (allogeneic)	6 and 18 million	hyaluronic acid (HA)	6 months and 3 years	14 locations across the United States	Jun-20
Jan-12	NCT01643681	2015	Withdrawn	0	19 - 70 yrs	Procedure: Autologous Adipose Tissue derived MSCs Transplantation	AD-MSCs (autologous)	40 million	1 mL	6 months	Korea	Jun-19
Aug-12	NCT01640457	2021	Completed	120	18 - 60 yrs	Drug: NOVOCARTÂ® Disc plus Device: NOVOCARTÂ® Disc basic	Autologous Disc Chondrocyte Transplantation System (ADCT)	not specified	0.5-2 mL	5 years	10 locations in Germany and Austria	Oct-21
Nov-12	NCT01771471	2020	Terminated	44	21+ yrs	Biological: NuQu Other: Placebo	juvenile chondrocytes (allogenic)	10-20 million	1-2mL fibrin carrier	1 year	10 locations across the United States	Aug-17
Apr-13	NCT01860417	2017	Completed	25	18 - 75 yrs	Biological: Allogenic Mesenchymal Stromal Cells Drug: Mepivacaine	AD-MSCs (allogenic)	10 million (pilot) 25 million (Phase1/2)	1 mL 2 mL	1 year	2 locations in Spain	Apr-17
Mar-14	NCT02097862	2017	Completed	15	18 - 85 yrs	Procedure: Adipose Stem Cells	AD-MSCs (autologous)	30 - 60 million PRP dependent	1 mL	-	United States	Mar-17
Jan-15	NCT02338271	2017	Unknown status	10	18 - 70 yrs	Other: autologous adipose derived mesenchymal stem cell	AD-MSCs (autologous)	20 and 40 million	1mLTissuefill (HA derivatives)	12 months	Korea	Jan-15

Mar-15	NCT02412735	2021	Completed: has results posted Jan 18 2022	404	18+ Yyrs	Drug: Rexlemestrocel-L Drug: Rexlemestrocel-L + HA Mixture Drug: Placebo	MPCs (allogeneic)	6 million	2 mL (HA)	-	48 locations across United States and Australia	Oct-22
Jul-17	NCT04499105	2020	Unknown status	10	20-65 yrs	Drug: Mesenchymal Stem Cell + NaCl 0,9% 2ml	hUM-MSC (autologous)	not specified	2 mL	6 months	Indonesia	Aug-20
Aug-17	NCT03709901	2022	Active, not recruiting	218	18-60 yrs	Other: Active Allograft Other: Placebo	VAST	6 million	1.5-2 mL	6 and 12 months	13 locations in States	Jul-21
Feb-18	NCT03347708	2021	Unknown status	60	18-75 yrs	Biological: IDCT Drug: Saline Solution Drug: Sodium Hyaluronate	discogenic (autologous)	3 or 9 million (10 million pre-clinically)	Sodium Hyaluronate	2 years	14 locations across the United States	Mar-20
Oct-18	NCT03461458	2021	Terminated	1	18+ yrs	Drug: Autologous Adipose-Derived Mesenchymal Stromal Cells	AD-MSCs (autologous)	5 and 20 million	-	6, 12 and 24 months	United States	Jan-22
Nov-18	NCT04559295	2021	Unknown status	80	18-60 yrs	Biological: Bone Marrow Concentrate	BMAC (autologous)		-	-	United States	Sep-20
Feb-19	NCT03737461	2023	Active, not recruiting	113	18 - 60 yrs	Drug: Allogenic BM-MSCs Injection Other: Sham Procedure	BM-MSCs (allogenic)	20 million	2 mL (HypoThermosol isotonic transport solution)	1, 3,6,12 and 24 months	3 locations in France	Jul-22
Apr-19	NCT03912454	2022	Active, not recruiting	20	18-60 yrs	Other: Autologous Bone Marrow Aspirate Concentrate (BMAC) Injection	BMAC (autologous)		-	1 year	States	Mar-22
May-19	NCT03955315	2021	Unknown status	38	18-75 yrs	Biological: IDCT Procedure: Sham	discogenic (autologous)	3 and 9 million	Sodium Hyaluronate Vehicle	1 year	6 locations in Japan	Aug-19
Jun-19	NCT03692221	2022	Withdrawn: stalled due to covid	0	18 - 80 yrs	Drug: MSC Treatment group 1 (low dose) Drug: MSC Treatment group 2 (high dose) Other: Healthy Control (no treatment)	MSCs (autologous)	2 and 4 million	1-2 mL	1 year	United States	May-22

Aug-20	NCT04414592	2023	Recruiting	20	18 - 60 yrs	Other: human umbilical cord mesenchymal stem cells	hUC-MSCs	20 million	-	3, 6 and 12 months	2 locations in China	Jun-20
Aug-20	NCT04530071	2022	Unknown status	36	19 - 70 yrs	Biological: CordSTEM-DD (0.7 x 10 ⁷ cells) Biological: CordSTEM-DD (2.1 x 10 ⁷ cells)	CordSTEM-DD	7 or 21 million	-	-	Korea	Aug-20
Nov-20	NCT04759105	2022	Recruiting	52	18 - 65 yrs	Drug: Autologous BM-MSC Other: Sham Procedure	BM-MSCs (autologous)	15 million	-	1, 3, 6 and 12 months	Italy	Feb-21
Mar-21	NCT05066334	2023	Recruiting	52	18-65 yrs	Drug: Autologous BM-MSC Procedure: Sham	BM-MSCs (autologous)	15 million	-	6, 12 and 24 months	Italy	Oct-21
Apr-21	NCT05011474	2022	Enrolling by invitation	4	19-70 yrs	Biological: administered an autologous adipose-derived mesenchymal stem cell spheroid pretreated with matrillin 3	AD-MSCs (autologous)	not specified	-	1 and 6 months	Korea	Aug-21
Sep-21	NCT04849429	2022	Completed	30	18-60 yrs	Biological: Platelet rich plasma (PRP) with exosomes Drug: Normal Saline	PRP		2 mL	12 months	India	Aug-22
Apr-22	NCT04816747	2024	Not yet recruiting	50	18-60 yrs	Biological: Autologous PRP	PRP (autologous)		-	-	Greece	Mar-22
Jun-22	NCT04042844	2025	Recruiting	99	18-60 yrs	Biological: BRTX-100 Drug: Saline	BM-MSCs (BRTX-100)	40 million	-	1 and 2 years	11 locations across the United States	Dec-22
Nov-22	NCT04735185	2027	Suspended (awaiting sponsor + FDA feedback)	106	18-100 yrs	Other: Autologous stem cells Drug: Corticosteroid Drug: Local anesthetic	BM-MSCs (autologous)	not specified	2 mL	3-, 6- and 12-months	United States	Dec-22

Appendix C – Chapter 5 (FE culture)

C.1 List of reviewed manuscripts for nucleus pulposus (NP) culture and relevant experimental details extracted from the literature to inform the development of *in-silico* models

2D cell expansion									
Year	DOI	First/last author	Culture flask/dish	Expansion	Media volume	Media change	Glucose	Oxygen	Species
2005	10.1097/01.brs.0000184365.28481.e3	D. Sakai/T. Hotta	-	P2	-	-	-	-	Rabbit
2006	10.1016/j.biomaterials.2005.06.038	D. Sakai/T. Hotta	T-25	12 - 15days	-	-	Low glucose (LG): 1 g/L or 5.5 mM	-	Rabbit
2008	10.1002/jor.20584	A. Hiyama/D. Sakai	-	12 - 27 days	-	Every 2 days	-	-	Canine
2008	10.1097/BRS.0b013e31817b8f53	K. Wuertz/J. Iatridis	T-25	-	-	-	LG	Normoxia (NX): 20% and Hypoxia (HX): 2%	Rat
2009	10.1186/ar2611	C. Le Maitre/J. Hoyland	T-75	Up to P2 (~ 7 days)	10 mL	-	-	-	Human
2009	10.1016/j.bbrc.2008.12.145	K. Wuertz/J. Iatridis	T-25 or 24-well plate	-	-	-	-	NX	Rat
2012	10.1007/s00586-011-1976-2	M. Peroglio/D. Eglin	96-well plate	-	100 µL	-	High glucose (HG): 4.5 g/L or 25 mM	-	Bovine
2013	10.1186/scrt331	B. Chon/J. Chen	24-well plate (with transwell insert)	P3 or P5	-	-	-	Physioxia (PX): 5%	Human

2013	10.1371/journal.pone.0075548	J. Chen/L. Setton	-	-	-	-	HG	HX	Mouse
2013	10.1155/2013/326828	C. Bucher/B. Gantenbein	-	~ 7 days	-	-	LG	-	Human
2014	10.1371/journal.pone.0099621	R. Maidhof/N. Chahine	-	P2 - P4	-	-	HG	-	Bovine
2014	10.1016/j.actbio.2013.11.013	A. Francisco/L. Setton	-	-	-	-	-	-	Porcine
2015	10.1016/j.joca.2015.02.017	K. Philips/C. Le Maitre	T-75	Up to P2	-	Twice weekly	-	-	Human
2015	10.1007/s12195-014-0373-4	P. Hwang/L. Setton	well-plate	-	-	-	-	-	Human & porcine
2015	10.1016/j.actbio.2014.10.030	D. Kim/R. Mauck	-	P2	1 mL	-	HG	-	Bovine
2015	10.1002/jor.22821	D. Gorth/L. Smith	-	P2	-	-	HG	NX	Bovine
2015	10.1016/j.joca.2014.09.012	M. Farrell/R. Mauck	-	P2	-	-	HG	NX and HX	Bovine
2015	10.22203/ecm.v029a15	D. Sakai/S. Kato	6-well plate	4 days	-	-	-	-	Human
2015	10.1089/ten.TEA.2013.0719	M. Naqvi/C. Buckley	T-75	P2	-	Every 3 days	LG	PX	Porcine
2015	10.1111/joa.12305	M. Naqvi/C. Buckley	T-175	P2	-	-	LG	NX and PX	Porcine
2015	10.1186/s13075-015-0900-2	S. Chan/B. Gantenbein	12-well plate	P2	-	-	LG	-	Human
2015	10.1097/BRS.0000000000000932	B. Walter/J. Iatridis	-	P4	-	-	HG	PX	Human
2015	10.1016/j.spinee.2015.02.003	D. Purmessur/J. Iatridis	6-well plate	P19	-	-	-	-	Human
2015	10.1186/s13075-015-0569-6	I. Arkesteijn/M. Tryfonidou	-	-	-	-	HG	PX	Canine
2016	10.1038/srep37360	H. Gilbert/J. Hoyland	6-well plate (for experiment)	Up to P4	2 mL	Every 2 - 3 days	HG	-	Human

2016	10.1055/s-0034-1376573	D. Sakai/J. Mochida	well-plate	4 days	-	-	-	-	Canine
2016	10.1097/BRS.000000000001314	M. Naqvi/C. Buckley	T-25	-	3 mL	Every 3 days	LG	NX and PX	Porcine
2016	10.1186/s13287-016-0337-9	A. Tekari/B. Gantenbein	-	~ 7 days	-	-	-	NX and HX	Bovine
2016	10.1016/j.jbiomech.2016.02.029	M. Likhitanichkul/J. Iatridis	-	P1 - P2	-	-	HG	NX	Human
2016	10.22203/ecm.v033a08	B. Walter/J. Iatridis	-	-	-	-	HG	-	Bovine
2017	10.1016/j.actbio.2017.03.010	A. Thrope/C. Le Maitre	-	Up to P7	-	-	-	-	Human
2017	10.1016/j.actbio.2017.04.019	D. Bridgen/L. Setton	96 half-well plate	P2	-	-	-	-	Human
2017	10.1016/j.tice.2017.05.002	S. Vedicherla/C. Buckley	T-175	7 days (P1)	-	-	LG	NX and PX	Bovine
2017	10.1089/ten.TEC.2016.0355	R. May/B. Gantenbein	T-150	P2	-	Thrice weekly	LG	-	Human & bovine
2017	10.22203/eCM.v033a18	D. Rosenzweig/L. Haglund	Petri-dish (35mm; 55mm; 100mm)	~ 5 days	-	Every 3 days	HG	-	Bovine
2017	10.1038/s41598-017-17472-1	E. Krock/L. Haglund	-	P1 or P2	-	-	HG	-	Human
2017	10.1089/ten.TEA.2016.0251	F. Bach/M. Tryfonidou	-	P2	-	-	-	NX	Human & canine
2017	10.1371/journal.pone.0187831	F. Bach/M. Tryfonidou	-	P2	-	-	-	NX	Human, bovine & canine
2017	10.18632/oncotarget.21483	F. Bach/M. Tryfonidou	-	P2	-	-	-	NX	Human & canine
2018	10.1002/jsp2.1004	N. Hodson/J. Hoyland	-	Up to P4	-	Every 2 - 3 days	HG	-	Human
2018	10.1115/1.4038758	B. Shah/N. Chahine	-	P2 - P4	-	-	HG	-	Bovine

2018	10.1186/s13287-018-0797-1	R. Tang/L. Setton	6-well plate	-	-	-	-	-	Human (cell line)
2018	doi.org/10.1371/journal.pone.0202640	D. Sakai/M. Watanabe	T-25	Up to P3	-	Twice weekly	-	HX	Human
2018	10.1088/1748-605X/aaab7f	M. Naqvi/C. Buckley	-	-	-	-	-	PX	Porcine
2018	10.3390/ijms19041195	R. May/B. Gantenbein	-	P2	-	Thrice weekly	LG	HX	Human
2018	10.22203/eCM.v036a15	D. Rosenzweig/L. Haglund	-	-	-	-	HG	-	Human
2018	10.1089/ten.TEA.2017.0334	M. Cruz/J. Iatridis	-	P3 - P5	-	-	HG	NX	Bovine
2018	10.1016/j.jconrel.2018.08.019	A. Tellegen/M. Tryfonidou	24-well plate	-	-	-	HG	NX	Canine
2019	10.1002/jor.24154	B. Shah/N. Chahine	-	P2 - P4	-	-	HG	-	Human
2019	10.1096/fj.201802725RRR	B. Fearing/L. Setton	-	P3	-	-	-	-	Human
2019	10.22203/eCM.v037a09	M. Naqvi/C. Buckley	T-75	P2	-	-	LG	PX	Porcine
2019	10.3390/jcm8040433	H. Cherif/L. Haglund	6-well plate	P0 - P1	-	-	-	-	Human
2020	10.1016/j.biomaterials.2020.120057	M. Barcellona/L. Setton	-	P4	-	-	-	-	Human
2020	10.14245/ns.2040002.001	R. May/B. Gantenbein	-	-	-	-	LG	-	Human

2020	10.22203/eCM.v039a14	C. Panebianco/J. latridis	-	-	-	-	HG	-	Bovine
------	----------------------	---------------------------	---	---	---	---	----	---	--------

Alginate bead culture											
Year	DOI	First/last author	Alginate conc.	Dimensions	Cell density	Duration	Culture vessel/media vol.	Media change	Glucose	Oxygen	Species
2005	10.1186/ar1732	C. Le Maitre/J. Hoyland	1.2%	-	1x10 ⁶ cells/mL	-	2 mL per well	Every 2 days	-	NX	Human
2011	10.1186/ar3344	D. Purmessur/J. latridis	1.2%	-	2x10 ⁶ cells/mL	4 days	12-well plate (10 beads/well); 2 mL	-	LG	PX	Porcine
2013	10.1155/2013/326828	C. Bucher/B. Gantenbein	1.2%	Vol. = 30 µl	2x10 ⁶ cells/mL	-	-	-	HG	-	Human
2013	10.1016/j.spinee.2013.05.029	M. Peroglio/S. Grad	1.2%	Vol. = 30 µl	8x10 ⁶ cells/mL	1 week	12-well plate (4 beads per well)	-	-	PX	Human
2013	10.22203/eCM.v026a08	R. Gawri/F. Mwale	1.2%	20G needle	-	-	48-well plate (5 beads per well)	-	HG	NX	Human & bovine
2013	10.1097/BSD.0b013e31826e0ca4	R. Abbott/J. latridis	1.2%	-	2x10 ⁶ cells/mL	3 weeks	12-well plate (10 beads/well); 2 mL	Twice weekly	LG	PX	Human
2014	10.1186/1471-2474-15-422	B. Gantenbein/S. Chan	1.2%	Vol. = 30 µl	4x10 ⁶ cells/mL	1 week	-	-	HG	NX	Porcine & bovine
2015	10.1016/j.joca.2015.02.017	K. Philips/C. Le Maitre	1.2%	19G needle	2x10 ⁶ cells/mL	2 weeks	-	Twice weekly	-	NX	Human
2015	10.1186/s13075-015-0900-2	S. Chan/B. Gantenbein	1.2%	Vol. = 30 µl	-	-	12-well plate	Thrice weekly	-	-	Human
2015	10.1097/BRS.0000000000000932	B. Walter/J. latridis	1.2%	-	2x10 ⁶ cells/mL	2 weeks	12-well plate; 2 mL	-	LG	PX	Human

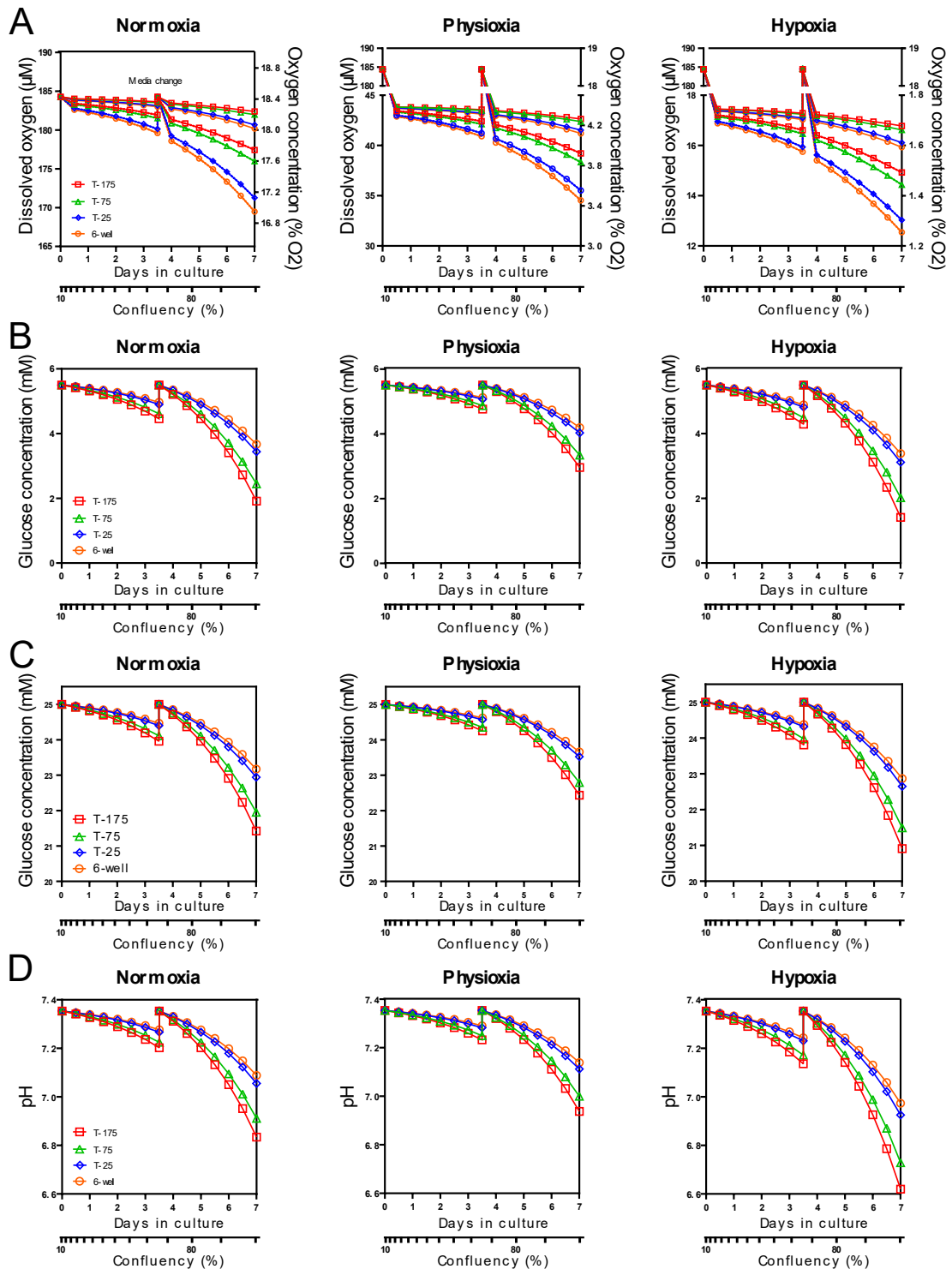
2015	10.1186/s13075-015-0569-6	I. Arkesteijn/M. Tryfonidou	1.2%	-	3x10 ⁶ or 6x10 ⁶ cells/mL	4 weeks	-	-	HG	PX	Canine
2016	10.1097/BRS.0000000000001314	M. Naqvi/C. Buckley	1.5%	Diameter (D) = 5 mm (12G needle)	4x10 ⁶ cells/mL	-	24-well plate; 2 mL	Twice weekly	LG	NX and PX	Porcine
2016	10.22203/ecm.v032a11	F. Bach/M. Tryfonidou	1.2%	Vol. = 20 µl	3x10 ⁶ cells/mL	4 weeks	-	-	-	PX	Bovine
2017	10.1016/j.tice.2017.05.002	S. Vedicherla/C. Buckley	-	D = 5mm	4x10 ⁶ cells/mL	3 weeks	24-well plate; 2 mL	Twice weekly	LG	NX and PX	Bovine
2018	10.1115/1.4038758	B. Shah/N. Chahine	1.2%	21G needle	1x10 ⁶ or 4x10 ⁶ cells/mL	-	12-well plate (9 beads per well)	-	-	NX	Bovine
2018	10.1088/1748-605X/aaab7f	M. Naqvi/C. Buckley	1%	D = 240 µm	10x10 ⁶ or 20x10 ⁶ cells/mL	2 weeks	6-well plate	Twice weekly	LG	PX	Porcine
2018	10.3390/ijms19041195	R. May/B. Gantenbein	1.2%	Vol. = 30 µl	4x10 ⁶ cells/mL	3 weeks	12-well plate	-	-	HX	Human
2019	10.1002/jor.24154	B. Shah/N. Chahine	1.2%	-	3.3x10 ⁴ cells/bead	5 weeks	-	-	-	-	Human
2020	10.14245/ns.2040002.001	R. May/B. Gantenbein	1.2%	Vol. = 30 µl	4x10 ⁶ cells/mL	3 weeks	-	-	-	HX	Human

Cylindrical hydrogel constructs											
Year	DOI	First/last author	Hydrogel	Dimensions	Cell density	Duration	Culture vessel/media vol.	Media change	Glucose	Oxygen	Species
2008	10.1016/j.biomaterials.2007.09.018	S. Richardson/J. Hoyland	Chitosan glycerophosphate	250 µL (in transwell insert)	4x10 ⁶ cells/mL	4 weeks	24-well plate	Every 3 days	-	NX	Human
2010	10.1002/art.27710	B. Minogue/J. Hoyland	Type I collagen	200 µL	4x10 ⁶ cells/mL	-	24-well plate	Every 2 - 3 days	HG	-	Human

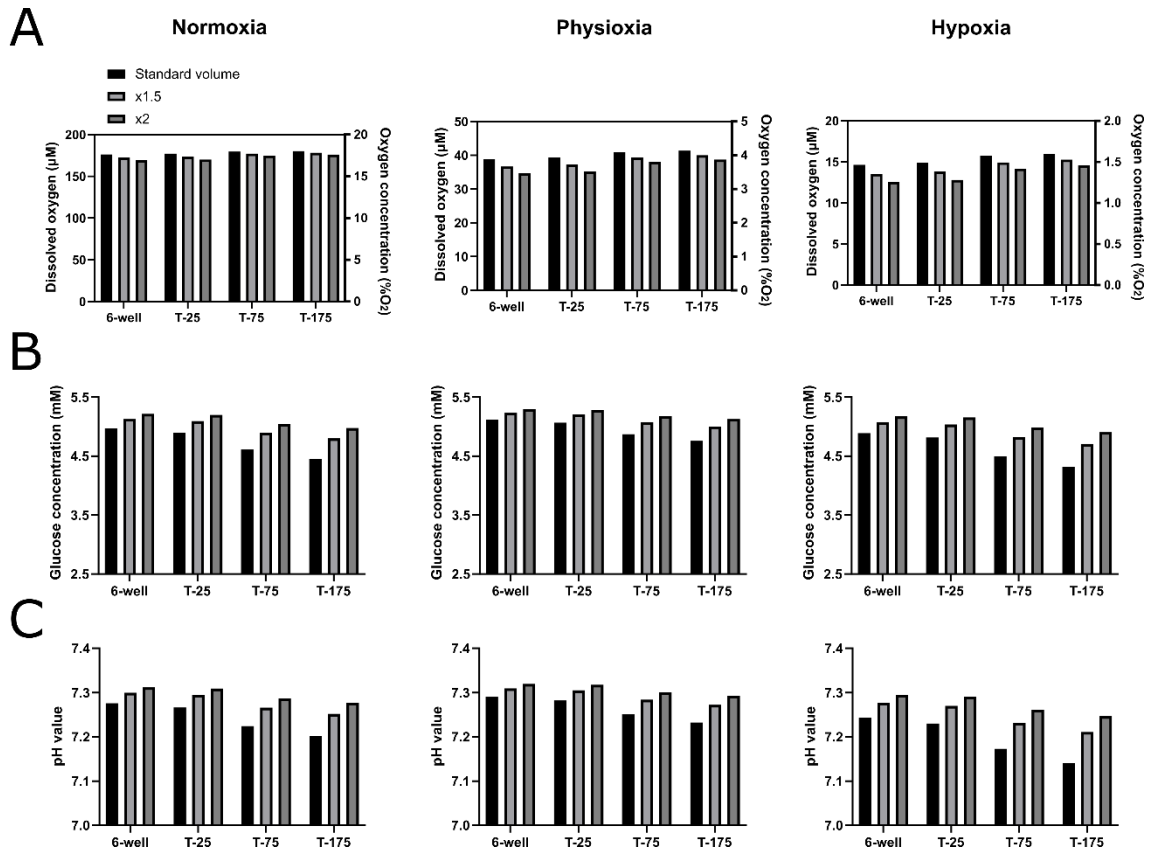
2010	10.1186/scrt18	C. Korecki/J. Iatridis	Alginate	D = 5.82 mm and h = 3.27 mm (~ 100 μ l)	2x10 ⁶ cells/mL	4 days	6-well plate (5 gels per well); 5 mL	-	HG	PX	Pocine
2013	10.1186/scrt331	B. Chon/J. Chen	Matrigel	60 μ L (in transwell insert)	-	3 weeks	24-well plate	-	-	HX	Human
2015	10.1016/j.actbio.2014.10.030	D. Kim/R. Mauck	Methacrylated hyaluronic acid (HA)	D = 4 mm and height (h) = 1.5 mm	20x10 ⁶ or 60x10 ⁶ cells/mL	8 weeks	1 mL each	Thrice weekly	HG	-	Bovine
2015	10.1002/jor.22821	D. Gorth/L. Smith	2% agarose	D = 4 mm and h = 2.25 mm	20x10 ⁶ cell/mL	6 weeks	1 mL each	Every 3 days	HG	NX and HX	Bovine
2015	10.1016/j.joca.2014.09.012	M. Farrell/R. Mauck	2% agarose	D = 4 mm and h = 2.25 or 0.75 mm	20x10 ⁶ cell/mL	4 weeks	-	Twice weekly	LG and HG	NX and HX	Bovine
2015	10.1089/ten.TEA.2013.0719	M. Naqvi/C. Buckley	1.5% alginate or chitosan	D = 5 mm and h = 3 mm	4x10 ⁶ or 8x10 ⁶ cells/mL	3 weeks	12-well plate; 2 mL	Twice weekly	-	PX	Porcine
2015	10.1111/joa.12305	M. Naqvi/C. Buckley	1.5% alginate	D = 5 mm and h = 3 mm	-	-	24-well plate; 2 mL	-	1, 5 and 25 mM	NX and PX	Porcine
2017	10.1016/j.actbio.2017.07.025	S. Gullbrand/L. Smith	7.5% oxidized dextran	D = 4 mm and h = 2.26 mm	20x10 ⁶ cell/mL	2 weeks	-	-	HG	NX	Goat
2018	10.22203/eCM.v036a15	D. Rosenzweig/L. Haglund	2% agarose	250 μ L	2x10 ⁶ cells/mL	-	-	-	-	-	Human
2018	0.1089/ten.TEC.2017.0226	A. Krouwels/L. Creemers	Alginate, agrose, gelma, fibrin, HA-PEG & Col2	~ 50 μ L	2x10 ⁶ cells/mL	-	-	-	-	-	Human
2019	10.22203/eCM.v037a09	M. Naqvi/C. Buckley	1.5% alginate	OuterD = 9 mm, innerD = 5 mm and h = 3 mm	4x10 ⁶ cells/mL	-	-	-	LG	PX	Porcine
2021	10.1089/ten.tea.2020.0123	H. Zlotnick/R. Mauck	Agarose	D = 4 mm and h = 2.25 mm	~ 565,000 cells (total)	8 weeks	1, 3 or 5 mL	Twice weekly	HG	-	Bovine

Cell pellets and microaggregates										
Year	DOI	First/last author	Culture vessel	Cell density	Duration	Media volume	Media change	Glucose	Oxygen	Species
2010	10.1186/scr18	C. Korecki/J. Iatridis	96-well plate	250,000 cells/pellet	-	-	Twice weekly	HG	PX	Pocine
2015	0.22203/ecm.v030a10	F. Bach/M. Tryfonidou	96-well plate	35,000 cells/microaggredate	-	-	-	HG	NX and PX	Human, canine, porcine
2016	10.1186/s13075-016-0960-y	F. Bach/M. Tryfonidou	96-well plate	35,000 cells/microaggredate	2 weeks	50 µL	-	HG	NX	Human & canine
2017	10.22203/eCM.v033a18	D. Rosenzweig/L. Haglund	-	1 x10 ⁶ cells/pellet	3 weeks	-	Every 3 days	HG	-	Bovine
2017	10.1089/ten.TEA.2016.0251	F. Bach/M. Tryfonidou	96-well plate	35,000 cells/microaggredate	4 weeks	50 µL	Twice weekly	HG	NX	Human & canine
2017	10.1371/journal.pone.0187831	F. Bach/M. Tryfonidou	96-well plate	35,000 cells/microaggredate	4 weeks	50 µL	Twice weekly	HG	NX	Human, bovine & canine
2017	10.18632/oncotarget.21483	F. Bach/M. Tryfonidou	96-well plate	35,000 cells/microaggredate	1 or 3 weeks	50 µL	Twice weekly	HG	NX	Human & canine
2019	10.1177/1947603519841675	S. Peck/L. Smith	-	250,000 cells/pellet	2 weeks	-	-	LG	HX	Bovine
2019	10.3390/jcm8040433	H. Cherif/L. Haglund	-	300,000 cells/pellet	-	1 mL	Every 3 days	2.25 g/L	NX	Human

C.2 Additional two-dimensional cell culture *in-silico* models

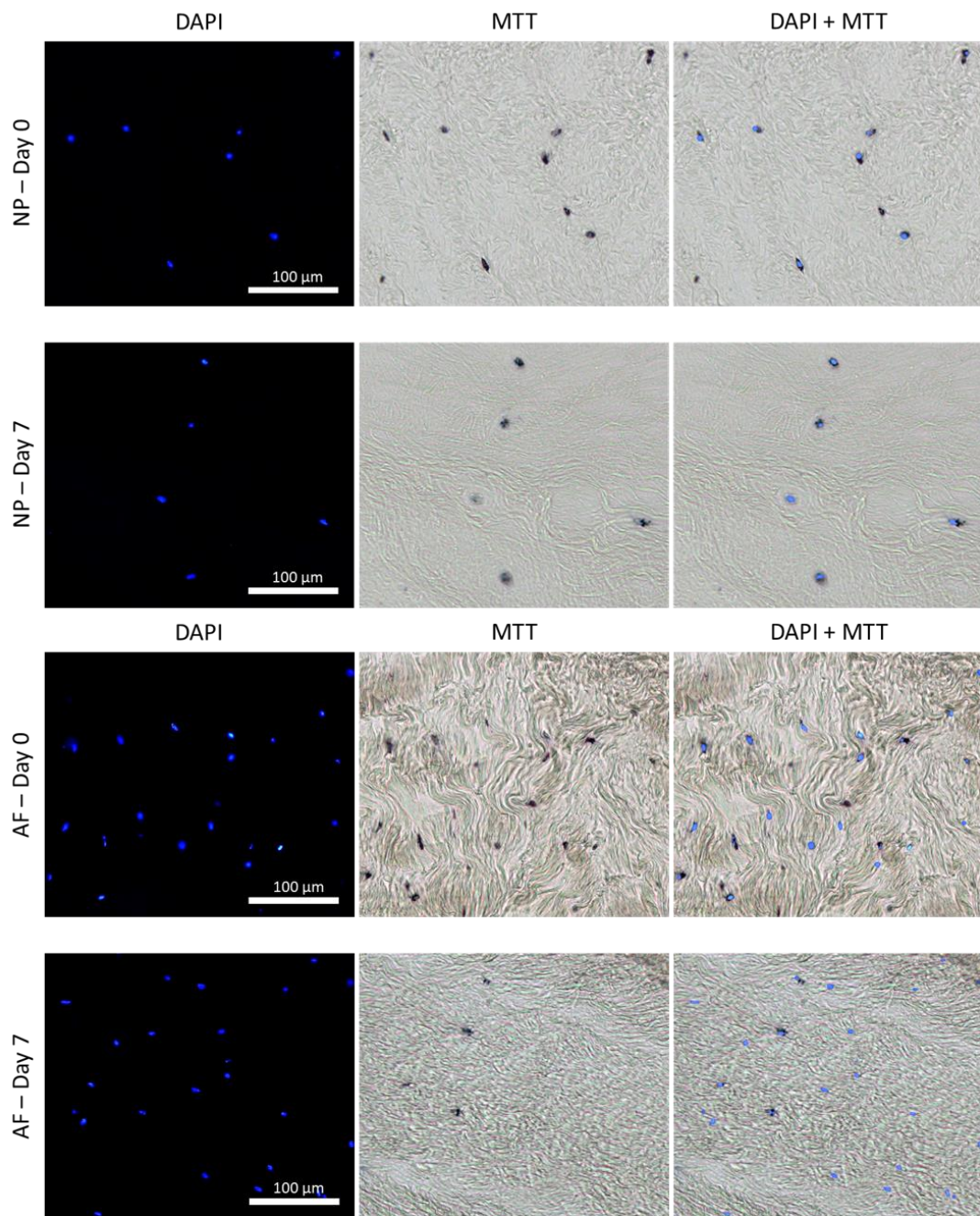


A temporal analysis of the oxygen concentration (**A**), glucose concentration when using low glucose media (**B**), and high glucose media (**C**) and pH level (**D**) at the cell surface for cells proliferating over a 7-day period in either normoxia, physioxia and hypoxia. Solid line indicates a lower animal/healthy human metabolism, dashed lines indicate a higher degenerated phenotype.



Investigating the effect of media volume on the **(A)** oxygen, **(B)** glucose and **(C)** pH level at the cell surface at 80% confluency and prior to a media exchange under normoxia, physioxia and hypoxia. Standard volume for a 6-well, T-25, T-75 and T-175 was assumed to be 2 mL, 5 mL, 10 mL, and 20 mL, respectively.

Appendix D – Chapter 6 (Organ culture)



DAPI images identifying the fluorescing blue nuclei of all cells in the nucleus pulposus (NP) and annulus fibrosus (AF) at day 0 and day 7. MTT brightfield images showing deposited formazan crystals around metabolically active cells. Merging of the fluorescence and bright field enabled identification of metabolically active (dual stained) and inactive cells (blue only). Scale bar is 100 μm.

Appendix E – Chapter 7 (Species comparison)

E.1 List of reviewed manuscripts and relevant experimental details extracted for rat tail models

Year	DOI	Rat details			No. of discs punctured; disc level	Degeneration model	Time from induction of degeneration to treatment	Treatment details (if applicable)	Study duration
		No. of rats	Age (weeks); Sex (M/F)	Strain					
2022	10.1007/s10495-022-01707-2	40	200-230 g (~6-8 week); M	Sprague-Dawley (SD)	1; C7-C8	Digital palpation guided percutaneous puncture with 21G needle	At time of insult	Intradiscal delivery of 2 μ L through 21G	8 weeks
2022	10.1038/s12276-022-00729-9	7	12; sex not specified	SD	2; C8-C9, C9-C10	Digital palpation guided percutaneous puncture with 29G needle to depth of 5 mm	At time of insult and repeated weekly for 1 month	Intradiscal percutaneous delivery of 2 μ L through 29G	1 month
2021	10.1016/j.jot.2021.04.003	24	12; M	SD	1; C7-C8	Digital palpation, percutaneous puncture with 21G needle to depth of 5 mm	Immediately after insult	Intradiscal; 10 μ L, no needle gauge specified	Euthanasia 8 weeks after initial puncture
2021	10.1002/ar.24519	36	12; M	SD	2; C5-C6, C7-C8	Open surgery, puncture with 20G needle to depth of 5 mm	6 weeks after insult	Systemic (subcutaneous treatment delivery)	Euthanized 8 weeks after puncture
2021	10.1155/2021/6672978	60	No specified age or weight; M	SD	1; C8-C9	Digital palpation, percutaneous disc puncture with 20G needle to depth of 5 mm	Treatment delivered following surgery	Systemic (oral gavage)	Euthanized 6 weeks after puncture
2021	10.1155/2021/6631562	36	8; M	SD	no details	Fluoroscopy guided percutaneous puncture with 27G needle to depth of 4 mm	Immediately after insult	Systemic (intragastric delivery)	Euthanized 8 weeks after puncture
2021	10.1155/2021/5510124	Stage 1: 36; Stage 2: 9	12; F	SD	3; C5-C6 to C7-C8	Open surgery, puncture with 21G needle to depth of 3 mm	Immediately after insult	Systemic (subcutaneous delivery)	Euthanized at 4, 8 and 12 weeks after puncture

2021	10.1155/2021/5556122	40	12; M	SD	1; C8-C9	Digital palpation, percutaneous disc puncture with 20G needle to depth of 5 mm	Immediately after insult	Systemic (intraperitoneal delivery)	Euthanized 4 weeks after puncture
2021	10.7150/THNO.47723	10	12; F	SD	1; C7-C8	Fluoroscopy guided percutaneous puncture with 29G needle to depth of 2 mm	No treatment	No treatment	Euthanasia at 8 weeks after initial puncture
2021	10.1080/15476286.2021.1898176	64	12; M	SD	1; C7-C8	Fluoroscopy guided percutaneous puncture with 21G needle	Immediately	Intradiscal delivery of treatment; no volume or needle gauge reported	4, 7, 14, 28 days post puncture
2021	10.3389/fcell.2021.687024	18	8-12; M	SD	1; C8-C9	Digital palpation, percutaneous puncture with 20G needle to depth of 5 mm	Every other day	Systemic (intraperitoneal) treatment delivery	7 days
2021	10.1016/j.lfs.2021.119874	18	12; F	SD	1; C6-C7	Digital palpation guided percutaneous puncture with 21G needle to depth of 3 mm	3 days post insult	Systemic (subcutaneous treatment delivery)	8 weeks
2021	10.1155/2021/6632786	15	12; no sex specified	SD	2; C8-C9, C9-C10	Digital palpation + fluoroscopy guided percutaneous puncture with 20G needle to depth of 5 mm	3 days post insult	Intradiscal; 2 μ L through 33G	7 days after initial puncture, 4 days after treatment
2021	10.3390/ijms222111355	10	8; M	SD	4; C4-C5 to C7-C8	Fluoroscopy guided percutaneous puncture with 21G needle	At time of insult	Intradiscal delivery of unknown volume through 21G needle	8 weeks
2021	10.1186/s10020-021-00351-x	40	400 g (~10-14 week); M	SD	1; C7-C8	Fluoroscopy guided percutaneous puncture with 21G needle	Weekly	Open surgery, intradiscal delivery of 2 μ L, no needle gauge stated for treatment delivery	1, 2, 3, 4 weeks

2021	10.1038/s41598-021-94173-w	30	12; F	Wistar (W)	5; no details	Fluoroscopy guided percutaneous puncture with 26G needle through contralateral AF	10 weeks post injury	Percutaneous intradiscal delivery of 8 μ L through 32G; cells at 150,000 cells/disc	10 weeks post treatment
2020	10.1002/jor.24757	15	8; F	W	4; C4-C5 to C7-C8	Open surgery, puncture with 23G needle	Started 1 week prior to insult	Systemic (oral administration)	Euthanized 5 months after puncture
2020	10.1016/j.spinee.2020.04.024	18	10; no sex specified	SD	2; C8-C9, C9-C10	Digital palpation + fluoroscopy, percutaneous puncture with 20G needle	1 week	Intradiscal; 2 μ L, no needle gauge specified	Euthanized 8 weeks after puncture
2020	10.1002/jbm.b.34541	24	300 g (~8-10 week); M	No details	3; C6-C7 to C8-C9	Fluoroscopy guided percutaneous puncture with 21G needle to depth of 5 mm w/ negative pressure (suction)	At the time of insult	Intradiscal; 2 μ L, no needle gauge specified, cell delivery at 1×10^4 /disc	Euthanized at 1, 2 and 3 months after transplantation
2020	10.1152/ajpcell.00271.2019	85	12; M	SD	1; C6-C7	Open surgery, puncture with 20G needle	1 week	Intradiscal, 2 μ L through 33G needle	Euthanized 9 weeks after induction of degeneration
2020	10.2147/DDDT.S274812	18	8; M	SD	2; level not specified	Digital palpation, percutaneous puncture with 21G to depth of 5 mm	Treatments delivered weekly	Systemic (IP delivery)	Euthanasia at 4 weeks after initial puncture
2020	10.1155/2020/8319516	12	12; M	SD	1; no details	Digital palpation + fluoroscopy, percutaneous puncture with 27G needle	siRNA delivered 1 day before IDD operation, and twice a week afterwards	Systemic (intravenous injection)	Euthanasia at 2 weeks after initial puncture
2020	10.1155/2020/6660429	60	12; M + F	SD	1; C8-C9	Digital palpation, percutaneous puncture with 20G through tail	Treatment delivered immediately following puncture	Systemic (oral administration)	Euthanasia 4 weeks after operation
2020	10.12998/wjcc.v8.i16.3431	21	10-12; M	SD	1; C8-C9 or C9-C10	Digital palpation, percutaneous puncture with 18G needle	No treatment	No treatment	2-3 weeks
2019	10.1002/jsp2.1069	72	12-16; F	SD	3; C6-C7 to C8-C9	Fluoroscopy guided percutaneous puncture with 20G needle	Treatment started immediately following surgery	Exposure to pulsed electromagnetic field	4 or 7 days post insult

2019	https://pubmed.ncbi.nlm.nih.gov/31337166/	24	12; M	SD	3; C7-C8 to C9-C10	Fluoroscopy guided percutaneous puncture with 16, 18, or 26G needles	No treatment	No treatment	Sacrificed at 1, 2, or 4 weeks post-insult
2019	10.1007/s00586-019-05924-3	21	12; F	SD	1; C6-C7 or C7-C8	Fluoroscopy guided percutaneous puncture with 21G needle to depth of 5 mm	No treatment	No treatment	Up to 14 days
2019	10.1016/j.jos.2018.08.006	30	8-10; M	W	1; C7-C8	Open surgery, puncture with 20G needle	Diet modified 8-weeks prior to surgery	Systemic (dietary changes)	8 weeks from puncture
2019	10.1155/2019/7189854	40	12; M	SD	2; C8-C9, C9-C10	Digital palpation + fluoroscopy guided percutaneous puncture with 20G needle to depth of 5 mm	3 days post puncture	Intradiscal; 2 μ L through 33G	7 days following insult
2019	10.1186/s13075-019-1986-8	10	12; M	SD	3; C6-C7 to C8-C9	Digital palpation + fluoroscopy guided percutaneous puncture with 21G needle	At the time of insult	Intradiscal; 2 μ L through 31G	Euthanasia 4 weeks after puncture
2018	10.1016/j.intimp.2018.10.024	48	150 g (~6 week); M	SD	1; C7-C8 or C8-C9	Fluoroscopy guided percutaneous puncture with 20G needle to depth of 5 mm	At the time of insult and repeated weekly	Intradiscal; 2 μ L through 31G	8 weeks after initial injection
2018	10.1038/s41598-018-35011-4	27	12; F	W	5; no details	Fluoroscopy guided percutaneous puncture with 27G	4 weeks	Intradiscal; 8 μ L through 32G	10 weeks post insult
2018	10.1016/j.actbio.2018.07.008	42	10-12; M	Athymic nude (AN)	1; C3-C4	Open surgery, puncture with 18G needle	At the time of insult	Focus on annular repair model	2 weeks and 5 weeks
2018	10.1016/j.jot.2018.07.008	30	12; M	SD	2; C8-C9, C9-C10	Digital palpation percutaneous puncture with 18G needle	No treatment	No treatment	1 week
2018	10.12659/MSM.910636	36	16-24; no sex specified	SD	3; C5-C6, C7-C8, C9-C10	Fluoroscopy guided percutaneous puncture with 18, 21, or 25G needle	No treatment	No treatment	2, 4 and 6 weeks

2018	10.1038/s41419-017-0151-z	80	12; M	SD	2; C7-C8, C8-C9	Digital palpation percutaneous puncture with 20G needle	At the time of insult	Intradiscal; 2 μ L through 33G	4,7,14,28 days
2018	10.1002/jor.23628	Stage 1: 12; Stage 2: 30	12; no sex specified	W	Stage 1: 6, no details; Stage 2: 3, C6-C7 to C8-C9	Digital palpation + fluoroscopy guided percutaneous puncture with 18, 21, 23, 25, 27, or 29G needle	No treatment	No treatment	2, 4, 6, 8 weeks post insult
2018	10.7150/ijbs.24081	48	8; M	SD	1; C7-C8	Digital palpation + fluoroscopy guided percutaneous puncture with 27G to depth of 4 mm	Immediately after insult	Systemic (intra gastric)	0, 4, 8 weeks post insult
2018	10.22603/ssrr.2017-0026	48	250-300 g (~8-10 week); M	SD	3; C5-C6 to C7-C8	Open surgery, punctured with 26G needle to a depth of 2 mm 10 times	No treatment	No treatment	1, 7, 14, 28 days
2018	10.3389/fphar.2018.01043	30	12; M	SD	2; C7-C8, C8-C9	Digital palpation, percutaneous puncture with 21G needle to depth of 5 mm	One day	Systemic (dietary supplement)	4 weeks
2017	10.1038/s41598-017-17289-y	32	12; no sex specified	SD	2; C6-C7, C7-C8	Digital palpation, percutaneous puncture with 20G needle either to depth of 5 mm, or through entire tail	One day	Systemic (dietary supplement)	4, 8 weeks
2017	10.1016/j.otsr.2017.04.005	12	400-500 g (~10-14 week); M	SD	1; C4-C5	Digital palpation, percutaneous puncture with 18G needle to depth of 5 mm	At the time of insult	Intradiscal; 5 μ L through 18G	12 Weeks
2017	10.1007/s00586-016-4898-1	48	5-6; M	SD	1; C3-C4	Open surgery, puncture with 18G needle	At the time of insult	Focus on annular repair model	4 weeks
2017	10.1016/j.phrs.2017.01.005	48	12; M	SD	1; C7-C8	Digital palpation, percutaneous puncture with 20G needle to depth of 4 mm	Immediately after insult	Systemic (IP delivery)	4 and 8 weeks

2017	10.1002/jor.23114	14	10; M	W	3; C5-C6 to C7-C8	Fluoroscopy guided percutaneous puncture with 21 or 25G needle to depth of 5 mm	No treatment	No treatment	2, 6 weeks
2017	10.1002/jor.23350	46	350-400 g (~10-12 week); M	SD	3; C4-C5 to C6-C7	Open surgery, puncture with 27G to depth of 4 mm	3, 14, or 30 days post injury	Open surgery; intradiscal delivery of 5 µL through 33G, cells at 5×10^3 /disc	0, 1, 7, or 14 days post treatment
2017	10.18632/oncotarget.14389	40	12; M	SD	1; C5-C6 to C7-C8	Fluoroscopy guided percutaneous puncture with 21G needle to depth of 5 mm	At the time of insult; 9 more doses given over the next 15 days	Percutaneous puncture; Intradiscal delivery of 2 µL through 31G	4 weeks
2017	10.1007/s12640-016-9676-7	40	10; M	W	3; C6-C7 to C8-C9	Digital palpation + fluoroscopy guided percutaneous puncture with 21G needle until tactile resistance from contralateral AF was observed	Immediately after insult	Percutaneous puncture; intradiscal delivery of 2 µL through 30G	2 or 21 days
2017	10.1016/j.yexcr.2017.08.011	60	12; no sex specified	SD	1; C6-C7	Open surgery, puncture with 31G needle to depth of 1.5 mm	At the time of insult	Open surgery; intradiscal delivery through 31G, no volume stated	4 weeks
2017	10.1117/12.2255761	5	12; F	SD	3; no details	Fluoroscopy guided percutaneous puncture with 20G needle until contralateral AF was reached	30 minutes following insult, and daily for 5 days	Systemic (ultrasound exposure)	5 days
2016		44	12; M	SD	2; C7-C8, C8-C9	Digital palpation guided percutaneous puncture with 20G needle to depth of 5 mm	No treatment	No treatment	4, 8, 12, 24 weeks post-surgery

2016	10.1007/s10735-015-9651-2	40	8-10; M	W	1; C6-C7	Open surgery, puncture with 20G needle to depth of 5 mm	No treatment for caudal model	No treatment for caudal model	5 weeks
2016	10.3390/ijms17020147	Stage 1: 12; Stage 2: 60	8; M	Lewis (L)	2; C6-C7, C8-C9	Fluoroscopy guided percutaneous puncture with 18 or 22G needle.	At time of insult, 2 weeks, or 4 weeks after insult	Intradiscal; no needle gauge discussed for treatment delivery; cells delivered at 1×10^4 /disc	8 Weeks
2016	10.1590/1413-785220162401152960	12	12; M	W	3; C6-C7 to C8-C9	Fluoroscopy guided percutaneous puncture with 20G needle	No treatment	No treatment	15 or 28 days post puncture
2015	10.1016/j.biomaterials.2015.02.024	32	12; no sex specified	SD	2; C5-C6, C7-C8	Open surgery puncture with 21G needle to depth of 5 mm	2 weeks	Fluoroscopy guided percutaneous puncture; intradiscal delivery of 2 μ L through 31G	6 weeks after initial puncture (4 weeks after treatment)
2015	10.1590/S0102-865020150080000009	14	300-350 g (~8-10 week); M	W	3; C7-C8 to C9-C10	Digital palpation + fluoroscopy guided percutaneous puncture with 21G needle	At the time of puncture	Percutaneous intradiscal delivery of 2 μ L through 30G	2, 15, 42 days
2015	10.1097/BSD.0000000000000141	25	12; M	L	2; C7-C8, C8-C9	Digital palpation + fluoroscopy guided percutaneous puncture with 18G needle to depth of 5 mm	4, 6, 8 weeks post puncture	Digital palpation percutaneous puncture; intradiscal delivery of 5 μ L through 27G	6 weeks post treatment
2015	10.1016/j.actbio.2015.06.006	35	10-12; no sex specified	AN	1; C3-C4	Open surgery, puncture with 18G needle	At time of insult	Focus on annular repair model	5 and 18 weeks
2014	10.1371/journal.pone.0113161	19	300-350 g (~8-10 week); M	W	2; C6-C7, C8-C9	Digital palpation guided percutaneous puncture with 21G needle to contralateral AF	At time of insult	Intradiscal; 2 μ L through 30G	15 days after the disc puncture

2014	10.1016/j.spinee.2014.03.050	12	12; no sex specified	W	6; no details	Fluoroscopy guided percutaneous puncture with 27G needle	At time of insult	Intradiscal; 50 μ L through 27G	2 or 4 weeks
2014	10.1016/j.spinee.2013.11.034	272	12; no sex specified	SD	2; C5-C6, C7-C8	Digital palpation + fluoroscopy guided percutaneous puncture with 21G needle to depth of 5 mm	6 weeks post insult	Percutaneous intradiscal delivery of 2 μ L through 31G	2, 4, 8, 12, and 24 weeks post treatment
2014	10.1097/BRS.0000000000000194	24	190-250 g (~8-10 week); M	AN	1; C3-C4	Independent sets testing open surgery and percutaneous punctures, both with 18G needle	At time of insult	Focus on annular repair model	1 and 3 months
2014	10.1097/BRS.0000000000000103	42	10-12; M	AN	1; C3-C4	Open surgery, puncture with 18G needle	At time of insult	Focus on annular repair model	5 weeks
2014	10.1177/0885328213515034	N/A	12; M	SD	3; C4-C5, C5-C6, C7-C8	Open surgery, puncture with 21G needle	4 weeks post insult	Intradiscal; unknown volume, through 31G	8 weeks post treatment
2013	10.1016/j.actbio.2013.08.019	96	12; M	SD	2; C7-C8, C8-C9	Digital palpation percutaneous puncture with 20G needle to depth of 5 mm	2 weeks post injury	Intradiscal; 2 μ L through 31G, cells at 1×10^6 cells/mL	4, 8, 16, 24 weeks post treatment
2013	10.3892/mmr.2013.1450	30	200-250 g (~6-8 week); M	SD	2; C5-C6, C7-C8	Fluoroscopy guided percutaneous puncture with 21G needle	4 weeks post insult	Intradiscal delivery; 2 μ L through 31G	2 or 4 weeks post treatment
2013	10.1186/ar4224	N/A	26-32; no sex specified	SD	1; C6-C7	Open surgery with fluoroscopy to confirm appropriate depth; puncture with either 26G, 22G, or 18G	No in vivo treatment	No in vivo treatment	2 weeks
2013	10.1590/1414-431X20122429	16	300-350 g (~8-10 week); M	W	2; C6-C7, C8-C9	Digital palpation + fluoroscopy guided puncture with 20G needle, until resistance from contralateral AF was observed	No treatment	No treatment	7 or 30 days post puncture

2013	10.1016/j.spinee.2013.01.040	8	8; M	L	2; C6-C7, C8-C9	Digital palpation + fluoroscopy guided puncture with 18G needle	No treatment	No treatment	8 weeks post puncture
2013	10.1590/S1413-78522013000300003	3	12; M	W	2; C6-C7, C8-C9	Digital palpation, percutaneous puncture with 20G needle	No treatment	No treatment	0, 15, 30 days
2011	10.3171/2011.5.SPINE10811	32	12; M	SD	2; C5-C6, C7-C8	Fluoroscopy guided percutaneous puncture with 21G needle to depth of 5 mm	No treatment	No treatment	3, 10, 17, 42 days
2010	10.1016/j.spinee.2010.08.013	36	12-14; M	L	2; C6-C7, C8-C9	Digital palpation + fluoroscopy guided percutaneous puncture with 18, 20, or 22G needle to depth of 5 mm	No treatment	No treatment	2, 4, 6, 8 weeks
2009	10.1186/ar2861	30	12; no sex specified	SD	2; C5-C6, C7-C8	Open surgery using fluoroscopy to guide puncture depth; puncture using 21G needle to depth of 5 mm	4 weeks post insult	Intradiscal delivery of 2 μ L through 31G	2 weeks post treatment
2009	10.3171/2009.4.SPINE08744	72	200-250 g (~6-8 week); M	SD	2; C4-C5, C8-C9	Open surgery, puncture with 21G needle to depth of 3 mm	No treatment on caudal model	No treatment on caudal model	2 weeks
2009	10.3171/2009.2.SPINE08925	9	12; M	SD	2; C5-C6, C7-C8	Open surgery + fluoroscopy guided puncture with 18G or 21G to depth of 5 mm	No treatment	No treatment	3 months
2009	10.1097/BRS.0b013e31819c09c4	36	32-36; no sex specified	SD	1; C6-C7	Fluoroscopy guided percutaneous puncture with 18, 22, or 26G needle to depth of 2 mm	No treatment	No treatment	1, 2, 4 weeks

2008	10.1097/BRS.0b013e31817c64a9	163	12; M	SD	2; C7-C8, C8-C9	Digital palpation + fluoroscopy guided percutaneous puncture with 20G needle either to depth of 5 mm or through contralateral aspect of tail	No treatment	No treatment	1, 2, 4 weeks
2007	10.1097/BRS.0b013e31815b9850	48	12; sex not specified	SD	3; C5-C6 to C7-C8	Open surgery and disc stab with number 11 blade, then fluoroscopy guided percutaneous puncture with 23G needle to depth of 1.5 mm (either single stab or triple stab)	No treatment	No treatment	Single-stab discs were examined 4, 7, 14, 28, and 56 days. Triple-stab discs were examined 9, 14, 28, and 56 days
2007	10.1097/01.brs.0000251013.07656.45	24	12; sex not specified	SD	3; C5-C6 to C7-C8	Open surgery, stab with number 11 blade to depth of 1.5 mm	No treatment	No treatment	4, 7, 14, 28 days

E.2 List of reviewed manuscripts and relevant experimental details extracted for goat/caprine models

Year	DOI	First/last author	Goat details	Lumbar level	Degeneration model	Implanted	Cell density	Study duration
2022	10.31083/j.fbl2704131	Yuan Q./Xu B.	N = 15 (female, 24 months, ~48kg)	L2/3-L4/5	Discectomy	autologous BM-MSCs combined in gelatin spong matrix (5x5x2.5mm)	1 million cells (P3)seeded into gelatin sponge cube	4 and 24 weeks
2021	10.1016/j.spinee.2021.05.196	Fusco A./Schaer T.	N = 6	3 levels	Chondroitinase (Ch) ABC (1 Unit)	noncrosslinked injectable hydrogel	-	-
2021	10.1089/ten.TEA.2020.0103	Zhang C./Smith L.J.	N = 10 (male, skeletally mature, castrated large frame)	L1-L5	ChABC	Hydrogel + allogeneic BM-MSCs (250uL syringe - injection volume was ~550 uL (using tactile feedback, the max. injectable vol.until ejection was observed refluxing into the needle track)	10 million cells/mL	12 and 14 weeks
2020	10.1002/jor.24639	Zhang C./ Smith L.J.	N = 9 (male, large framed ~ 3 years)	L1-L5	Nucleotomy or ChABC (1 or 5 Units)	degeneration model	-	12 weeks
2019	10.1186/s13018-019-1188-8	Yin S./Liu M.	N = 8 (female, chinese guanzhong, 24 months old, 35 - 45 Kg)	L2-L4	bone cement blocking EP nutritional pathway	degeneration model	-	2, 12, 24 and 48 weeks
2019	10.1016/j.joca.2019.02.508	Sun Y./Leung V.	N = 4	L2/3 and L4/5	ChABC (0.5 U/ML, 200ul)	Alginate-bovine NP cells	-	6 months
2018	10.1126/scitranslmed.aau0670	Gullbrand S.E/Mauck R.L.	N = 7 (male, large framed)	cervical	-	eDAPS	-	4 and 8 weeks
2017	10.1016/j.joca.2016.08.006	Gullbrand S.E./Smith L.J.	N = 9 (male, large framed ~ 3 years)	L1-L5	Nucleotomy or ChABC (0.5, 1 or 5 Units)	degeneration model	-	Up to 12 weeks
2016		Xu T./Shen Q.	N = 6 (male and female, 6 months)	L4/5	5 mm incision	degeneration model	-	4 weeks
2015	10.1007/s00586-015-3803-7	Detiger S.E./Hoogendoorn R.J.	N = 12 (female, adult dutch milk goats)	L1-L5	ChABC (0.25 U/mL)	100 ul PBS suspension of AD-MSCs (stromal vascular fraction)	1x10 ⁵ or 1x10 ⁶ cells in 100ul	3 months before treatment; 3 months regeneration

2015	10.1089/biores.2015.0025	Peeters M./Helder M.N.	N = 7 (female, adult dutch milk goats)	L1-L6	ChABC (0.25 U/mL)	FB/HA hydrogel with BMPs	-	12 weeks before treatment; 12 weeks regeneration
2011	10.1097/BRS.0b013e3181f60b39	Zhang Y./Anderson D.G.	N = 6 (male, Nubian goats, ~ 4 years)	L1-L4	1) #10 blade inserted parallel; 2) #15 inserted parallel then vertically; 3) drill bit (D=4.5mm, 15mm depth and 360 degree rotation)	degeneration model	-	2 months
2011	10.1097/BRS.0b013e3181d10401	Zhang Y./Anderson D.G.	N = 24 (male, Nubian goats, ~ 4 years)	L1/2 and L3/4	#15 blade	Hydrogel + BM-MSCs	2.5x10 ⁵ cells in 40 uL (10uL PBS + 30 UL hydrogel)	3 and 6 months
2008	10.1097/BRS.0b013e31816c90f0	Hoogendoorn R.J./Wuisman P.I.	N = 12 (female, skeletally mature dutch milk goats)	L1-L6	ChABC (0.25 U/mL)	degeneration model	-	12, 18 and 26 weeks
2007	10.1097/BRS.0b013e31811ebac5	Hoogendoorn R.J./Helder M.N.	N = 29 (female, skeletally mature dutch milk goats, >3.5 years, ~68 kg)		longitudinal: 0.25 U/ml or ChABC (0.2, 0.25, 0.3 and 0.35 U/mL)	degeneration model	-	Longitudinal: 4, 8, 12, 18 and 26 weeks; Concentrations: 12 weeks

E.3 Full geometrical analysis of goat lumbar disc L1-2 to L5-6 (N = 3)

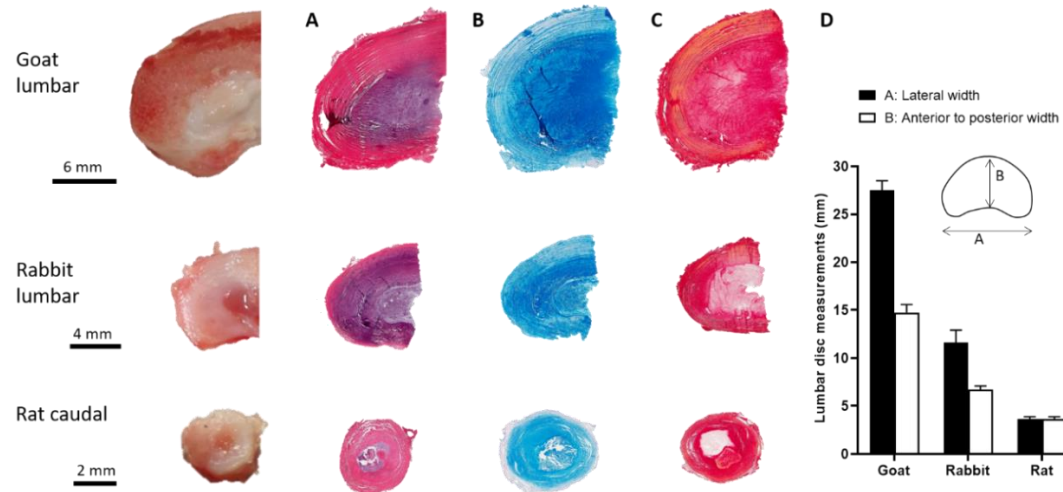
L1-2	Posterior thickness	Minimum thickness	Central thickness	Anterior thickness	Anterior to posterior (A-P) width	Half lateral width	Lateral width	Offset	Anterior to posterior (NP)	Half Lateral width (NP)	Lateral width (NP)	Offset (NP)
D1	6.43	2.42	4.05	10.24	17.40	12.74	25.47	3.85	10.99	9.67	19.34	3.00
D2	5.82	2.90	4.21	8.42	18.17	13.41	26.82	3.76	11.32	10.73	21.45	3.01
D3	4.55	3.94	5.90	7.99	17.60	12.68	25.35	4.40	12.15	9.91	19.82	2.76
Average	5.60	3.09	4.72	8.89	17.72	12.94	25.88	4.00	11.49	10.10	20.20	2.92
STD	0.96	0.77	1.03	1.19	0.40	0.41	0.82		0.60	0.55	1.11	
L2-3	Posterior thickness	Minimum thickness	Central thickness	Anterior thickness	Anterior to posterior (A-P) width	Half lateral width	Lateral width	Offset	Anterior to posterior (NP)	Half Lateral width (NP)	Lateral width (NP)	Offset (NP)
D1	5.53	2.32	2.78	6.34	16.52	12.13	24.26	4.25	10.20	9.88	19.76	5.30
D2	5.33	2.13	3.13	6.60	16.94	12.61	25.22	4.80	8.30	9.13	18.25	6.16
D3	5.21	3.15	4.41	7.86	17.02	13.59	27.18	6.47	9.03	9.76	19.52	3.53
Average	5.35	2.53	3.44	6.93	16.83	12.78	25.55	5.17	9.18	9.59	19.18	5.00
STD	0.16	0.55	0.86	0.81	0.27	0.74	1.49		0.96	0.40	0.81	
L3-4	Posterior thickness	Minimum thickness	Central thickness	Anterior thickness	Anterior to posterior (A-P) width	Half lateral width	Lateral width	Offset	Anterior to posterior (NP)	Half Lateral width (NP)	Lateral width (NP)	Offset (NP)
D1	3.62	2.30	3.49	6.18	15.24	12.46	24.92	3.41	8.81	9.88	19.76	3.57
D2	5.21	3.25	4.79	8.22	18.30	13.97	27.95	6.55	11.38	11.10	22.20	3.28
D3	3.27	2.52	3.47	6.89	16.23	13.12	26.24	4.32	9.80	8.81	17.62	3.31
Average	4.03	2.69	3.92	7.10	16.59	13.18	26.37	4.76	10.00	9.93	19.86	3.38
STD	1.03	0.50	0.76	1.04	1.56	0.76	1.52		1.30	1.15	2.29	

L4-5	Posterior thickness	Minimum thickness	Central thickness	Anterior thickness	Anterior to posterior (A-P) width	Half lateral width	Lateral width	Offset	Anterior to posterior (NP)	Half Lateral width (NP)	Lateral width (NP)	Offset (NP)
D1	5.52	2.54	3.69	5.99	15.02	13.18	26.36	1.36	9.16	9.04	18.08	3.30
D2	6.85	3.35	4.81	10.09	16.68	12.33	24.66	3.05	10.58	12.41	24.82	2.56
D3	6.27	2.94	3.57	7.78	15.69	14.99	29.99	2.75	10.05	12.12	24.25	2.13
Average	6.21	2.95	4.02	7.95	15.80	13.50	27.00	2.39	9.93	11.19	22.38	2.66
STD	0.67	0.41	0.68	2.06	0.84	1.36	2.72		0.71	1.87	3.74	
L5-6	Posterior thickness	Minimum thickness	Central thickness	Anterior thickness	Anterior to posterior (A-P) width	Half lateral width	Lateral width	Offset	Anterior to posterior (NP)	Half Lateral width (NP)	Lateral width (NP)	Offset (NP)
D1	7.28	3.55	4.92	8.22	14.43	16.10	32.20	3.32	8.27	9.72	19.43	3.71
D2	7.19	4.52	6.97	9.58	15.41	15.71	31.41	2.93	8.72	11.77	23.55	4.85
D3	7.00	4.44	6.65	8.77	15.47	15.26	30.52	1.50	8.51	12.46	24.91	1.92
Average	7.15	4.17	6.18	8.86	15.11	15.69	31.38	2.58	8.50	11.31	22.63	3.49
STD	0.14	0.54	1.10	0.69	0.58	0.42	0.84		0.22	1.43	2.85	

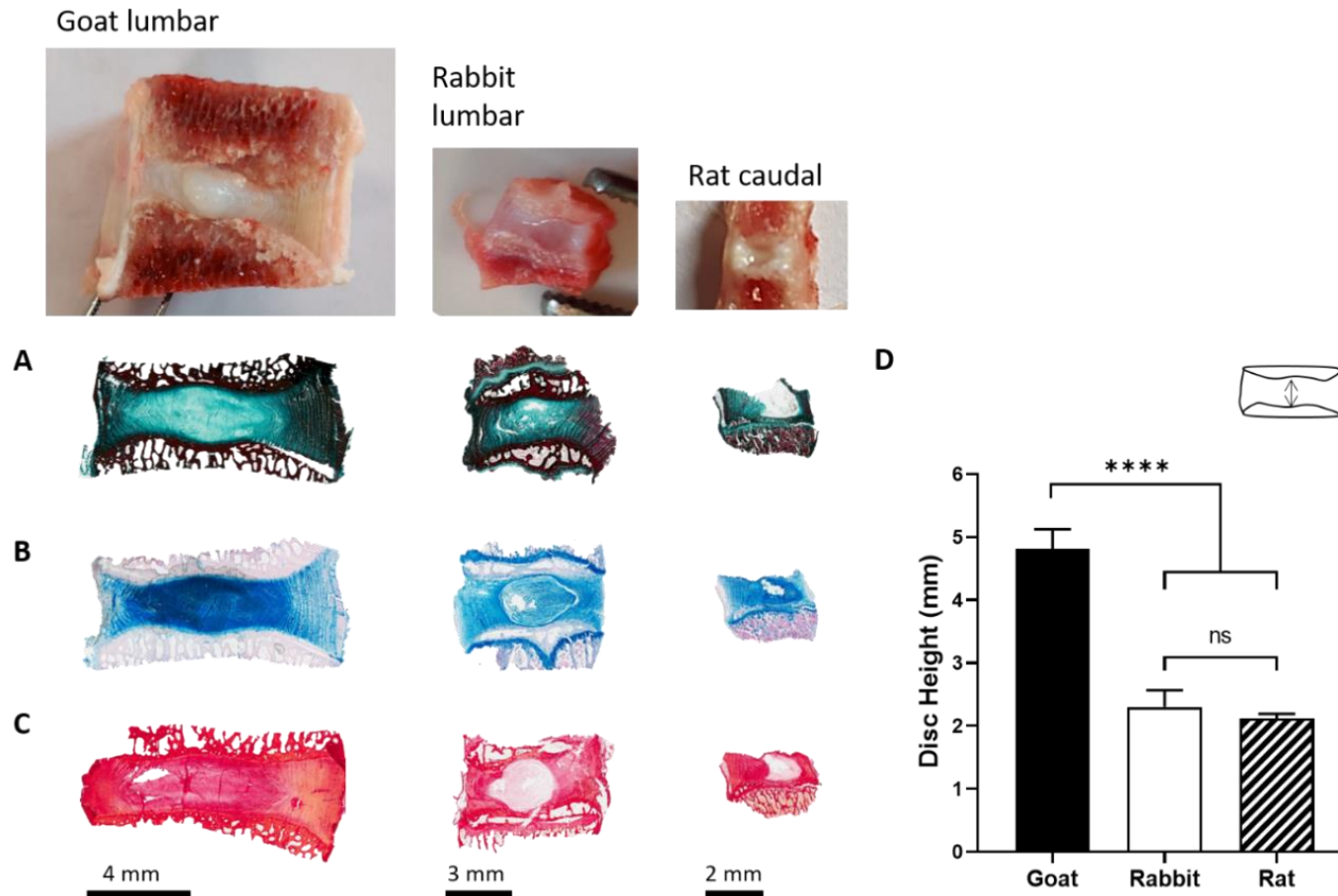
E.4 List of studies using Seahorse Flux analysis on disc cells

Cell type	Test	Passage	Cell density	Normalised	Control values	Hypothesis/finding	Ref.
Rat and human NP cells	Substrate (bafilomycin) + antimycin A	P1-P4	XF24 15,000 cells/well	To protein (µg)	ECAR (mpH/min): 1 – 3.5 OCR (pmol/min): 3 – 8	Inhabitation of autophagy results in no change in ECAR, however a slight reduction in basal OCR.	376
Rat NP cells	Basal metabolic assay + antimycin	-	XF24 15,000 cells/well	Total protein (BCA assay)	ECAR (mpH/min): 1.5 – 2.5 OCR (pmol/min): 8 – 11	Basal ECAR and OCR relatively low, especially OCR (10-fold lower than other cell types). Inhibition of ETC (Ant. A) no effect on ECAR or OCR, confirming NP rely minimally on mitochondria for energy production.	324
Rat NP cells	Other + antimycin A	-	XF24 15,000 cells/well	Total protein (BCA assay)	ECAR (mpH/min): 2 – 5 OCR (pmol/min): 5 – 8	Silencing Carbonic Anhydrase III (notochordal NP marker) had no effect on ECAR, total or mitochondrial OCR before Ant. A treatment. No effect on relative contribution of glycolysis and CO ₂ hydration to extracellular proton production rate.	377
Rabbit NP and AF cells	Mito stress test - Oligomycin + FCCP +2DG + rotenone	P1	XF96 10,000 - 15,000 cells/well	Protein per well (Crystal Violet Dye)	ECAR (mpH/min): 1 – 12 (NP) and 1 – 25 (AF) OCR (pmol/min): 9 – 12 (basal NP and AF)	Aging significantly reduced glycolytic and mitochondrial reserve capacity, maximum aerobic capacity, and non-glucose-dependent respiration in NP cells. AF cells did not show changes in mitochondrial respiration with age but did see an increase in glycolysis.	323
Rat NP cells	Other + antimycin A	P2-P4	XF24 20,000 cells/well	Normalised to (µg protein)	ECAR (mpH/min): 0.25 – 1.75 OCR (pmol/min): 3 – 11	Inhibition of HuR (regulator of HIF-1a) in NP saw sig. decrease in ECAR and mito. OCR and acidic pH, without appreciable changes in total OCR - likely due to decreased Ca12 expression in HuR silenced cells.	378
Human NP cells	Mito stress test - Oligomycin + FCCP +2DG + rotenone	-	XF96 80,000 cells/well	Cell number per well (Trypan Blue exclusion assay)	ECAR (mpH/min): 15 – 40 (non-senescent) 40 – 110 (senescent) OCR (pmol/min): 25 – 60 (non-senescent) 25- 210 (senescent)	Basal OCR and ECAR, as well cellular reliance upon glycolysis and oxidative phosphorylation, were recorded through the addition of metabolic inhibitors (oligomycin, FCCP, 2DG and rotenone + ant. A). Results showed increased basal and ATP-linked respiration in senescent compared to non-senescent disc cells.	213
Rat NP cells	Other + antimycin A	-	XF24 15,000 cells/well	To protein (µg)	ECAR (mpH/min): 1 – 2 OCR (pmol/min): 8 – 14	Inhibition of H ⁺ /lactate efflux decreased ECAR without increasing mito. OCR, resulting intracellular lactate accumulation increases HIF-1a activity (responses to oxygen-deficiency for survival/ growth).	325
Rat NP cells	Other + antimycin A	-	XF24 15,000 cells/well	To protein (µg)	ECAR (mpH/min): 2 – 5 (NX) 1 – 3 (HX-re-oxy.) OCR (pmol/min): 8 – 15 (NX) and 10 – 18 (HX-re-oxy.)	ECAR of NP cells was investigated under normoxia and hypoxia-re-oxygenation before and after Ant. A treatment. A small increase in basal OCR but decrease in mitochondrial OCR was seen after re-oxygenation of hypoxic cells.	379

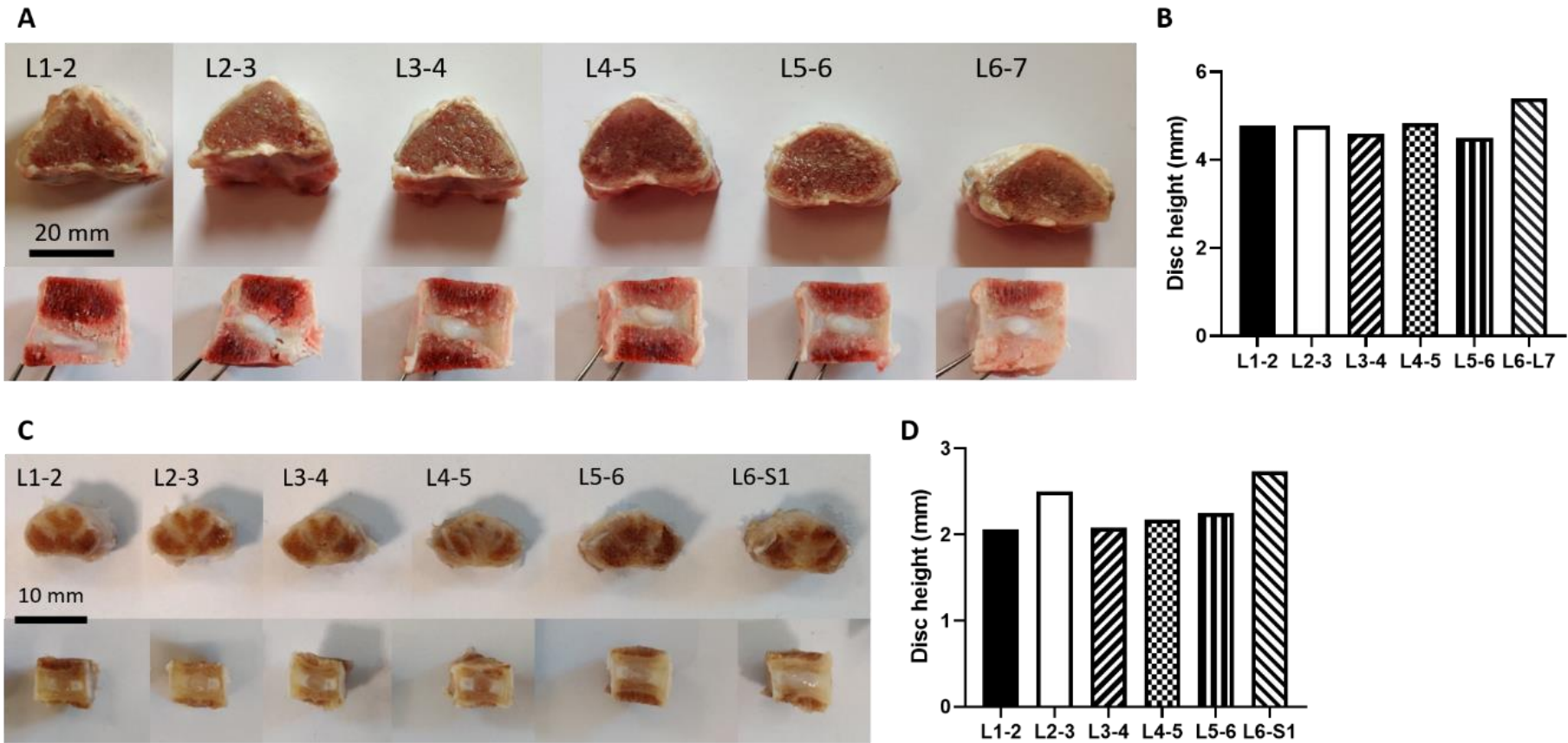
E.5 Miscellaneous species histology – including lapin/rabbit lumbar



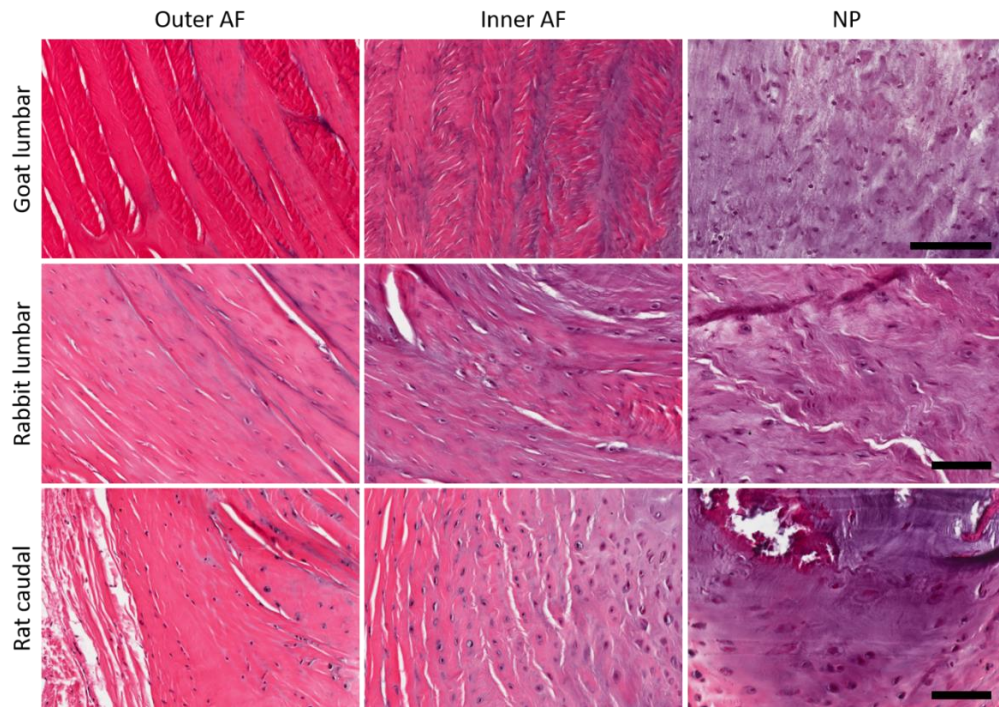
Histological evaluation and geometrical analysis of goat lumbar, rabbit lumbar and rat caudal discs in the transverse plane. (A) Hematoxylin and eosin (H&E) staining indicating the cellular distribution between regions of the disc and species. **(B)** Alcian blue indicating the native GAG distribution across the species, with a nuclear fast red counterstain. **(C)** Histological staining of collagen distribution using picosirius red. **(D)** Geometrical measurements of discs from different species in the transverse plane.



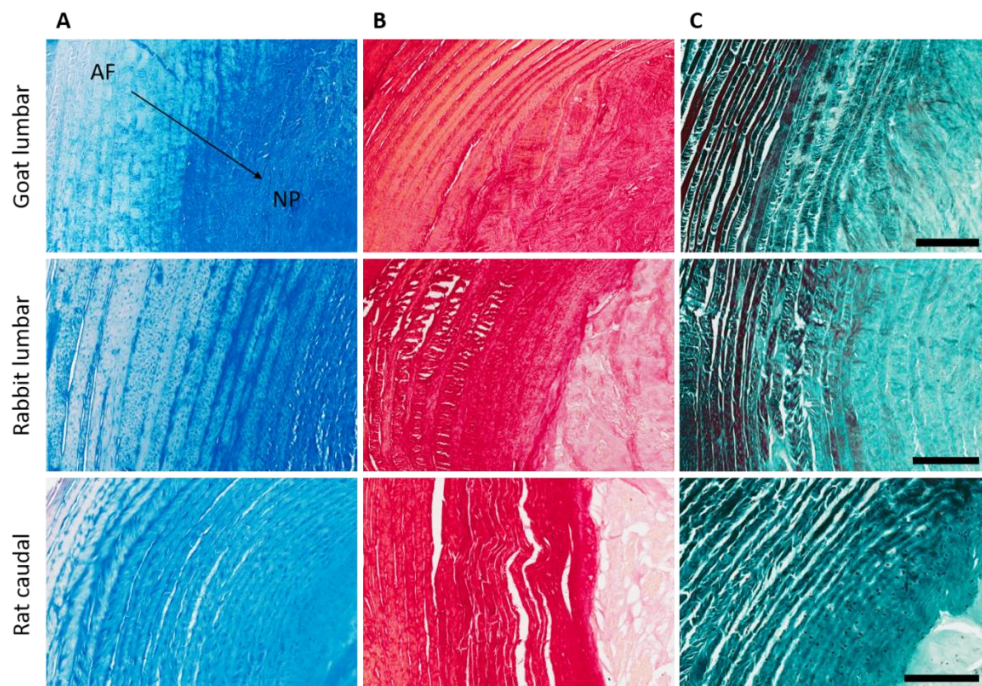
Histological evaluation and geometrical analysis of goat lumbar, rabbit lumbar and rat caudal discs in the sagittal plane. (A) Goldner's method of trichrome staining the nuclear chromatin a brownish black, the cytoplasm red, collagen green and blood cells orange. **(B)** Alcian blue staining the GAGs with a nuclear fast red counterstain. **(C)** Histological staining of collagen across species using picrosirius red. **(D)** The central disc height compared between species. It is the most important geometrical measurement in the sagittal plane. Ns denotes no significance and **** indicates $P < 0.001$.



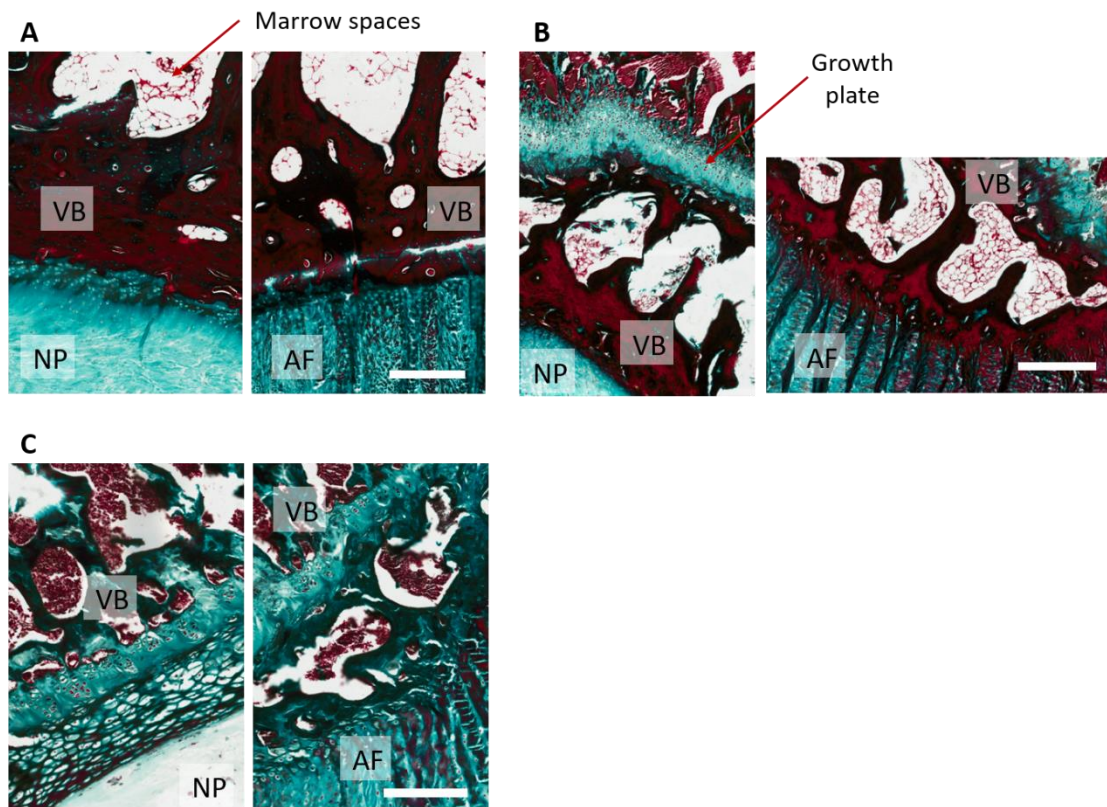
Additional photos for geometrical analysis of goat and rabbit lumbar discs. (A) Lateral and sagittal images of goat discs from each lumbar level. **(B)** Central disc height of each lumbar level of the goat, measured from the sagittal plane (n=1). **(C)** Lateral and sagittal images of rabbit discs from each lumbar level. **(D)** Central disc height of each lumbar level of the rabbit, measured from the sagittal plane (n=1).



Histological staining of the outer annulus fibrosus (oAF), inner annulus fibrosus (iAF) and the nucleus pulposus (NP) with H&E. Histological slices shown are from the lateral plane. The scale bar is 300 μm for the goat lumbar and 100 μm for both the rabbit lumbar and the rat caudal disc. Hematoxylin stains the cell nuclei blue and eosin stains the extracellular matrix and cytoplasm pink.

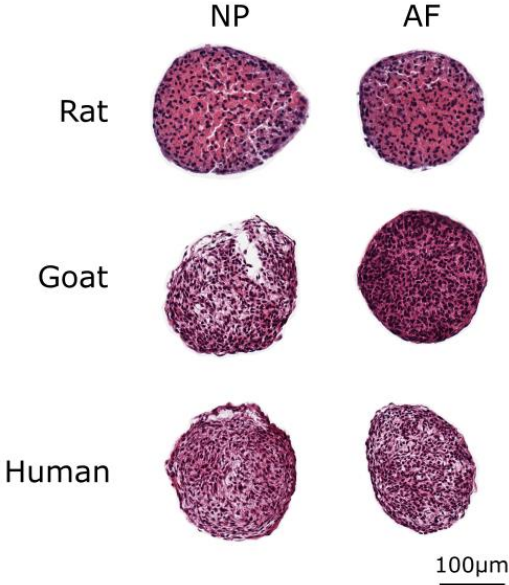


Histological staining of the transition from annulus fibrosus (AF) to nucleus pulposus (NP) across the three animal species. (A) Alcian blue indicating native sGAG distribution. (B) Picrosirius staining indicating collagen distribution. (C) Goldner's method of trichrome staining nuclear chromatin a brownish black, the cytoplasm red, collagen green and red blood cells orange. The scale bar is 300 μm for the goat lumbar and 100 μm for both the rabbit lumbar and the rat caudal disc.



Microscopic images of Goldner's method of trichrome staining at the interface of the vertebral body (VB) and the disc tissue. The interface is investigated at both the nucleus pulposus (NP) and the annulus fibrosus (AF) regions of the disc tissue. The method stains the nuclear chromatin a brownish black, the cytoplasm red, collagen green and red blood cells orange. **(A)** Goat lumbar disc indicating the marrow spaces with its vascular sinusoids. Scale = 400 μm . **(B)** Rabbit lumbar disc indicating the growth plate running through the VB above the NP. Scale = 500 μm . **(C)** Rat caudal disc with a more notable cartilage endplate above the NP and more densely stained hematopoietic marrow elements. Scale = 200 μm .

E.6 Histological evaluation of metabolic spheroids



Hematoxylin and eosin (H&E) staining indicating the cellular distribution within rat, goat and human nucleus pulposus (NP) and anulus fibrosus (AF) spheroids after 7 days of culture.

Appendix F – Abstract

Lower back pain is a major global socio-economic concern, with the primary cause believed to be degeneration of the intervertebral disc (IVD). While the spine field is filled with a growing body of basic research and many promising regenerative therapies, the avascular nature of the IVD and its limited nutrient supply remain the greatest obstacles on the path towards clinical adoption of cell-based therapies. Subsequently, this thesis focuses on the importance of the nutrient microenvironment throughout the full development and assessment process, in order to accelerate the translation of therapies all the way from “bench to bedside”. Firstly, this work sought to consolidate early metabolite measurements and employ *in-silico* models, underpinned by more recent experimental parameters of degeneration and nutrient transport, with the objective of re-evaluating current knowledge in terms of grade-specific stages of degeneration. Secondly, this work aimed to characterise the local nutrient microenvironment of 2D cell monolayers, commonly used 3D *in vitro* culture systems and *ex vivo* disc organ culture systems in order to highlight the effect of culturing parameters and to place “standard practice” culturing conditions into context in terms of physiological relevance. The results revealed that large variations and gradients in metabolite concentrations are easily established without the careful consideration of key parameters and that this diversity currently exists across the research field and may explain heterogeneous results on the regenerative potential of cell therapies. Moreover, every culture system is unique and while one external concentration may be suitable for one culture configuration, it may not be appropriate for another. It is believed that with careful deliberation of the external boundary and *in vitro* culture design, harmony and standardisation of physiologically relevant local microenvironments will push towards greater reproducibility across the field and accelerate innovative therapeutics for clinical translation.

Even after demonstrating safety and efficacy in animals, many of these promising therapies appear to have stunted success in humans. This work presents *in-silico* models which correlate favourably to the pre-clinical literature in terms of the capabilities of animal regeneration and predict that compromised nutrition is not a significant challenge in small animal discs. On the contrary, this work highlights a very fine clinical balance between an adequate cell dose for sufficient repair, through de novo matrix deposition, without exacerbating the human microenvironmental niche. While these findings help to explain the failed translation of promising pre-clinical data and the limited results emerging from clinical trials at present, they also enable the research field and clinicians to manage expectations on cell-based regeneration. Moreover, this work provides a platform to inform the design of clinical trials, and as computing power and software capabilities increase, it is conceivable that the future holds the generation of patient-specific models which could be used for patient assessment, as well as pre- and intraoperative planning.